

EFFECT OF CO₂ INJECTION ON THE POROMECHANICAL AND MULTIPHASE FLOW
CHARACTERISTICS OF SUBSURFACE ROCK

BY

KISEOK KIM

DISSERTATION

Submitted in partial fulfillment of the requirements
for the degree of Doctor of Philosophy in Civil Engineering
in the Graduate College of the
University of Illinois Urbana-Champaign, 2022

Urbana, Illinois

Doctoral Committee:

Assistant Professor Roman Y. Makhnenko, Chair
Professor Albert J. Valocchi
Professor John S. Popovics
Professor Scott M. Olson
Dr. Steven G. Whittaker, Illinois State Geological Survey

ABSTRACT

Geologic carbon storage has a great potential in reducing atmospheric CO₂ emissions by permanently sequestering large volumes of carbon dioxide in reservoir formations sealed with tight rock. During CO₂ injection, multi-physical processes occur, affecting the mechanical stresses, pore pressures, temperature, and chemistry of the participating subsurface rocks and pore fluids. These processes are coupled, meaning that changes in each aspect do impact the others mutually. Thus, the interdependent factors need to be understood as a combined system, while it should also incorporate the time-dependent response, as CO₂ is projected to be stored for thousands of years.

Experimental techniques are introduced to characterize the poroviscoelastic and hydraulic behavior of reservoir rock, including two-phase flow, with CO₂ treatment tests conducted under high-pressure conditions. Berea sandstone is selected to represent silica-rich rock, while Apulian and Indiana limestones are chosen as calcite-rich rock. This study investigates the effect of CO₂ treatment on the compressibility, time-dependent response, and relative permeability.

The compressibility is measured for the selected materials and their composing minerals. By comparing pristine and CO₂ treated specimens, experiments reveal that the compressibilities of sandstone, quartz, and calcite minerals do not change, while the limestone's response can be affected by creating new connected and non-connected pores. Then, the effect of CO₂ treatment on the time-dependent response is investigated. In contrast to the compressibility measurements, it is reported that the treatment significantly promotes the time-dependent behavior of the sandstone and limestones. It is argued that the mechanism for the effect of CO₂ treatment is different for sandstone and limestones, where the dissolution of calcite is the main reason for the

changes in the properties of the latter ones, while the generation of microcracks due to stress corrosion is the main mechanism for silica-rich rock.

The hydro-mechanical-chemical constitutive model is adopted to address the coupled response of subsurface rock, with investigation of the impact of duration of CO₂ injection. The importance of considering the chemical aspect in the constitutive equations is highlighted by comparing the hydro-mechanical and hydro-mechanical-chemical coupling for the porosity change. Moreover, the multiphase flow response of water and CO₂ is experimentally studied with the impact of CO₂ treatment. A novel method to determine the degree of saturation for the relative permeability curve is introduced, and additional measurements of the microscale properties are conducted for the capillary pressure, wettability, and surface roughness. The experiments show that CO₂ treatment alters the relative permeability curve by increasing the permeability and maximum CO₂ saturation for the limestones, while no significant effect is observed for the sandstone.

Furthermore, the experimental techniques developed in this study are utilized for reporting the poromechanical and hydraulic properties of two shales and one granite representing the sealing layers for CO₂ storage. Ultra-low permeability of the sealing formations is accurately measured in a few month-long experiments and is coupled to the mechanical and pore network characteristics of the rock. By establishing the porosity-permeability relationship, the findings reveal that the exponent value for tight rock is significantly larger than that of porous rock, which is often misused. This implies that for tight rock, a small increase in porosity can result in a considerable change in permeability, which is crucial for the sealing layers.

In summary, this thesis provides a comprehensive experimental workflow aimed at characterizing the poromechanical and hydraulic response of representative rock types during CO₂ injection, where the time-dependent and chemical effects are also considered.

ACKNOWLEDGMENTS

I would like to sincerely acknowledge the following people for their support on this thesis.

First and foremost, I express my greatest and profound gratitude to my advisor, Professor Roman Y. Makhnenko. During the five years of PhD, he has shown another level of enthusiasm towards research, unfailing guidance, tremendous patience, and encouragement. On top of being a great advisor, he has been a great mentor, as I enjoyed our small talks about life. I still vividly remember the day we met at the lab, excited to run the first CO₂ injection test, although it was during extreme cold and snow on New year's eve in 2017. The high standard and discipline I learned from the rock mechanics group will always follow me.

I also would like to give my appreciation to the committee members for my PhD thesis, Professor Albert J. Valocchi, Professor John S. Popovics, Professor Scott M. Olson, and Dr. Steven G. Whittaker, for their insightful comments and productive discussions that helped me to finish this work. Also, the advice and small talks with my master's degree advisor Professor Hangseok Choi encouraged me a lot during my PhD.

The three years of Technip FMC fellowship I received financially supported me during my PhD, and I would like to acknowledge it.

I was lucky to be in the best rock mechanics research group, as I would like to thank Ali Tarokh, Gabriel Mishaan, Jose Ciocca, Nikita Bondarenko, Hyunbin Kim, and Ekaterina Barteneva. The heated research discussions during the group meetings helped me a lot to proceed with my study, and I appreciate their help in supporting some of my experiments.

I would also like to thank my colleagues for their academic support, where Dr. Hongbo Shao and Dmytro Lukhtai helped me continue my experiments at ISGS. Sangmin Lee and Sai Evani assisted me with ultrasonic wave velocity measurements. The mechanical shop always was there

for me, as they supported me in developing experimental devices and solving technical problems.

The mental support I had from my friends must be acknowledged, as it really helped me during the hard and good times of my PhD. I was very fortunate to be surrounded by the best Geotech colleagues, Thiero Kane, Ozgun Numanoglu, Vashish Taukoor, and Pouyan Asem, and I will always remember the time we spent in the basement of Newmark. My friends from high school, Donggyun Lim, Changhyun Kim, and Seokyoung Lee, always encouraged me. Byungkyu Kim, Sangyeob Kim, Jongchan Kim, Junseok Lee, Yoontaek Oh, Mingu Kang, Seokjae Lee, Hyobum Lee, and Hyunjun Choi from Korea University always emotionally supported me from far away. My online best friends at UIUC – Jade Kwon, Unchae Chung, Yeaguen Lee, Bonhyun Ku, and Changhee Son- inspired me greatly running through the PhD battle grounds together. Also, the invaluable moments I shared with my friends I met in church, Sooyeol Kim, Sunjoong Kim, Jaeseok Hwang, Woongbi Kwon, and Choonggi Rhee, will never be forgotten. Meeting my lifetime mentors, pastor Sangwon Shin and Doyeon Kim, was really one of the most grateful things I obtained during my PhD.

I would like to give my most sincere gratitude to my family. My parents and in-laws always supported me physically and mentally with unceasing prayers night and day. Most of all, my wife, Anne Lee, makes achieving the PhD degree the most meaningful, as studying at UIUC also allowed me to meet her. This PhD definitely would not have been available without her support and love. And of course, my beloved amazing daughter Sunny Kim and my soon-coming son are deeply appreciated, as they now make my life even more meaningful. Lastly, I thank god for his presence every step along the way and for all the blessings.

This thesis is dedicated to my respectful parents and in-laws for their unceasing prayers and encouragement with love. Most of all, a very special gratitude is expressed to my beloved wife Anne, wonderful daughter Sunny, and awaited son who is on his way.

TABLE OF CONTENTS

CHAPTER 1: INTRODUCTION	1
CHAPTER 2: METHODS	11
CHAPTER 3: CO ₂ INJECTION EFFECT ON GEOMECHANICAL AND FLOW PROPERTIES OF CALCITE-RICH RESERVOIRS	33
CHAPTER 4: CHANGES IN ROCK MATRIX COMPRESSIBILITY DURING DEEP CO ₂ STORAGE	68
CHAPTER 5: SHORT- AND LONG-TERM RESPONSES OF RESERVOIR ROCK INDUCED BY CO ₂ INJECTION	116
CHAPTER 6: DEVELOPMENT OF HYDRO-MECHANICAL-CHEMICAL MODEL DESCRIBING RESERVOIR ROCK RESPONSE DURING CO ₂ STORAGE	177
CHAPTER 7: EFFECT OF CO ₂ INJECTION ON THE MULTIPHASE FLOW RESPONSE OF RESERVOIR ROCK	203
CHAPTER 8: COUPLING BETWEEN POROMECHANICAL BEHAVIOR AND FLUID FLOW IN TIGHT ROCK	259
CHAPTER 9: IMPLICATIONS AND FUTURE WORK	308
CHAPTER 10: CONCLUSIONS	319

CHAPTER 1: INTRODUCTION

1.1 Problem Statement

The emission of greenhouse gases to the atmosphere has been widely recognized for its negative impacts on the global environment by warming the ecosystem, resulting in rapid changes in the atmosphere, ocean, and land (Cox et al., 2000; IPCC, 2007). Recent reports stated that carbon dioxide (CO₂) plays a dominant role among other greenhouse gases, as the global surface temperature has been increasing with the cumulative amount of CO₂ discharge (IPCC, 2005; 2021). Although it is unequivocal that CO₂ emission is warming the planet, fossil fuel combustion has been continuously growing to satisfy the global energy demand, accelerating the production of CO₂ (Anderson and Peters, 2016; Metz et al., 2005). As an effort to mitigate climate change, geologic carbon storage (GCS) has been introduced as a promising method to reduce the atmospheric emission of anthropogenic CO₂ (Bachu, 2008; IPCC, 2005).

The objective of GCS is to inject large volumes of CO₂ into geologic formations for long-term storage and to prevent its release into the atmosphere. The reservoir rock is carefully selected considering the sealing layers on the top (caprock) and bottom (basement rock), which should be low permeable and have high entry pressures to safely capture CO₂ (Nordbotten and Celia, 2012). The geologic formations targeted for CO₂ injection are usually deep saline aquifers with a total capacity of thousands of Gt, mostly comprised of sandstones and limestones (Guéguen and Palciauskas, 1994; IPCC, 2005). For caprock, claystones are the typical representative materials due to their low permeability, while crystalline formations usually serve as the basement rocks (Orr, 2009).

As the main objective of GCS is to store the injected CO₂ securely, the trapping mechanisms need to be considered for efficient storage, and they include structural and stratigraphic trapping,

residual trapping, solubility trapping, and mineral trapping (Gunter et al., 2004; IPCC, 2005). During the CO₂ storage process, the injected CO₂ plume rises due to buoyancy, and the structural and stratigraphic trapping occurs at the micropore level, preventing leakage through the caprock layer. Also, as CO₂ acts as the non-wetting phase in the water-wet system, residual trapping takes place in the small pores, where the injected CO₂ remains as a stagnant residual phase due to drainage/imbibition processes that are closely related to the storage capacity. While CO₂ may dissolve and generate an acidic solution (solubility trapping) that can induce chemical reactions with the reservoir formations (mineral trapping), these reactions are considered to play a significant role at the later stages of the injection, while the first two trapping mechanisms are dominating the initial injection processes (IPCC, 2005). Nevertheless, it is vital to properly assess the pore-scale mechanism and capillary pressure of the reservoir formations, which are also coupled with the relative permeability functions (Craig, 1971).

Based on the trapping mechanisms above, this study investigates the poromechanical and multiphase flow responses of subsurface rock that are directly related to safe and efficient CO₂ storage. As high-pressure CO₂ is injected into the reservoir, an instant and direct poromechanical response occur due to the pore pressure increase, decreasing the effective stress tensor (Rutqvist, 2012). Thus, the stress state would migrate closer to the failure conditions, accompanied by mechanical deformation from overpressure that may jeopardize the system's stability and result in induced seismicity and reactivation of faults (Bachu, 2003). Furthermore, while the poromechanical response of porous rock incorporates both elastic and inelastic behavior, it is vital to concentrate mainly on the elastic response for GCS, because any inelastic behavior should be avoided to exclude large deformations and failure. Thus, considering the permanent time scale of carbon storage (up to thousands of years), the poroelastic response of the involved

formation needs to be extensively examined for both short-term (poroelasticity) and long-term behavior (poroviscoelasticity), and it can be done by adopting the constitutive models that include the immediate and time-dependent deformation (Coussy, 2004; Cheng, 2016; Yarushina and Podladchikov, 2015).

Another important aspect that needs to be assessed is the multiphase flow behavior, as it is closely related to the CO₂ injectivity, migration of the CO₂ plume, and storage capacity (Bachu and Bennion, 2008; Krevor et al., 2013). The two-phase flow of water and CO₂ in the reservoir can be described by the relative permeability, since most reservoir formations are infiltrated with aqueous fluid. Understanding the multiphase flow phenomenon is a complex task, as it involves knowledge of the hydromechanical response, interaction between the wetting and non-wetting fluids, and capillary forces at pore scale (Kumar et al., 2005; Spiteri et al., 2005; Kopp et al., 2009; Bachu, 2013).

After injection, the plume of high-pressure CO₂ rises due to buoyancy and reaches the caprock, which may end up in undesirable leakage to the upper aquifers (Cavanagh and Haszeldine, 2014). Besides, for cases where the injection happens near the basement rock, there exist risks that the injected fluid may affect the ambient pore pressure and trigger seismic activities (Dyer et al., 2008; Evans et al., 2012). Thus, the poromechanical and hydraulic characteristics of the sealing layer need to be studied. The fluid flow through the subsurface rock is directly affected by the in-situ stress state, changes in which may alter the pore structure and modify the flow paths (Biot, 1973). Thus, coupling the mechanical and hydraulic properties of the participating formations is a requisite that can be accomplished by establishing the porosity-permeability relationship (Bernabé et al., 2003). For GCS, understanding these responses is of great interest since the stability in terms of leakage needs to be evaluated for the tight sealing layers, as in many cases,

the measurements of the material properties are limited (Trimmer, 1981). Moreover, as the porosity-permeability relationships are often misused between the porous and tight rock, accurately evaluating their applicability is vital for the proper reservoir modeling (Zhang et al., 2015).

On top of the poromechanical and hydraulic responses occurring during CO₂ injection, the chemical aspect can complicate the problem (Wawersik et al., 2001). As the injected CO₂ generates an acidic mixture of brine and CO₂, it may chemically react with the composing minerals of the reservoir rock. Consequently, the poromechanical and hydraulic responses - the short- and long-term deformation, relative permeability, and the porosity-permeability relationship, may be affected by CO₂ injection. Therefore, understanding coupled hydro-mechanical-chemical (HMC) response of the subsurface formations to CO₂ treatment becomes essential for safe long-term storage (Figure 1.1). As the injected CO₂ is at a lower temperature than the adjacent rock due to the geothermal gradient, the thermal stresses are induced (Vilarrasa et al., 2013). This effect is not considered in this study to simplify the problem, as it allows to focus on the chemical effect of CO₂ treatment on the poromechanical and hydraulic characteristics during GCS (Figure 1.2). Moreover, the thermal effect on the properties of reservoir rock is not that significant for the temperature gradients of 20-30 °C considered for a few km depth storage (Somerton, 1992)

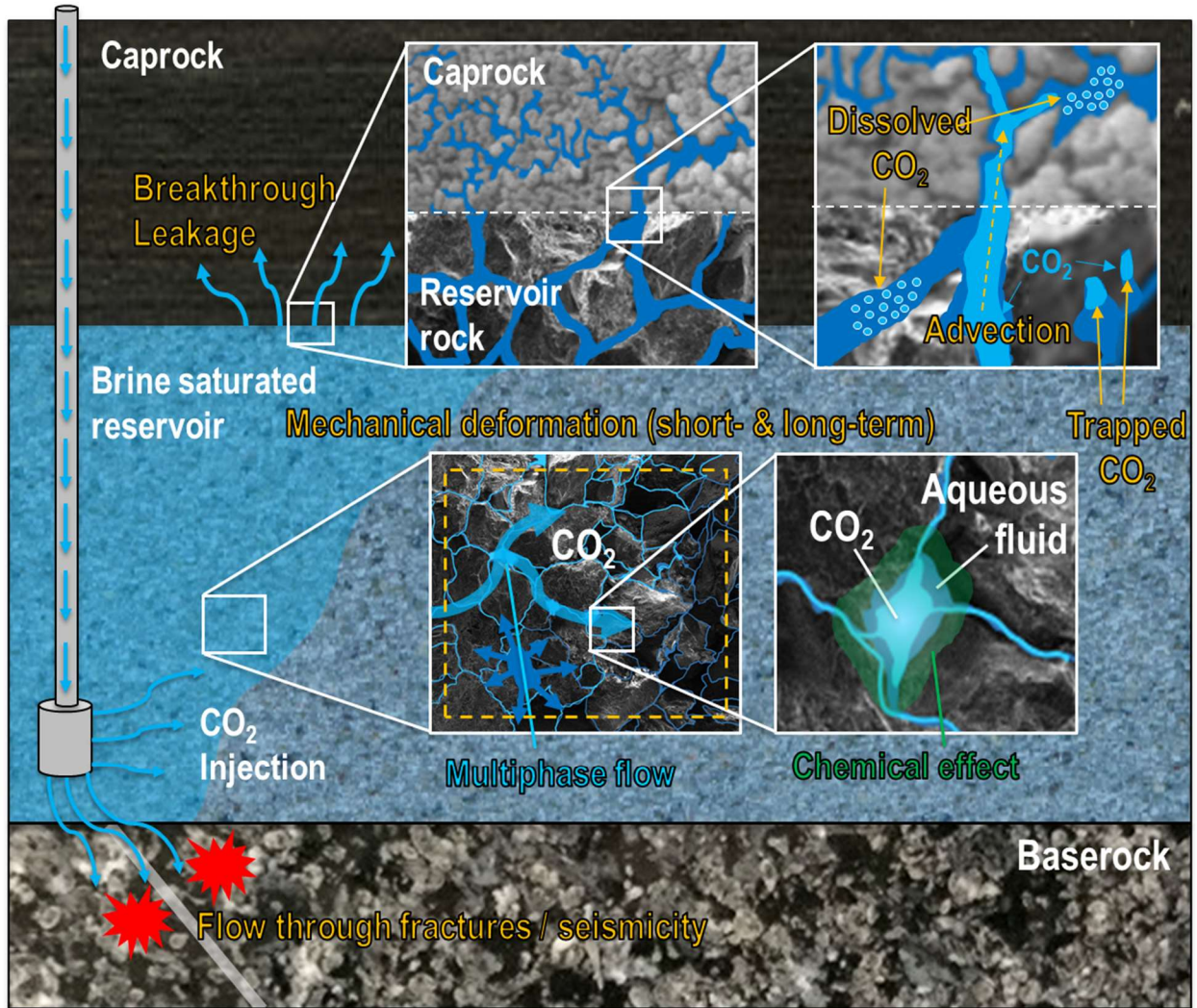


Figure 1.1. Schematic illustration of the geological carbon storage system and potential risks.

1.2 Research Objective

This study involves a large set of laboratory experiments aimed at measurements of the poroviscoelastic and hydraulic properties of reservoir rock and sealing layers. The parameters and constitutive models adopted to explain the multi-physical behavior of the materials are presented. Experimental methods are introduced to accurately measure the compressibility, time-dependent behavior, and multiphase flow properties, and evaluate the coupling parameters. The chemical effect of CO₂ injection is investigated by comparing the material properties before and

after the treatment, while an additional study is conducted to examine the impact of the duration of CO₂ treatment. Three reservoir materials are selected, representing silica-rich rock (Berea sandstone), low-stiffness calcite-rich rock (Apulian limestone), and high-stiffness calcite-rich rock (Indiana limestone). Although these materials are not directly utilized for GCS, their isotropic and homogeneous poromechanical properties provide advantages that allow the adoption of the linear constitutive models for monomineralic rocks. Opalinus Clay and Eau Claire shale are tested as the caprock representatives, while Charcoal granite is selected as the basement rock material. The primary focus of this study is to provide extensive experimental knowledge of the poromechanical and hydraulic response of subsurface formations during CO₂ injection, and adopt a constitutive model to adequately describe the phenomenon. The following five main objectives are addressed in this dissertation:

- 1) Introduce experimental methods to accurately measure the hydromechanical properties of subsurface rock, including the time-dependent behavior and the CO₂ injection process under the regime of poroviscoelasticity.
- 2) Investigate the chemical effect of CO₂ treatment on the poromechanical response of rock considering its mineral composition.
- 3) Explore the effect of CO₂ treatment on the time-dependent response of reservoir formations and introduce an appropriate chemo-poro-visco-elastic constitutive model.
- 4) Experimentally assess the effect of CO₂ treatment on the relative permeability of CO₂ and water by introducing a technique to estimate the degree of CO₂ saturation.
- 5) Accurately characterize coupled poromechanical and hydraulic properties of the sealing layer (tight) formations and establish a porosity-permeability relationship.

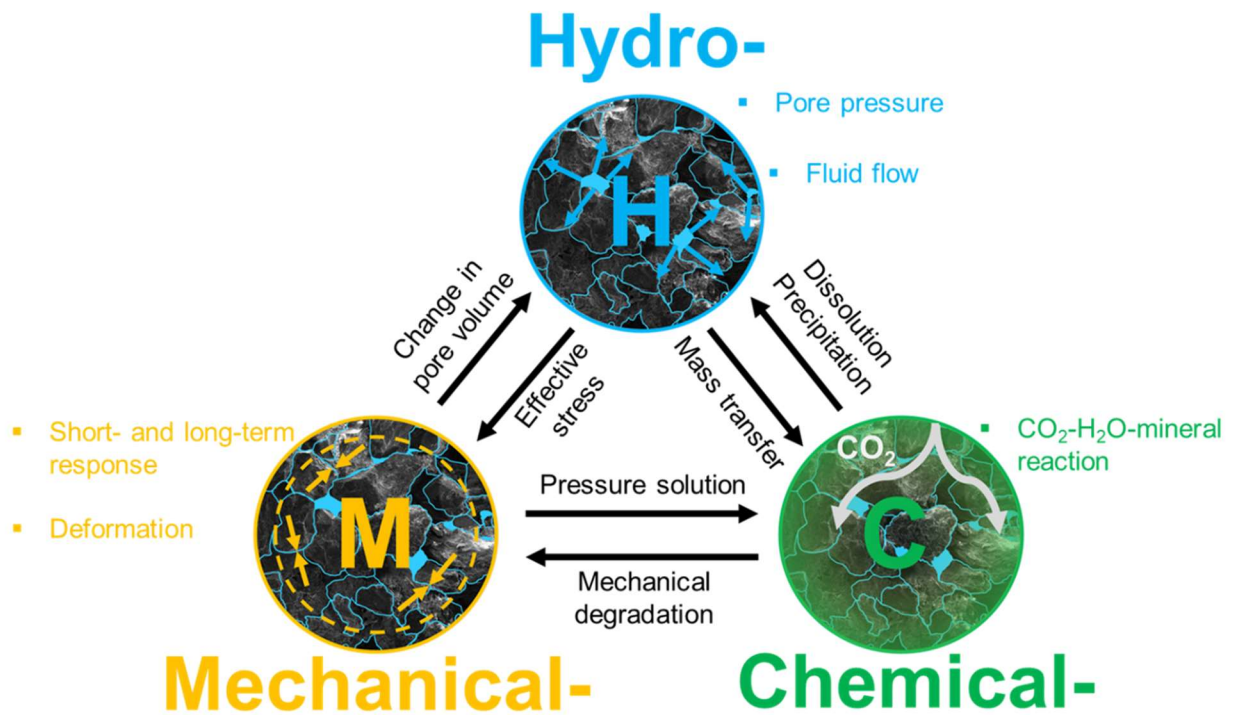


Figure 1.2. Conceptual illustration for hydro-mechanical-chemical coupling.

1.3 Dissertation Organization

For this dissertation, six different studies addressing the designated objectives are assigned as separate chapters. Before introducing the particular results, detailed experimental methods for the whole study are described in Chapter 2. Five of the following six chapters are presented as research papers, three are already published, and two are under review. The first paper, “CO₂ Injection Effect on Geomechanical and Flow Properties of Calcite-Rich Reservoirs”, has been published in *Fluids*, and is designated as Chapter 3. The second paper, “Changes in Rock Matrix Compressibility During Deep CO₂ storage”, has been published in *Greenhouse Gases: Science and Technology* and is presented in Chapter 4. “Short- and Long-term Responses of Reservoir Rock Induced by CO₂ Injection” makes up Chapter 5 and is currently under the second round of reviews in *Rock Mechanics and Rock Engineering*. Chapter 7 contains the manuscript on “Effect

of CO₂ Injection on Multiphase Flow Properties of Reservoir Rock” that has been submitted to *Transport in Porous Media*. “Coupling Between Poromechanical Behavior and Fluid Flow in Tight Rock”, published in *Transport in Porous Media*, makes up Chapter 8. Additionally, further discussions on the chemical effect of CO₂ injection are elaborated in Chapter 6, “Development of Hydro-Mechanical-Chemical Model Describing Reservoir Rock Response During CO₂ Storage”. Finally, Chapter 9 is devoted to the implications of the research findings and suggested future work and Chapter 10 consists of the extended conclusions.

References

- Anderson, K., Peters, G. (2016) The trouble with negative emissions. *Science*. 354: 182–183.
- Bachu, S. (2003) Screening and ranking of sedimentary basins for sequestration of CO₂ in geological media in response to climate change. *Environ Geol*. 44: 277–289.
- Bachu S. (2008) CO₂ storage in geological media: Role, means, status and barriers to deployment. *Prog Energ Combust*. 34(2): 254-273.
- Bachu, S. (2013) Drainage and imbibition CO₂/brine relative permeability curves at in situ conditions for sandstone formations in western Canada. *Energy Procedia*. 37: 4428-4436.
- Bernabé, Y., Mok, U., Evans, B. (2003) Permeability-porosity relationships in rocks subjected to various evolution processes. *Pure Appl Geophys*. 160(5): 937-960.
- Biot, M.A. (1973) Nonlinear and semilinear rheology of porous solids. *J Geophys Res*. 78(23): 4924-4937.
- Cheng, A.H. (2016) *Poroelasticity*. Cham, Switzerland: Springer International Publishing.

- Cox, P.M., Betts, R.A., Jones, C.D., Spall, S.A., Totterdell, I.J. (2000) Acceleration of global warming due to carbon-cycle feedbacks in a coupled climate model. *Nature*. 408(6809): 184-187.
- Coussy, O. (2004) *Poromechanics*. John Wiley & Sons.
- Craig, F.C. (1971) *The reservoir engineering aspects of waterflooding*. Monograph Series, Soc Pet Eng J.
- Guéguen, Y., Palciauskas, V. (1994) *Introduction to the Physics of Rocks*. Princeton University Press.
- Gunter, W.D., Bachu, S., Benson, S. (2004) The role of hydrogeological and geochemical trapping in sedimentary basins for secure geological storage of carbon dioxide. *Geol Soc*. 233(1): 129-45.
- IPCC. (2005) *IPCC Special Report on Carbon Dioxide Capture and Storage*. Cambridge University Press.
- IPCC. (2007) *Climate change 2007: The physical science basis. Fourth assessment report*, IPCC Secretariat, Geneva, Switzerland.
- IPCC. (2021) *Climate Change 2021: The Physical Science Basis. Contribution of Working Group I to the Sixth Assessment Report of the Intergovernmental Panel on Climate Change*. Cambridge University Press.
- Kopp, A., Class, H., Helmig, R. (2009) Investigations on CO₂ storage capacity in saline aquifers: Part 1. Dimensional analysis of flow processes and reservoir characteristics. *Int J Greenh Gas Control*. 3(3): 263-276.
- Krevor, S., Pini, R., Benson, S.M. (2013) Measurement of the multiphase flow properties of the CO₂ brine system for carbon sequestration. *Energy Procedia*. 37: 4499-503.

- Kumar, A., Ozah, R., Noh, M., Pope, G.A., Bryant, S., Sepehrnoori, K., Lake, L.W. (2005) Reservoir simulation of CO₂ storage in deep saline aquifers. SPE J. 10(03): 336-348.
- Makhnenko, R.Y., Podladchikov, Y.Y. (2018) Experimental poroviscoelasticity of common sedimentary rocks. J Geophys Res: Solid Earth. 123(9): 7586-603.
- Metz, B., Davidson, O., De Coninck, H. (Eds.). (2005) Carbon dioxide capture and storage: special report of the intergovernmental panel on climate change. Cambridge University Press.
- Nordbotten, J.M., Celia, M.A. (2011) Geological storage of CO₂: modeling approaches for large-scale simulation. John Wiley & Sons.
- Orr, F.M. (2009) Onshore geologic storage of CO₂. Science. 325(5948): 1656-1658.
- Rutqvist, J. (2012) The geomechanics of CO₂ storage in deep sedimentary formations. Geotech Geol Eng. 30(3): 525-551.
- Somerton, W.H. (1992) Thermal properties and temperature-related behavior of rock/fluid systems. Elsevier.
- Spiteri, E., Juanes, R., Blunt, M.J., Orr, F.M. (2005) Relative-permeability hysteresis: trapping models and application to geological CO₂ sequestration. In SPE Annual Technical Conference and Exhibition.
- Trimmer, D.A. (1981) Design criteria for laboratory measurements of low permeability rocks. Geophys Res Lett. 8(9): 973-975.
- Yarushina, V.M., Podladchikov, Y.Y. (2015) (De) compaction of porous viscoelastoplastic media: Model formulation. J Geophys Res: Solid Earth. 120(6): 4146-4170.
- Vilarrasa, V., Silva, O., Carrera, J., Olivella, S. (2013) Liquid CO₂ injection for geological storage in deep saline aquifers. Int J Greenh Gas Control. 14: 84-96.

CHAPTER 2: METHODS

This section presents the experimental methods used to characterize the poromechanical and multiphase flow properties of subsurface rock. Before introducing the methods, theoretical background on Biot poroelasticity is presented. As the corresponding chapters introduce the devices and methods used for the measurements in detail, each technique is briefly described here with images of the experimental setup. In addition, experimental information not presented in the other chapters is reported along with the approaches to error analyses. A summary of the methods and measured material properties are provided in Table 2.1.

Table 2.1. Summary of the experimental methods.


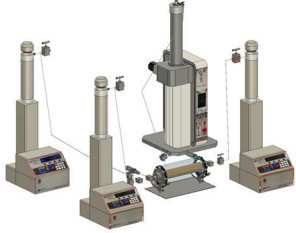
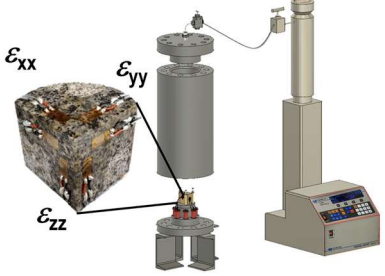



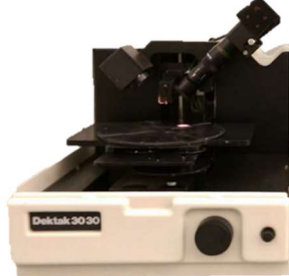
Device	Setup	Measured Parameters	Specimen size
Mercury Intrusion Porosimetry		<ul style="list-style-type: none"> - Porosity (ϕ) - Pore size distribution 	0.5cm ³
Core Flooding Device		<ul style="list-style-type: none"> - Intrinsic permeability (k) - Relative permeability (k_r) - Skempton's B coefficient 	$D = 50.8 \text{ mm}$ $L = 100\text{-}110 \text{ mm}$
Hydrostatic Compression Cell		<ul style="list-style-type: none"> - Drained (dry) bulk modulus (K) - Unjacketed bulk modulus (K_s') 	Prismatic shape with at least 20 mm in each dimension, usually 50×35×35mm

Table 2.1. Cont.

<p>Modified Hydrostatic Compression Cell</p>		<ul style="list-style-type: none"> - Drained (dry) bulk modulus (K) - Unjacketed bulk modulus (K_s') - Skempton's B coefficient - Bulk viscosity (η_ϕ) - Reaction parameter (R_X) 	<p>23×23×30mm</p>
<p>Conventional Triaxial Compression System</p>		<ul style="list-style-type: none"> - Drained/Undrained Young's modulus (E/E_u) - Drained/Undrained Poisson's ratio (ν/ν_u) - Skempton's B coefficient - Bulk viscosity (η_ϕ) - Permeability (k) - Strength (c and ϕ) 	<p>$D = 50\text{mm}$ $L = 90\text{-}110\text{mm}$</p>
<p>Microgoniometer</p>		<ul style="list-style-type: none"> - Apparent contact angle (θ) 	<p>$D = 1\text{-}2\text{cm}$ $L = 0.5\text{cm}$</p>
<p>Profilometry</p>		<ul style="list-style-type: none"> - Surface roughness 	<p>$D = 2\text{cm}$ $L = 1\text{cm}$</p>

2.1 Biot Poroelasticity

As this thesis suggests a more advanced model coupling the hydro-mechanical-chemical aspects and considering the time-dependent behavior of reservoir rock during CO₂ injection, it is important to understand the fundamental basis of the mechanical response of porous media. In this section, the classical constitutive model for poroelastic response of isotropic and homogeneous fluid-saturated porous material is introduced. The behavior of a fluid-saturated rock can be described by the Biot poroelasticity, which defines the porous media as a coherent solid skeleton and freely moving pore fluid (Biot, 1941). The kinematic parameters for the components can be presented as the solid displacement and specific discharge, followed by the strain parameters: strain tensor ε_{ij} and the increment of fluid content ζ (Biot, 1941; Detournay and Cheng, 1993). Also, the dynamic parameters that affect the mechanical response of the porous media need to be introduced, which are the applied total mean stress $P = (\sigma_1 + \sigma_2 + \sigma_3)/3$ and the pore fluid pressure p^f . Then, the Terzaghi effective mean stress $P' = P - p^f$ can be defined (Terzaghi, 1923).

Assuming linearity and elasticity, Biot's constitutive equations for the fluid-filled porous media can be established, where the strain ε , increment of fluid content ζ , and change in porosity $\Delta\phi$ can be expressed with a set of poroelastic parameters (Equations 2.1 to 2.3) (Detournay and Cheng, 1993).

$$\varepsilon = \frac{1}{K} (P - \alpha p^f) \quad (2.1)$$

$$\zeta = \frac{\alpha}{K} \left(P - \frac{p^f}{B} \right) \quad (2.2)$$

$$\Delta\phi = \left(\frac{1-\phi}{K} - \frac{1}{K'_s} \right) P' - \phi \left(\frac{1}{K'_s} - \frac{1}{K''_s} \right) p^f \quad (2.3)$$

Then, the poroelastic constants introduced in the constitutive relationships can be defined under three boundary conditions:unjacketed, drained, and undrained (Detournay and Cheng, 1993). The unjacketed condition implies that the change in the total mean stress is equal to that of the pore pressure ($\Delta P = \Delta p^f$). Under this boundary condition, the unjacketed bulk modulus K_s' and unjacketed pore modulus K_s'' can be defined, giving an understanding of the compressibility of the solid matrix and the pores, respectively (Equations 2.4 and 2.5).

$$K_s' = V \frac{\Delta p^f}{\Delta V} \Big|_{\Delta p^f = \Delta P} \quad (2.4)$$

$$K_s'' = V_p \frac{\Delta p^f}{\Delta V_p} \Big|_{\Delta p^f = \Delta P} \quad (2.5)$$

Under the drained condition, the fluid can freely move in or out of the pores while the pore fluid pressure remains constant ($\Delta p^f=0$). The drained bulk modulus K and Biot coefficient α can be defined under the drained condition. Drained bulk modulus K can be calculated from the change in the volume of the material due to the applied mean stress:

$$K = V \frac{\Delta P}{\Delta V} \Big|_{\Delta p^f = 0} \quad (2.6)$$

Biot coefficient α is introduced as the ratio between the volume of fluid expelled from the element during the drained loading and the change in the element volume. Also, α can be expressed with the drained and unjacketed bulk moduli:

$$\alpha = \frac{\Delta V_\phi}{\Delta V} \Big|_{\Delta p^f = 0} = 1 - \frac{K}{K_s'} \quad (2.7)$$

The undrained condition is defined by zero change in the increment of fluid content: $\zeta=0$, indicating that the fluid cannot move in or out of the porous material, causing changes in the pore

pressure when external loading is applied. Skempton's (1954) B coefficient is introduced to describe the undrained loading, where it is defined as the change in the pore pressure due to the variation in the total mean stress:

$$B = \frac{\Delta p^f}{\Delta P} \Big|_{\zeta=0} \quad (2.8)$$

Based on Biot poroelasticity, this study extends the constitutive behavior by adopting additional aspects to the equations, regarding time-dependent response and chemical reactions.

2.2 Material

Representative reservoir rock, caprock, and base rock materials are selected for this study. As most reservoir formations are sandstones (silica-rich) or limestones (calcite-rich), Berea sandstone, Apulian limestone, and Indiana limestone are tested. Although the chosen reservoir rocks are not directly used for carbon storage, the materials provide advantages considering their isotropy and homogeneity, which allow adopting Biot's poroviscoelastic constitutive equations. Also, as the selected materials can be assumed monomineralic, the effect of CO₂ treatment on a particular rock-forming minerals can be investigated. In addition to the reservoir formations, the two major minerals - quartz and calcite, are examined separately in the form of crystals. For caprock, Eau Claire shale and Opalinus clay are chosen, while Charcoal granite represents the base rock. The reported porosity, and permeability are accurately measured using the mercury intrusion porosimetry and core flooding device, respectively. All tested specimens are presented with scanning electron microscopy (SEM) images in Figure 2.1. Detailed descriptions for each sample are elaborated in the corresponding chapters.

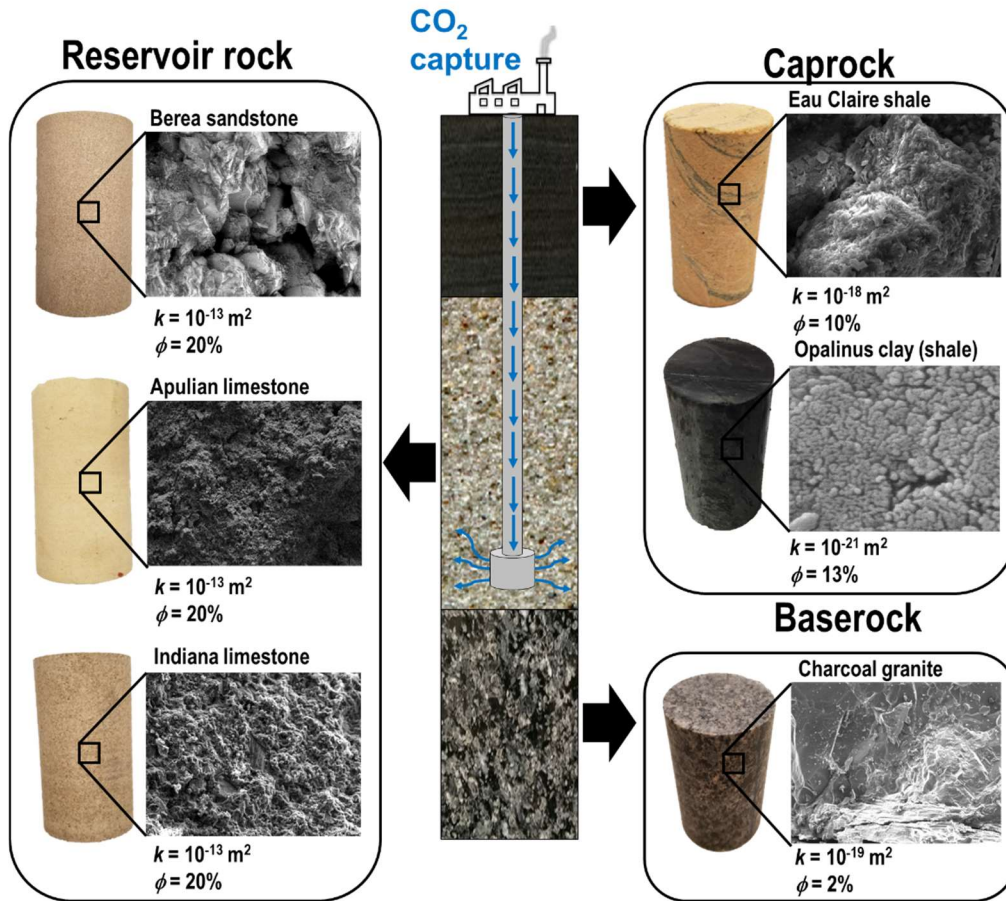


Figure 2.1. Rock formations that are selected for this thesis representing the reservoir rock, caprock, and crystalline basement.

2.3 Mercury Intrusion Porosimetry

The porosity measurements and evaluation of the pore size distribution are measured using the mercury intrusion porosimetry (MIP) device Quantachrome Poremaster 60. The device forces mercury to penetrate the interconnected pores while accurately measuring the volume of the intruded mercury. The pressure is increased up to 413.7 MPa, followed by the unloading procedure. Also, the bulk density of the rock can be calculated by measuring the weights of the dry sample and the sample in the cell filled with mercury up to ambient pressure.

For sample preparation, it is crucial to completely clean and dry the sample cell since even a minor amount of remaining mercury in it can induce a critical error, considering the small size of

the samples. Also, the temperature condition needs to be monitored to resume the isothermal condition, as the thermal change can affect the measurements. The relative error for the reported porosity values is 3% and it considers the variation between values measured on different samples. Detailed descriptions of this method are introduced in Sections 4.2e and 8.2e.

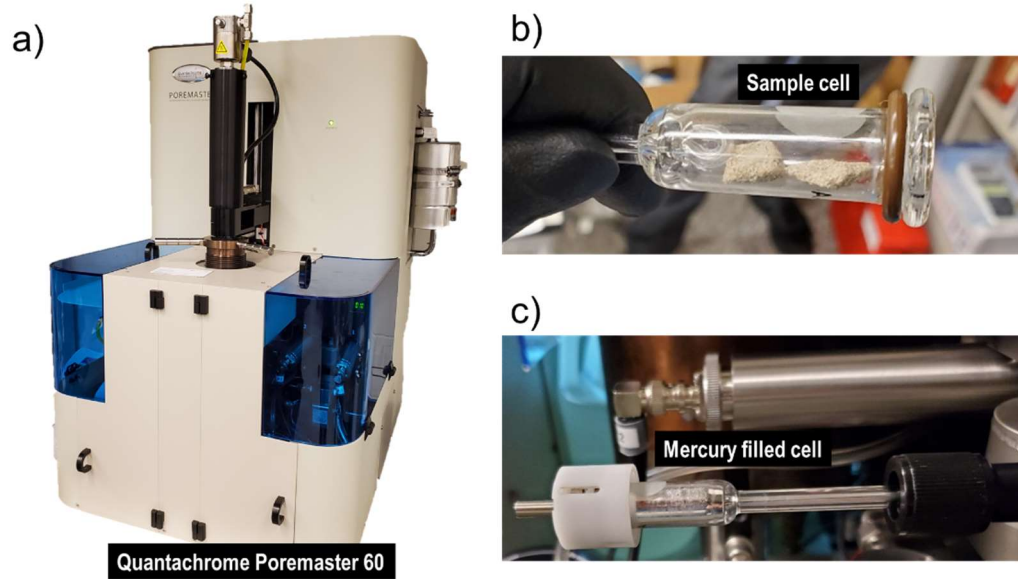


Figure 2.2. Experimental setup for a) mercury intrusion porosimetry device, b) sample installation in the sample cell, and c) cell filled with mercury after intrusion.

2.4 Core Flooding Device

2.4.1 Intrinsic Permeability

The permeability can be measured using the core flooding device and three syringe pumps (Figure 2.3a). With the confining pressure applied, the pore water pressure is induced by two syringe pumps – one for the upstream and another for the downstream pressure. Then, while preserving the total mean stress constant, differential upstream and downstream pore pressure ($p_{up}^f - p_{down}^f = \Delta p^f$) are applied to induce flow through the water-saturated specimen. The change in volume of both pumps is observed over time, and as the absolute change rates of these pumps

become identical, the steady-state flow is assumed. Subsequently, the change in volume of the pumps ΔV is recorded over time Δt , and the permeability of the rock is calculated.

It is to be noted that the permeability measurements are conducted after reaching full saturation, with verification of the repeatability for all formations. Moreover, considering the calcite dissolution in water, we assume that the pore fluid reaches an equilibrium state for mineral dissolution, as the saturation process before any measurements for limestones usually takes at least a week. The effect of dissolution is negligible for the silica-rich formation. For all experiments, the temperature is controlled to be constant (Figure 2.3b). The relative error in the reported permeability values is 5%.

2.4.2 Relative Permeability

The core flooding device can also be utilized for CO₂ injection for the reservoir rock by installing another syringe pump filled with CO₂ at the upstream. The two-phase flow test of water and CO₂ can be experimentally conducted utilizing the core flooding device with the CO₂ injection experimental setup, assuming that both fluids flow independently in a steady-state and laminar flow condition. In order to assess the storage efficiency for CO₂ injection projects, a proper understanding of the degree of saturation for the two fluids (water and CO₂) is required. In addition, as the pore compressibility can be affected due to CO₂ injection, the poromechanical response needs to be coupled with the multiphase flow. In this study, an innovative method to determine the degree of saturation is adopted, where it can be calculated by measuring the poroelastic response of rock during the CO₂ injection (Chapter 7.2c). Thus, the relative permeability curve or – relative permeability versus degree of saturation, can be determined.

With the 5% relative error for the Skempton's B coefficient, that of the calculated degree of saturation is 10%.

As the volume of CO_2 is highly dependent on the ambient temperature, it is important to maintain the isothermal condition during experiments. Also, the pressure and volume of the CO_2 pump are preserved at the target state for at least a few hours before any measurements to assure the CO_2 is at an equilibrium state. In terms of the chemical reaction, the two-phase flow tests for reservoir rock are conducted for a short-term to confirm that the chemical effects from the relative permeability test on the material properties are minimal. Detailed explanations on measuring the intrinsic/relative permeability are elaborated in Chapters 3.3b, 5.3c, and 7.2b.

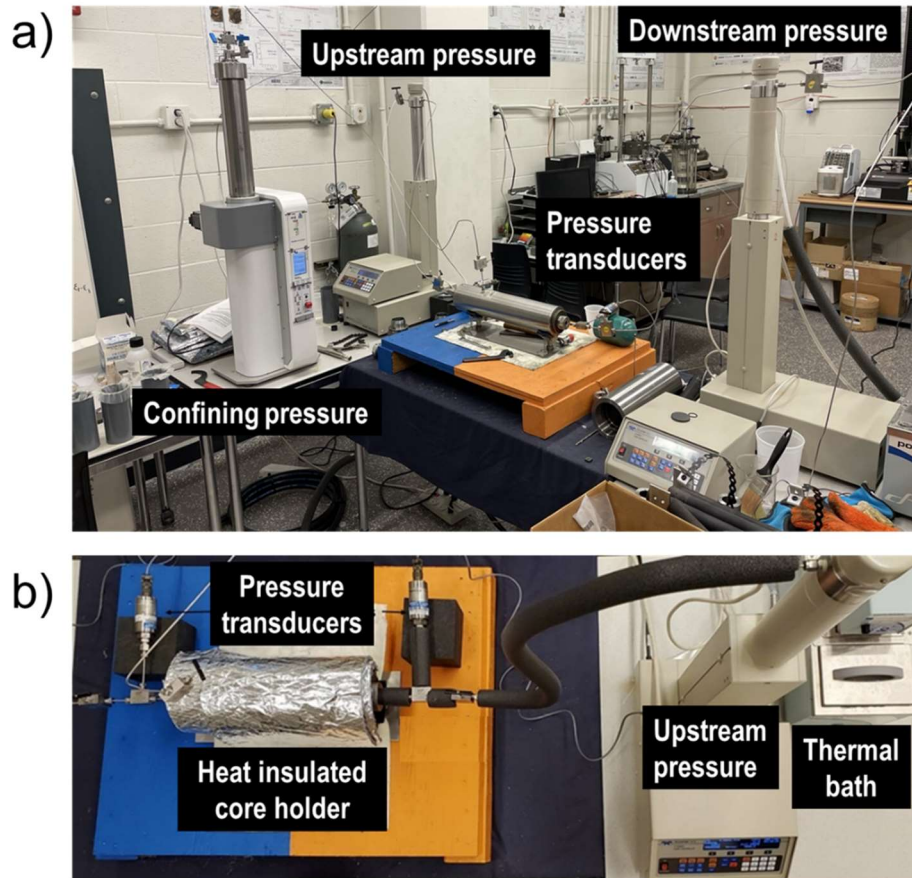


Figure 2.3. Images of the a) core flooding device setup with the syringe pumps and b) the heat insulation setup.

2.4.3 CO₂ Treatment

As this study aims to explore the effect of CO₂ injection on the poroviscoelastic and multiphase flow properties of water-saturated reservoir rock, CO₂ treated specimens are prepared as a comparison to pristine reservoir formations. The CO₂ treatment for reservoir formation is conducted utilizing the core flooding device with the CO₂ injection setup (Figure 2.3). Alternatively, a high-pressure vessel is used for CO₂ treatment of the mineral crystals (Figure 2.4). The samples are submerged in deionized water, as CO₂ is then injected into the steel vessel. For both core flooding device and high-pressure vessel, identical CO₂ pressure is retained during

the treatment process, assuming that the dissolution of the injected CO₂ reaches an equilibrium state.

Previous studies reported that the duration time of CO₂ treatment correlates with the degree of the change in the material properties (Shi et al., 2019). For this study, 21 days are selected as the treatment period for Berea sandstone and Indiana limestone, as we intend to introduce a controlled chemical effect to maintain the materials' elastic behavior without any macroscopic degradation (Tarokh et al., 2020). Furthermore, since Apulian limestone is recognized as a softer material that highly reacts with the acidic mixture of water and CO₂, the treatment period is reduced to 3 days (Luquot and Gouze 2009). For multiphase flow and CO₂ treatment experiments, liquid CO₂ is utilized. Although many studies report that CO₂ exists in the reservoir as a supercritical state, others propose injecting liquid CO₂ is more energetically efficient (Rayward-Smith and Woods, 2011; Vilarrasa et al., 2013). Moreover, adopting the supercritical CO₂ involves consideration of the thermal effect ($T > 31.04^{\circ}\text{C}$), changes in the fluid compressibility, density, and viscosity, complicating the problem (Figure 2.5). Therefore, for this study, the problem is simplified by using liquid CO₂ at room temperature to focus on the hydro-mechanical-chemical coupling effect. Detailed procedures for the CO₂ treatment are elaborated in Chapters 3.3c, 4.2b, 5.3b, and 7.2d.

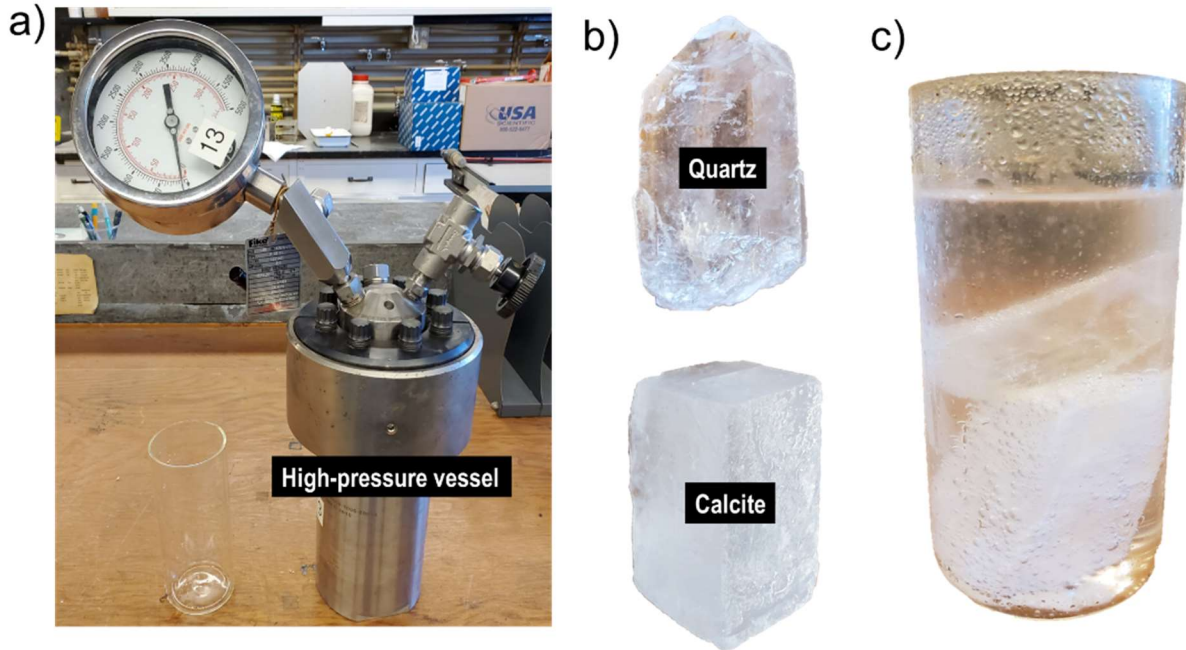


Figure 2.4. Experimental setup for a) high-pressure vessel, b) mineral crystal samples of quartz and calcite, and c) submerged samples in the inner beaker for CO₂ treatment.

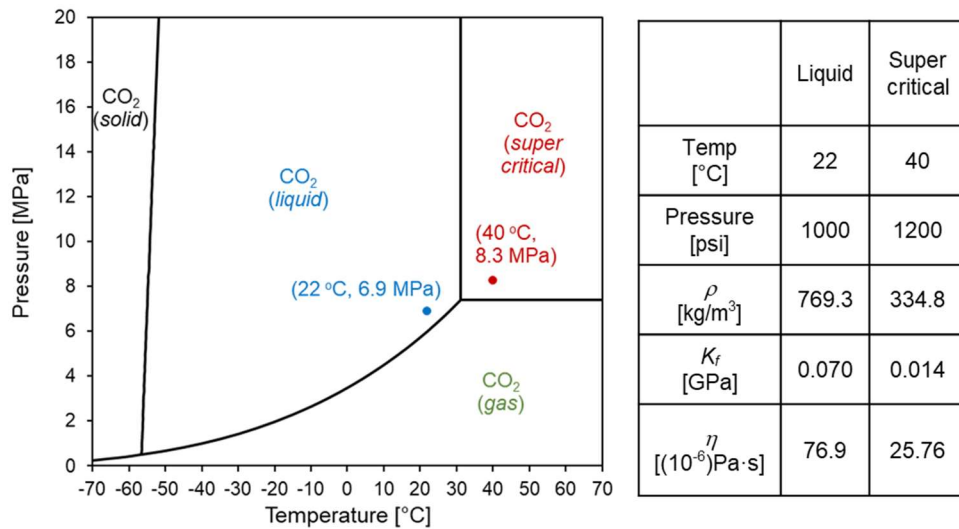


Figure 2.5. The phase diagram of CO₂. Two representative states, liquid (blue) and supercritical (red) CO₂ are selected, with the material properties (ρ : density, V_{pc} : P-wave velocity, K_f : fluid bulk modulus, η : viscosity) summarized in the below table.

2.5 Hydrostatic Compression Cell

2.5.1 Compressibility Test

The hydrostatic compression test apparatus is adopted in this study to measure the jacketed and unjacketed bulk responses of the reservoir rocks and the solid bulk modulus of the dominant minerals (Figure 2.6a). The specimen is submerged in hydraulic oil that fills the cell, and after closing the cell, hydrostatic pressure is applied with the syringe pump. As the pressure increases, the deformation of the specimen is measured by the resistive strain gauges installed on the surface of the specimen. After measuring the jacketed bulk modulus (K), the unjacketed bulk modulus (K_s) is determined by removing the membrane, which allows the fluid to intrude the sample's pores. For both porous rock and mineral crystals, sufficient strain gages are installed to the specimen surface in three perpendicular directions, and, in some cases, in diagonal directions on each face (Figures 2.6b, c, and d). During the experiment, it is important to record the strain measurements after reaching equilibrium. The relative errors for the bulk moduli measurements are within 3%. Further explanations on the procedure of the hydrostatic compression test are presented in Chapters 4.2c and 8.3b.

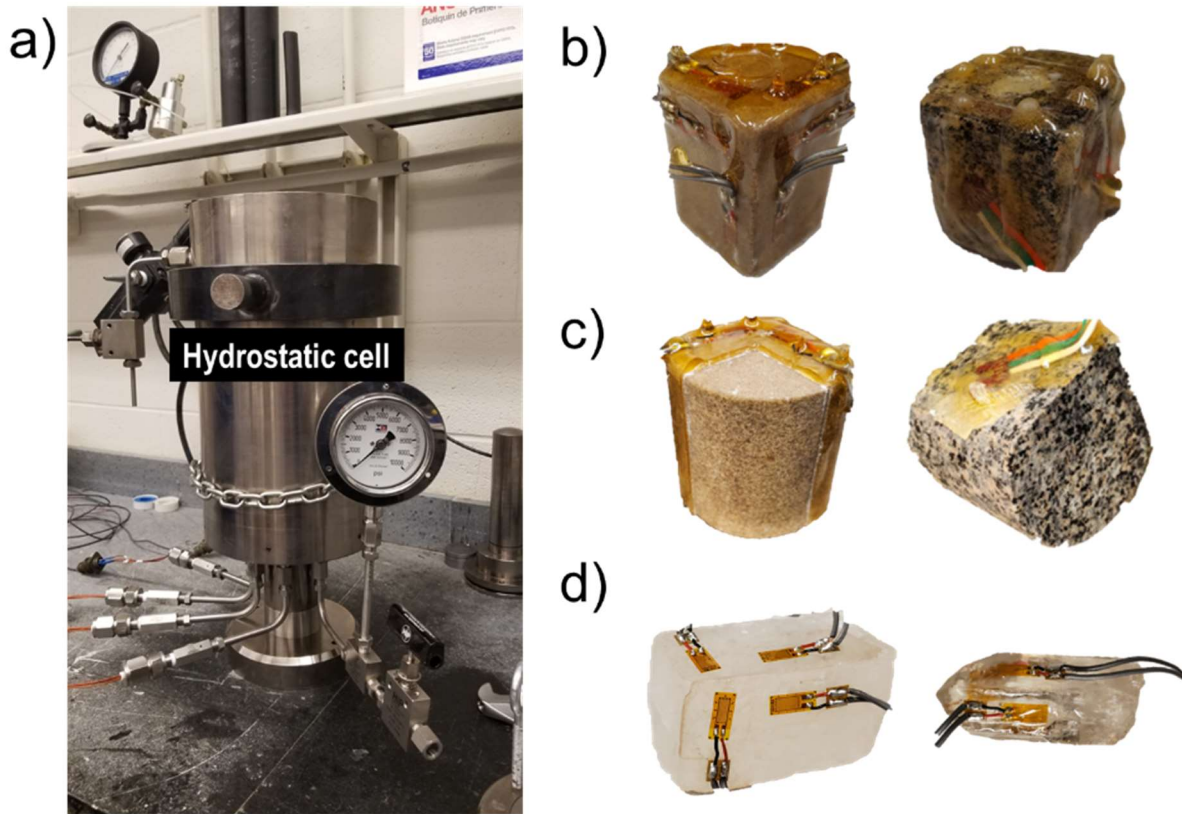


Figure 2.6. Experimental setup for the a) hydrostatic compression cell and samples for the b) jacketed test, c) unjacketed test, and d) mineral solid compressibility.

2.5.2 Modified Hydrostatic Compression Cell

As the original hydrostatic compression cell does not allow to control the pore pressure in the specimen, the modified hydrostatic compression system is developed by installing pressure lines, valves, and transducers (Figure 2.7b). Then, the hydrostatic compression test can be conducted with a separate control of the confining (all around) and pore pressures separately. Under this condition, the undrained response and time-dependent deformation can be measured in addition to the bulk compressibility. Also, by having pore fluid vessels of water and CO₂ (Figure 2.7c), the CO₂ treatment process can be conducted. The modified hydrostatic compression system is located in a temperature-controlled air bath that allows more accurate control of the isothermal

conditions (Figure 2.7a). As the deformation can be measured at high-pressure conditions during CO₂ injection, the effect of the duration of CO₂ treatment is investigated. Detailed experimental techniques are presented in Chapter 6.2c.

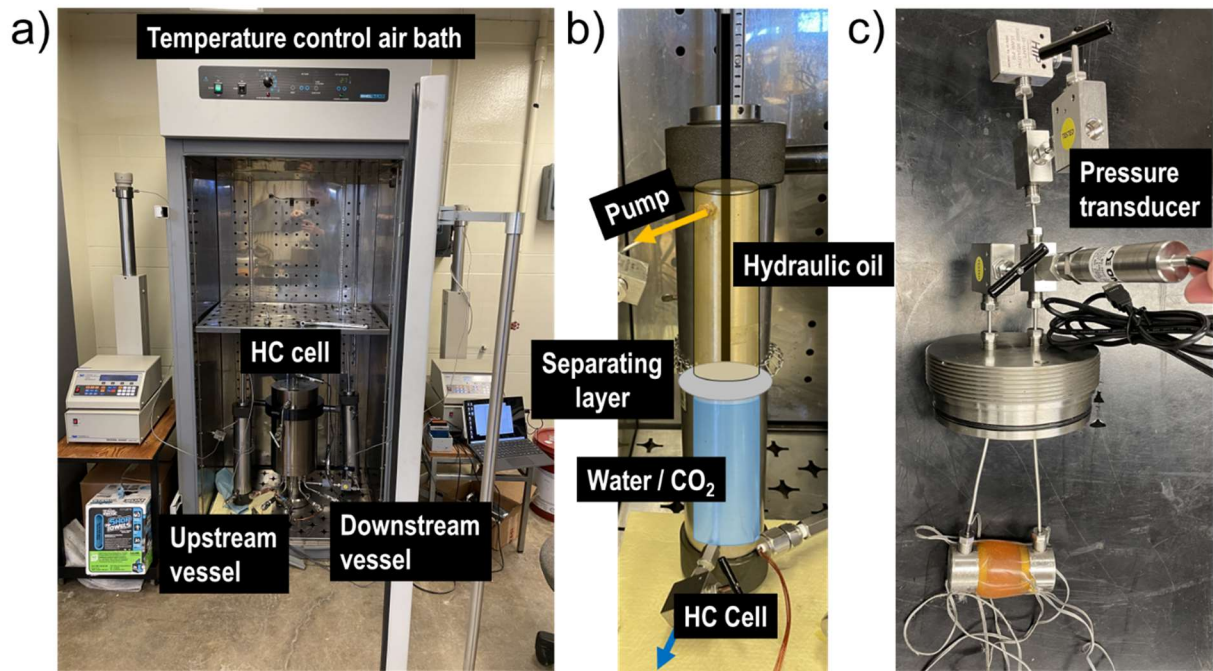


Figure 2.7. a) The modified hydrostatic compression system, b) pore fluid vessel, and c) pore pressure lines with the pressure transducer and connected specimen.

2.6 Triaxial Compression Test

Measurements of the poroviscoelastic response of rock are conducted in the conventional triaxial system. The system consists of the GDS triaxial compression cell (with 4 MPa capacity), 50 kN load frame, and three 4 MPa pressure controllers for application of the cell and upstream and downstream pore pressures (Figure 2.8a). In addition, two pressure transducers are installed at the input and output to monitor the inner pore pressure during the undrained response. The deformation of the specimen is measured by two axial and one radial LVDT (Figure 2.8b). Full

saturation is achieved by the back-pressure saturation method with Skempton's B coefficient measurements. Loading-unloading tests are conducted under drained and undrained conditions allowing the calculation of the drained (E) and undrained (E_u) Young's moduli, drained (ν) and undrained (ν_u) Poisson's ratios, and the strength characteristics (e.g., cohesion c and friction angle ϕ) of the rock. The poroviscoelastic behavior can be assessed under undrained boundary conditions, by monitoring the pore pressure buildup with constant total mean stress. Specifications on the triaxial compression test are introduced in Chapters 3.3d and 5.3e.

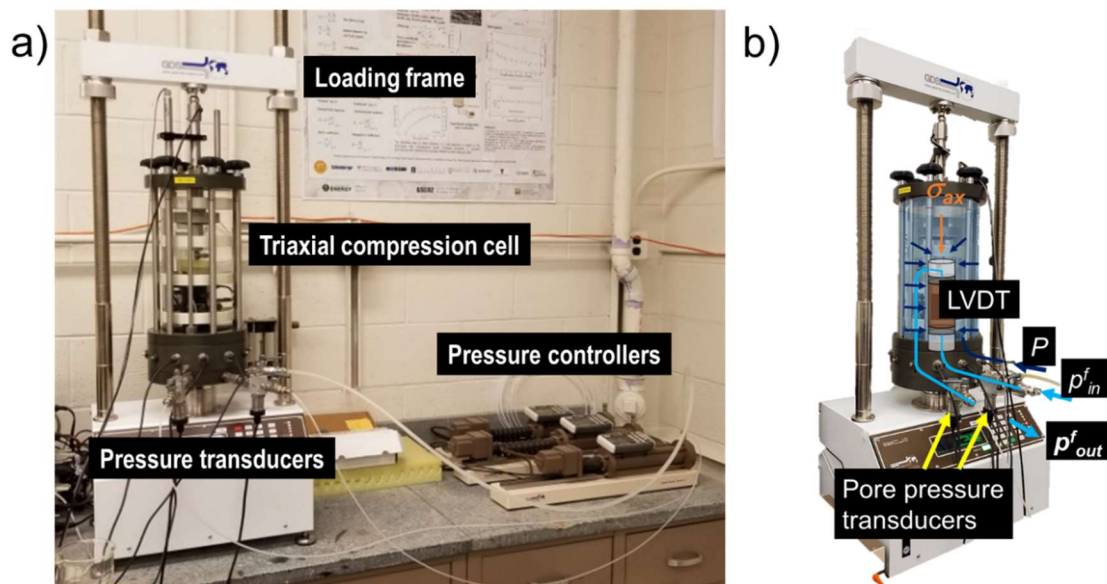


Figure 2.8. Experimental setup for the a) conventional triaxial compression system and b) installation of specimen.

2.7 Saturation

Measurements of poroviscoelastic properties should be performed at full saturation, that needs to be confirmed while utilizing any of the presented techniques. For the hydrostatic compression test, where hydraulic oil is utilized as the confining fluid, it is allowed to penetrate the specimen to make the pore pressure equal to the mean (all around) stress. The time to reach an equilibrium state during the increase in pressure can be estimated by the characteristic time for the pore fluid diffusion, and sufficient time is guaranteed before strain measurements. Estimation of the maximum oil pressure to be applied to reach full saturation can be inferred from the porosimetry analyses and provides values below 60 MPa even for the tight rock (see Chapter 8.3), being significantly smaller for the reservoir materials (Tarokh and Makhnenko, 2019). Since the unjacketed properties are measured during the unloading stage that follows the loading up to 69 MPa – the full saturation of the specimens is guaranteed and confirmed by the reported linear responses.

For the core flooding device, triaxial cell, and modified hydrostatic compression cell, full saturation is achieved by utilizing the backpressure technique (Lowe and Johnson, 1960; Makhnenko and Labuz, 2016). The Skempton's B coefficient is measured at a constant effective mean stress P' , while the pore pressure is increased in steps. When a constant value of B is measured, it can be assumed that full saturation has been achieved. However, due to the volume of pore fluid in the inner pore water lines (dead volume V_L) and the compressibility of the system itself, the measured B values need to be corrected (Bishop, 1976). The correction factors for the compressibility of the system are calculated with the theoretical equation for Skempton's B coefficient and the measured B value from the PVC specimen. The dead volume for the triaxial cell is $V_L = 7.0$ mL, as the correction factor (3.5×10^{-16} m³/Pa) affects the B measurements by 0.13

for Berea sandstone. This dead volume decreases significantly for the core flooding device, as $V_L = 1.7$ mL, where the applied correction factor (1.2×10^{-16} m³/Pa) appears to be within the accuracy of the measurements that can be neglected. More detailed discussions for saturation in the apparatus are available in Chapter 8.3d.

2.8. Microscopic Measurements

Characterization of the multiphase flow response relies on assumptions for the microscale properties that are generally maintained constant. However, questions may arise if this premise is valid, as the microscale factors that affect the relative permeability – wettability and surface roughness, are measured.

The contact angle is measured using a microgoniometer (MCA-3), which allows an image analysis with precise calculation of the angles between the droplets and the surface (Figure 2.9a). The device is capable of accurately controlling the size of the microscopic droplets, and can detect the droplet using a high magnification lens with a fast image capture system (Figure 2.9b). As the contact angles are measured at different locations and with the systematic error, the contact angle values showed a variation within $\pm 5^\circ$.

The profilometer (Sloan Dektak3ST) provides repeatable and accurate measurements of the height and 2D roughness of the material surface, ranging from a few nanometers to hundred microns (Figure 2.10). The contact technique is utilized to measure the surface topography without any damage as it scans across the surface of the specimen. Details on the microscopic measurements are explained in Chapters 7.2f and 7.2g.

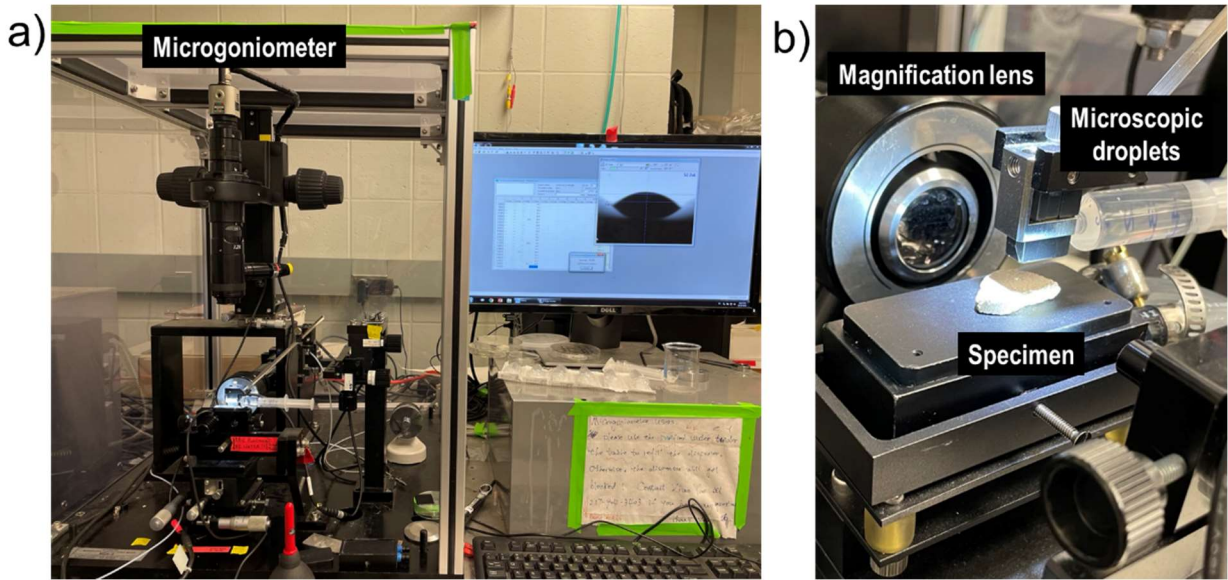


Figure 2.9. Experimental setup of the a) microgoniometer and b) specimen installation and measurements.

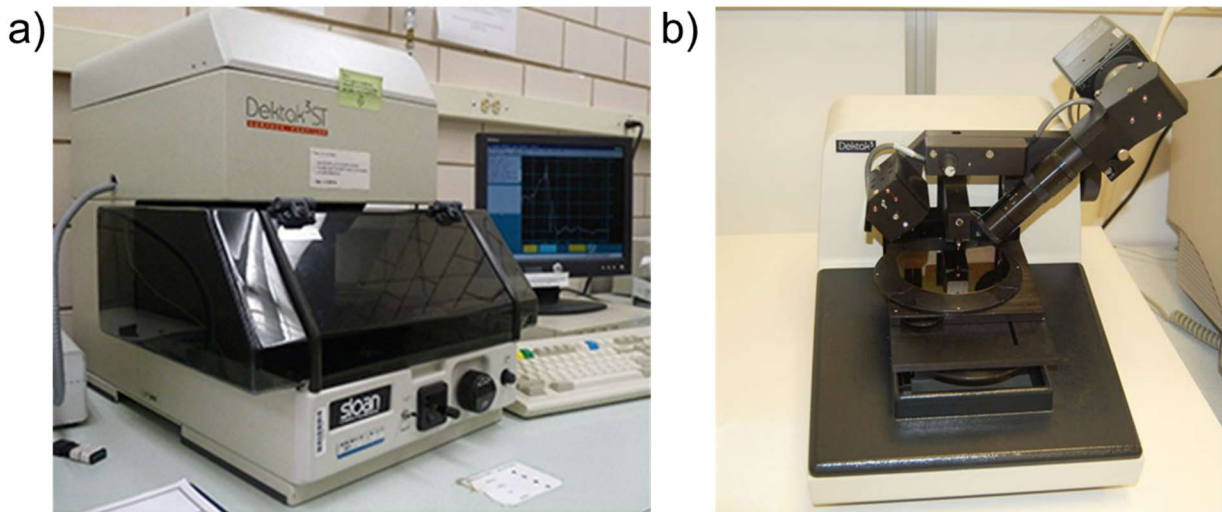


Figure 2.10. a) The profilometer apparatus setup and b) specimen installation for surface roughness measurements.

2.9. Error Analysis

All experimental measurements have some degree of uncertainty, also called as an error, which can be attributed to many reasons. Therefore, it is important to report the uncertainty with the measured value to provide confidence in the experimental results. As most findings of this study are based on experimental work, this section reports the errors associated with each experimental method and calculations.

In general, the experimental error consists of systematic and random errors, assuming that the person performing the measurement does not induce any blunder errors. The systematic error is the reproducible inaccuracies, occurring in the same direction that can be improved by calibrating the apparatus. The random error is unpredictable and cannot be replicated, as it is statistical fluctuations among the measurements. With all experimental devices accurately calibrated, it is assumed that the systematic error can be neglected, as it cannot be detected by increasing the number of testing specimens. Thus, for this study, the random error becomes important, which is due to the precision of the measurements and specimen sampling of at least three specimens. Then, the total relative error for each reported parameter can be evaluated by integrating the error ranges by multiplication. The relative error is defined as the ratio of the absolute error to the measurement value, where the average value regarding the sampling error is reported. The precision of the measurements can be described with the instrumental resolution. For the mercury intrusion porosimetry, the accuracies of the volume and pressure transducers are 1% of the stem volume and 0.1% for the maximum pressure capacity, giving $\sim 0.0001 \text{ cm}^3$ and $\sim 50 \text{ kPa}$. Then, with the sampling error range of the measured porosity values of 2-3%, the total relative error for porosity is determined as 3%. The accuracy of the strain gauges in the hydrostatic compression system is 0.3% for the maximum resistance. For the volume and

pressure accuracies of the ISCO syringe pump (500D), they are 31.71 nL and 0.5% of the maximum capacity (~50 kPa), respectively. Using this information, the relative errors for the poroviscoelastic properties can be evaluated. For the bulk moduli, the sampling error shows a 2% range, thus resulting in a 3% total relative error. The intrinsic and relative permeability measurements show a larger sampling error, and the total relative error is calculated as 5%. For Skempton's B coefficient, the sample variation gives a 2% fluctuation, as the total relative error does not exceed 3%. As the bulk viscosity for the time-dependent response is calculated from the measured poroelastic parameters, the error range is larger, giving a 10% total relative error. The sampling errors are shown to be larger for the microscale measurements, resulting in the relative total errors of ~10% and ~15% for contact angle and surface roughness measurements, respectively. For the strength measurements, the relative error is mostly due to the sampling error, not exceeding 5%.

References

- Biot, M.A. (1941) General theory of three-dimensional consolidation. *J Appl Phys.* 12(2): 155-64.
- Bishop, A.W. (1976) The influence of an undrained change in stress on the pore pressure in porous media of low compressibility. *Géotechnique.* 26: 371–375.
- Detournay, E., Cheng, A.H. (1993) Fundamentals of poroelasticity. In *Analysis and design methods* (pp. 113-171). Pergamon.
- Lowe, J., Johnson, T.C. (1960) Use of back pressure to increase degree of saturation of triaxial test specimens. In: *Proceedings of the Research Conference on Shear Strength of Cohesive Soils*, Boulder, Colorado, ASCE. 819-836.

- Luquot, L., Gouze, P. (2009) Experimental determination of porosity and permeability changes induced by injection of CO₂ into carbonate rocks. *Chem Geol.* 265(1-2): 148-159.
- Makhnenko, R.Y., Labuz, J.F. (2016) Elastic and inelastic deformation of fluid-saturated rock. *Philos Transact A: Math Phys Eng Sci.* 374(2078): 20150422.
- Rayward-Smith, W.J., Woods, A.W. (2011) Some implications of cold CO₂ injection into deep saline aquifers. *Geophys Res Lett.* 38(6).
- Shi, Z., Sun, L., Haljasmaa, I., Harbert, W., Sanguinito, S., Tkach, M., Goodman, A., Tsotsis, T.T., Jessen, K. (2019) Impact of Brine/CO₂ exposure on the transport and mechanical properties of the Mt Simon sandstone. *J Pet Sci Eng.* 177: 295-305.
- Skempton, A.W. (1954) The pore pressure coefficients A and B. *Geotechnique* 4: 143-147.
- Tarokh, A., Makhnenko, R.Y. (2019) Remarks on the solid and bulk responses of fluid-filled porous rock. *Geophysics.* 84(4): WA83-95.
- Tarokh, A., Makhnenko, R.Y., Kim, K., Zhu, X., Popovics, J.S., Segvic, B., Sweet, D.E. (2020) Influence of CO₂ injection on the poromechanical response of Berea sandstone. *Int J Greenh Gas Control.* 95: 102959.
- Terzaghi, K. (1923) Die berechnung der durchlassigkeitszifer des tones aus dem verlauf der hydrodynamischen spannungsercheinungen, *Sitzungsber. Akad. Wissen. Wien Math. Naturwiss. Kl. Abt. Iia.* 132: 105-124.
- Vilarrasa, V., Silva, O., Carrera, J., Olivella, S. (2013) Liquid CO₂ injection for geological storage in deep saline aquifers. *Int J Greenh Gas Control.* 14: 84-96.

CHAPTER 3: CO₂ INJECTION EFFECT ON GEOMECHANICAL AND FLOW PROPERTIES OF CALCITE-RICH RESERVOIRS

Based on a manuscript published in Fluids

Kim, K., Vilarrasa, V., Makhnenko, R.Y. (2018) CO₂ injection effect on geomechanical and flow properties of calcite-rich reservoirs. Fluids. 3(3): 66.

ABSTRACT

Geologic carbon storage is considered as a requisite to effectively mitigate climate change, so large amounts of carbon dioxide (CO₂) are expected to be injected in sedimentary saline formations. CO₂ injection leads to the creation of acidic solution when it dissolves into the resident brine, which can react with reservoir rock, especially carbonates. We numerically investigated the behavior of reservoir-caprock system where CO₂ injection-induced changes in the hydraulic and geomechanical properties of Apulian limestone were measured in the laboratory. We found that porosity of the limestone slightly decreases after CO₂ treatment, which lead to a permeability reduction by a factor of two. In the treated specimens, calcite dissolution was observed at the inlet, but carbonate precipitation occurred at the outlet, which was closed during the reaction time of three days. Additionally, the relative permeability curves were modified after CO₂-rock interaction, especially the one for water, which evolved from a quadratic to a quasi-linear function of the water saturation degree. Geomechanically, the limestone became softer and it was weakened after being altered by CO₂. Simulation results showed that the property changes occurring within the CO₂ plume caused a stress redistribution because CO₂ treated limestone became softer and tended to deform more in response to pressure

buildup than the pristine rock. The reduction in strength induced by geochemical reactions may eventually cause shear failure within the CO₂ plume affected rock. This combination of laboratory experiments with numerical simulations leads to a better understanding of the implications of coupled chemo-mechanical interactions in geologic carbon storage.

3.1. Introduction

Geologic carbon storage is deemed as a necessary action to reach the Paris Agreement goal of limiting temperature increase to 1.5 °C (Anderson and Peters, 2016). To this end, widespread deployment of carbon dioxide (CO₂) capture and storage (CCS) projects will have to take place in the next decade. CCS projects can keep down the overall cost of mitigation options to achieve large reductions in CO₂ emissions (Nordbotten, 2012). The Intergovernmental Panel on Climate Change (IPCC) report (2005) states that CO₂ storage in deep geological formations is one of the most promising techniques because gigatons of CO₂ can be potentially injected and trapped underground. The most suitable storage reservoirs are permeable sedimentary formations, which can be either siliciclastic or carbonate and saturated with saline water (IPCC, 2005). While siliciclastic formations are seen to be quite stable to CO₂ injection (Zhang et al., 2009), carbonate formations could be highly reactive (Luquot and Gouze, 2009).

Recent laboratory studies show that the greatest changes in the mechanical response of reservoir formations are expected for carbonate-rich rock or rock with carbonate cement (Rohmer et al., 2016). High-pressure CO₂ injection induces CO₂-brine-rock interactions in which geochemical reactions potentially lead to changes in hydraulic properties, i.e., porosity and permeability, and geomechanical properties, i.e., stiffness and strength of rock (Vilarrasa et al., 2018). Bemmer and Lombard (Bemmer and Lombard 2010) reported 1–2% increase in porosity for carbonate-rich

wackestone from Lavoux formation altered in the presence of CO₂. This resulted in a decrease in strength and elastic moduli of up to 20–30%. Similarly, Alam et al. (Alam et al., 2014) observed 2–3% increase in porosity in North Sea chalk treated with supercritical CO₂ (scCO₂), leading to a 2% increase in Biot coefficient, and hence a decrease in elastic rock stiffness. Vialle and Vanorio (2011) measured the changes in elastic properties of both saturated and dry limestones and observed a gradual loss of strength upon injection, as testified by the continuous decrease in the dry P- and S-wave velocity (20–25%). The decrease was also accompanied by a relative increase in permeability (up to 500%) and porosity (up to 19%), while the change in microstructure was monitored over time via scanning electron microscopy. Grombacher et al. (2012) explained the ultrasonic velocities reduction in different carbonate rocks subjected to CO₂-rich water injection by the decrease in stiffness at grain contacts caused by dissolution that was observed through microimaging. However, the reduction rates of the bulk and shear moduli with injected pore volume decrease with increasing effective mean stress, which reduces the porosity and the reactive surfaces through compaction, so the effect of dissolution becomes less important (Vanorio et al., 2011).

Some other studies do not support the observations of significant decrease in strength and elastic properties of carbonates caused by CO₂ injection. Sterpenich et al. (2009) showed that for brine-saturated Lavoux limestone, scCO₂ injection at 80 °C had a minor effect on microstructure (less than 1% calcite dissolution) and ultrasonic velocities. Liteanu et al. (2013) observed the effect of water-weakening on Maastrichtian chalk, but the effect of scCO₂ on rock deformation was negligible. This minor effect was also reported by Grgic (2011). Saaltink et al. (2013) found through numerical simulations that calcite dissolution at the field scale within the CO₂ plume is low. This weak interaction may be explained by the carbonate buffering effect on pH: The

increase of pore fluid acidity due to CO₂ dissolution into water causes dissolution of calcite, which consumes protons, leading to pH stabilization.

Relative permeability and retention curves are used to describe the multi-phase flow induced by CO₂ injection in deep saline aquifers (Juanes et al., 2006). Specifically, the dissolution or precipitation of calcite may influence the pore structure and wetting and non-wetting procedures that occur in multi-phase flow. Bennion and Bachu (2008) conducted comparative tests on relative permeability in various rocks including carbonates and provided a valuable data set to assess the fluid flow and distribution in two-phase flow. Zekri et al. (2007) measured the relative permeability of limestones to evaluate the change in wettability of the porous media. The results showed that the scCO₂ flooding tends to change the wettability of saturated limestones to a more water-wet condition. Additionally, relative permeability was used as a fitting parameter for the numerical model to simulate CO₂ injection into a carbonate reservoir (2007). The simulation compared CO₂ saturated water injection and pure scCO₂ injection, concluding that the CO₂ saturated water tends to affect the reservoir structure more actively than pure scCO₂.

This paper aims to investigate how CO₂ injection affects the properties of porous carbonate reservoirs. We first present the geometry of the considered problem and explain the numerical model that includes the changes in hydro-mechanical properties of a limestone when it is altered with CO₂. Then, we describe the experimental techniques applied to saturate water-filled limestone with liquid CO₂ and measure its hydraulic and mechanical response. Subsequently, we present the results of laboratory tests performed on a number of pristine and CO₂ treated limestone specimens. Additionally, the numerical model that utilizes the laboratory data is used to evaluate the stability of carbonate reservoir and predict its long-term behavior. Finally, we discuss the findings and implications of this study and draw the conclusions.

3.2 Numerical Model

We modeled CO₂ injection into a carbonate reservoir and investigated the effect of the changes in rock properties induced by geochemical reactions on the geomechanical response of the system. To this end, we considered the coupled hydro-mechanical problem, which implied solving simultaneously mass conservation of each phase and momentum balance. Mass conservation of each phase, neglecting the diffusive component, is expressed as (Bear, 1972):

$$\frac{\partial(\phi S_{\alpha} \rho_{\alpha})}{\partial t} + \nabla \cdot (\rho_{\alpha} \mathbf{q}_{\alpha}) = r_{\alpha}, \quad \alpha = c, w \quad (3.1)$$

where ϕ is porosity, S_{α} is saturation of the α -phase, ρ_{α} is the density of the α -phase, t is time, \mathbf{q}_{α} is the volumetric flux, r_{α} is the phase change term, and α is either CO₂ rich phase, c , or aqueous phase, w . Here, evaporation of water into CO₂ is neglected, i.e., $r_w = 0$. Fluid properties, i.e., density and viscosity, are functions of both pressure and temperature.

The volumetric flux is given by Darcy's law.

$$\mathbf{q}_{\alpha} = -\frac{k k_{r\alpha}}{\mu_{\alpha}} (\nabla p_{\alpha} + \rho_{\alpha} \mathbf{g} \nabla z), \quad \alpha = c, w \quad (3.2)$$

where k is intrinsic permeability, $k_{r\alpha}$ is the α -phase relative permeability, μ_{α} is its viscosity, p_{α} is its pressure, \mathbf{g} is gravity, and z is the vertical coordinate, which is positive upwards.

The saturation degree is a function of the capillary pressure. We adopt the van Genuchten model (1980), which reads:

$$S_e = \left(1 + \left(\frac{p_c}{p_0} \right)^{1/(1-m)} \right)^{-m} \quad (3.3)$$

where p_c is capillary pressure, p_0 is entry pressure, and m is the shape parameter and

$$S_e = \frac{S_l - S_{rl}}{S_{\max} - S_{rl}} \quad (3.4)$$

where S_l is liquid saturation, S_{rl} is residual liquid saturation, and S_{max} is the maximum liquid saturation.

For the mechanical problem, assuming that inertial terms are negligible, the momentum balance of the porous media reduces to the equilibrium of stresses.

$$\nabla \cdot \boldsymbol{\sigma} + \mathbf{b} = \mathbf{0} \quad (3.5)$$

where σ is the total stress tensor and b is the body forces vector. A complete description of the hydro-mechanical formulation is provided in Appendix A in Reference (Vilarrasa et al., 2010).

We assume that the medium behaves in a brittle manner and assess its stability by adopting the Mohr-Coulomb failure criterion

$$\tau = c' + \sigma_n' \tan \phi' \quad (3.6)$$

where τ is the shear stress, σ_n' is the normal effective stress, c' is cohesion, and ϕ' is the friction angle.

We considered a 100 m-thick carbonate reservoir that is overlaid and underlain by a 50 m-thick low-permeable formation (Figure 3.1). The top of the reservoir is placed at 1500 m. CO₂ is injected through a vertical well, and, thus, the model is axisymmetric. The injection rate is of 0.25 Mt/year and injection is performed during 3 years. The model extends radially for 5 km. A constant pressure equal to hydrostatic is imposed in the outer boundary. No displacement perpendicular to the boundary is imposed on the lateral and lower boundaries, and a constant overburden equal to 36.25 MPa is imposed on the top boundary. We considered a normal faulting stress regime, with the vertical stress following a lithostatic stress of 25 MPa/km and the horizontal total stresses equal to 0.65 times the vertical total stress. The model is assumed isothermal, with a temperature of 60 °C, which corresponds to a surface temperature of 10.5 °C and a geothermal gradient of 33 °C/km.

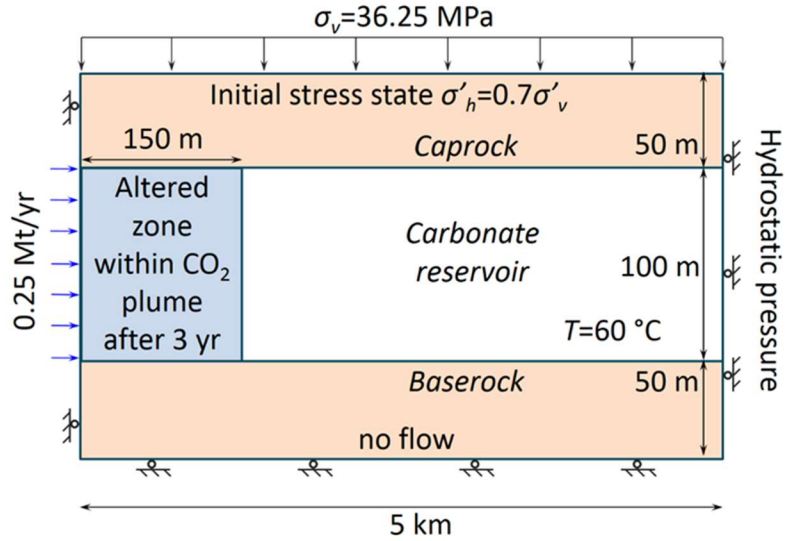


Figure 3.1. Schematic representation of the model geometry and boundary and initial conditions.

The material properties were measured in the laboratory (see Section 3.3). While the properties of the reservoir (Apulian limestone) are measured in this study (see Section 3.4 for results), the properties of the caprock (Opalinus clay—Jurassic shale from Switzerland) have been measured in previous studies and are reported in Table 3.1. Due to nanoDarcy scale permeability, the response of the caprock is assumed to be undrained during the time of injection (Vilarrasa et al., 2016; Vilarrasa and Makhnenko, 2017). Given the relatively low permeability of the reservoir ($\sim 10^{-15}$ m², see Section 3.4), viscous forces dominate during the injection phase, which leads to a plug-like advance of the CO₂ plume (Dentz and Tartakovsky, 2009; Vilarrasa et al., 2010). After a 3-year injection period, the CO₂ plume reached a radius of 150 m. To assess the effect of the property changes on the geomechanical response of the rock, we ran two models, one in which the whole reservoir had the properties of the pristine material and another one in which the cylinder of 150 m in radius around the injection well had the properties of the altered material as a result of its interaction with CO₂. We simulated this hydro-mechanical problem using the fully

coupled finite element numerical code CODE_BRIGHT (Olivella et al., 1996), which was extended to be applied to CO₂ injection (Vilarrasa et al., 2013).

Table 3.1. Properties of the caprock representative–Opalinus clay (shale) (Vilarrasa et al., 2016; Vilarrasa and Makhnenko, 2017).

Property	Pristine Rock
Permeability, k [m ²]	4×10^{-21}
Porosity, ϕ [-]	0.12
Relative water permeability, k_{rw} [-]	S_w^6
Relative CO ₂ permeability, k_{rc} [-]	S_c^6
Gas entry pressure, p_0 [MPa]	6.0
van Genuchten shape parameter m [-]	0.3
Undrained Young's modulus, E [GPa]	2.8
Undrained Poisson's ratio, ν_u [-]	0.40
Cohesion, c' [MPa]	5.0
Friction angle, ϕ [°]	24

3.3 Experimental Methods

3.3.1. Material

Apulian limestone (or Calcarenite) was selected for the laboratory study of CO₂ injection in carbonate reservoirs because of the reported effect of aqueous fluids on its mechanical behavior (Ciantia and Hueckel, 2013) and weak stress-dependence of its properties (Makhnenko and Labuz, 2014). It is a glauconitic fossiliferous limestone, showing a pale orange to grayish color, composed of mostly calcite (95–98%), with quartz, plagioclase, glauconite, and iron oxide. The rock matrix is supported with allochems, which chiefly comprises fragmental calcitic foraminifera that range from approximately 0.05 mm to 1 mm (rare) in maximum dimension and are cemented with calcitic mud (micrite). The P-wave velocity varies just by 2% in different directions (from 2.52 km/s to 2.57 km/s), meaning that the limestone is almost isotropic (Makhnenko and Labuz, 2014).

Rock interconnected porosity was measured by vacuum saturation technique and was found to be 0.35. This measurement was confirmed by mercury intrusion porosimetry test that provided not only the volume of the accessible pores but also the retention (or capillary pressure) curve shown in Figure 3.2. Suction was the difference between non-wetting and wetting fluid pressures. Supercritical CO₂ retention curve for water-saturated Apulian limestone was calculated from its pore size distribution by taking CO₂-water contact angle in calcite to be 40° and interfacial tension of 0.032 N/m (Espinoza and Santamarina, 2010). This allowed for the evaluation of CO₂ entry pressure (0.02 MPa) and van Genuchten (1980) parameter $m = 0.42$. We assumed that this parameter did not change after CO₂ treatment.

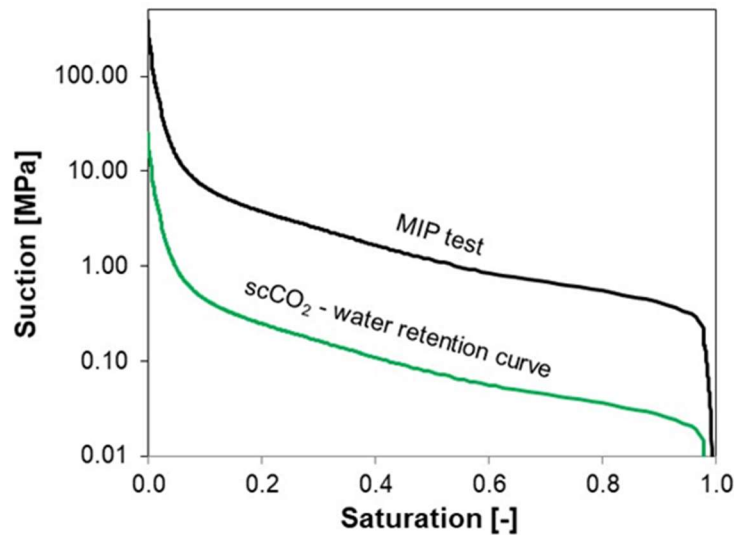


Figure 3.2. Retention curves obtained from mercury intrusion porosimetry and calculated curve that considers capillary properties of carbon dioxide (CO₂) in water-saturated carbonate rock.

3.3.2. Hydraulic Properties

The permeability was measured on limestone cores (50 mm in diameter and 100 mm long) installed inside a core flooding device that was connected to three syringe pumps: one syringe pump (70 MPa, SANCHEZ, Frépillon, France) for confining pressure applied with hydraulic oil and two other syringe pumps (25 MPa, Teledyne ISCO, Lincoln, NE, USA) for upstream and downstream pore water pressure control (Figure 3.3a). The confining pressure pump could be operated in three different regimes: pressure control (50 kPa accuracy), volume control (0.2 mL accuracy), and flow control (0.1% of setpoint). The pore water pressure pumps could be controlled in two regimes: pressure control (25 kPa accuracy) and flow control (0.5% of setpoint). The lateral stress (confining pressure) was the major principal stress in this setup, while the axial stress was provided through a passive restraint (fixed platens) and calculated from generalized Hooke's law, $\sigma_{ax} = 2\nu \sigma_{lat}$ with ν = Poisson's ratio of rock. A steady-state flow was implemented by assigning different pressures for upstream and downstream syringe pumps. Pure deionized water with viscosity of 0.001 Pa·s was used in these experiments. Assuming that the viscosity of pore fluid was constant (all tests were performed at $T \approx 22$ °C), and measuring the inflow and outflow fluid pressure difference Δp , inflow and outflow fluid volumes (ΔV in steady-state flow) during time step Δt , the intrinsic permeability (k) was calculated as:

$$k = \frac{\mu \cdot L \cdot \Delta V}{A \cdot \Delta t \cdot \Delta p} \quad (3.7)$$

where L and A are the length and cross-section area of the specimen, respectively. The flow occurs in the horizontal direction, so the effect of gravity is disregarded.

To induce a two-phase flow in the specimen, another syringe pump (50 MPa, Teledyne ISCO, USA) was connected in parallel with the upstream pore pressure pump. CO₂ was injected in liquid state (7 MPa, 22 °C, $7.7 \cdot 10^{-5}$ Pa·s viscosity), just 1 MPa above the transition pressure

between liquid and gaseous phases. Liquid CO₂ injection conditions are favorable to minimize the injection cost and are usually encountered in CO₂ injection wells within the first 1–2 km depth (Vilarrasa et al., 2013). The mean stress was preserved at 12 MPa, and the pore pressure was 6.7 MPa (effective mean stress $P' = 5.3$ MPa). The injected CO₂ initially dissolved in water, and additional CO₂ was subsequently injected. This procedure was repeated until saturation of water with CO₂ was reached and the latter one started flowing as a separate fluid. The CO₂ pump and the upstream water pump were operated by flow control, and the fraction of the two fluids in the two-phase flow could be represented by the ratio of the two flow rates of the two pumps. The flow rates of the two pumps (upstream water–CO₂) were controlled as 5–0 mL/min, 4–1 mL/min, 2.5–2.5 mL/min, 1–4 mL/min, and 0–5 mL/min, where the sum of the two flow rates were always constant and equal to 5 mL/min. Each pair of the flow rates represented the ratio of the volume of two fluids in the two-phase flow (water : CO₂), such as 100:0%, 80:20%, 50:50%, 20:80%, and 0:100%. The flow rates 5–0 mL/min and 0–5 mL/min were related to one-phase flow and measurements of permeability (k) for water ($\alpha = w$) and CO₂ ($\alpha = c$), respectively.

$$k_{r\alpha} = \frac{\mu_{\alpha} \cdot L \cdot \Delta V_{\alpha}}{k \cdot A \cdot \Delta t \cdot \Delta p_{\alpha}} \quad (3.8)$$

Here ΔV_{α} is the change of the volume of α -phase in the syringe pump, and Δp_{α} is the pressure difference between the α -phase and the downstream pressure. Δp_{α} is changing at the beginning of injection and then reaches a constant value, so the relative permeability is reported for steady flow. For this study, the intrinsic permeability and relative permeability curves of water and CO₂ were measured for pristine and CO₂ treated specimens. For the pristine specimens, the conducted tests should be short term (a couple of hours), such that the influence of the acidic CO₂–water mixture on limestone does not affect the results of relative and absolute permeability tests.

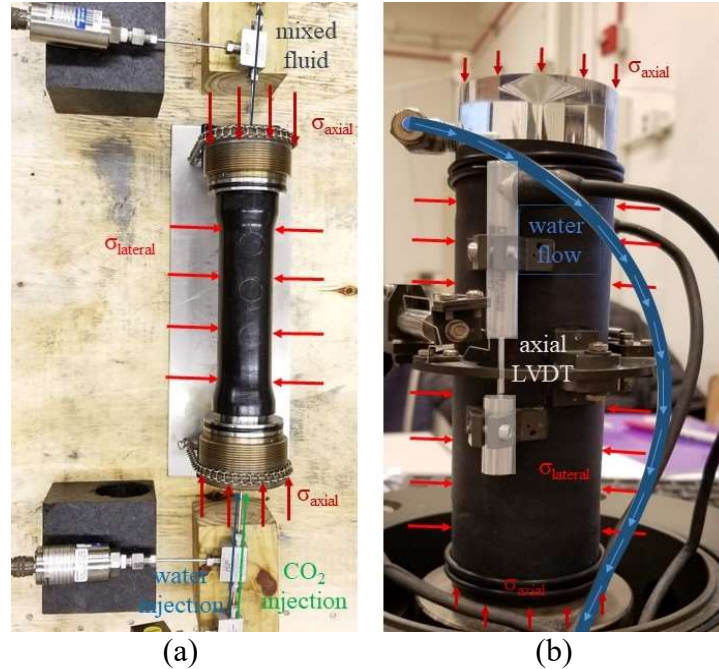


Figure 3.3. Experimental setup: (a) core flooding device for CO₂ treatment and permeability measurements on cylindrical (50 mm in diameter and 100 mm long) specimens and (b) cylindrical specimen (50×100 mm) with instrumented Linear Variable Differential Transformers (LVDTs) and pore pressure lines that is tested in 3.5 MPa GDS triaxial cell.

3.3.3. CO₂ Saturation and Treatment

Proper assessment of relative permeability required evaluation of the degree of saturation of two fluids, water and CO₂, during the relative permeability tests. Recent studies on relative CO₂ permeability are based on the calculation of water and CO₂ saturation using X-ray computed tomography (CT) scanning (Bennion and Bachu, 2008; Krevor et al., 2012; Andrew et al., 2014; Huo and Benson, 2016). Here, we propose a method to calculate the saturation of water and CO₂ from the changes in (undrained) mechanical response of the rock during the injection of the second fluid.

During the relative permeability tests, two fluids were continuously injected at a constant flow rate until their pressures reached equilibrium. After measuring relative permeability, the valves

on the upstream and downstream channels were closed simultaneously, setting the specimen in an undrained (no flow) condition. For the core flooding device, the increment in confining pressure was not equal to the mean stress like it would be in a conventional triaxial apparatus. Specimen deformation was limited in the axial direction ($\varepsilon_{ax} = 0$), and from generalized Hooke's law, the change in the mean stress could be expressed as $\Delta P = (2 + 2\nu_u)\Delta\sigma_{lat}/3$, where ν_u is the undrained Poisson's ratio of rock, since the specimen was deforming under the undrained condition. The Skempton's B coefficient (Skempton, 1954) was then measured by recording the change in pore pressure (Δp) caused by the increase in the mean stress (ΔP).

$$B = \frac{1}{\frac{\Delta P}{\Delta p} - C_{cor}} = \frac{\left(1 - \frac{K}{K_s'}\right)}{\left(1 - \frac{K}{K_s'}\right) + \phi K \left(\frac{1}{K_f} - \frac{1}{K_s''}\right)} \quad (3.9)$$

The effect of pore water lines that connect pressure transducers to the specimen (Figure 3.3a) was taken into account through the correction factor C_{cor} (Bishop, 1976), which appeared to be very small for core flooding device (0.5×10^{-2}), so the applied correction was within the accuracy of our B measurements (± 0.005). As shown in Equation (3.9), Skempton's B coefficient can also be expressed through poroelastic parameters (Detournay and Cheng, 1993), where K is the drained bulk modulus, K_s' is theunjacketed bulk modulus, K_s'' is theunjacketed pore modulus, and K_f is the bulk modulus of the saturating fluid ($K_w \approx 2.3$ GPa for water). Since the fluid in the pores consists of water and CO_2 , its bulk modulus K_f depends on the degree of saturation. For each test stage that involved differential flows of water and CO_2 , a sufficient amount of fluid (a few pore volumes) needed to be flushed through the specimen to guarantee that the outflow fluid had the same ratio of fluid phases. Subsequently, the residual degree of saturation of water and CO_2 could be measured. If all poromechanical parameters and correction factors are known, K_f

can be calculated for the mixture of two fluids (K_{mix}). The bulk modulus of liquid CO₂, K_c is calculated from the knowledge of its density and P-wave velocity ($\rho_c = 769.3 \text{ kg/m}^3$, $V_{pc} = 302.1 \text{ m/s}$) at testing conditions, $T = 22 \text{ }^\circ\text{C}$ and $p = 7 \text{ MPa}$ (Achenbach, 1984)

$$K_c = \rho_c V_{pc}^2 = 0.070 \text{ GPa} \quad (3.10)$$

At each stage of relative permeability test, the bulk modulus of the mixed fluid K_{mix} ($=K_f$) can be calculated from Equation (3.9). Then, knowing the bulk modulus of water and CO₂, the corresponding degree of water saturation S_w can be obtained from Wood's formula (Wood, 1955)

$$\frac{1}{K_{mix}} = \frac{S_w}{K_w} + \frac{1-S_w}{K_c} \quad (3.11)$$

Carbonate reservoirs are reported to react with the injected CO₂ when it mixes with the aqueous pore fluid. In this study, after measuring the properties of pristine specimen, such as porosity, intrinsic permeability, relative permeability, and Skempton's B coefficient, we injected CO₂ in the specimen and treated it for three days (72 h). High porous, weakly-bonded Apulian limestone seemed to be quickly affected by acidic water-CO₂ mixture when left under the condition of no outward flow. It was observed that the pressure of the mixture of CO₂ and water had a tendency to decrease towards the boundary of the liquid state with gas state ($\sim 6 \text{ MPa}$ at $22 \text{ }^\circ\text{C}$). Therefore, the upstream CO₂ pressure was controlled by the CO₂ pump to preserve it at 7 MPa . After CO₂ treatment, we flushed the specimen with water and periodically emptied the downstream pump until no CO₂ was left in the downstream fluid. Additionally, we released the pore pressure in the specimen to get rid of the trapped CO₂ and then fully saturated the specimen with only water. After that, we repeated the relative permeability tests for the CO₂ treated specimen for comparison.

3.3.4. Geomechanical Properties

The elastic and strength properties of Apulian limestone were measured within 3.5 MPa Global Digital Systems (GDS) triaxial cell that allowed testing of 50 mm in diameter and 90–110 mm long soil and rock cores. Three 3.5 MPa pressure pumps provided the control of the confining pressure and input and output pore pressures. The pumps could work in either pressure (1 kPa accuracy) or volume control (1 mm³ accuracy) regimes. The triaxial cell was fixed on the bottom piston inside the 50 kN load frame and axial load was applied by the passive restraint on the top of the frame through the movement of the piston (Figure 3.3b). Two additional pore pressure transducers were installed at the input and output pore pressure lines to provide measurements of the upstream and downstream pore pressure in flow and undrained mechanical tests. Measurements of axial and lateral specimen deformation were conducted by attaching the set of three Linear Variable Differential Transformers (LVDTs), two axial and one lateral, to the rubber membrane (1 mm thick) around the specimen (Figure 3.3b).

Constant Terzaghi effective mean stress, $P' = P - p = 1$ MPa, was applied by preserving the same difference between the mean stress (=confining pressure) and pore pressure. For all geomechanical experiments, the specimens were fully saturated with water. Water saturation was achieved by a back pressure saturation technique. Initially, water was flushed through the specimen until the outlet fluid volume equalized with the injected (inlet) volume. The outlet valve was then closed and pore (back) pressure was gradually increased while preserving the effective mean stress constant. At each stage of injection, Skempton's B coefficient was measured. The back pressure saturation procedure was stopped when the measured B -value became constant (Makhnenko and Labuz, 2016). After that, the permeability of the specimen

was measured from Equation (3.7) when the steady-state flow through the specimen was established.

The drained condition was developed by imposing a constant pressure on the pressure controllers connected to the specimen. The elastic parameters, such as Young's modulus (E) and Poisson's ratio (ν), were measured during the application of axial load with the axial strain rate equal to $10^{-5}/s$. The LVDTs attached to the specimen provide the calculation of axial and lateral strains. The slope of the linear (elastic) part of axial stress—axial strain curve provided the value of Young's modulus (E). The relationship between the axial and (negative) lateral strains allowed for the calculation of Poisson's ratio (ν). If the axial loading was continued until reaching the peak load, the strength characteristics of the rock were evaluated. Performing strength tests at different effective lateral stresses and obtaining a few data points for axial stress at failure, provided the evaluation of the strength characteristics of rock, e.g., cohesion c' and friction angle ϕ' if Mohr-Coulomb failure criterion is adopted (Equation 3.6) with $\tau = (\sigma_{ax} - \sigma_{lat})/2$ and $\sigma_n' = (\sigma_{ax} + \sigma_{lat})/2$. After the strength test, every specimen was trimmed to a cylindrical shape with a known volume and vacuum saturation method was applied to measure the porosity of treated rock.

3.4 Results

We measured the intrinsic and relative permeability, poroelastic properties, and strength properties of Apulian limestone on six pristine and four CO₂ treated specimens. The elastic properties and permeability of the pristine specimens were consistent between all the specimens and have little stress dependence, so we reported them only for one test (Calc-0). CO₂ treated specimens (Calc-1 to Calc-4) have some variation in their properties (Table 3.2).

3.4.1. Permeability and Porosity

Permeability and porosity were measured for pristine and CO₂ treated Apulian limestone. While pristine specimens had an intrinsic permeability of $9 \times 10^{-15} \text{ m}^2$ at $P' = 1 \text{ MPa}$, the CO₂ treated rock showed a decrease in permeability to $5\text{--}6 \times 10^{-15} \text{ m}^2$. This decrease in permeability may be related to the observed porosity variation, which was reduced from 0.35 to 0.34 when specimens were treated with CO₂. Additionally, porosity measurements on 10 mm thick discs cuts from the upstream and downstream ends of the specimen were performed for specimens Calc-3 and Calc-4. The results showed that the porosity for the upstream part was 0.37–0.38, whereas the downstream part porosity was 0.28–0.30.

Table 3.2. Properties of pristine and carbon dioxide (CO₂) treated Apulian limestone.

	Pristine	CO ₂ -Treated			
	Calc-0	Calc-1	Calc-2	Calc-3	Calc-4
Min. principal stress, σ_{lat} [MPa]	2.0	3.5	3.5	3.5	3.5
Pore pressure p^f , [MPa]	1.8	3.4	2.0	0.5	1.0
Permeability, k [m ²] (at $P' = 1 \text{ MPa}$)	9×10^{-15}	3.5×10^{-15}	5.1×10^{-15}	5.6×10^{-15}	5.8×10^{-15}
Porosity, ϕ [-]	0.35	0.34	0.34	0.32	0.34
Young's modulus, E [GPa]	7.1	3.4	4.4	4.7	4.5
Poisson's ratio, ν [-]	0.25	-	-	0.25	0.25
Max. principal stress at failure, σ_{ax} [MPa]	15.6	7.7	10.7	12.5	12.6

3.4.2. Relative Permeability and Saturation

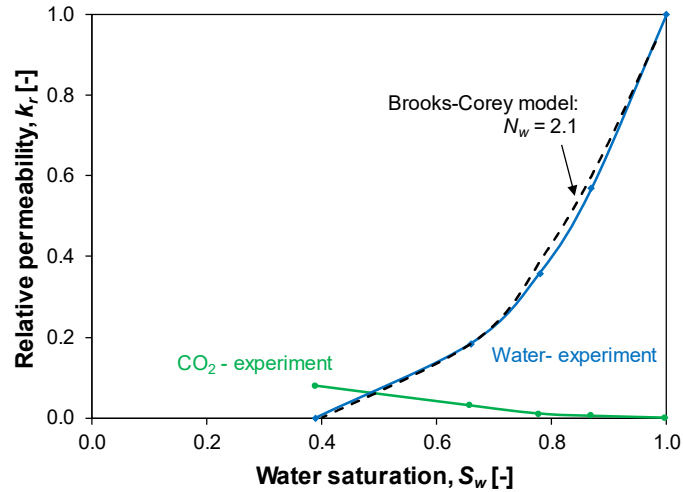
Results of the relative permeability tests were plotted as a function of the degree of saturation evaluated from compressibility of pore fluid K_f (Equation 3.11). K_f is calculated from the measurements of Skempton's B coefficient and knowledge of poroelastic properties from

Equation (3.9) (see Section 3.4 *c*). For 100% water saturation, Skempton's B coefficient is equal to 0.55. As the portion of CO₂ in the two-phase flow increased, the B coefficient decreased significantly, giving values of 0.18 (water: CO₂ = 80:20), 0.13 (water: CO₂ = 50:50), 0.10 (water: CO₂ = 20:80), and decreasing down to 0.06 (water: CO₂ = 0:100) for pure CO₂ flow. These tests were performed under Terzaghi effective mean stress equal to $P' = 5$ MPa. For pristine Apulian limestone, the relative permeability of water decreased from 1 to 0 for a reduction in the water saturation from 1.0 to 0.39 (Figure 3.4a). The relative permeability of CO₂ increased with the decrease in water saturation, but the increase rate of the relative permeability to CO₂ was much smaller, reaching only a value of approximately 0.1. For CO₂ treated limestone, the change in relative CO₂ permeability was insignificant (Figure 3.4b). However, the relative water permeability turned from a quadratic to a quasi-linear function of water saturation degree. Additionally, the maximum degree of CO₂ saturation increased from 0.61 to 0.66 in CO₂-treated limestone. We acknowledge that an even higher degree of CO₂ saturation could be achieved if the controllers with higher maximum flow rates are used.

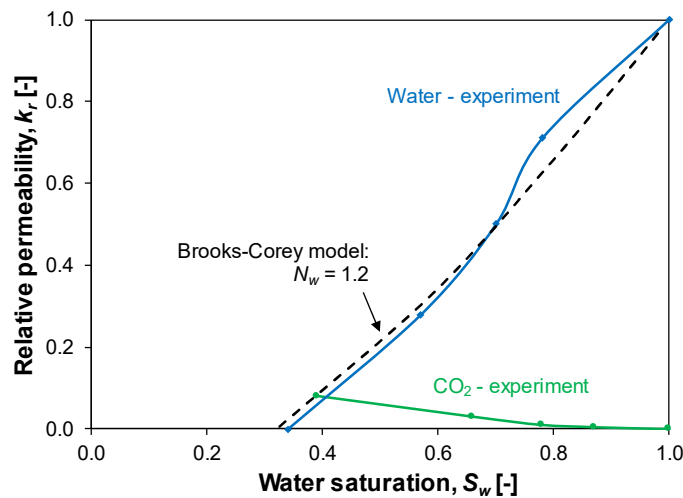
The obtained relative permeability curves are fitted as power-law functions of the degree of saturation, similarly to the Brooks–Corey model (Brooks and Corey, 1964).

$$k_{rw} = (S_e)^{N_w} \quad \text{and} \quad k_{rc} = (1 - S_e)^{N_c} \quad (3.12)$$

where, S_e is the saturation parameter from Equation (3.4), and N_w and N_c are the exponent coefficients for water and CO₂, respectively. Note that N_w value for Apulian limestone changes from 2.1 to 1.2 after CO₂ treatment (Figure 3.4).



(a)



(b)

Figure 3.4. Relative permeability curves and fitting with the Brooks–Corey model for Apulian limestone: (a) pristine specimen and (b) CO₂ treated specimen.

3.4.3. Geomechanical Properties

Conventional triaxial tests were conducted on both pristine and CO₂ treated Apulian limestone and the results of the experiments conducted at $\sigma_{lat}' = 2.5$ MPa are shown in Figure 4.5. Young's modulus E decreased from 7.1 GPa to 4.5 GPa and also the deviatoric stress (=axial stress–lateral stress) at failure decreased from 17.1 MPa to 9.2 MPa after CO₂ treatment. Measurements of

Poisson's ratio with lateral LVDT displacement were not successful on treated specimens, so it was evaluated for specimens Calc-3 and Calc-4 from the ultrasonic wave velocity ("dynamic") measurements. P- and S-wave velocities (c_p , c_s) measured before (2.55 km/s, 1.46 km/s) and after (2.38 km/s, 1.40 km/s) treatment show that Young's modulus decreased by 20%, but Poisson's ratio presents little changes due to CO₂ injection, so the constant value, $\nu = 0.25$, was used in the numerical model (Table 3.3). Obviously, the inhomogeneity of pore space distribution caused by injection may produce local changes in Poisson's ratio that need to be assessed from local strain measurements. Undrained Poisson's ratio ν_u was calculated from poroelastic relationship (Detournay and Cheng, 1993) to be 0.36. The bulk modulus $K = 4.7$ GPa for pristine rock and 3.0 GPa for treated limestone. K_s' of pristine rock was measured to be 42.9 GPa (Makhnenko and Labuz, 2014). Here, we assumed that the solid bulk properties of the rock did not change after treatment, so K_s' remains the same. Additionally, since Apulian limestone is a monomineralic rock, it is assumed that $K_s' = K_s''$. The strength tests provided the cohesion of pristine rock as $c' = 5.6$ MPa and the friction angle as $\phi' = 21^\circ$. After CO₂ treatment, both the cohesion and friction angle decreased to $c' = 3.0$ MPa and $\phi' = 14^\circ$, respectively (Figure 3.6).

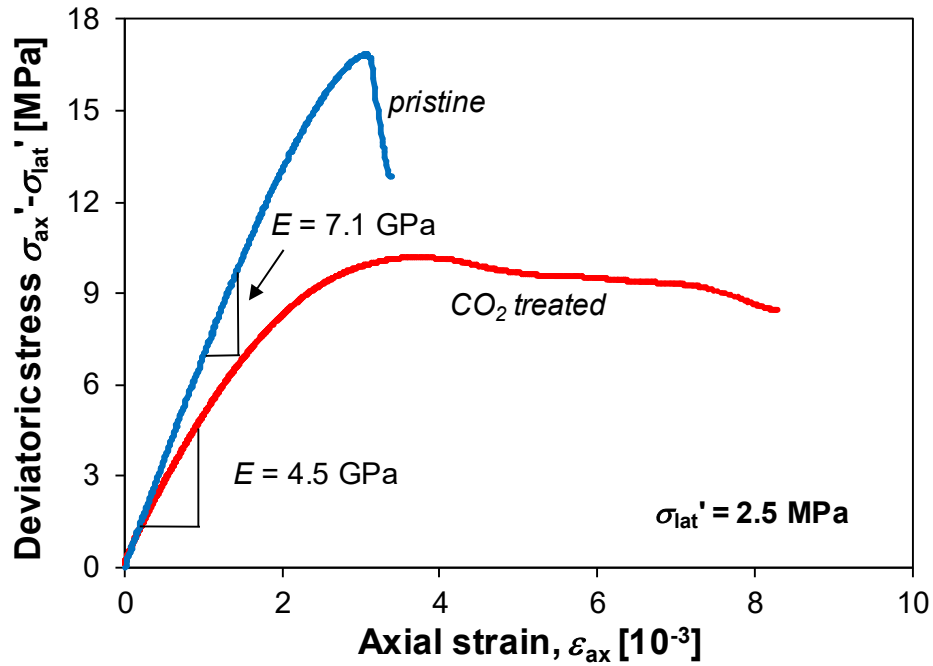


Figure 3.5. Effect of CO_2 injection on the geomechanical response of Apulian limestone tested in conventional triaxial compression at $\sigma'_3 = 2.5$ MPa.

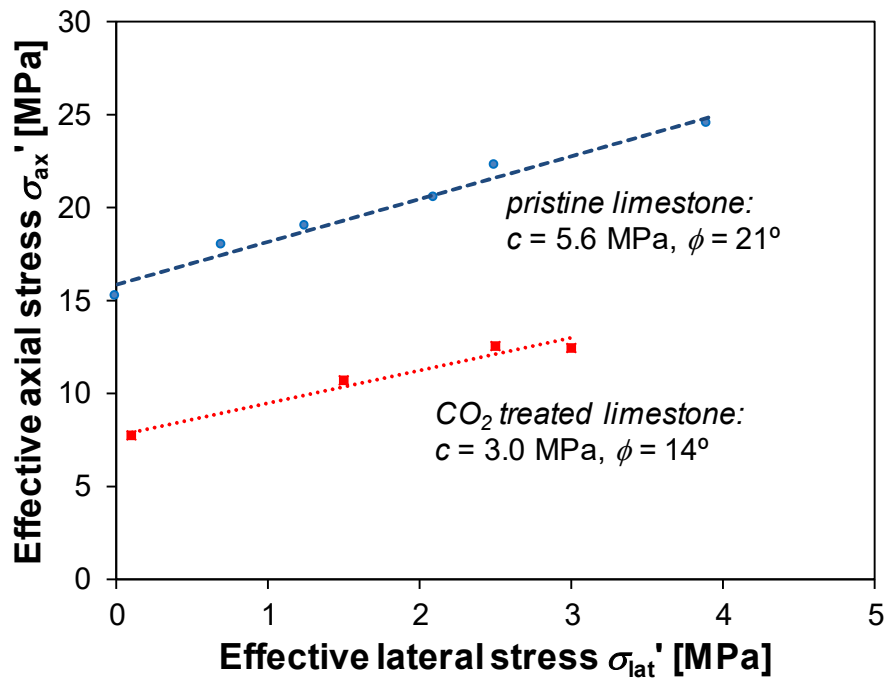


Figure 3.6. Failure envelopes for pristine and CO_2 treated Apulian limestone.

Table 3.3. Properties of pristine and CO₂ treated Apulian limestone.

Property	Pristine Rock	CO ₂ -Treated Rock
Permeability, k [m ²]	9×10^{-15}	$5-6 \times 10^{-15}$
Porosity, ϕ [-]	0.35	0.34
Relative water permeability, k_{rw} [-]	$S_w^{2.1}$	$S_w^{1.2}$
Relative CO ₂ permeability, k_{rc} [-]	S_c^6	$S_c^{5.5}$
Gas entry pressure, p_0 [MPa]	0.02	0.02
van Genuchten shape parameter m [-]	0.42	0.42
Young's modulus, E [GPa]	7.1	4.4
Poisson ratio, ν [-]	0.25	0.25
Cohesion, c' [MPa]	5.6	3.0
Friction angle, ϕ' [°]	21	14

3.4.4. Numerical Results

The changes in Apulian limestone properties as a result of interaction with CO₂ affect the hydro-mechanical response of the reservoir-caprock system. Even though laboratory measurements were not performed at representative conditions, they still can be used for the demonstration of CO₂ injection effect on carbonate reservoirs, especially considering weak stress-dependence of Apulian limestone properties (Makhnenko and Labuz, 2014).

On the one hand, the CO₂ plume dynamics and pore pressure evolution were slightly affected by the skin effect that results from the local reduction in permeability occurring within the CO₂ plume. This permeability reduction around the injection well caused a higher pressure buildup that lead to a slightly steeper CO₂-brine interface at early times of injection (during the first few months). Nevertheless, since the permeability reduction was local, the effective permeability of the reservoir became equal to that of the intact rock in the long term (Meier et al., 1998). Thus, pressure buildup eventually became the same as if there were no local permeability reduction around the injection well (Butler, 1988; Vilarrasa et al., 2011), leading to a practically identical CO₂ plume shape after 3 years of injection (Figure 3.7). The long-term pressure buildup at the injection well was 4.3 MPa. On the other hand, contrary to the transient effect of the change in

the hydraulic properties of the reservoir within the CO₂ plume, the effect of the changes in the geomechanical properties is permanent.

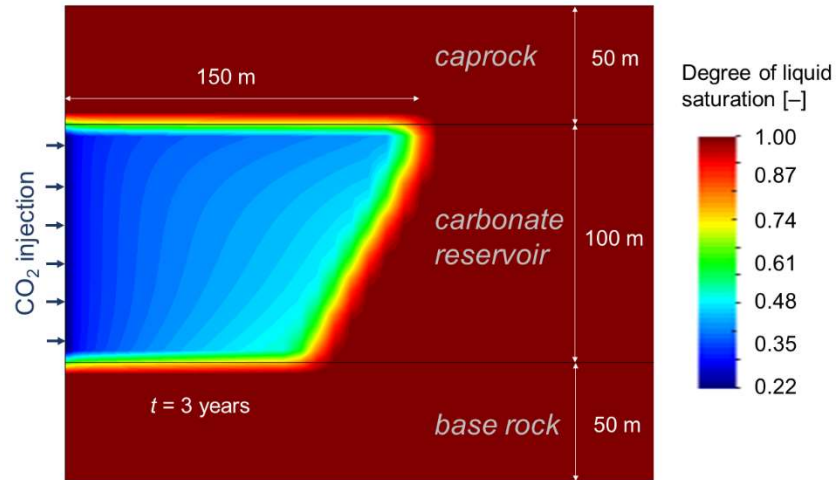


Figure 3.7. CO₂ plume after 3 years of injection presenting a subvertical CO₂-brine boundary 150 m away from the injection well.

Figure 3.8 shows the changes in reservoir and caprock stability, in terms of mobilized friction angle, with distance to the injection well. The mobilized friction angle is the angle of the tangent to the Mohr's circle, considering that there is no cohesion. Rock stability was clearly affected by the changes in Apulian limestone stiffness within the CO₂ plume, which extended laterally for 150 m after 3 years of injection. These changes were caused by the limestone becoming softer while interacting with CO₂. As a result, the rock within the CO₂ plume expanded more in response to pressure buildup, than the rock outside the plume. However, the expansion of the rock within the CO₂ plume was highly constrained laterally by the stiffer rock around it. This constraint on deformation lead to a higher increase in the horizontal total stresses than in the case where the reservoir was homogeneous. Additionally, to satisfy equilibrium of stresses, an increase in the vertical stress occurred within the zone affected by CO₂ plume, especially at the CO₂-brine interface, where shear stresses concentrate as a result of the stiffness contrast between

the altered and intact rock. These stress changes caused a slight rotation of the stress tensor in the vicinity of the CO₂-brine interface. As for the effect on the stability within the reservoir, the stress changes that occurred within the altered rock inside the CO₂ plume caused a lower decrease in stability than when no changes in the geomechanical properties were accounted for. The situation in the caprock was reversed, leading to a higher decrease in stability above the CO₂ plume when the changes in the geomechanical properties were accounted for. This is a consequence of the stress redistribution that occurred as a result of the increase in the vertical stress within the CO₂ plume to satisfy stress equilibrium. Since the overburden is constant, the increase in the vertical stress inside the CO₂ plume caused a decrease in the horizontal stresses outside it. This geomechanical response is analogous to the one that takes place when cooling occurs around the injection well, but with the opposite sign (Vilarrasa et al., 2013).

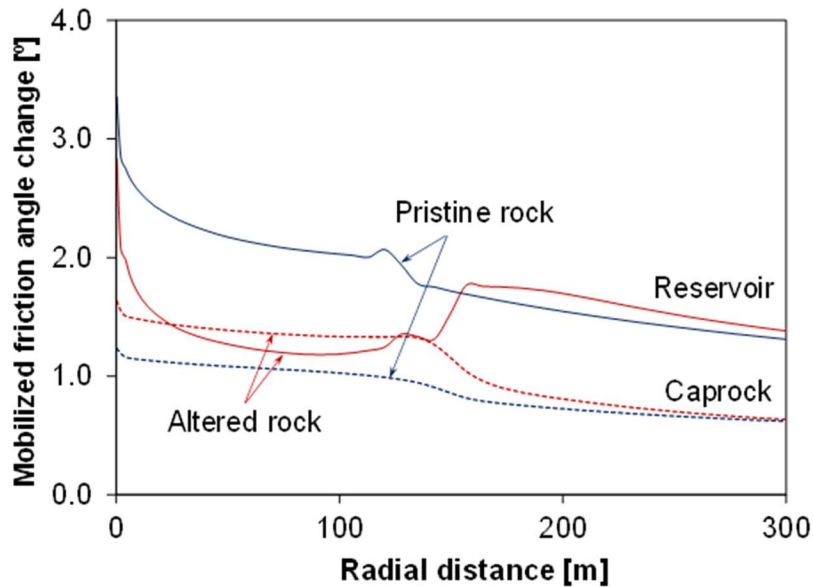


Figure 3.8. Changes in mobilized friction angle along the radial distance in the middle of the reservoir (continuous lines) and in the caprock, 10 m above the reservoir-caprock interface (dashed lines) for pristine and altered rock after 3 years of CO₂ injection.

The described stress changes can be represented by Mohr's circles (Figure 3.9). In the reservoir (Figure 3.9a), the initial stress state is far from failure conditions. This state of stress is displaced towards the left during injection as a result of pressure buildup. However, the Mohr's circle also experiences a decrease in its size because of the poromechanical response of the rock (pore pressure increase), which induces an increase in the horizontal total stress. If the changes in Apulian limestone properties due interaction with CO₂ are also accounted for, the horizontal total stresses undergo a higher increase and the vertical total stress also increases. These changes slightly shift the Mohr's circle to the right and reduce its size, leading to a lower decrease in stability. However, interaction with CO₂ also decreases the strength of the limestone. As a result, the failure envelope of the altered limestone approaches the Mohr's circle, which may lead to failure conditions depending on the initial stress state and induced pressure buildup.

Considering the caprock (Figure 3.9b), the pore pressure slightly dropped as a result of the caprock deformation induced by the expansion of the reservoir, displacing the Mohr's circle to the right. The expansion of the reservoir caused an increase in the volumetric strain of the caprock, and since the caprock permeability was extremely low and fluid flow was negligible, the fluid within the pores of the caprock was accommodated in a larger volume, which resulted in a slight pressure drop (Vilarrasa et al., 2013). This phenomenon is known as the reverse-water level fluctuation (Hsieh, 1996). Additionally, the horizontal total stresses decreased in the caprock, leading to an increase in the size of the Mohr's circle. As a result, caprock stability slightly decreased but not dramatically, since the strength of the caprock is not affected due to the inability of CO₂ to penetrate into it at considered overpressures (Vilarrasa and Makhnenko, 2017).

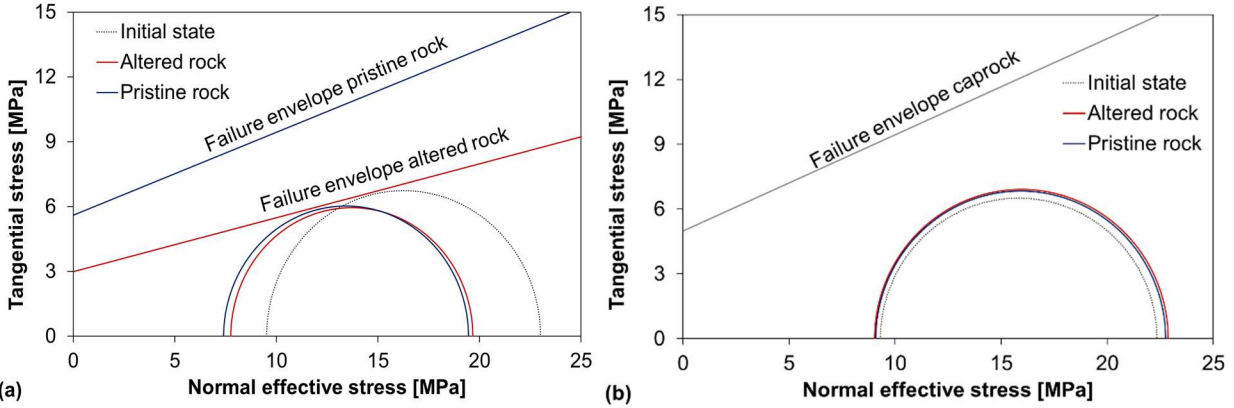


Figure 3.9. Mohr's circles 50 m away from the injection well (a) in the middle of the reservoir and (b) 10 m above the reservoir-caprock interface, showing the initial stress of state and the resulting stress of state after 3 years of injection when considering (altered rock) and not considering (pristine rock) changes in the reservoir properties as a result of geochemical reactions.

3.5. Discussion

In this study, comprehensive experimental testing was conducted to assess hydraulic, poroelastic, and failure properties of Apulian limestone (calcarenite). In particular, relative permeability considering two-phase flow of water and CO₂ was measured. For all these measurements, the experimental procedures were performed for both pristine and CO₂ treated limestone to evaluate the influence of CO₂ injection on mechanical and hydraulic properties. Given the low strength of the material, it is less likely to be chosen as the host formation for deep geological storage. This study can be seen, though, as a demonstration of a strong effect of CO₂ injection on carbonate-rich rock. Low shear strength, almost pure calcite framework, and large specific surface area of the pores allow for quick (within a few days) observations of the deterioration in rock properties. The choice of boundary conditions for the tests was dictated by linearity of material response within the elastic range, so high pressures were avoided.

Pure deionized water was used to saturate the specimens and, in general, its use can trigger chemical reactions and affect measurements of permeability and drained properties (Gouze et al.,

2017). Here, the saturation of specimens with water was performed for at least 2-3 days and this period of time has been observed to be enough to establish chemical equilibrium between the pore fluid and carbonate rock (Gouze et al., 2017). This observation is confirmed by the constant values of rock permeability obtained during the repetitive measurements. Saline water that would represent the *in-situ* fluid for deep carbonate aquifers was not used because possible effects of salt precipitation and evaporation are involved and could not be captured by the model, even though we recognize that these effects may influence the evolution of rock's petrophysical properties.

CO₂ injection produced change in mean porosity within 1%, indicating that the mass balance was fairly followed in the experiment. Some dissolved calcite may remain in an aqueous state (Ciantia et al., 2015), and may have induced 1% error to the total porosity. Therefore, mean porosity of the specimens can be considered to be practically constant after CO₂ treatment, but permeability decreased by a factor of two as a result of CO₂-rock interaction. Luquot and Gouze (2009) observed that CO₂-rich brine reacts with calcite, dissolving it and leading to an increase in permeability, especially near an injection well, while the macroscopic porosity was just moderately affected. It should be noted that in this study, the CO₂ treatment procedure was conducted by establishing an undrained condition, whereas Luquot and Gouze (2009) continuously injected brine with dissolved CO₂. This means that here, CO₂ was injected through the upstream, but during the CO₂ treatment process, it did not flow throughout to the downstream pump basically being trapped in the specimen. Porosity measurements for the upstream and downstream part of the specimen differed, showing a porosity increase upstream and decrease downstream. This difference suggests that calcite dissolution occurred upstream, and precipitation of carbonates took place downstream, where it was undrained. In addition to this

qualitative analysis, a further detailed study will be conducted in the future to identify the dissolution/precipitation patterns.

CO₂ treatment of Apulian limestone causes changes in the relative permeability. The main change is that the exponent of the relative permeability to water varies from quadratic to quasi-linear after CO₂ treatment. This implies that for a given saturation degree, the relative permeability to water becomes higher after CO₂ treatment. This effect is considered to have implications for long-term CO₂ injection (Gouze et al., 2017) and highlights that predictive simulations of industrial-scale CO₂ storage should incorporate the change in relative permeability.

Drained conventional triaxial compression tests showed that CO₂ treatment tends to decrease the strength of Apulian limestone. The strength parameters decrease significantly (cohesion by a factor of 2, friction angle by a factor of 1.5), highlighting the importance of considering these chemo-mechanical changes when evaluating the stability of the reservoir. In addition, changes in the stress–strain curve indicate that the CO₂ treatment makes carbonate rock a more ductile material compared to pristine limestone. Therefore, for low-stress conditions, more deformation may be expected for post-treated rock.

These changes in hydro-mechanical properties induced by geochemical reactions affect the response of the reservoir-caprock system to CO₂ injection. Simulation results show that the portion of the reservoir that has been affected by CO₂–rock interactions alter both the two-phase flow dynamics and the geomechanical response of the rock. While the changes in the hydraulic properties are transient, the geomechanical response is permanent. The stiffness contrast between the pristine and CO₂ treated portion of the reservoir causes differential deformation that results in stress redistribution that improves stability in the reservoir, but worsens it in the caprock, in

comparison with the case in which no changes in the geomechanical properties are considered. Nevertheless, the changes in stability are minor and limited to a few degrees in the mobilized friction coefficient. What may really compromise reservoir stability is the reduction in the limestone strength after being exposed to CO₂. Geochemical reactions bring the failure envelope close to the effective stress state, which could induce shear failure depending on the initial stress state and injection conditions, i.e., injection pressure and temperature. If shear failure occurs, shear slip of fractures or creation of new fractures may occur, inducing microseismic events. If failure is local, around the injection well, sheared fractures will enhance injectivity. Such enhancement would be beneficial for storage operations, especially if caprock stability is not compromised, as it is the case of the modeled scenario. These simulation results show the importance of accounting for chemo-mechanical couplings to assess caprock integrity and the geomechanical response of carbonate storage formations to CO₂ injection.

3.6. Conclusions

We have measured in the laboratory the effect of geochemical reactions induced by CO₂ injection on hydraulic and geomechanical properties of water-saturated Apulian limestone (calcarenite) and evaluated the implications of these property changes at the field scale through numerical simulations. CO₂–rock interactions cause calcite dissolution where CO₂ injection occurs, i.e., upstream of the specimens, but leads to carbonate precipitation downstream, which has been set as undrained. This dissolution/precipitation pattern resulted in a slight porosity decrease, but a permeability reduction by a factor of two. The relative permeability curves were also affected, especially the one of water, which changed from being quadratic to being quasi-linear with the water saturation degree. CO₂ treatment induced a reduction in the stiffness and

strength of the limestone. Accounting for these property changes in numerical simulations at the industrial scale leads to stress redistribution within the CO₂ plume altered rock. This stress redistribution reduces caprock stability comparing with the case in which rock properties are considered to remain unaltered by CO₂–rock interaction.

References

- Achenbach, J.D. (1984) *Wave Propagation in Elastic Solids*. North-Holland Publishing Co. Amsterdam, The Netherlands.
- Alam, M.M., Hjuler, M.L., Foged, H., Lykke, I., Christensen, H.F., Fabricius, I.L. (2014) Petrophysical and rock-mechanics effects of CO₂ injection for Enhanced oil recovery: Experimental study on chalk from south Arne field, North Sea. *J Pet Sci Eng.* 122: 468–487.
- Anderson, K., Peters, G. (2016) The trouble with negative emissions. *Science.* 354: 182–183.
- André, L., Audigane, P., Azaroual, M., Menjoz, A. (2007) Numerical modeling of fluid-rock chemical interactions at the supercritical CO₂-liquid interface during CO₂ injection into a carbonate reservoir, the Dogger aquifer (Paris Basin, France). *Energy Convers Manag.* 48.
- Andrew, M., Bijeljic, B., Blunt, M.J. (2014) Pore-scale imaging of trapped supercritical carbon dioxide in sandstones and carbonates. *Int J Greenh Gas Control.* 22: 1–14.
- Bear, J. (1972) *Dynamics of Fluids in Porous Media*; Elsevier: New York, NY, USA.
- Bemer, E., Lombard, J.M. (2010) From injectivity to integrity studies of CO₂ geological storage: Chemical alteration effects on carbonates petrophysical and geomechanical properties. *Oil Gas Sci Technol—Rev Inst Fr Pétrol.* 65: 445–459.

- Bennion, D.B., Bachu, S. (2008) Drainage and imbibition relative permeability relationships for supercritical CO₂/Brine and H₂S/Brine systems in intergranular sandstone, carbonate, shale, and anhydrite rocks. *SPE Res Eval & Eng.* 11(3): 487–496.
- Bishop, A.W. (1976) The influence of an undrained change in stress on the pore pressure in porous media of low compressibility. *Géotechnique.* 26: 371–375.
- Brooks, R.H., Corey, A.T. (1964) Hydraulic properties of porous media and their relation to drainage design. *Trans ASAE.* 7: 26–28.
- Butler, J.J., Jr. (1988) Pumping tests in nonuniform aquifers—The radially symmetric case. *J Hydrol.* 101: 15–30.
- Ciantia, M.O., Castellanza, R., di Prisco, C. (2015) Experimental Study on the Water-Induced Weakening of Calcarenes. *Rock Mech Rock Eng.* 48: 441-461.
- Ciantia, M.O., Hueckel, T. (2013) Weathering of submerged stressed calcarenites: Chemo-mechanical coupling mechanisms. *Geotechnique.* 63: 768–785.
- Dentz, M., Tartakovsky, D.M. (2009) Abrupt-interface solution for carbon dioxide injection into porous media. *Transp Porous Media.* 79: 15.
- Detournay, E., Cheng, A.H.-D. (1993) Fundamentals of Poroelasticity. In *Comprehensive Rock Engineering: Principles, Practice and Projects, Vol. II, Analysis and Design Methods*; Fairhurst, C., Ed. Pergamon Press: Oxford, UK. Chapter 5.
- Espinoza, D.N., Santamarina, J.C. (2010) Water-CO₂-mineral systems: Interfacial tension, contact angle, and diffusion—Implications to CO₂ geological storage. *Water Resour Res.* 46: W07537.
- Gouze, P., Edlmann, K., McDermott, C.I., Luquot, L. (2017) Laboratory Experiments. In *Geological Storage of CO₂ in Deep Saline Formations*. Niemi, A., Bear J., Bensabat J. Eds.

- Theory and Applications of Transport in Porous Media. vol. 29; Springer: Dordrecht, Netherlands, Chapter 6.
- Grgic, D. (2011) Influence of CO₂ on the long-term chemomechanical behavior of an oolitic limestone. *J Geophys Res: Solid Earth*. 116: B07201.
- Grombacher, D., Vanorio, T., Ebert, Y. (2012) Time-lapse acoustic, transport, and NMR measurements to characterize microstructural changes of carbonate rocks during injection of CO₂-rich water. *Geophysics*. 77: WA169–WA179.
- Hsieh, P.A. (1996) Deformation-induced changes in hydraulic head during ground-water withdrawal. *Groundwater*. 34: 1082–1089.
- Huo, D., Benson, S.M. (2016) Experimental investigation of stress-dependency of relative permeability in rock fractures. *Transp Porous Media*. 113: 567–590.
- IPCC. (2005) Special Report on Carbon Dioxide Capture and Storage. Cambridge University Press: Cambridge, UK.
- Juanes, R., Spiteri, E.J., Orr, F.M., Jr., Blunt, M.J. (2006) Impact of relative permeability hysteresis on geological CO₂ storage. *Water Resour Res*. 42: W12418.
- Krevor, S.C.M., Pini, R., Zuo, L., Benson, S.M. (2012) Relative permeability and trapping of CO₂ and water in sandstone rocks at reservoir conditions. *Water Resour Res*. 48: W02532.
- Liteanu, E., Spiers, C.J., De Bresser, J.H.P. (2013) The influence of water and supercritical CO₂ on the failure behavior of chalk. *Tectonophysics*. 599: 157–169.
- Luquot, L., Gouze, P. (2009) Experimental determination of porosity and permeability changes induced by injection of CO₂ into carbonate rocks. *Chem Geol*. 265: 148–159.

- Makhnenko, R.Y., Labuz, J. (2014) Calcarenite as a possible host rock for geologic CO₂. In Proceedings of the 48th U.S. Rock Mechanics/Geomechanics Symposium, Minneapolis, MN, USA.
- Makhnenko, R.Y., Labuz, J.F. (2016) Elastic and inelastic deformation of fluid-saturated rock. *Philos Trans R Soc A*. 374: 20150422.
- Meier, P.M., Carrera, J., Sánchez-Vila, X. (1998) An evaluation of Jacob's method for the interpretation of pumping tests in heterogeneous formations. *Water Resour Res*. 34: 1011–25.
- Nordbotten, J.M., Celia, M.A. (2012) *Geological Storage of CO₂*. John Wiley and Sons: Hoboken, NJ, USA.
- Olivella, S., Gens, A., Carrera, J., Alonso, E.E. (1996) Numerical formulation for a simulator (CODE_BRIGHT) for the coupled analysis of saline media. *Eng Comput*. 13: 87–112.
- Rohmer, J., Pluymakers, A., Renard, F. (2016) Mechano-chemical interactions in sedimentary rocks in the context of CO₂ storage: Weak acid, weak effects? *Earth-Sci Rev*. 157: 86–110.
- Saaltink, M.W., Vilarrasa, V., De Gaspari, F., Silva, O., Carrera, J., Rötting, T.S. (2013) A method for incorporating equilibrium chemical reactions into multiphase flow models for CO₂ storage. *Adv Water Resour*. 62: 431–441.
- Skempton, A.W. (1954) The pore-pressure coefficients A and B. *Geotechnique*. 4: 143–147.
- Sterpenich, J., Sausse, J., Pironon, J., Géhin, A., Hubert, G., Perfetti, E., Grgic, D. (2009) Experimental ageing of oolitic limestones under CO₂ storage conditions. Petrographical and chemical evidence. *Chem Geol*. 265: 99–112.
- Van Genuchten, M.T. (1980) A closed-form equation for predicting the hydraulic conductivity of unsaturated soils. *Soil Sci Soc Am J*. 44: 892–898.

- Vanorio, T., Nur, A., Ebert, Y. (2011) Rock physics analysis and time-lapse rock imaging of geochemical effects due to the injection of CO₂ into reservoir rocks. *Geophysics* 76: O23–O33.
- Vialle, S., Vanorio, T. (2011) Laboratory measurements of elastic properties of carbonate rocks during injection of reactive CO₂-saturated water. *Geophys Res Lett.* 38: 1–5.
- Vilarrasa, V., Bolster, D., Dentz, M., Olivella, S., Carrera, J. (2010) Effects of CO₂ compressibility on CO₂ storage in deep saline aquifers. *Transp Porous Media.* 85: 619–639.
- Vilarrasa, V., Bolster, D., Olivella, S., Carrera, J. (2010) Coupled hydromechanical modeling of CO₂ sequestration in deep saline aquifers. *Int J Greenh Gas Control.* 4: 910–919.
- Vilarrasa, V., Carrera, J., Jurado, A., Pujades, E., Vázquez-Suné, E. (2011) A methodology for characterizing the hydraulic effectiveness of an annular low-permeability barrier. *Eng Geol.* 120: 68–80.
- Vilarrasa, V., Carrera, J., Olivella, S. (2013) Hydromechanical characterization of CO₂ injection sites. *Int J Greenh Gas Control.* 19: 665–677.
- Vilarrasa, V., Makhnenko, R., Gheibi, S. (2016) Geomechanical analysis of the influence of CO₂ injection location on fault stability. *J Rock Mech Geotech Eng.* 8: 805–818.
- Vilarrasa, V., Makhnenko, R.Y. (2017) Caprock integrity and induced seismicity from laboratory and numerical experiments. *Energy Procedia.* 125: 494–503.
- Vilarrasa, V., Makhnenko, R.Y., Rutqvist, J. (2018) Field and laboratory studies of geomechanical response to the injection of CO₂. In *Science of Carbon Storage in Deep Saline Formations: Process Coupling across Time and Spatial Scales*; Elsevier: New York, NY, USA.

- Vilarrasa, V., Silva, O., Carrera, J., Olivella, S. (2013) Liquid CO₂ injection for geological storage in deep saline aquifers. *Int J Greenh Gas Control*. 14: 84–96.
- Wood, A.W. (1955) *A Textbook of Sound*; McMillan Co.: New York, NY, USA.
- Zekri, A.Y., Shedid, S.A., Almehaideb, R.A. (2007) Possible alteration of tight limestone rocks properties and the effect of water shelding on the performance of SC CO₂ flooding for carbonate formation. Society of Petroleum Engineers. Richardson, TX, USA.
- Zhang, W., Li, Y., Xu, T., Cheng, H., Zheng, Y., Xiong, P. (2009) Long-term variations of CO₂ trapped in different mechanisms in deep saline formations: A case study of the Songliao Basin, China. *Int J Greenh Gas Control*. 3: 161–180.

CHAPTER 4: CHANGES IN ROCK MATRIX COMPRESSIBILITY DURING DEEP CO₂ STORAGE

Based on a manuscript published in Greenhouse Gases: Science and Technology

Kim, K., Makhnenko, R.Y. (2021) Changes in rock matrix compressibility during deep CO₂ storage. Greenhouse Gases: Science and Technology. 11(5): 954-73.

Abstract

Geologic carbon storage projects aim to permanently trap large volumes of CO₂ in reservoir rock sealed with low permeability layers. As high-pressure supercritical or liquid CO₂ is injected, hydromechanical and chemical processes caused by the reaction between the rock and acidic mixture of brine and CO₂ are initiated. The compressibility of reservoir rock needs to be properly characterized in order to assess the deformation and stability of the host formations, and there are a number of factors to be considered, including the matrix structure, solid, pores, and fluid. This study triggers from a fundamental question of whether CO₂ treatment affects the compressibility of the rock matrix and its dominant composing solid minerals. Three different reservoir representatives are selected: Berea sandstone for silica-rich rock, and Apulian limestone and Indiana limestone for calcite-rich rock. Quartz and calcite are the main composing minerals of the reservoir rock, and their crystals are separately examined. Experimental methods are introduced for high-pressure CO₂ treatment of water-saturated materials, and measurements of the unjacketed and solid compressibilities are conducted. No change in the solid compressibility of the sandstone and quartz after CO₂ treatment is observed, whereas it increases by 18-21% for the limestones and by 15% for calcite. The latter observation is inconsistent with the ultrasonic

wave velocities measurements and is believed to be due to the local dissolution of the calcite crystal surface. The results show that only the solid matrix of the limestones becomes more compressible after CO₂ treatment. Consequent microimaging and mercury intrusion porosimetry analyses allowed observations of dissolution and precipitation of calcite, and new connected and non-connected pores, respectively. Finally, the changes in limestone solid compressibilities and pore structure could significantly affect the rock properties and behavior during and after CO₂ injection and should be accounted for in the reservoir models.

4.1. Introduction

The increasing global demand for energy has been elevating the inevitable consumption of fossil fuels that generates an enormous amount of greenhouse gases such as CO₂ (IEA,2015). The emission of these byproducts into the atmosphere has been reported for their negative effects on the environment, particularly focused on the climate change (Metz et al., 2005). As an effort to reduce the atmospheric emission of the anthropogenic CO₂, geologic carbon storage (GCS) has been introduced as a promising method by permanently isolating CO₂ in the subsurface reservoirs (Bachu, 2000). The reservoirs should be relatively highly porous and permeable and be confined by the low-permeable sealing layers on the top (caprock) and bottom (basement rock) to permanently trap the CO₂ underground (Vilarrasa et al., 2019).

As high-pressure CO₂ is injected into the reservoir, usually in the liquid or supercritical state, it induces the changes of the stress state, pore pressure, and temperature (Johnson et al., 2004). These coupled processes result in the deformation of the host formation and may affect its compressibility (McLatchie et al., 1957; Makhnenko and Labuz, 2016). The deformation of porous media is dependent on the compressibilities of its elements, such as the bulk framework,

pores, solid matrix, and pore fluid (Biot and Willis, 1957; Wang, 2000). Therefore, evaluation of these parameters becomes essential for successful implementation of geo-engineering projects.

For porous rock, the compressibility of the rock matrix is peculiarly important, since it solely provides an understanding of the volume response of the rock frame (Tarokh and Makhnenko 2019). This pressure-independent material property can be measured under theunjacketed boundary condition, where the change in the total mean stress P is equal to the change in the pore pressure p^f ($\Delta P = \Delta p^f$) (Detournay and Cheng, 1993). With the measurements of the volume response, theunjacketed bulk modulus K_s' can be defined as:

$$K_s' = V \left. \frac{\Delta p^f}{\Delta V} \right|_{\Delta p^f = \Delta P} \quad (4.1)$$

where V is the volume of the representative element volume. Also, for the solid components of the porous rock occupying the volume V_s , the bulk modulus K_s can be written as:

$$K_s = V_s \left. \frac{\Delta p^f}{\Delta V_s} \right|_{\Delta p^f = \Delta P} \quad (4.2)$$

Ideal porous medium is introduced as a microscopically isotropic and homogeneous material with all the pore spaces interconnected (Gassmann, 1951). Considering that a porous medium consists of solid grains that form the rock matrix, these two components deform in an identical proportion, thus resulting in equal bulk responses ($K_s = K_s'$) (Cheng, 2016). However, the bulk moduli of the solid and the matrix can differ under conditions where the material is microscopically inhomogeneous (*e.g.*, consisting of several minerals with different compressibilities) or contains non-connected or occluded pores (Tarokh and Makhnenko 2019). Additionally, while it was sometimes reported that theunjacketed bulk modulus could be a function of applied stress (Blöcher et al., 2014; Ingraham et al., 2017; Pimienta et al., 2017), it is

generally accepted that if the tested rock is fully saturated and the appropriate diffusion times for pore fluid pressure are considered, K_s' should not depend on the level of the applied total and effective mean stress (Zisman, 1933; Nur, 1971; Fabre and Gustkiewicz, 1997; Tarokh and Makhnenko 2019).

Besides the poroelastic response, a chemical interaction between the rock, brine, and CO₂ may occur, which has long been generating a considerable interest for researchers related to its effect on the hydromechanical behavior of geomaterials. The geological formations targeted for GCS are usually deep saline aquifers with capacities of thousands of megatons that are mostly composed of silica-rich (sandstone) or calcite-rich (dolomite and limestone) rock (IPCC, 2005). The previous laboratory studies on the effect of CO₂ treatment on reservoir rock were usually limited in time (days to weeks) and mainly focused on observing and describing carbonate dissolution (Rohmer and Seyedi, 2010; Ilgen et al., 2019; Vilarrasa et al., 2019). A number of measurements of geomechanical properties and the ultrasonic wave velocities showed that for carbonate-rich rock, the acidic mixture of CO₂ and brine would affect the internal structure in terms of strength and compressibility, also increasing the materials' porosity and permeability (Le Guen et al., 2007; Luquot and Gouze, 2009; Bemmer and Lombard, 2010; Alam et al., 2014; Rohmer et al., 2016; Kim et al., 2018). Some other tests reported minor influences on rock properties due to the carbonate buffering effect on the pH – dissolved calcite in positively charged pore fluid that stabilized its acidity (Sterpenich et al., 2009; Grgic, 2011). Many studies on silica-rich rock also indicated minor to no effect on compressibility and porosity when scCO₂ or CO₂-rich water were injected (Rimmelé et al., 2010; Hangx et al., 2013; Choens et al., 2020; Tarokh et al., 2020). However, there were examples of (mainly carbonate-cemented) sandstones where the material properties altered (Lamy-Chappuis et al., 2016; Aman et al., 2017) or

enhanced (Yasuhara et al., 2017) after the CO₂ treatment. The mineralogical composition and testing conditions influenced the results of CO₂ treatment and showed that these could significantly differ from those observed in the field considering the time and length scales of large-scale projects (Ilgen et al., 2019).

Understanding the effect of chemical reactions on the solid mineral properties could also be essential for the assessment of the impact of CO₂ treatment. Putnis (2002; 2009) came to a conclusion that the mineral replacement reaction mechanisms are ruled by the equilibrium energy, and the re-equilibrium induces dissolution or precipitation. Moreover, it was shown that the reaction highly depends on the existence of the fluid phase with free energy. Nakamura and Watson (1981) introduced the recrystallization and coarsening of minerals with silica-saturated fluid by adopting the dissolution-precipitation mechanism. The study showed that a new porosity can be generated by dissolution of silica in the fluid phase, and that it highly depends on its pressure and temperature. The dissolution and precipitation on calcite surfaces from calcareous solutions involve the CO₂-water system and can be characterized by rate-dependent processes for the conversion of CO₂ into HCO₃⁻, that are a function of CO₂ pressure, temperature, and pH (Plummer et al., 1979). Plummer et al. (1978) conducted various experiments on the dissolution of calcite and presented that under constant CO₂ pressure and temperature, the dissolution rate decreased gradually until it reached equilibrium and the pH of the fluid became constant.

Several studies were conducted on assessing the compressibility of the minerals constituting the reservoir rock (Adams and Williamson, 1923; Bridgman, 1923; Bridgman, 1925; Anderson and Liebermann, 1966; McSkimin, 1965; Kaga, 1968; Redfern and Angel, 1999; Mavko et al., 2009). Bridgman (1923) proposed a method to measure the deformation of solid minerals by applying hydrostatic pressure to the specimens in the piston-cylinder apparatus. The bulk moduli for

quartz and calcite were calculated as 35.7 GPa and 75.2 GPa, respectively (Bridgman, 1925). Advanced technologies provided innovative methods to measure the compressibilities of these minerals, using dynamic ultrasonic waves or X-ray diffraction (Anderson and Liebermann, 1966). McSkimin et al. (1965) reported the ultrasonic wave velocities of single-crystal quartz adopting the pulse superposition method and calculated the bulk modulus as 37.1 GPa. Kaga (1968) utilized the improved pulse-superposition method for sound velocities and evaluated the bulk modulus of calcite as 71.6 GPa at room temperature. The mechanical response of calcite at elevated pressures was also studied by Redfern and Angel (1999) with the X-ray diffraction technique, reporting the bulk modulus as 73.5 GPa from the linear and volume compressibilities. In summary, the bulk moduli for quartz and calcite are reported to be 37 GPa and 64-77 GPa, respectively, and they are generally recognized as material properties that are assumed to be constant (Hart and Wang, 1995; Mavko et al., 2009; Hart and Wang, 2010).

An essential question then arises on how the compressibilities of the rock matrix and the composing minerals are affected by CO₂ injection into water-saturated media. In this study, we measure the compressibilities of water-saturated reservoir rocks and their constituent solid minerals with different approaches to observe the influence of CO₂ treatment. Berea sandstone, Apulian limestone, and Indiana limestone are selected as the representative reservoir materials, while quartz and calcite crystals are tested as the dominant minerals forming sandstones and limestones, respectively (Figure 4.1). Hydrostatic compression tests are conducted to characterize the bulk response of the rocks and minerals, P- and S-wave velocities are measured to observe the dynamic material properties, and by using the environmental scanning electron microscope (ESEM), high-resolution images of the reservoir rock and the composing solid minerals are obtained for both pristine and CO₂ treated samples. Also, changes in the pore

structure of the rocks are accurately examined using the mercury intrusion porosimetry (MIP) technique.

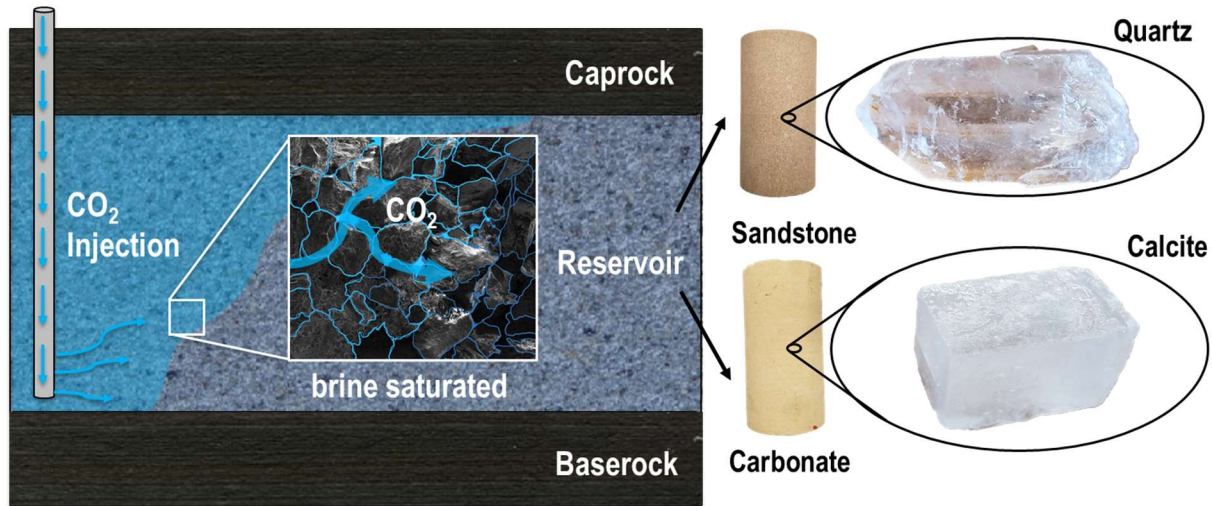


Figure 4.1. Schematic illustration of the geologic carbon storage system (GCS) and the types of reservoir rocks with their dominantly composing minerals.

4.2. Experimental methods

4.2.1. Material

Sandstone (silica-rich rock) and limestone (carbonate-rich rock) are the two common types of sedimentary formations that can possibly serve as the reservoir material for CO₂ storage. In this study, three different rock formations are considered: Berea sandstone, Apulian limestone, and Indiana limestone.

Berea sandstone is a light gray colored, fine-grained sandstone, formed in the late Devonian period. Located between the Bedford/Ohio shale and Sunbury shale, Berea sandstone served as a host rock for oil and natural gas (Collins, 1979) with the permeability reported to be on the order of 10^{-13} m² (Tarokh et al., 2020). The material tested is mainly composed of quartz (~85%), with small inclusions of kaolinite, K-feldspar, and muscovite.

Apulian limestone is a pale orange-colored, glauconitic fossiliferous limestone that consists of mostly calcite (95-98%), with minor portions of plagioclase, glauconite, and iron oxide. Allochems, which are fragmental calcitic foraminifera in the size of 0.05-1 mm, support the matrix of the limestone with cementation of calcitic mud (micrite). The permeability is measured to be on the order of 10^{-15} m^2 (Kim et al., 2018).

Indiana limestone is a gray and buff-colored, Mississippian age rock. Like most of the limestones, it is dominantly formed with calcite (97%), with small traces of quartz, aluminum oxide, and sulfur. Its permeability is $\sim 10^{-14} \text{ m}^2$ (Tarokh and Makhnenko, 2019). Indiana limestone is also known as a freestone, which indicates that no preferential splitting direction exists, providing an advantage in utilizing the material for buildings and public structures (Patton and Carr, 1982).

Quartz and calcite are selected for this study as the major minerals forming the considered two types of reservoir rock. Quartz is the most abundant mineral found on the Earth's surface, also the major component of sandstone, where the chemical compound consists of one part of silicon and two parts of oxygen (SiO_2) with a hexagonal crystal system (Deer et al., 1966). It is well known for its high resistance to both mechanical and chemical weathering and makes it a durable material that can be used for countless applications (Morris and Fletcher, 1987; Wray, 1997). Calcite is the most stable polymorph of calcium carbonate (CaCO_3), which is the principal constituent of limestones. The structure can be described as a rhombohedral system with cleavages in three directions. Calcite can be disintegrated by acid generated from the dissolution of CO_2 in water (H_2O) (Dana, 1864).

4.2.2. CO₂ treatment

Core flooding experiments

For reservoir rock, a core flooding device is used to simulate high-pressure conditions and inject liquid CO₂ into the water-saturated cylindrical specimens with a diameter of 50.8 mm (2 inch) and length of 101.6 mm (4 inch). With the viton rubber sleeve covering the specimen and two pore pressure platens at each end, the sample is installed in the steel core holder and fixed in the axial direction with steel spacers. Stigma 500/700 controller from Sanchez Technologies (70 MPa capacity) is utilized for application of the confining pressure with silicon oil on the rubber sleeve in the circumferential direction of the specimen. For application of the pore pressure, Teledyne Isco syringe pumps with a capacity of 37.5 MPa are installed at the upstream and downstream channels, while another Teledyne Isco pump is connected to the upstream for CO₂ injection. De-ionized water is selected as the pore fluid to solely observe the chemical effect of the mixture of CO₂ and water on the rock response. Two external Honeywell pressure transducers with a capacity of 34.5 MPa are installed between the specimen and the valves that are connected to the pumps, which allow measurements of the pore pressure during the flow tests and under the undrained condition when the valves are closed. Teledyne Isco syringe pumps and Stigma controller have an accuracy of 0.5% of their capacity, while the pressure transducers perform with a 0.1% accuracy.

Biot poroelasticity (Biot and Willis, 1957) assumes full saturation of a porous media, which also needs to be assured before any CO₂ injection. It is achieved using the back-pressure saturation technique, where the applied back pressure is gradually increased and the changes in pore pressure due to the applied mean stress are measured at each step under the undrained condition (Lowe and Johnson, 1960; Makhnenko and Labuz, 2016). If the effective mean stress P' ($P' = P$

– p^f) is maintained to be constant during the process, the full saturation is assumed when the value of the undrained pore pressure increment becomes constant at a few constitutive back pressure steps.

After reaching full saturation with only water, CO₂ is injected into the reservoir rock specimens in a liquid state at ambient temperature (22 °C). Under 12 MPa total mean stress and 6.7 MPa pore pressure, 40-50mL of liquid CO₂ at 7 MPa are injected from the upstream, whereas the downstream valve is kept closed. After that, the upstream valve is closed and the pore pressure readings from the transducers show that the pore pressure gradually drops to that of the boundary state of liquid and gaseous CO₂ (6.2 MPa). Therefore, to maintain the CO₂ in the liquid state, supplementary CO₂ is injected daily from the upstream at a pressure of 7 MPa. The continuous flow experiments are not possible with the setup; however, it allows observing different effects at upstream and downstream sides of the tested specimens.

Few studies showed that as the treatment time for CO₂ increases, its effect on different properties of rock also enhances (Shi et al., 2019; Kim and Makhnenko, 2020). For consistency, we select 21 days as a sufficient time for CO₂ treatment. However, for Apulian limestone the treatment time is reduced to 3 days in order to avoid excessive chemical degradation and introduce a controlled process, considering the materials' high reactivity with the acidic water-CO₂ mixture (Luquot and Gouze, 2009; Kim et al., 2018). The main advantage of utilizing the core flooding device for CO₂ treatment is the possibility of testing rock under elevated effective mean stress in contrast to experiments where specimens are just submerged into a mixture of CO₂ and water.

High-pressure CO₂ treatment

Preparation of perfectly shaped cylinders from the mineral samples is a complicated and expensive procedure, so they were not tested in the core flooding device. Instead, a high-pressure vessel is utilized for the CO₂ treatment of quartz and calcite crystals. It consists of a steel chamber with a pressure gauge and a plastic beaker that fits in the vessel where the specimen of any shape is located. The specimen is then submerged in de-ionized water and consequently, CO₂ is injected into the perfectly sealed steel vessel at a pressure of 7 MPa and temperature of 22 °C. The injection is conducted until equilibration of the pressure is reached, considering the dissolution of CO₂ in water. The specimens are submerged in 150 mL of de-ionized water located in the inner liner beaker ($D = 57$ mm and $L = 140$ mm) of the vessel. Considering the solubility of CO₂ in water (the ratio of the solute mass to the solvent mass) being 0.06 at adopted pressure and temperature (Perry and Chilton, 1973; Ma et al., 2017), the dissolved mass of CO₂ is approximately 9 g or 11.7 mL of liquid CO₂ at 7 MPa. It is to be noted that only the dissolved amount of CO₂ can be estimated, while the total injected volume was not recorded but is expected to be larger.

After the injection, the valve to the vessel is closed and CO₂ treatment is conducted for 21 days, an identical time for treatment of the reservoir rocks in the core flooding device. Previous studies showed that the dissolution of CO₂ into water occurs rapidly at the beginning of the injection process under the tested pressure conditions, while the process slows down and stops after reaching the maximum solubility within 2-3 hours (Ma et al., 2017). Thus, it assumed for the tests performed in both devices that the solubility of 0.06 has been reached and represented a similar testing condition, while the only difference is the non-zero effective mean stress applied in the core flooding device. Besides the mineral crystals, another prismatic Berea sandstone

specimen is treated in the high-pressure vessel. By comparing the two CO₂ treatment methods, the effect of the testing condition (confined vs unconfined) on the rock properties is investigated.

4.2.3. Hydrostatic compression test

The hydrostatic compression cell is adopted in this study to measure theunjacketed and solid bulk response of the reservoir rock and minerals, respectively. Teledyne Isco syringe pump with a 51.7 MPa capacity is connected to the hydrostatic cell and utilizes hydraulic oil as the pressurizing fluid for rock specimens located inside the cell. As pressure increases, the deformation of the specimen is measured by the resistive strain gauges installed on the surface of the sample. For the unjacketed condition, no membrane is sealing the specimens, and the increase in the confining pressure eventually becomes equal to the increase in the pore pressure as the fluid intrudes into the pores ($\Delta P = \Delta p^f$). On the other hand, the mineral crystals do not have any internal pores and the solid bulk response can be measured with the same procedure as the hydrostatic unjacketed modulus.

For each reservoir rock representative, two prismatic specimens (approximately 50 × 40 × 40 mm) are prepared from the cylindrical samples: one pristine and another one after CO₂ treatment in the core flooding device. Considering the high reactivity of calcite-rich rock, the upstream and downstream parts of the CO₂ treated limestones are separately tested to observe if the different boundary conditions during the treatment process affected its compressibility. A few sets of mutually perpendicular strain gauges (CEA-06-250 UN-120, Micro Measurements, USA) are installed on the surface of the reservoir rock specimens with epoxy adhesive M-bond AE-10 (Micro measurements, USA), and the bulk volume strain can be calculated as the sum of the three normal strains ($\varepsilon_v = \varepsilon_{xx} + \varepsilon_{yy} + \varepsilon_{zz}$). The axes directions are chosen in no preferential

direction for the limestones that appeared to be isotropic, and the direction of the z-axis is perpendicular to the apparent bedding planes for Berea sandstone. For minerals, specimens containing smooth surfaces are selected for strain gauge installation for both pristine and CO₂ treated samples, with their shape not being perfectly prismatic. Thus, the installed strain gauges are positioned in three different directions that are not exactly perpendicular to each other. For quartz, the strain gauges are installed at (0°, 0°, 0°), (30°, 0°, 30°), and (60°, 30°, 0°) degrees, with the relative angles ($\Delta\theta_a, \Delta\theta_b, \Delta\theta_c$) measured from each strain gauges that are aligned with a, b, c axes, respectively. For calcite, due to the clear cleavage of the specimen where the angle is 78°/102°, the strain gauges are installed parallel to the cleavage direction (x', y', z'). The strain gauge responses for minerals under hydrostatic compression show that all strain measurements are almost identical for each material, indicating that the tested minerals are isotropic. Therefore, the solid volume strain is calculated by adding three strain gauge values measured in different directions ($\varepsilon_v = \varepsilon_a + \varepsilon_b + \varepsilon_c$ or $\varepsilon_v = \varepsilon_{x'} + \varepsilon_{y'} + \varepsilon_{z'}$).

For all materials, the loading-unloading cycle is conducted up to 50 MPa, and the data is recorded at every 2 MPa step. At every step, the equilibration between the confining pressure and the pore pressure ($P = p^f$) is required to guarantee theunjacketed boundary condition. The equilibration time depends on the diffusivity of the material, which is a function of permeability, fluid viscosity, and the compressibility of the rock and the pore fluid. The diffusion coefficient c of the oil-saturated reservoir rock is estimated to be on the order of 10⁻² m²/s for Berea sandstone, 10⁻⁴ m²/s for Apulian limestone, and 10⁻³ m²/s for Indiana limestone (Tarokh and Makhnenko, 2019). Considering the drainage distance in the specimens being $H_{dr} = 20$ mm, the characteristic time t_{char} for the pore fluid diffusion is on the order of H_{dr}^2/c meaning that it does not exceed 10 seconds for any of the tested rock. To guarantee the efficient drainage of the pore

fluid, 10 minutes were taken between each stage ofunjacketed loading and unloading. Based on the pore size distribution, full saturation with oil in the hydrostatic compression tests is guaranteed to be achieved at 15 MPa for Berea sandstone, 20 MPa for Apulian limestone, and 50 MPa for Indiana limestone (Tarokh and Makhnenko, 2019). As the volume strain and the hydrostatic pressure are recorded during the experiment, the unjacketed bulk modulus K_s' and solid bulk modulus K_s can be calculated.

4.2.4. Ultrasonic wave velocities

Measurements of compressional (P-wave) and shear (S-wave) velocities (V_p and V_s) are conducted for reservoir rock specimens and mineral crystals before and after CO₂ treatment. The data acquisition system is comprised of the ultrasound pulse receiver (Olympus 5077PR), the digital oscilloscope (Tektronix TBS1064), and ultrasonic transducers generating P- and S-waves (General Electric Alpha 2.25 MHz and Panametrics V154 2.25 MHz). The transducers are located on the smooth sample surfaces, and a couplant is applied between the sample and the transducer. An ultrasonic pulse is generated from the transmitting transducer by a negative step function excitation (200V) and is received at the other transducer. The signal is then digitized with 8-bit dynamic range resolution with a frequency of 10 MHz and signal duration of 0.25 ms. Consequently, depending on the arriving signal, it is amplified with a gain level of 20-30 dB. Ultrasonic velocity measurements are repeated for 2-3 samples several times to assure their accuracy and consistency, and the results are reported based on the first arrival time of the signal and the shortest wave path length.

Measurements of the P- and S-wave velocities (V_p and V_s) allow determination of the dynamic properties assuming that the material is linearly elastic and homogeneous. The bulk modulus K

can then be calculated with the knowledge of the bulk density of the material ρ_{bulk} (Mavko et al., 2009):

$$K = \rho_{bulk} \left(V_p^2 - 4V_s^2 / 3 \right) \quad (4.3)$$

4.2.5. Mercury intrusion porosimetry

Measurements of porosity and evaluation of the pore size distribution are conducted with Quantachrome Poremaster 60 using the mercury intrusion porosimetry (MIP) technique. With the low- and high-pressure chambers, the device allows for pressure generation up to 413.7 MPa and forces mercury to penetrate the rock pores while accurately measuring the injected volume. As the pressure increases, the interconnected pores from larger to smaller sizes get intruded and then the extrusion is performed during the unloading procedure. Due to the high cohesive forces within liquid mercury, it does not spontaneously enter the pores until it is forced up to a certain pressure, which can be expressed as a function of the pore throat diameter d , contact angle θ , and the surface tension γ of liquid mercury in contact with its own vapor, adopting the Young-Laplace equation:

$$p^{Hg} = -\frac{4\gamma \cos \theta}{d} \quad (4.4)$$

As the increase in the volume of the intruded mercury is measured with each applied step in pressure, the pore size distribution can be assessed. For this study, the intrusion data is selected. Measuring the weight of the dry sample and the sample in the cell filled with mercury at ambient pressure allows accurate determination of its bulk volume V_{bulk} . Then, with the recorded volume of intruded mercury into the pores, the interconnected porosity ϕ can be accurately calculated using the measured values of the rock's bulk density ρ_{bulk} .

The specimens for this study are prepared to be approximately 1.0 gram in mass that would fit into the sample cell. Considering the potential inhomogeneity of the samples and measurement errors, several pieces of each material are tested together, and each test is duplicated. The mercury has a contact angle of 140° , a surface tension of 480.0 erg/cm^2 , and a density of 13.54 g/cm^3 at room temperature (22°C). All experimental methods utilized in this study are illustrated in Figure 4.2, including the scanning electron microscopy (ESEM) that is introduced in the discussion session.

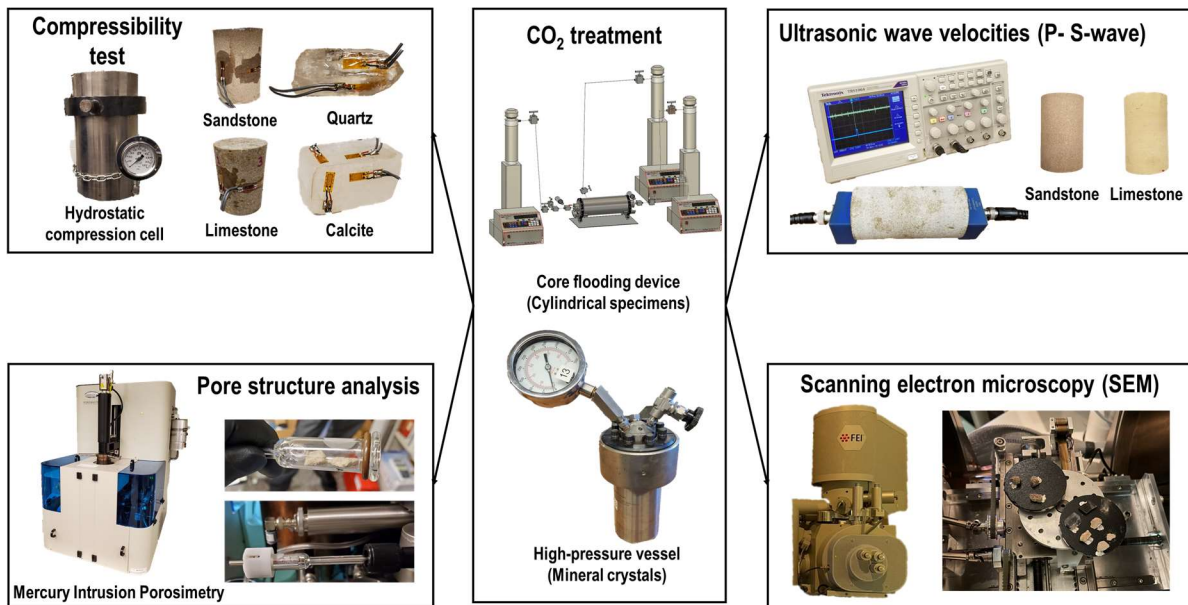


Figure 4.2. Sketch of the experimental methods and the samples instrumented for this study.

4.3. Results

4.3.1. Reservoir rock – unjacketed bulk response

Unjacketed hydrostatic compression tests are conducted on the reservoir rock to accurately measure the properties of its matrix before and after CO₂ injection. Additionally, for Berea sandstone, the effect of CO₂ treatment method is compared for the confined specimens tested in

the core flooding device and the unconfined specimens tested in the high-pressure vessel. Considering the high reactivity of limestones with acidic fluid and how the CO₂ injection process is performed, limestone specimens are prepared from each side (upstream and downstream) of the treated cores. The loading-unloading procedure to 50 MPa hydrostatic pressure is repeated twice to assure reproducibility of the results. For all materials, the test results from theunjacketed hydrostatic compression tests in terms of the directional (normal) strains exhibit a linear response, and the unloading data is selected to be presented (Figures 4.3-4.5).

The data for Berea sandstone indicates an anisotropy in the solid matrix, where the normal strain in the z-direction (perpendicular to the bedding planes) is 15-20% larger than these in the other two directions for pristine and two CO₂ treated specimens. These three specimens appear to have the same unjacketed compressibility, implying the effect of CO₂ treatment and the method how it is performed do not affect the matrix response. For Apulian limestone, small differences exist in the initial slopes of the normal strains, but eventually become identical implying isotropy. The CO₂ treatment causes 20% increase in the normal strains for both the upstream and downstream specimens. Indiana limestone also shows an isotropic response for both pristine and CO₂ treated specimens, where for the latter the normal strains are 18% larger meaning the increased compressibilities for both the upstream and downstream parts.

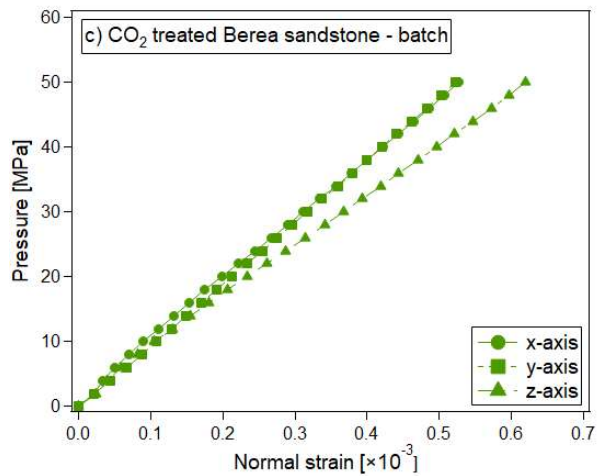
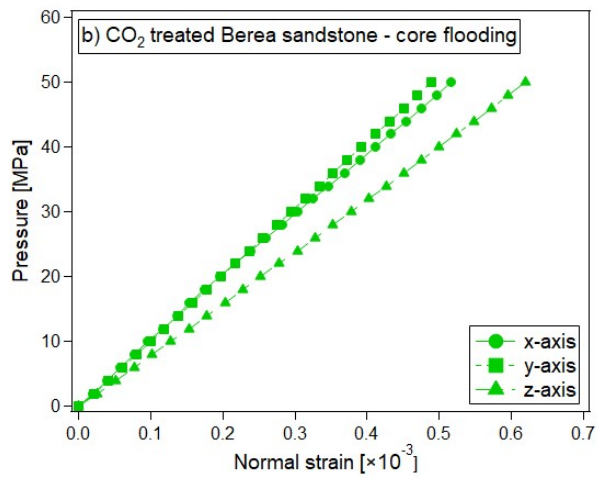
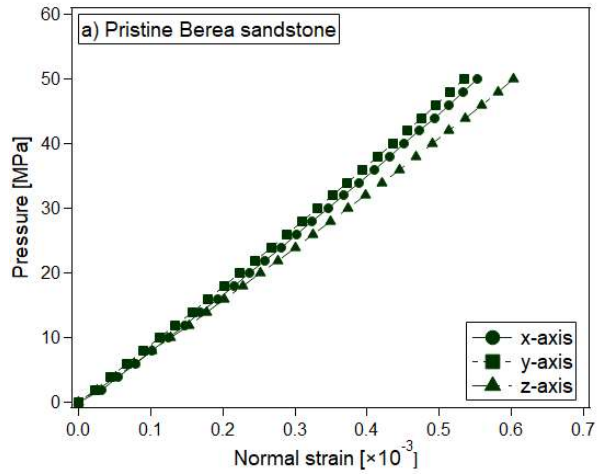


Figure 4.3. Results of the unjacketed hydrostatic compression tests for Berea sandstone specimens: (a) pristine, (b) CO₂ core flooding treated, and (c) CO₂ batch treated.

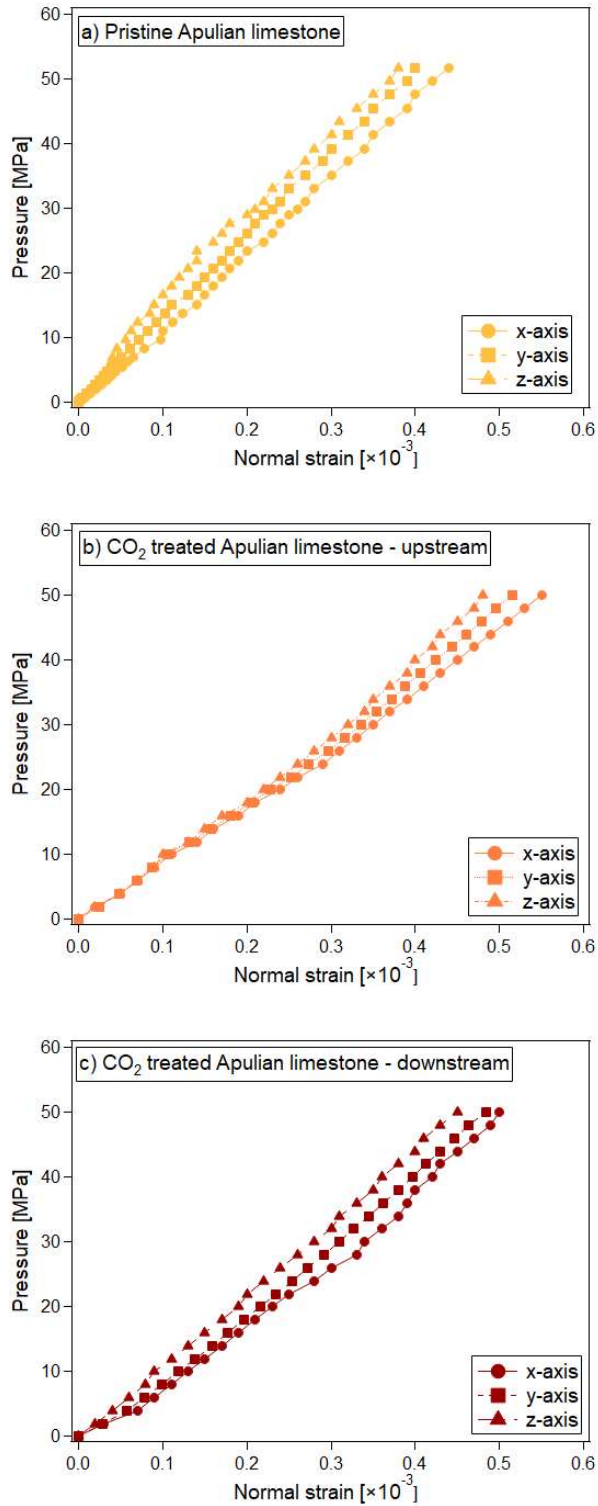


Figure 4.4. Results of theunjacketed hydrostatic compression tests for Apulian limestone specimens: (a) pristine, (b) CO₂ treated - upstream, and (c) CO₂ treated – downstream.

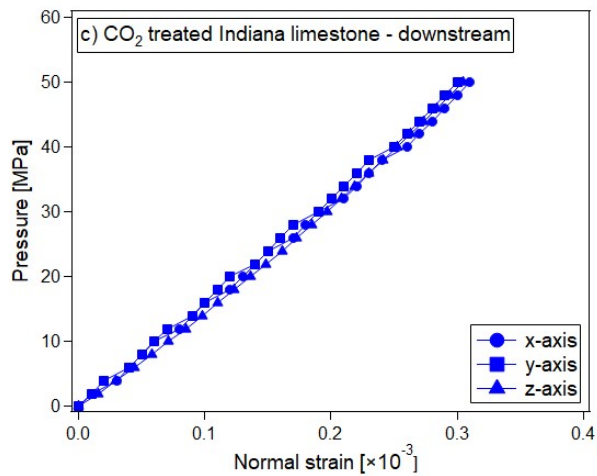
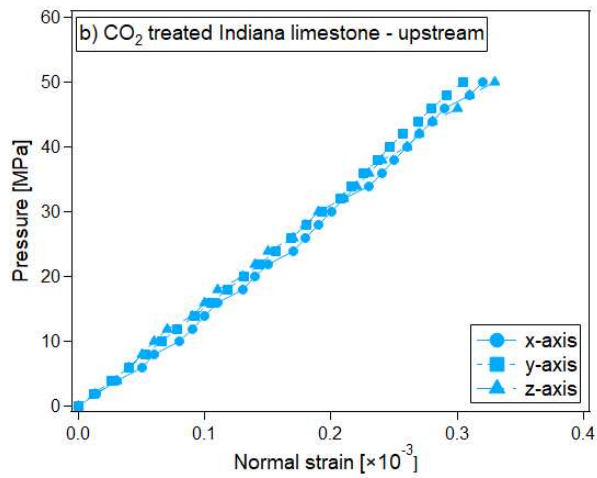
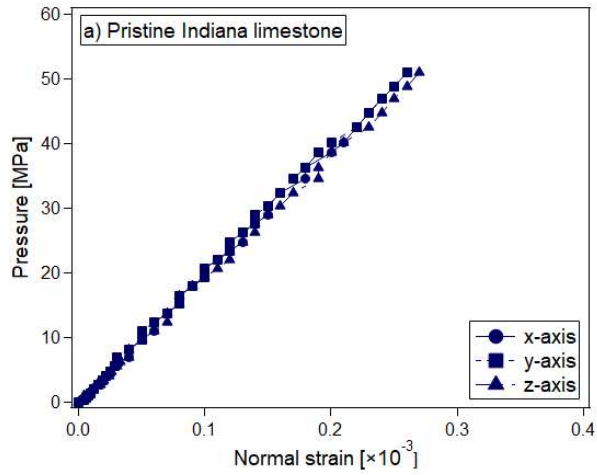


Figure 4.5. Results of the unjacketed hydrostatic compression tests for Indiana limestone specimens: (a) pristine, (b) CO₂ treated - upstream, and (c) CO₂ treated – downstream.

4.3.2. Minerals – solid bulk response

The same experimental procedure utilized to determine theunjacketed bulk response of the reservoir rock also provides measurements of the solid bulk moduli of quartz and calcite. The hydrostatic loading-unloading procedures up to 50 MPa are performed twice to ensure the repeatability of the test data. The results from the hydrostatic compression tests on the pristine and CO₂ treated minerals are introduced in Figures 4.6 and 4.7. The directions of the installed strain gauges are considered, where the angles to the coordinate system (x, y, z) are 0°, 40°, 20° for quartz and 0°, 15°, 15° for calcite, though it does not affect the results since for both quartz and calcite, the three different strain measurements show an identical (isotropic) response before and after CO₂ treatment. The effect of CO₂ treatment is negligible for quartz, while for calcite, the directional strains measured on the surface of the crystal appear to increase by 15% compared to the pristine case.

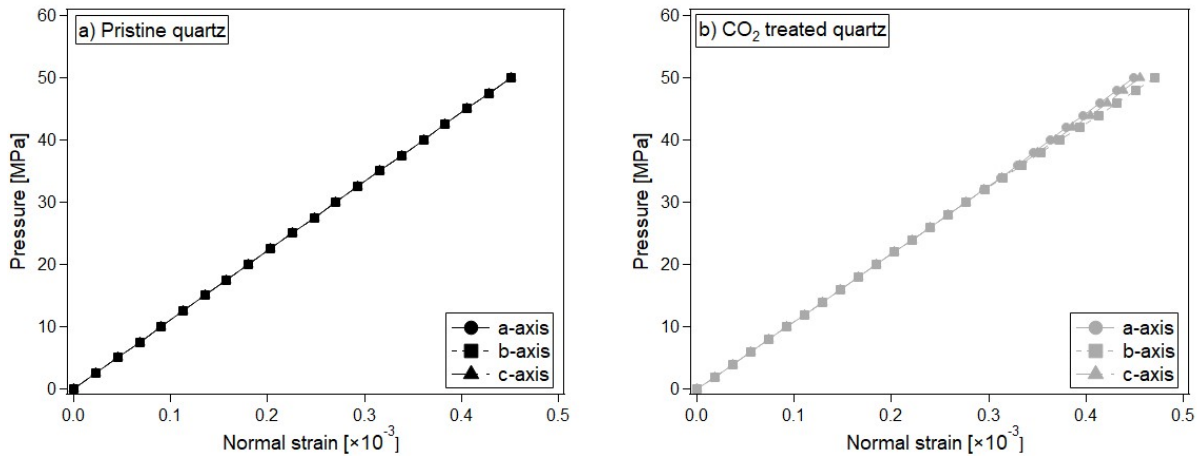


Figure 4.6. Hydrostatic compression data for quartz crystals: (a) pristine and (b) CO₂ treated.

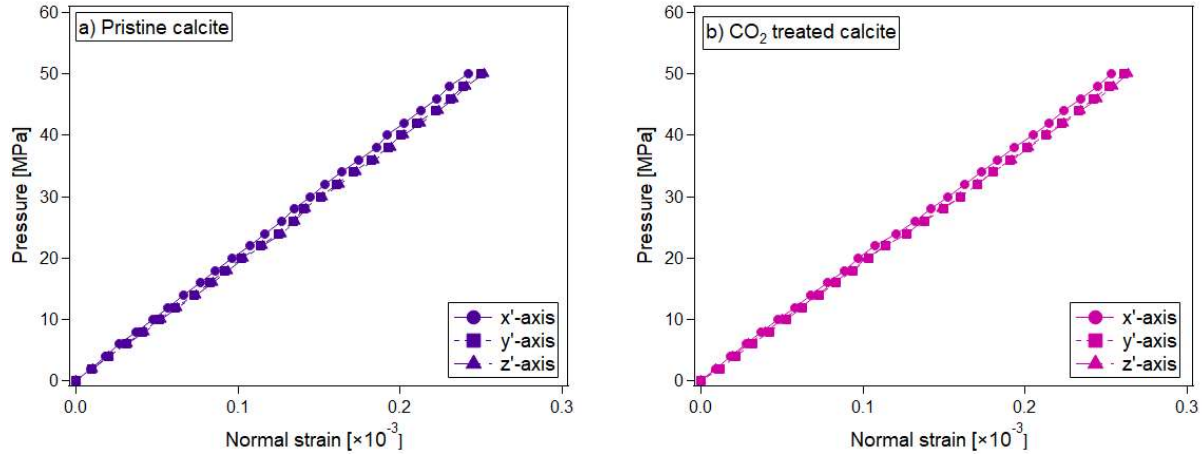


Figure 4.7. Hydrostatic compression data for calcite crystals: (a) pristine and (b) CO₂ treated.

4.3.3. Ultrasonic wave velocities

Measurements of the P- and S-wave velocities are conducted before and after CO₂ treatment on dry mineral samples. For quartz, the P- and S-wave velocities are measured to be similar (within ± 0.02 km/s) before and after the treatment ($V_p = 5.72$ km/s and $V_s = 3.68$ km/s) meaning that the solid bulk modulus (dynamic) remains unchanged: $K = 39$ GPa. For calcite, both P- and S- wave velocities are measured to slightly decrease after CO₂ treatment: $V_p = 6.64$ km/s and $V_s = 3.56$ km/s for pristine specimen and $V_p = 6.62$ km/s and $V_s = 3.54$ km/s for CO₂ treated specimen. This results in a small decrease in calcite bulk modulus from 73.7 GPa to 73.5 GPa, indicating that no significant effect of CO₂ treatment is observed for both mineral crystals.

4.4. Discussion

The matrix and solid deformations of reservoir rocks and its main composing minerals are measured in the hydrostatic compression tests. Observed linear responses indicated constant unjacketed moduli for the rock and constant solid moduli for the minerals (Figures 4.8 and 4.9). Three different specimens of Berea sandstone are examined: pristine, CO₂ treated in the core

flooding device (confined), and CO₂ treated in the high-pressure vessel (unconfined) samples. For all three silica-rich rock samples, theunjacketed bulk moduli are measured to be 30 GPa, indicating no observable effect from the CO₂ treatment (Figure 4.8a), as well as from the applied confinement.

For Apulian limestone, the pristine and CO₂ treated specimens are compared, where two specimens are prepared from the treated core: one from the upstream side and another one from the downstream side. The unjacketed bulk modulus K_s' for pristine Apulian limestone is calculated as 42.7 GPa. For the treated specimens, the K_s' values are evaluated as 33.7 GPa and 34.7 GPa for the upstream and downstream parts, respectively, meaning that CO₂ injection decreases the unjacketed bulk modulus of the upstream part by 21% and the downstream part by 19% (Figure 4.8b).

The values of K_s' for Indiana limestone are measured to be the highest among the tested rocks. The CO₂ treatment causes a decrease in the unjacketed bulk modulus of the limestone from 65.9 GPa to 54.0/55.8 GPa or by 18/15% respectively for the upstream/downstream parts (Figure 5.8c). Hence, despite the difference in the boundary conditions for CO₂ injection, both the upstream and downstream parts of the limestones become more compressible. Even though the compressibility of the upstream part becomes a few percent higher, it can be stated that significant amounts of the dissolved CO₂ reach the downstream part, and by the end of the treatment, dissolved CO₂ becomes almost evenly distributed within the specimen.

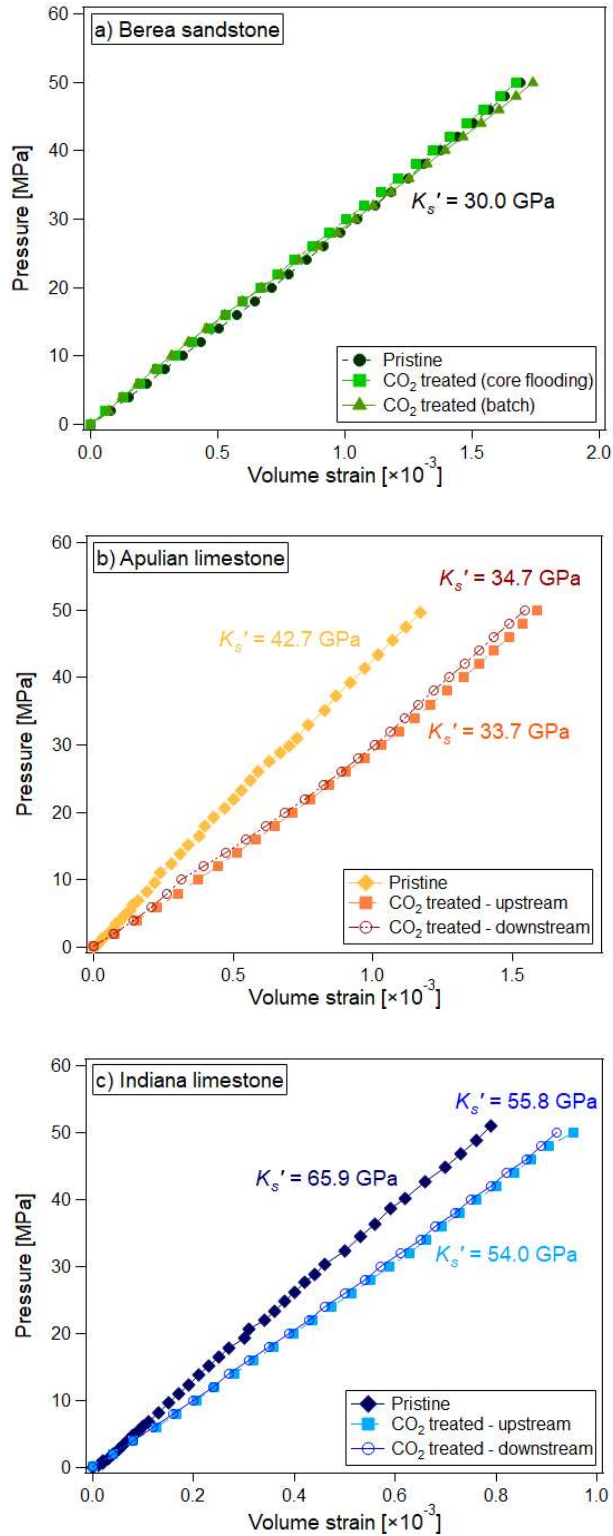


Figure 4.8. Unjacketed compression test results for pristine and CO₂ treated (a) Berea sandstone, (b) Apulian limestone, and (c) Indiana limestone.

The solid bulk moduli are calculated for quartz and calcite, also examining the effect of CO₂ treatment on the compressibility of these minerals. K_s of quartz is measured to be 37.0 GPa (Figure 4.9a), which is in a good agreement with other studies (Koga et al., 1958; Greenwald, 1980; Tarokh and Makhnenko, 2019). The solid bulk modulus of the CO₂ treated quartz demonstrates an identical response to the pristine material, meaning that the treatment does not affect its compressibility. Alternatively, the surface strain based calculation of the bulk moduli of the pristine and CO₂ treated calcite specimens showed that K_s decreased from 74.0 GPa to 63.2 GPa (Figure 4.9b), approximately by 15%.

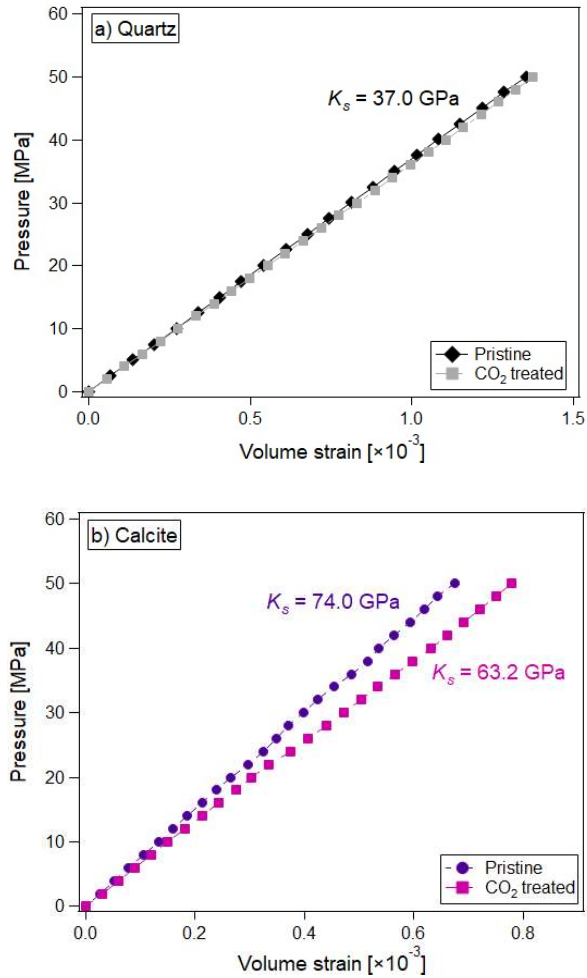


Figure 4.9. Hydrostatic compression test results for pristine and CO₂ treated (a) quartz and (b) calcite.

A possible explanation for the discrepancy between the elastic parameters of the calcite calculated from the ultrasonic tests and retrieved from the local strain measurements is the effect of acidic CO₂-water mixture on the mineral surface, since there are no pores in the mineral crystals. We believe that the compressibility of the CO₂ treated calcite calculated from the hydrostatic compression test is affected by the local chemical effect on the surface of the mineral, but the global elastic parameters do not change, which is confirmed by ultrasonic velocities measurements.

Petrographic and microimaging methods have been previously adopted to characterize the effect of CO₂ injection on the microstructure of subsurface formations (Evans and Chester, 1995; Hangx et al., 2010; Vanorio et al., 2011; Fuchs et al., 2019). The mineral and rock surfaces treated with CO₂ indicated the formation of microcracking that increased the creep rates in granular aggregates of quartz and feldspar (Hangx et al., 2010), salt precipitation and increased compressibility in sandstones and carbonates (Vanorio et al., 2011), and detachment of clay cementation from quartz and feldspar grain surfaces in Mt. Simon sandstone and weakening of its rock matrix (Fuchs et al., 2019). In order to further explore the effect of CO₂ treatment on the reservoir rock and minerals, high-resolution images of the sample surfaces are taken using the environmental scanning electron microscope (ESEM) (Figures 4.10 and 4.11).

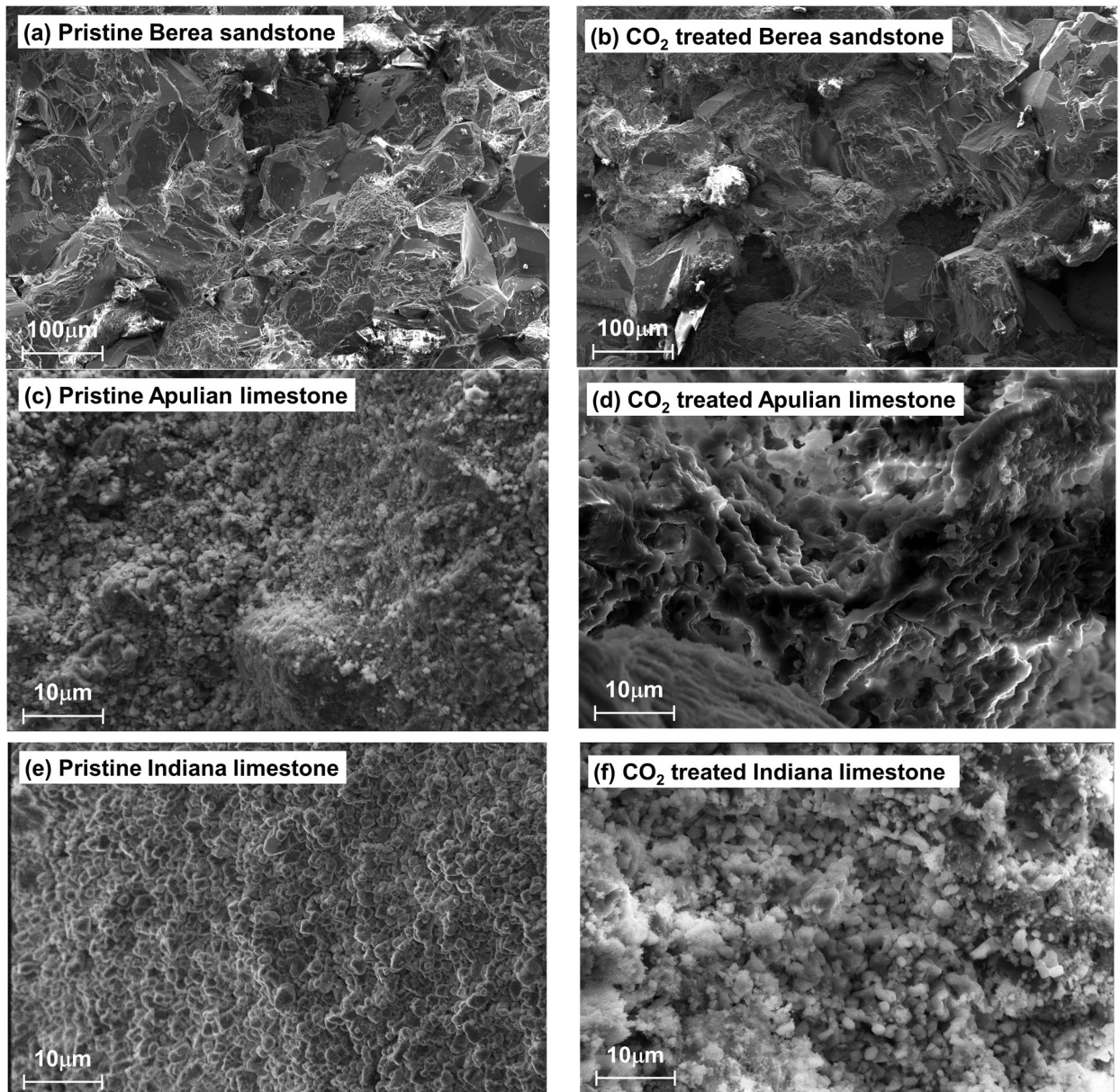


Figure 4.10. ESEM images of (a) pristine and (b) CO₂ treated Berea sandstone, (c) pristine and (d) CO₂ treated Apulian limestone, and (e) pristine and (f) CO₂ treated Indiana limestone.

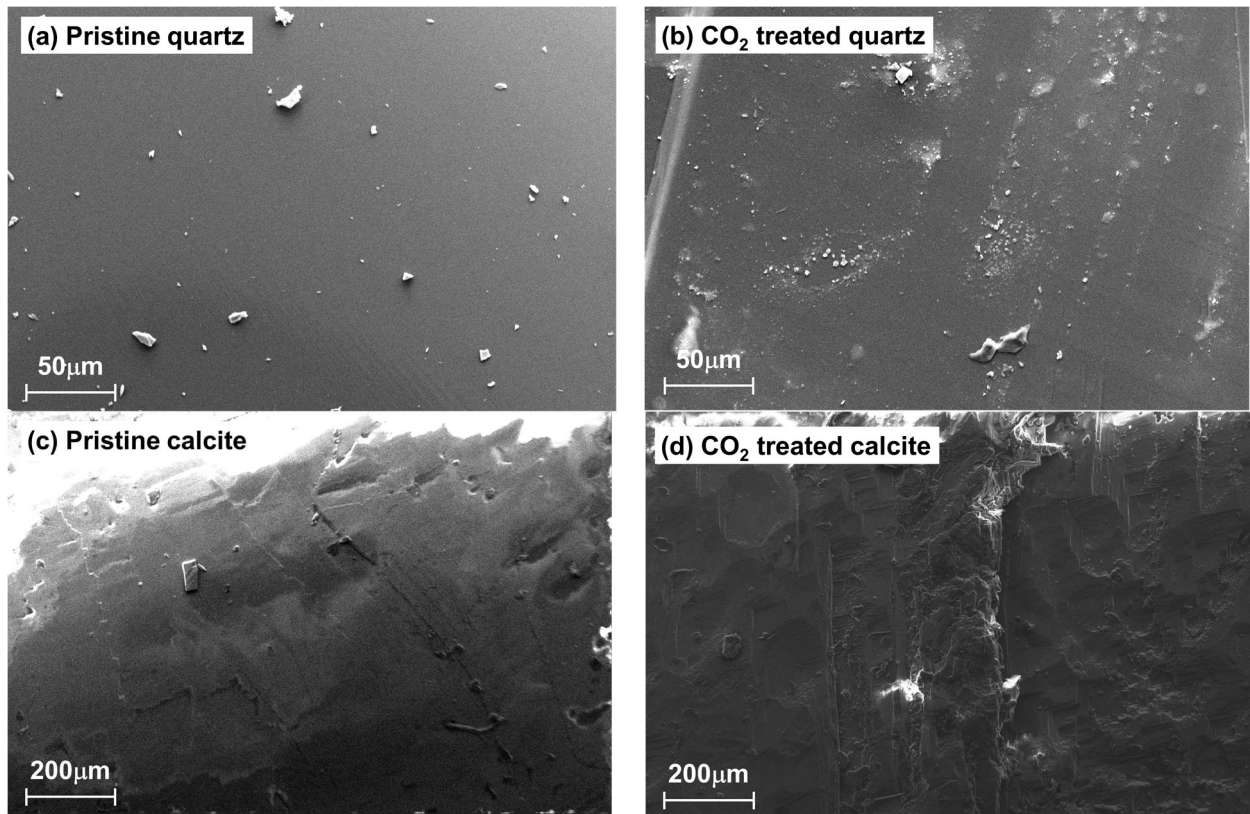


Figure 4.11. ESEM images of (a) pristine and (b) CO₂ treated quartz and (c) pristine and (d) CO₂ treated calcite.

The micro-imaging analysis indicates that for Berea sandstone, no significant effect of CO₂ treatment on the microstructure is observed. However, for Apulian limestone and Indiana limestone, there are visible dissolution effects on the surface which result in the generation of micropores. Utilization of the EDAX light-element energy-dispersive spectroscopy (EDS) allowed for the analysis of more than 10 elements in each image including pores and solid matrix. It appears that CO₂ treatment decreases the net intensity of Ca by approximately 35% but increases the porosity. This implies that the changes in the matrix compressibility of the limestones could be due to calcite dissolution and modifications in the matrix structure. While the overall increase in Apulian limestone permeability is reported (Kim et al., 2018) and the

ESEM images highlight the increase in porosity, this effect appears to be uniformly distributed within the samples and no locally focused wormholes are observed.

In addition, no visible pores were created on the mineral surfaces due to CO₂ treatment. The EDS tests verify that quartz mostly (>99%) consists of SiO₂, with minor inclusions of CaCO₃ in a form of small particles that are present on both pristine and treated specimens. Calcite specimen is mostly (>99%) CaCO₃ with a minor inclusion of SiO₂. The treated calcite specimen appeared to have the same net intensity of Ca as the pristine one, but indicated some signs of surface dissolution without generation of new porosity that supports the statement that the compressibility measurements from the strain gauges are affected by the local chemical effect, but do not reflect the global bulk behavior of the material.

For isotropic and homogeneous ideal porous media, it is assumed that theunjacketed bulk modulus K_s' is equal to the solid bulk modulus K_s , considering that all pores are fully connected. However, despite the dominant proportion of quartz and calcite in sandstones and limestones, respectively, measurements of the unjacketed bulk moduli for reservoir rocks show a considerable difference between the two moduli ($K_s' \neq K_s$): for Berea sandstone, $K_s' = 30.0$ GPa and $K_{s,quartz} = 37.0$ GPa, while $K_{s,calcite} = 74.0$ GPa and $K_s' = 42.7$ GPa and $K_s' = 65.9$ GPa, for Apulian limestone and Indiana limestone, respectively. These differences can be explained either by the presence of other minerals with considerably different compressibilities (which is not the case for the tested rock) or the presence of inhomogeneities such as non-connected or occluded pores.

The total pore volume consists of the interconnected pore space V_p and the non-connected pores V_p' . The total bulk volume V also includes the solid: $V = V_s + V_p + V_p'$. Thus, the interconnected porosity (Equation 4.5) and total porosity (Equation 4.6) can be defined as:

$$\phi = \frac{V_p}{V} \quad (4.5)$$

$$\phi_t = \frac{V_p + V'_p}{V} = 1 - \frac{V_s / M_s}{V / M_s} = 1 - \frac{\rho_d}{\rho_s} \quad (4.6)$$

The interconnected porosity ϕ and the bulk density of the sample can be determined from MIP. The calculation of the total porosity involves the knowledge of the dry and solid densities. Since the dissolution of calcite-rich rock would occur only on the surface that is in contact with the acidic fluid, we assume that CO₂ treatment does not affect the remaining solid density, and refer to the values measured by Tarokh and Makhnenko (2019) ($\rho_{s,Berea} = 2.74 \text{ g/cm}^3$, $\rho_{s,Apulian} = 2.76 \text{ g/cm}^3$, and $\rho_{s,Indiana} = 2.72 \text{ g/cm}^3$). Therefore, the non-connected porosity can be calculated as $\phi_n = \phi_t - \phi$, where the average values are taken for the measured properties. For Berea sandstone, the porosity and density are measured to be almost identical for the pristine and CO₂ treated samples with $\phi = 21.9\%$ and $\rho_{bulk} = 2.05 \text{ g/cm}^3$. For Apulian limestone, the properties of the pristine samples are measured as $\phi = 37.1\%$ and $\rho_{bulk} = 1.66 \text{ g/cm}^3$, while they changed to $\phi = 39.2\%$ and $\rho_{bulk} = 1.58 \text{ g/cm}^3$ for the treated upstream specimen and $\phi = 38.3\%$ and $\rho_{bulk} = 1.61 \text{ g/cm}^3$ for the downstream specimen. The properties for Indiana limestone are reported as $\phi = 12.7\%$ and $\rho_{bulk} = 2.36 \text{ g/cm}^3$ for pristine samples, while it altered after CO₂ treatment to $\phi = 14.0\%$ and $\rho_{bulk} = 2.31 \text{ g/cm}^3$ for upstream specimen and $\phi = 13.1\%$ and $\rho_{bulk} = 2.34 \text{ g/cm}^3$ for the downstream specimen (Table 4.1).

With these reported values, the total and non-connected porosities are calculated as $\phi_t = 25.1\%$ and $\phi_n = 3.2\%$ for Berea sandstone, $\phi_t = 40.0\%$ and $\phi_n = 2.9\%$ for pristine Apulian limestone, $\phi_t = 42.8 / 41.7\%$ and $\phi_n = 3.6 / 3.4\%$ for CO₂ treated Apulian limestone (upstream/downstream), and $\phi_t = 13.2\%$ and $\phi_n = 0.5\%$ for pristine Indiana limestone, which changes to $\phi_t \sim 15.1 / 14.0\%$ and

$\phi_n \sim 1.1 / 0.9\%$ after CO_2 treatment. These results indicate that CO_2 treatment does not affect the measured interconnected porosity and the calculated total porosity for the sandstone, but causes the increase of those for the limestones (Figure 4.11). Injection of CO_2 in water-saturated specimens promotes calcite dissolution and increases the fraction of the interconnected pore space, but at the same time generates new non-connected pores in the samples due to precipitation. Moreover, the increase in the non-connected porosity can also explain the enhanced differences between the solid and unjacketed moduli of treated limestones.

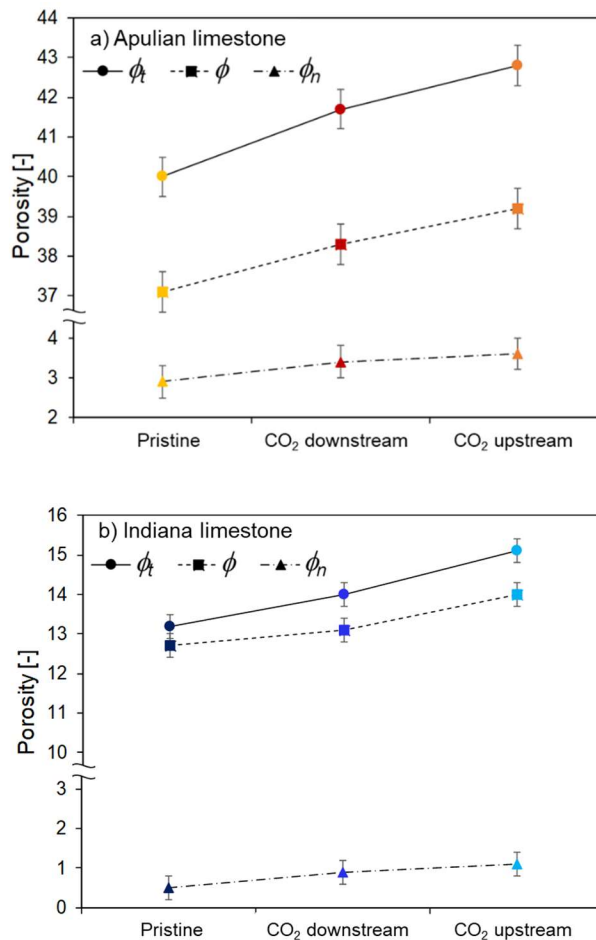


Figure 4.12. The total (ϕ_t), interconnected (ϕ), and non-connected (ϕ_n) porosity changes due to CO_2 treatment for (a) Apulian limestone and (b) Indiana limestone.

The effective medium models can be utilized to estimate the solid and bulk moduli of the tested materials if the properties of composing minerals and pores are known (Budiansky and O’Connell, 1976; Berryman, 1995). The nonconnected pores can be included in the solid compressibility with the assumption that their bulk modulus is equal to the pressure of the air trapped in them (not exceeding 50 MPa) and the shear modulus is zero (Berryman, 1995; Tarokh and Makhnenko, 2019). Without knowing the exact shape of the pores and neglecting a slight anisotropy in Berea sandstone’s response, we adopt the isotropic-generalized Hashin-Shtrikman upper and lower boundaries (Hashin and Shtrikman, 1963):

$$K_s^{HS,upper} = \lambda(G_{\max}) \quad (4.7)$$

$$K_s^{HS,lower} = \lambda(G_{\min}) \quad (4.8)$$

where

$$\lambda(z) = \left\langle \frac{1}{K_s(r) + 4/3 \cdot z} \right\rangle^{-1} - \frac{4}{3}z \quad (4.9)$$

The parenthesis $\langle Q(r) \rangle$ in Equation (4.9) indicate the volume average of a quantity $Q(r)$. For Berea sandstone, the following mineral composition and mineral moduli are utilized for calculation (Mavko et al., 2009; Tarokh et al., 2020): quartz - 87% ($K_q = 37.0$ GPa, $G_q = 31.0$ GPa), muscovite - 6% ($K_m = 58.2$ GPa, $G_m = 35.3$ GPa), kaolinite – 3% ($K_k = 1.5$ GPa, $G_k = 1.4$ GPa), feldspar - 2% ($K_f = 56.9$ GPa, $G_f = 28.6$ GPa), and albite – 2% ($K_a = 37.5$ GPa, $G_a = 15.0$ GPa). The upper Hashin-Shtrikman bound for the solid modulus of the sandstone decreases linearly from 36 GPa with the increase in the nonconnected porosity, while the lower boundary decreases drastically from 22 GPa and converges to zero (Figure 4.12a). The measuredunjacketed bulk modulus ($K_s' = 30$ GPa) falls within the calculated boundaries, while the “dynamic” bulk modulus calculated from the values of P- and S-wave velocities of quartz

($K_{s,quartz}^{dyn} = 39.0$ GPa) lies slightly above the upper boundary since quartz does not contain the compressible clayey inclusions.

The following mineral composition and mineral bulk moduli are used for calculating the Hashin-Shtrikman boundaries for Apulian limestone (Tarokh and Makhnenko, 2019): calcite - 98% ($K_c = 74.0$ GPa, $G_c = 30.0$ GPa), plagioclase -1% ($K_p = 56.9$ GPa, $G_p = 28.6$ GPa), and glauconite – 1% ($K_g = 59.7$ GPa, $G_k = 42.3$ GPa) and Indiana limestone (Tarokh and Makhnenko, 2019): calcite – 97% and quartz – 3%. Theunjacketed bulk moduli of pristine and CO₂ treated specimens appear to be approximately in the middle between the upper and lower boundaries for both limestones (Figures 4.12b and 4.12c). The dynamic bulk modulus of calcite $K_{s,calcite}^{dyn} = 73.6$ GPa is very close to the upper boundary for the solid modulus of the limestones since they are dominantly composed (~97-98%) of this mineral.

The pore size distribution for the three reservoir rocks is presented in Figure 4.13. For Berea sandstone, it is shown that CO₂ treatment has no significant effect on the distribution where the dominant pore size is measured as ~ 20 μm. For Apulian limestone, the pore size density for larger pores (from 2 μm to 10 μm) increases. The results for Indiana limestone (dominant pore size ~1 μm) also show that the dominant pore size slightly increases due to CO₂ treatment, but it is less significant compared to Apulian limestone. The tendency of the CO₂ treatment to increase the pore size density in the micron range can be explained by dissolution of the calcite-rich rock matrix. These results are in some agreement with the previous studies on carbonates tested under elevated pressures. For different types of limestones, the increase in porosity from 2% to 10% due to dissolution caused by high-pressure CO₂ treatment has been reported along with the decrease in elastic moduli from 10 to 25% (Bemer and Lombard, 2010; Vialle and Vanorio, 2011; Lamy-Chappuis et al., 2016).

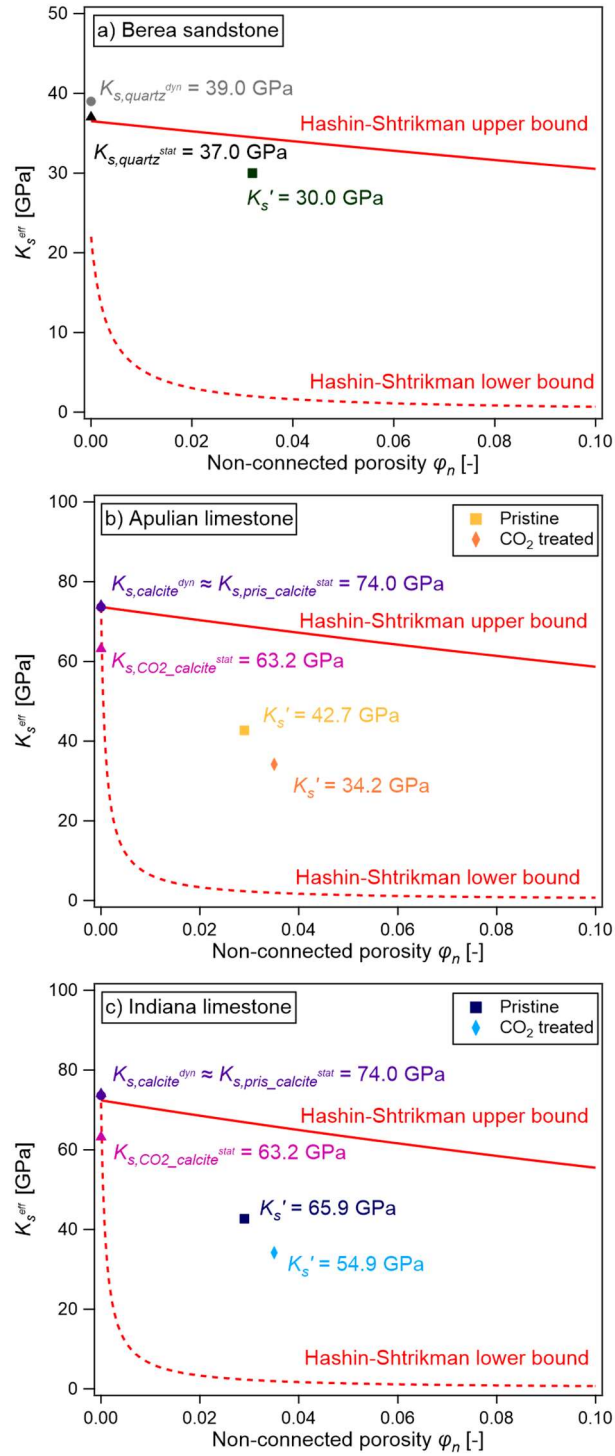


Figure 4.13. The dependence of isotropic-generalized Hashin-Shtrikman bounds for the solid bulk moduli from the value of the non-connected porosity and theunjacketed bulk moduli for (a) Berea sandstone, (b) Apulian limestone, and (c) Indiana limestone.

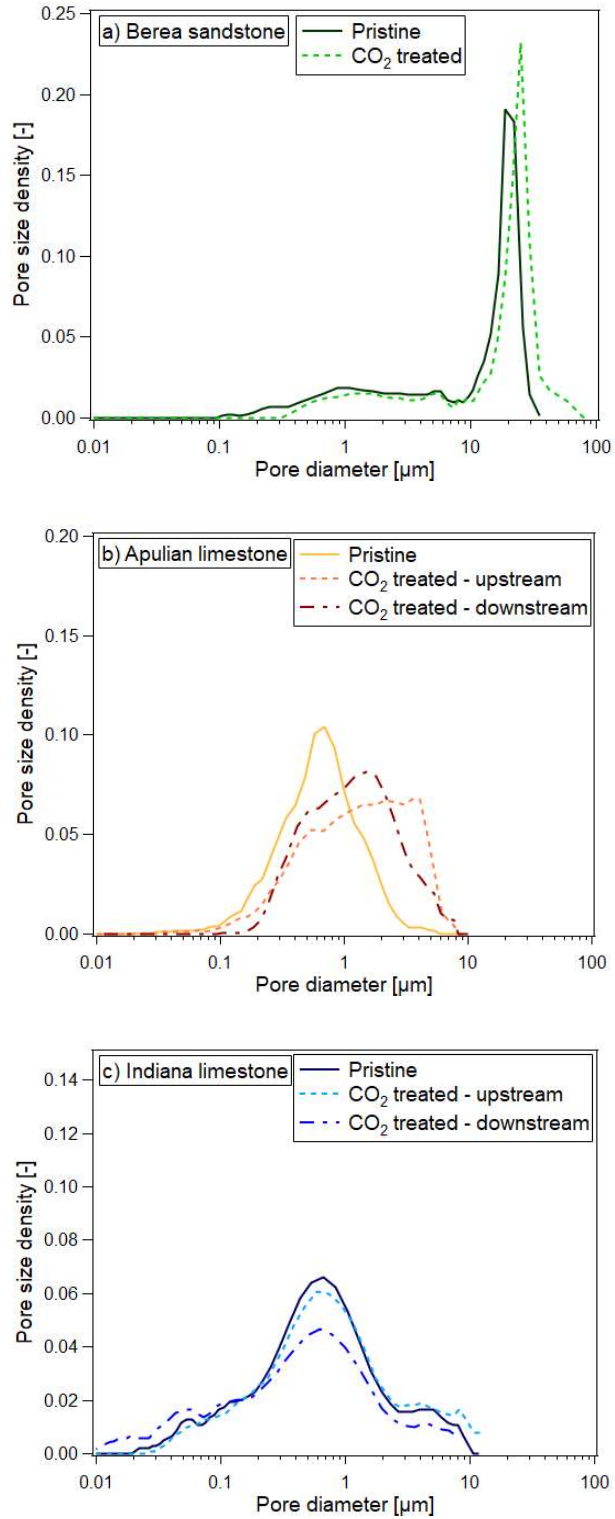


Figure 4.14. Pore size distribution of pristine and CO₂ treated (a) Berea sandstone, (b) Apulian limestone, and (c) Indiana limestone.

Utilizing various analyses, this study concludes that CO₂ treatment increases the matrix (unjacketed) compressibility of limestones due to calcite dissolution and increase in porosity, while these for the sandstone remain the same. CO₂ injection operations can change the elastic properties of the materials and their flow characteristics, which would potentially affect the storage capacity of the host rock and CO₂ trapping mechanisms (Bachu et al., 2007; Kopp et al., 2009). Changes in poroelastic parameters would also influence the inelastic (Aman et al., 2017; Kim et al., 2018; Fuchs et al., 2019; Ilgen et al., 2019; Choens et al., 2020; Tarokh et al., 2020) and viscous (Hangx et al., 2010; Makhnenko and Podladchikov, 2018; Kim and Makhnenko, 2020; Tarokh et al., 2020) response of the host formations. Additional hydro-mechanical-chemical simulation studies at the reservoir scale are necessary to assess the large-scale implications of carbonate mineral dissolution for reservoir and caprock integrity.

Table 4.1. Summary of the test data for reservoir rock and minerals for pristine and CO₂ treated specimens.

		Berea sandstone	Apulian limestone		Indiana limestone		Quartz	Calcite
			upstr.	downstr.	upstr.	downstr.		
Dominant mineral		~85% quartz	95-98% calcite		97% calcite		>99% quartz	>99% calcite
Bulk modulus [GPa] (static)	Pristine	30.0	42.7		65.9		37.0	74.0
	CO ₂ treated	30.0 (CF/batch)	33.7	34.7	54.0	55.8	37.0	63.2
Porosity	ϕ_t [%]	Pristine	40.0		13.2		-	-
		CO ₂ treated	25.1	42.8	41.7	15.1	14.0	-
	ϕ [%]	Pristine	37.1		12.7		-	-
		CO ₂ treated	21.9	39.2	38.3	14.0	13.1	-
	ϕ_h [%]	Pristine	2.9		0.5		-	-
		CO ₂ treated	3.2	3.6	3.4	1.1	0.9	-
ρ_{bulk} [g/cm ³]	Pristine	2.05	1.66		2.36		2.65	2.71
	CO ₂ treated	2.05	1.58	1.61	2.31	2.34	2.65	2.71
V_p [km/s]	Pristine	-	-		-		5.72	6.64
	CO ₂ treated	-	-		-		5.74	6.62
V_s [km/s]	Pristine	-	-		-		3.68	3.56
	CO ₂ treated	-	-		-		3.69	3.54
Bulk modulus [GPa] (dynamic)	Pristine	-	-		-		38.9	73.7
	CO ₂ treated	-	-		-		39.2	73.5

4.5. Conclusions

In this study, the effect of CO₂ treatment on the compressibility of the solid matrix of reservoir rock and the composing solid minerals are experimentally investigated. Berea sandstone, Apulian limestone, and Indiana limestone are selected as the representative materials for reservoir rock, while quartz and calcite are the dominant composing minerals. As a contrast, another set of 21-days CO₂ treated reservoir rock and mineral samples are prepared. CO₂ injection into water-saturated reservoir rock is conducted in the core flooding device to simulate the storage operations at the in-situ conditions, while due to the geometry and lattice structure, the minerals are treated in the high-pressure vessel. Hydrostatic compression tests are conducted to measure the unjacketed bulk moduli of reservoir rocks and solid bulk moduli of the minerals. Based on the local strain measurements, it is shown that the CO₂-water mixture does not affect the silica-rich rock and quartz in terms of compressibility, while for calcite-rich rocks and calcite, the bulk moduli decrease by 15-21%. The ultrasonic wave velocity measurements confirm these findings for the silica-rich and calcite-rich rocks and quartz, but not for calcite minerals where no change in the elastic moduli is observed. Further ESEM images indicate that locally the surfaces of limestones and calcite minerals are chemically affected by the CO₂-water mixture. While some new connected and non-connected pores are created in the limestones, calcite remains to have zero porosity, so the global bulk response of the minerals remains unchanged. Finally, CO₂ injection induced dissolution and precipitation of calcite would affect the overall behavior of calcite-rich reservoir rock both in terms of its elastic and inelastic response, as well as the flow and storage properties.

References

- Adams, L.H., Williamson, E.D. (1923) On the compressibility of minerals and rocks at high pressures. *J Franklin Inst.* 195(4): 475-529.
- Alam, M.M., Hjuler, M.L., Foged, H., Lykke, I., Christensen, H.F., Fabricius, I.L. (2014) Petrophysical and rock-mechanics effects of CO₂ injection for enhanced oil recovery: experimental study on chalk from south Arne field, North Sea. *J Pet Sci Eng.* 122: 468-487.
- Aman, M., Espinoza, D.N., Ilgen, A.G., Major, J.R., Eichhubl, P., Dewers, T.A. (2017) CO₂-induced chemo-mechanical alteration in reservoir rocks assessed via batch reaction experiments and scratch testing. *Greenh Gas Sci Technol.* 1-17.
- Anderson, O.L., Liebermann, R.C. (1966) Sound velocities in rocks and minerals, VESIAC State-of-the-Art Report. Ann Arbor: Univ. of Michigan.
- Bachu, S. (2000) Sequestration of CO₂ in geological media: criteria and approach for site selection in response to climate change. *Energy Convers Manage.* 41(9): 953–970.
- Bachu, S., Bonijoly, D., Bradshaw, J., Burruss, R., Holloway, S., Christensen, N.P., Mathiassen, O.M. (2007) CO₂ storage capacity estimation: Methodology and gaps. *Int J Greenhouse Gas Control.* 1(4): 430-443.
- Bemer, E., Lombard, J.M. (2010) From injectivity to integrity studies of CO₂ geological storage: chemical alteration effects on carbonates petrophysical and geomechanical properties. *Oil Gas Sci Technol Rev Inst Fr Pet.* 65: 445-459.
- Berryman, J.G. (1995) Mixture theories for rock properties. *Rock physics and phase relations: A handbook of physical constants.* 3: 205-28.

- Biot, M.A., Willis, D.G. (1957) The elastic coefficients of the theory of consolidation. *J Appl Mech.* 79: 594-601.
- Blöcher, G., Reinsch, T., Hassanzadegan, A., Milsch, H., Zimmermann, G. (2014) Direct and indirect laboratory measurements of poroelastic properties of two consolidated sandstones. *Int J Rock Mech Min Sci.* 67: 191-201.
- Bridgman, P.W. (1923) The Compressibility of Thirty Metals as a Function of Pressure and Temperature. *Proc Amer Acad.* 58: 166-242.
- Bridgman, P.W. (1925) Linear compressibility of fourteen natural crystals. *Am Jour Sci.* 10: 483-498.
- Budiansky, B., O'Connell, R.J. (1976) Elastic moduli of a cracked solid. *Int J Solids Struct.* 12(2): 81-97.
- Cheng, A.H. (2016) Poroelasticity. Switzerland: Springer International Publishing.
- Choens II, R.C., Ilgen, A.G., Espinoza, D.N., Aman, M., Wilson, J., Dewers, T.A. (2020) Impacts on mechanical strength of chemical reactions induced by hydrous supercritical CO₂ in Boise Sandstone. *Int J Greenh Gas Control.* 95: 102982.
- Collins, H.C. (1979) The Mississippian and Pennsylvanian (Carboniferous) systems in the United States. Ohio, United States Geological Survey.
- Dana, J.D. (1864) *Manual of Mineralogy.* Wiley.
- Deer, W.A., Howie, R.A., Zussman, J. (1966) *An introduction to the rock forming minerals,* Longman Group Limited. London, England.
- Detournay, E., Cheng, A.H.D. (1993) Fundamentals of poroelasticity. In *Comprehensive rock engineering, vol. II* (ed. C Fairhurst), Oxford, UK: Pergamon Press 113-171.

- Evans, J.P., Chester, F.M. (1995) Fluid-rock interaction in faults of the San Andreas system: Inferences from San Gabriel fault rock geochemistry and microstructures. *J Geophys Res.* 100.
- Fabre, D., Gustkiewicz, J. (1997) Poroelastic properties of limestones and sandstones under hydrostatic conditions. *Int J Rock Mech Min Sci.* 34: 127-134.
- Fuchs, S.J., Espinoza, D.N., Lopano, C.L., Akono, A.T., Werth, C.J. (2019) Geochemical and geomechanical alteration of siliciclastic reservoir rock by supercritical CO₂-saturated brine formed during geological carbon sequestration. *Int J Greenh Gas Control.* 88: 251-260.
- Gassmann, F. (1951) Über die elastizität poröser medien (On elasticity of porous media). *Veierteljahrsschrift der Naturforschenden Gesellschaft in Zürich.* 96: 1–23.
- Greenwald, R.F. (1980) Volumetric Response of Porous Media to Pressure Variations. Ph.D. dissertation, University of California at Berkeley.
- Grgic, D. (2011) Influence of CO₂ on the long-term chemomechanical behavior of an oolitic limestone. *J Geophys Res: Solid Earth.* 116: B07201.
- Hangx, S.J.T., Spiers, C.J., Peach, C.J. (2010) Creep of simulated reservoir sands and coupled chemical-mechanical effects of CO₂ injection, *J Geophys Res.* 115: B09205.
- Hangx, S., van der Linden, A., Marcelis, F., Bauer, A. (2013) The effect of CO₂ on the mechanical properties of the Captain sandstone: geological storage of CO₂ at the Goldeneye field (UK). *Int J Greenh Gas Control.* 19: 609–619.
- Hart, D.J., Wang, H.F. (1995) Laboratory measurements of a complete set of poroelastic moduli for Berea sandstone and Indiana limestone. *J Geophys Res.* 100(B9): 17741–17.

- Hart, D.J., Wang, H.F. (2010) Variation ofunjacketed pore compressibility using Gassmann's equation and an overdetermined set of volumetric poroelastic measurements. *Geophysics*. 75(1): N9–N18.
- Hashin, Z., Shtrikman, S. (1963) A variational approach to the theory of the elastic behaviour of multiphase materials. *J Mech Phys Solids*. 11(2): 127–140.
- IEA (2015) CO₂ Emissions From Fuel Combustion Highlights 2015. International Energy Agency.
- Ilgen, A.G., Newell, P., Hueckel, T., Espinoza, D.N., Hu, M. (2019) Coupled chemical-mechanical processes associated with the injection of CO₂ into subsurface. In *Science of Carbon Storage in Deep Saline Formations: Process Coupling Across Time and Spatial Scales*. 337-359.
- Ingraham, M.D., Bauer, S.J., Issen, K.A., Dewers, T.A. (2017) Evolution of permeability and Biot coefficient at high mean stresses in high porosity sandstone. *Int J Rock Mech Min Sci*. 96: 1-10.
- IPCC (2005) Underground Geological Storage. In *IPCC Special Report on Carbon Dioxide Capture and Storage*; Cambridge University Press: Cambridge, U.K. 195–276.
- Johnson, J.W., Nitao, J.J., Morris, J.P. (2004) Reactive transport modeling of cap rock integrity during natural and engineered CO₂ storage. In: Thomas, D.C., Benson, S.M. (Eds.), *Carbon Dioxide Capture for Storage in Deep Geologic Formations*. Elsevier, Oxford, UK 787-813.
- Kaga, H. (1968) Third-order elastic constants of calcite. *Phys Rev*. 172: 900-914.

- Kim, K., Makhnenko, R.Y. (2020) Evolution of poroviscoelastic properties of silica-rich rock after CO₂ injection. In: E3S Web of Conferences EDP Sciences, ICEGT conference proceedings.
- Kim, K., Vilarrasa, V., Makhnenko, R.Y. (2018) CO₂ injection effect on geomechanical and flow properties of calcite-rich reservoirs. *Fluids*. 3(3): 66.
- Koga, I., Aruga, M., Yoshinaka, Y. (1958) Theory of plane elastic waves in a piezoelectric crystalline medium and determination of elastic and piezo-electric constants of quartz. *Phys Rev*. 109: 1467-1473.
- Kopp, A., Class, H., Helmig, R. (2009) Investigations on CO₂ storage capacity in saline aquifers—Part 2: Estimation of storage capacity coefficients *Int J Greenh Gas Control*. 3(3): 277-287.
- Lamy-Chappuis, B., Angus, D., Fisher, Q.J., Yardley, B.W. (2016) The effect of CO₂-enriched brine injection on the mechanical properties of calcite-bearing sandstone. *Int J Greenh Gas Control*. 52: 84-95.
- Le Guen, Y., Renard, F., Hellmann, R., Brosse, E., Collombet, M., Tisserand, D. (2007) Enhanced deformation of limestone and sandstone in the presence of high fluids. *J Geophys Res: Solid Earth*. 112(B5).
- Lowe, J., Johnson, T.C. (1960) Use of back pressure to increase degree of saturation of triaxial test specimens. *Proceedings of the research conference on shear strength of cohesive soils*, Boulder, Colorado, ASCE. 819-836.
- Luquot, L., Gouze, P. (2009) Experimental determination of porosity and permeability changes induced by injection of CO₂ into carbonate rocks. *Chem Geol*. 265: 148–159.

- Makhnenko, R.Y., Labuz, J.F. (2016) Elastic and inelastic deformation of fluid-saturated rock. *Phil Trans R Soc A*. 374: 20150422.
- Makhnenko, R.Y., Podladchikov, Y.Y. (2018) Experimental poroviscoelasticity of common sedimentary rocks. *J Geophys Res: Solid Earth*. 123: 7586-7603.
- Mavko, G., Mukerji, T., Dvorkin, J. (2009) *The Rock Physics Handbook: Tools for Seismic Analysis in Porous Media*. Cambridge Univ. Press, Cambridge, U.K.
- Ma, X., Abe, Y., Kaneko, A., Fujimoto, S., Murakami, C. (2017) Study on dissolution process of liquid CO₂ into water under high pressure condition for CCS. *Energy Procedia*. 114.
- McLatchie, A.S., Hemstock, R.A., Young, J.W. (1957) The Effective Compressibility of Reservoir Rock and Its Effects on Permeability. *Trans Soc Pet Eng AIME*. 213: 386-388.
- McSkimin, H.J., Andreatch, P., Thurston, R.W. (1965) Elastic moduli of quartz versus hydrostatic pressure at 25° and -195.8°C, *J Appl Phys*. 36: 1624-1632.
- Metz, B., Davidson, O., De Coninck, H.C., Loos, M., Meyer, L. (2005) *Special Report on Carbon Dioxide Capture and Storage*. IPCC—Intergovernmental Panel on Climate Change. Cambridge University Press.
- Morris, R.C., Fletcher, A.B. (1987) Increased solubility of quartz following ferrous–ferric iron reactions. *Nature*. 330(6148): 558-561.
- Nakamura, M., Watson, E.B. (1981) Experimental study of aqueous fluid infiltration into quartzite: implications for the kinetics of fluid redistribution and grain growth driven by interfacial energy reduction. *Geofluids*. 1: 73-89.
- Nur, A., Byerlee, J.D. (1971) An exact effective stress law for elastic deformation of rock with fluids. *J Geophys Res*. 76: 6414-6419.

- Patton, J.B., Carr, D.D. (1982) The Salem limestone in the Indiana building-stone district. Indiana Geological Survey.
- Perry, R.H., Chilton, C.H. (1973) Chemical engineer's Handbook, New York: McGraw-Hill Book Company.
- Pimienta, L., Fortin, J., Gueguen, Y. (2017) New method for measuring compressibility and poroelasticity coefficients in porous and permeable rocks. *J Geophys Res.* 122: 2670-2689.
- Plummer, L.N., Parkhurst, D.L., Wigley, T.M.L. (1979) Critical review of the kinetics of calcite dissolution and precipitation chemical modeling-speciation, sorption, solubility, and kinetics. *Chemical modeling in aqueous systems.* ACS, Washington, DC. 537-573.
- Plummer, L.N., Wigley, T.M.L., Parkhurst, D.L. (1978) The kinetics of calcite dissolution in CO₂-water systems at 5 degrees to 60 degrees C and 0.0 to 1.0 atm CO₂. *Am J Sci.* 278(2): 179-216.
- Putnis, A. (2002) Mineral replacement reactions: From macroscopic observations to microscopic mechanisms. *Mineral Mag.* 66: 689–708.
- Putnis, A. (2009) Mineral replacement reactions. *Rev Miner Geochem.* 70: 87–124.
- Redfern, S.A.T., Angel, R.J. (1999) High-pressure behaviour and equation of state of calcite, CaCO₃. *Contrib Miner Petrol.* 134: 102–106.
- Rimmelé, G., Barlet-Gouédard, V., Renard, F. (2010) Evolution of the petrophysical and mineralogical properties of two reservoir rocks under thermodynamic conditions relevant for CO₂ geological storage at 3 km depth. *Oil Gas Sci Technol.* 65(4): 565-580.

- Rohmer, J., Seyedi, D.M. (2010) Coupled large scale hydromechanical modelling for caprock failure risk assessment of CO₂ storage in deep saline aquifers. *Oil Gas Sci Technol.* 65(3): 503-517.
- Rohmer, J., Pluymakers, A., Renard, F. (2016) Mechano-chemical interactions in sedimentary rocks in the context of CO₂ storage: Weak acid, weak effects? *Earth Sci Rev.* 157: 86-110.
- Shi, Z., Sun, L., Haljasmaa, I., Harbert, W., Sanguinito, S., Tkach, M., Goodman, A., Tsotsis, T.T., Jessen, K. (2019) Impact of Brine/CO₂ exposure on the transport and mechanical properties of the Mt Simon sandstone. *J Petro Sci Eng.* 177.
- Sterpenich, J., Sausse, J., Pironon, J., Géhin, A., Hubert, G., Perfetti, E., Grgic, D. (2009) Experimental ageing of oolitic limestones under CO₂ storage conditions: Petrographical and chemical evidence. *Chem geol.* 265(1-2): 99-112.
- Tarokh, A., Makhnenko, R.Y. (2019) Remarks on the solid and bulk responses of fluid-filled porous rock. *Geophysics.* 84(4): 83-95.
- Tarokh, A., Makhnenko, R.Y., Kim, K., Zhu, X., Popovics, J.S., Segvic, B., Sweet, D.E. (2020) Influence of CO₂ injection on the poromechanical response of Berea sandstone. *Int J Greenh Gas Control.* 95.
- Vanorio, T., Nur, A., Ebert, Y. (2011) Rock physics analysis and time-lapse rock imaging of geochemical effects due to the injection of CO₂ into reservoir rocks. *Geophysics.* 76(5): 23-33.
- Vialle, S., Vanorio, T. (2011) Laboratory measurements of elastic properties of carbonate rocks during injection of reactive CO₂-saturated water. *Geophys Res Lett.* 38(1).

- Vilarrasa, V., Makhnenko, R.Y., Rutqvist, J. (2019) Field and laboratory studies of geomechanical response to the injection of CO₂. In: Science of Carbon Storage in Deep Saline Formations. Elsevier, Oxford, UK 209-236.
- Wang, H.F. (2000) Theory of linear poroelasticity with applications to geomechanics and hydrogeology. Princeton, NJ: Princeton University Press.
- Wray, R.A. (1997) A global review of solutional weathering forms on quartz sandstones. Earth Sci Rev. 42(3): 137-160.
- Yasuhara, H., Kinoshita, N., Lee, D., Choi, J., Kishida, K. (2017) Evolution of mechanical and hydraulic properties in sandstone induced by simulated mineral trapping of CO₂ geo-sequestration. Int J Greenh Gas Control. 56: 155-164.
- Zisman, W.A. (1933) Compressibility and anisotropy of rocks at and near the earth's surface. Proceedings of the National Academy of Sciences. 19: 666-679.

CHAPTER 5: SHORT- AND LONG-TERM RESPONSES OF RESERVOIR ROCK INDUCED BY CO₂ INJECTION

A manuscript under review in Rock Mechanics Rock Engineering

Kim, K., Makhnenko, R.Y.

Abstract

CO₂ injection for geologic carbon storage is commonly conducted into sedimentary reservoir rock and influences the stress state and pore pressure resulting in coupled hydro-mechanical processes. Consideration of the presence of aqueous fluids in reservoir formations is crucial for describing their mechanical response, both short- and long-term. As CO₂ is injected into the reservoir, the chemical reaction of the acidic mixture of CO₂ and water with rock minerals may alter the poromechanical and hydraulic responses that need to be appropriately characterized. We conduct laboratory experiments aimed at accurate measurements of the stress-dependent poroviscoelastic rock properties to describe short- and long-term deformations. The chemical effects of CO₂ treatment on the poroviscoelastic and hydraulic properties are explored by duplicating each experiment before and after CO₂ treatment, while Berea sandstone, Apulian limestone, and Indiana limestone are selected as representative reservoir materials. CO₂ treatment increases the bulk compressibility of the sandstone and limestones by 15-20%. The undrained response is characterized through measurements of Skempton's B coefficient, which decreases for Berea sandstone, but increases for the limestones. For calcite-rich rock, the porosity and unjacketed compressibility increase by 4-6% and 20%, respectively, while these

parameters remain unchanged for silica-rich rock. As the time-dependent behavior is measured indirectly by monitoring the pore pressure buildup under an undrained condition, the CO₂ treatment appears to significantly facilitate the viscous response by 50-60% for all materials. Additionally, CO₂ injection causes the increase in permeability but does not change the porosity-permeability exponents for the tested rock. Porosimetry and microimaging analyses reveal that for the limestones the main effect is caused by the dissolution of calcite, but for the sandstone the main explanation for the observed results is stress corrosion cracking. This study outlines CO₂ injection influence on the poroviscoelastic response of reservoir rock and emphasizes the importance of properly characterizing the time-dependent behavior for geologic storage projects.

5.1. Introduction

Carbon dioxide (CO₂) is a greenhouse gas that is widely recognized for its adverse effect on climate change, though its emission from fossil fuel consumption has been continuously increasing to meet the growing energy demand (IEA, 2004; IPCC, 2005). In order to mitigate its discharge into the atmosphere, geologic carbon storage (GCS) has been suggested as one of the most efficient methods, where large volumes of CO₂ can be injected into underground formations (Bachu, 2004; 2008). Considering the sufficient potential storage capacity (~ thousands of Gt), deep saline aquifers have been proposed as suitable target formations for GCS and are mostly represented by porous sandstones and limestones (Orr, 2004; US DOE, 2010; Bachu, 2003). Moreover, for safe immobilization of the injected CO₂, the reservoir formation should be carefully selected so that it is sealed with low-permeable layers (caprock and basement rock) to prevent leakage or excessive dissipation (Bachu, 2008).

By selecting appropriate subsurface formations for GCS, many pilot- and commercial-scale CO₂ injection projects have been conducted to ensure the reliability of underground storage at a scale ~1 megaton/year (Chadwick et al., 2012; Hansen et al., 2013; Smith and Jaques, 2016; Vilarrasa et al., 2019; Will et al., 2016). However, field monitoring of the displacement, pressure, and induced microseismic events raised concerns that the mechanical behavior of subsurface rock can be affected by CO₂ injection, resulting in jeopardizing the integrity of the GCS system (Verdon et al., 2011). For example, at In Salah, Algeria, instant responses were observed during the injection into the Carboniferous sandstone formation, where surface uplifts of ~1 cm/year were monitored at the three injection wells, accompanied by microseismic activities (Vasco et al., 2010). Verdon et al. (2013) reported that the CO₂ injection could also potentially affect the subsurface rock's long-term time-dependent behavior, as modeled pore pressures in sandstone formations gradually increased by more than 5 MPa over 6 years, after the injection has been already stopped. CO₂ storage in Mt. Simon sandstone in Decatur, Il resulted in observation of induced microseismicity at distances up to 2 km away from the well and a number of those events occurred before the near-well events (Goertz-Allmann et al., 2017). In Weyburn, Canada, CO₂ had been injected into a limestone layer since 2000 for storage and enhanced oil recovery purposes, and microseismic events occurrence was recorded during and after the injection process (Verdon et al., 2011), implying a possibility of time-dependent behavior.

Similar observations have also been reported for different subsurface fluid injection projects, where induced seismic events were monitored a few years after the shut-in of wastewater or geothermal well injection (Hsieh and Bredehoeft, 1981). Baisch and Vörös (2010) explored the seismic activities for a geothermal system at Soultz-sous-Forêts, France, and found that events continuously occurred at different distances from the injection well even after ceasing the fluid

injection. Eisner et al., (2010) and Williams-Stroud et al., (2020) stated that the induced microseismic activities from fluid injection should not necessarily be associated with the presence of faults, but could be caused by the behavior of the reservoir rock itself. In general, industrial activities involving fluid injection into subsurface formations may induce damaging earthquakes, the number of which is rapidly increasing (Ellsworth, 2013). Therefore, accurately characterizing both short- and long-term poromechanical behavior of the host formations becomes vital for the success of GCS projects.

The instant (short-term) poroelastic response is directly affected by the injection of high-pressure CO₂, as it increases the pore pressure and decreases the effective stresses (Wang, 2000). Thus, the stress state can migrate closer to the conditions associated with rock yield and failure, as it is accompanied by mechanical deformation from overpressure that may jeopardize system's stability and result in induced seismicity and reactivation of faults (Bachu, 2003). In particular, to avoid any excessive deformations, the poromechanical response needs to be limited to the elastic regime. The short-term response or instant deformation of the reservoir rock can be evaluated from the knowledge of the compressibilities of its components (i.e., frame, pores, solid phase, and pore fluid) and the relationships between these compressibilities and the behavior of the bulk (Biot and Willis, 1957; Wang, 2000).

In addition to the short-term response, the deformation of the reservoir rock should also include the long-term (viscous) behavior, considering the permanent time scale of CO₂ storage (~thousands of years). Analogous to the viscous characteristics of the pore fluid, the reservoir rock matrix itself can also demonstrate a viscoelastic behavior that is affected by the presence of the aqueous fluid in the pores (Biot 1941, 1956; Griggs, 1939). Some theoretical explanations on the time-dependent phenomena were provided by introducing intergranular frictional sliding,

intrinsic solid grain deformation, and solid-fluid interactions in fissures at the sub-granular scale, but lacked validation of the theoretical models and direct measurements of the adopted parameters (Abousleiman et al., 1996; Biot, 1962; Cleary, 1978). Therefore, coupled poroviscoelastic response of reservoir rock requires detailed investigation for geologic carbon storage regarding the long-term stress and deformation evolutions.

As the injected CO₂ partially dissolves into the pre-existing aqueous fluid and generates an acidic mixture, chemical reactions may be facilitated and affect the reservoir rock's poromechanical responses (Johnson et al., 2005; Rutqvist, 2012). The pH of the fluid decreases and the dissolution/precipitation processes occur simultaneously, as it may change the chemical equilibrium state and the rock structure (Zhang et al., 2009). Therefore, on top of the short- and long-term response, the complex multi-physical process of CO₂ injection requires proper evaluation of the chemical effect on the reservoir rock's poromechanical behavior.

Previous studies describing the chemical effect on the short-term behavior of reservoir rock indicate that it is more pronounced for limestones rather than sandstones (Rohmer et al., 2016; Vilarrasa et al., 2019). Generally, there is an agreement that CO₂ treatment induces a considerable chemical reaction that decreases the stiffness of limestones by 20-30% due to dissolution (Alam et al., 2014; Bemmer and Lombard, 2010; Grombacher et al., 2012; Kim et al., 2018; Vanorio et al., 2011; Vialle and Vanorio, 2011), while on the other hand, some cases reported no chemical effect (Grgic, 2011; Liteanu et al., 2013). At the same time, the chemical effect of CO₂ treatment on the compressibility is shown to be weak for silica-cemented sandstones (Lei and Xue, 2009; Rimmelé et al., 2010; Tarokh et al., 2020; Vanorio et al., 2011), while the ambiguous results were reported for carbonate cemented silica-rich rock (Aman et al., 2018; Hangx et al., 2013; Marbler et al., 2013). For instance, Hangx et al. (2013) presented no

effect of CO₂ injection in calcite-cemented Captain sandstone even after a few weeks of CO₂ circulation through the rock's pore space. However, Marbler et al. (2013) showed that four weeks of CO₂ treatment decreased the elastic modulus of a carbonate cemented sandstone from the North German Basin by 10-20% due to carbonate dissolution. Also, Choens et al. (2020) studied the effect of scCO₂ exposure on Boise sandstone and proposed that mechanical weakening occurred due to the chemical reactions. Espinoza et al. (2018) concluded that the dissolution and precipitation of minerals due to CO₂-acidified brine injection could decrease or increase the strength and stiffness of the rock, depending on the particular material and its composing minerals.

Various studies have been conducted to characterize the chemical effect of CO₂ treatment on the reservoir rock time-dependent response. Liteanu and Spiers (2009) and Liteanu et al. (2012) reported uniaxial compaction experiments on calcite aggregates, where the dry/wet condition, temperature, and CO₂ pressure were controlled. The intergranular pressure solution and microcracking were suggested to explain the long-term behavior, while a few hour-long experiments demonstrated that CO₂ injection accelerates the time-dependent deformation by a factor of up to 50. Le Guen et al. (2007) observed the effect of CO₂ treatment on the time-dependent deformation for more than 200 days. It appeared that the plastic strain rate (associated with subcritical crack growth) increased after the treatment of sandstones and limestones, and similar observations are reported by Jung and Espinoza (2017), Schimmel et al. (2019), and Bao et al. (2021). Foroutan et al. (2021) conducted a CO₂ injection test using a core flooding device and measured the time-dependent behavior, ultrasonic wave velocities, and strength for the pristine and CO₂ treated Triassic Peco sandstone. It was reported that the viscous creep has

significantly accelerated, while the strength and ultrasonic wave velocities decreased due to CO₂ treatment, which induced the dissolution of grain boundaries and cementing materials.

If the kinetic rate laws for calcite dissolution are introduced in the governing equations, the evolution of porosity, concentration of Calcium ion, and grain radius can be calculated. The simulations of Renard et al. (2005) suggested that the partial pressures of the dissolved CO₂ can promote the compaction rates in treated limestone by a factor of 50-75. However, other studies concluded that the chemical effect on the viscous responses of porous rock were minor (Alam et al., 2014; Oikawa et al., 2008). Hangx et al. (2010) conducted uniaxial compaction experiments with quartz and feldspar and showed that the effect of CO₂ treatment was minimal, and the viscous strain could be negligible compared to the instant elastic strain. While most studies performed uniaxial compression tests to observe time-dependent deformation, the creep indentation testing method can be adopted for reservoir rock in combination with high-resolution SEM-EDS and X-ray spectroscopy to characterize its viscous response (Vandamme and Ulm, 2009; Zhang et al., 2014). Microimaging and indentation tests on pristine and CO₂-aged Mt. Simon sandstone conducted by Akono et al. (2020) reported increase in rock's porosity and enlargement of pore throats that were associated with the decrease in quartz volume fraction and CO₂-induced K-feldspar and clay dissolution reactions. As a result of these geochemical reactions and the related microstructural changes, a 55–60% decrease in the macroscopic logarithmic creep modulus was predicted. Arguably, most existing studies still show significant inconsistencies that highly depend on the deviatoric stress, material, and testing conditions, as it highlights the importance of adequately characterizing the time-dependent response of reservoir rock.

In this study, we select one silica-rich rock, Berea sandstone, and two calcite-rich rocks, Apulian limestone and Indiana limestone, to investigate the effect of CO₂ treatment on the hydraulic and poromechanical properties of reservoir formations encompassing both short- and long-term responses. We adopt a poroviscoelastic constitutive model (Yarushina and Podladchikov, 2015) and measure all model parameters under the same conditions for pristine and treated rock. The experimental methods to introduce a controlled effect of CO₂ treatment are presented and include core flooding experiments, hydrostatic compression tests, and triaxial compression tests (Figure 5.1). Consequently, additional measurements of the stress-dependent poroviscoelastic properties are reported along with the porosity-permeability relationship for the tested rock. Lastly, a thorough discussion on the poroviscoelastic model is provided. The injected CO₂ is maintained to be in the liquid state since it has some advantages in terms of energy efficiency and eliminates the thermal effect that would introduce another level of complexity (Gor et al., 2013; Paterson et al., 2008; Rayward-Smith and Woods, 2011; Vilarrasa et al., 2013). Here, we only focus on the chemical effect on the poromechanical behavior of reservoir rock, regarding both its short- and long-term responses.

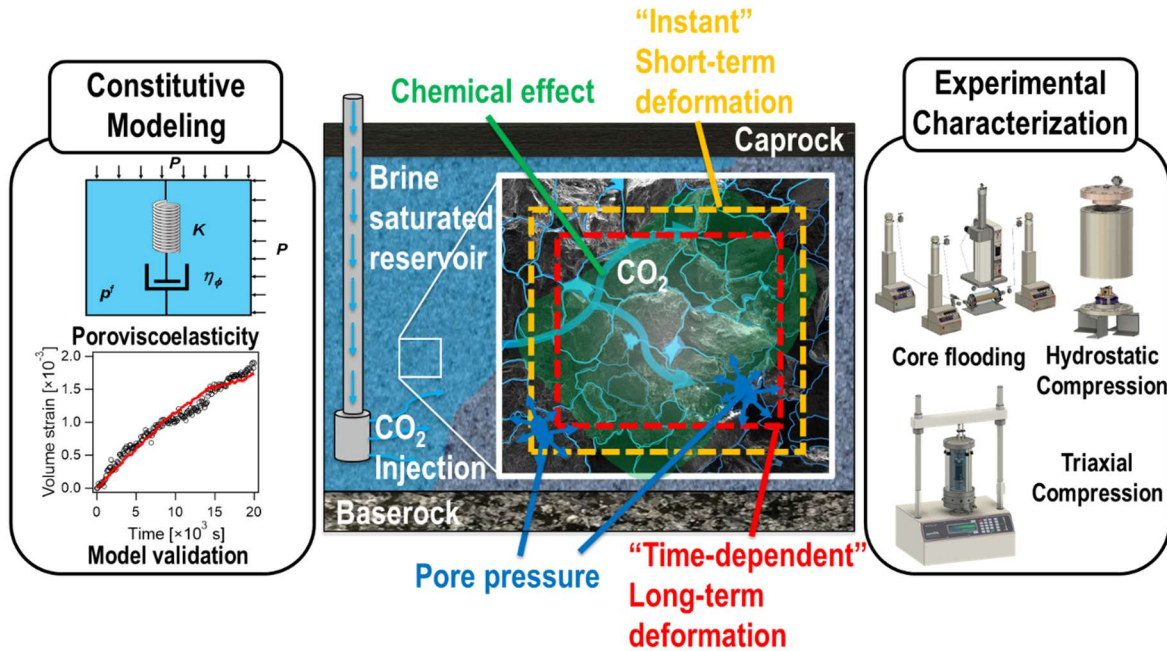


Figure 5.1. Sketch of the multi-physical processes occurring during CO₂ injection into a reservoir rock and the experimental and analytical approaches utilized to characterize them.

5.2. Background

Reservoir rock consists of the solid phase and the pore space that is generally infiltrated with aqueous fluid. This involves consideration of the pore pressure p^f for the poromechanical responses, so the stress state in the isotropic homogeneous porous media can be described by adopting the Terzaghi effective mean stress $P' = P - p^f$, where P is the total mean stress: $P = (\sigma_1 + \sigma_2 + \sigma_3)/3$ (Terzaghi, 1923). P and p^f are the dynamic parameters that govern the poromechanical behavior, and the corresponding kinematic parameters are the volume strain $\varepsilon_v = \varepsilon_1 + \varepsilon_2 + \varepsilon_3$ (the sum of the three normal strains) and increment of the fluid content ζ defined as the ratio between the fluid volume ΔV_f that enters the framework and the unit volume of the element: $\zeta = \Delta V_f/V$ (Biot, 1941). Adding Maxwell's viscoelasticity (second term on right hand side in equations 5.1 and 5.2) to Biot's poroelastic relationship and differentiating them with

respect to time (d/dt), allows writing the poroviscoelastic constitutive equations in the following form (Yarushina and Podladchikov, 2015):

$$\frac{d\varepsilon}{dt} = \frac{1}{K} \frac{d(P - \alpha p^f)}{dt} + \frac{(P - p^f)}{(1 - \phi)\eta_\phi} \quad (5.1)$$

$$\frac{d\zeta}{dt} = \frac{\alpha}{K} \left(\frac{dP}{dt} - \frac{1}{B} \frac{dp^f}{dt} \right) + \frac{(P - p^f)}{(1 - \phi)\eta_\phi} \quad (5.2)$$

Here, K is the drained bulk modulus, α is Biot coefficient, B is the Skempton's coefficient, ϕ is the interconnected porosity, and η_ϕ is the effective bulk viscosity. The bulk viscosity is responsible for the time-dependent response of the porous rock and depends on its pore structure and the viscous and failure parameters of its mineral grains.

The poroelastic parameters can be defined under three primary boundary conditions, considering the relative movement of the fluid in the porous media:unjacketed, drained, and undrained (Detournay and Cheng, 1993). Theunjacketed condition is achieved when the increment (designated by Δ) in the total mean stress P is equal to that of the pore pressure p^f : $\Delta P = \Delta p^f$. After reaching equilibrium, this state indicates that the variation of the pressures on the external and internal surfaces are equal. Under this condition, theunjacketed bulk modulus K_s' can be defined to characterize the compressibility of the porous rock frame:

$$K_s' = V \left. \frac{\Delta p^f}{\Delta V} \right|_{\Delta p^f = \Delta P} \quad (5.3)$$

Under the drained condition, the pore fluid can freely move in or out of the pores, while the pore fluid pressure is controlled to be constant ($\Delta p^f = 0$). The fluid pressure is equilibrated within the rock element and does not affect the loading procedure. The drained bulk modulus K and Biot

coefficient α can be determined within this condition, where K is a measure of the stiffness of a porous media disregarding the pore fluid and can be defined as:

$$K = V \left. \frac{\Delta p^f}{\Delta V} \right|_{\Delta p^f=0} \quad (5.4)$$

The Biot coefficient α is the ratio between the volume of fluid (V_f) expelled from the volume element to the volume change in the element itself when drained loading is applied. It can also be calculated with the knowledge of the unjacketed and drained bulk moduli as shown:

$$\alpha = \left. \frac{\Delta V_f}{\Delta V} \right|_{\Delta p^f=0} = 1 - \frac{K}{K'_s} \quad (5.5)$$

The undrained response is defined as a condition where the fluid cannot enter or exit the porous media and can be characterized by no change in the increment of fluid content $\zeta = 0$. Under this condition, the stiffness of the porous media can be determined through the undrained bulk modulus (K_u). Moreover, the pore pressure responds to the applied external loading, and the Skempton's B coefficient can be defined as the ratio between them.

$$K_u = V \left. \frac{\Delta p^f}{\Delta V} \right|_{\zeta=0} \quad (5.6)$$

$$B = \left. \frac{\Delta p^f}{\Delta P} \right|_{\zeta=0} = \frac{K_u - K}{\alpha K} \quad (5.7)$$

The undrained poroelastic parameters of rock depend on the compressibility of the fluid saturating its pores.

5.3. Methods

5.3.1. Materials

One silica-rich and two calcite-rich reservoir formations are selected for this study: Berea sandstone, Apulian limestone, and Indiana limestone. Although they are not practically utilized as host rocks for CO₂ storage projects, the isotropic and homogeneous properties of these materials provide advantages in testing the constitutive models. The interconnected porosity and dominant pore size are measured accurately using the mercury intrusion porosimetry (MIP) device for all materials, where the relative error for porosity is reported as 3%. At least three specimens are tested for all measurements, and the average value is reported.

Berea sandstone is a sedimentary rock with predominantly fine to medium-sized grains and is well known for its high porosity and permeability (10^{-13} m²). Formed in the late Devonian period, it is located between the Bedford/Ohio shale and Sunbury shale and is also recognized as the host rock for oil and natural gas (Collins, 1979). This light gray-colored sandstone primarily comprises sub-rounded to rounded quartz grains of 0.12-0.25 mm (85-90% of mass), with kaolinite, K-feldspar, and muscovite traces. The interconnected porosity is measured as $\phi = 21.9\%$, with the dominant pore size on the order of 10 μm .

Apulian limestone is chosen to represent the soft calcite-rich (95-98%) rock that also contains small inclusions of plagioclase, glauconite, and iron oxide. As this pale orange-colored formation is geologically classified as a glauconitic fossiliferous limestone, the matrix of Apulian limestone is supported by calcitic mud (micrite) cementations with allochems, which are fragmental calcitic foraminifera with sizes of 0.05-1 mm. The interconnected porosity is measured to be the largest among the tested reservoir rocks with $\phi = 37.1\%$, while the dominant pore size is ~ 1 μm . The permeability is the smallest of the tested reservoir formations (10^{-15} m²).

Indiana limestone, a rigid and stable calcite-rich rock, is well-known for its common application for buildings and public structures, as it is also called a ‘freestone’, meaning that no preferential splitting direction exists (Patton and Carr, 1982). This grey and buff-colored Mississippian rock is composed mainly of calcite (97%), with minor quartz, aluminum oxide, and sulfur portions. The permeability is 10^{-14} m², with the interconnected porosity $\phi = 12.7\%$, the dominant grain size is 1 mm, and the dominant pore size is ~ 1 μm .

5.3.2. CO₂ treatment

The CO₂ treatment tests are conducted in the core flooding system, where the high-pressure conditions can be experimentally simulated. The laboratory setup consists of the core holder, the Stigma 500/700 controller (Sanchez Technologies, France, 70 MPa capacity) for the application of confining pressure, and three syringe pumps (Teledyne ISCO, USA, 25.9 MPa capacity) for the CO₂ and water upstream and downstream pressure application (Tarokh et al., 2020). Cylindrical specimens with a diameter of 50.8 mm (2 inch) and length of 101.6 mm (4 inch) are tested by installing the viton rubber membrane to isolate them from the confining fluid (hydraulic oil). Subsequently, using the steel pore pressure platens and spacers, the specimen is fixed in the core flooding device that generates a passive restraint boundary condition in the axial direction. The induced axial stress σ_{ax} can be calculated by implementing the generalized Hooke’s law under the assumption of Biot poroelasticity, while the confining pressure is only applied in the lateral direction σ_{lat} . By assuming the axial strain to be zero, the total mean stress P can be calculated as

$$P = \frac{\sigma_{ax} + 2\sigma_{lat}}{3} = \frac{2(1+\nu)}{3}\sigma_{lat} - \frac{(1-2\nu)}{3}\alpha p^f \quad (5.8)$$

where ν is the Poisson's ratio. Two external pore pressure transducers (Honeywell, USA, capacity 34.5 MPa) with a resolution of 0.7 kPa are connected to the upstream and downstream ends of the specimen before the valves leading to the pressure controllers, allowing pore pressure measurements under the undrained condition.

Before any CO₂ treatment experiments, full saturation with water must be achieved to avoid free-phase air affecting the hydromechanical and flow properties measurements. The back pressure saturation technique is used to reach full saturation (Lowe and Johnson, 1960; Makhnenko and Labuz, 2016). At a fixed level of Terzaghi effective mean stress $P'=P - p^f$, the applied pore (back) pressure is increased gradually, and the Skempton's B coefficient is measured after every step, with the accuracy of ± 0.01 . Once its value stops changing, the compressibility of the pore fluid becomes constant, indicating that there is no more air trapped in the pores and the specimen has achieved full saturation.

The calculation of the Skempton's B coefficient involves measurement of the pore pressure under the undrained condition. Due to the compressibility of the pore pressure system that consists of the pressure transducers, tubes, and valves outside of the specimen, a correction needs to be applied to report the true B values for rock (Bishop, 1976). The correction factor C_{cor} can be determined by accurately measuring the "dead" volume that refers to the fluid volume within the pore pressure lines or drainage system and compressibility of the system.

$$B = \frac{1}{\frac{\Delta P}{\Delta p^f} - C_{cor}} = \frac{1}{\frac{2(1+\nu)\Delta\sigma_{lat}}{3\Delta p^f} - \frac{(1-2\nu)\alpha}{3} - C_{cor}} \quad (5.9)$$

For the core flooding device used in this study, the value of the correction factor is evaluated to be $C_{cor} = 0.5 \times 10^{-2}$, and it only affects reported B values by +0.005 that is smaller than the

accuracy of the measurements. Thus, for the core flooding device, this correction factor is neglected.

The CO₂ treatment is conducted by injecting liquid CO₂ into the specimen after achieving full saturation with water under the isothermal condition at room temperature (22°C). Deionized water is selected as the pore fluid to solely focus on the chemical effect of CO₂ injection, as it eliminates the potential chemical reactions due to salinity and mineral impurities when using brine or tap water. CO₂ is injected from the upstream at 7 MPa, while the downstream valve is kept closed, and the total mean stress is controlled in order to maintain $P'=4.5$ MPa. After the injection of 40-50 mL of liquid CO₂, the upstream valve is closed, and the pore pressure is monitored under the undrained condition. Since it is observed that the pore pressure gradually decreases to that of the boundary state of liquid and gaseous CO₂ (6.2 MPa), additional CO₂ is injected daily to maintain the CO₂ in liquid state while keeping the effective mean stress constant.

Although the injected amount of water and CO₂ differs among the tested specimens, the CO₂ treatment process is assumed to be identical for all materials due to the same CO₂ mass solubility of 0.06 under the experimental conditions. Moreover, as CO₂ dissolution into water is rapid in high-pressure conditions and all materials follow the same process, the change in the CO₂ dissolution rate during the treatment is neglected. Considering that the time duration of CO₂ treatment and the type of material may affect the degree of degradation for reservoir rock (e.g., Shi et al., 2019), a three-day treatment period is selected for the soft Apulian limestone to introduce a controlled (i.e., no macroscopic damage) chemical effect (Kim et al., 2018), while Berea sandstone and Indiana limestone are treated with CO₂ for 21 days (Liteanu et al., 2013; Luquot and Gouze, 2009).

After completing the CO₂ treatment, the resaturation of the specimens with water is performed by running the imbibition tests where CO₂ pressure is decreased down to the water pressure. Consequently, the poroviscoelastic and flow properties are measured again for the treated specimens. The pristine and CO₂ treated specimens are cored in the same direction from the same rock block, and the poromechanical measurements are conducted before treatment to verify that their properties are identical. The main advantage of utilizing the core flooding device for the CO₂ injection experiments is the ability to simulate the representative in-situ conditions. Unlike many studies where specimens are submerged into a batch with a mixture of CO₂ and water without any effective confinement applied to the specimen, the core flooding device allows exertion of realistic stress state and pore pressure during the CO₂ treatment. As the poromechanical measurements for the treated specimens are conducted after reaching full saturation with water, we assume that no chemical reaction occurs at this stage. Moreover, duplication of the experiments validates the repeatability of the results, emphasizing that presence of water alone in the reservoir rocks' pore space does not affect their poromechanical properties.

5.3.3. Hydraulic properties

Permeability is a material property that measures the capacity of the porous medium to transmit fluids through an interconnected porous medium, and the constitutive response can be obtained from coupling the increment of fluid content ζ with the fluid flux q , based on the mass conservation equation (Detournay and Cheng, 1993).

$$\frac{d\zeta}{dt} + \nabla \cdot \vec{q} = 0 \quad (5.10)$$

Permeability can be introduced from Darcy's law, an empirical relationship that assumes laminar and steady-state flow. According to it, the fluid flow rate is a function of the viscosity of the fluid μ_f and the differential pressure dp^f along the differential distance x_i , and their dependence is expressed through the permeability coefficient k when the rock is fully saturated.

$$q_i = -\frac{k}{\mu_f} \frac{\partial p^f}{\partial x_i} \quad (5.11)$$

After achieving full saturation, the intrinsic permeability is measured with right cylindrical specimens using the core flooding device. Pure deionized water is selected as the pore fluid, and for constant room temperature (22°C), its viscosity μ^f is assumed to be 0.001 Pa·s. Water flow is induced through the specimen by applying differential upstream and downstream pore pressures ($p_{up}^f - p_{down}^f = \Delta p^f$), while the total mean stress is controlled to be constant. The effective mean stress is calculated by taking pore pressure as the average of the upstream and downstream pressures. The evolution of the volume of the upstream and downstream controllers is recorded during the flow that is assumed to be laminar with 10^{-4} cm/s being chosen as a flow rate for Berea sandstone, 10^{-6} cm/s - for Apulian limestone, and 10^{-5} cm/s - for Indiana limestone. As the absolute volume change rates for the upstream and downstream sides become equal, the steady-state condition is reached. Thus, the permeability can be calculated from knowing the specimen length L and cross-sectional area A in the direction perpendicular to the flow:

$$k = \frac{\mu^f \cdot L \cdot \Delta V}{A \cdot \Delta t \cdot \Delta p^f} \quad (5.12)$$

The permeability values are reported with 5% accuracy.

5.3.4. Bulk compressibility measurements

The jacketed and unjacketed bulk responses of reservoir rock are measured using the hydrostatic compression test apparatus (Tarokh and Makhnenko, 2019). The hydrostatic cell is filled with hydraulic oil, and by connecting a syringe pump with a capacity of 51.7 MPa (Teledyne ISCO, USA), confining pressure can be applied at constant room temperature (22°C). A prismatic 50 × 40 × 40 mm specimen is prepared from pristine or treated cylindrical samples. For the jacketed test, the specimen is instrumented with resistive strain gauges and then covered with a polyurethane liquid membrane that cures after a few days, preventing the confining fluid from penetrating the rock. Once the membrane is completely solidified, the specimen is submerged into hydraulic oil in the cell. After closing the cell, the hydrostatic pressure is controlled in steps of 2 MPa for the loading stage up to 50 MPa and the unloading stage down to 0 MPa. The strain gauge measurements are recorded for the corresponding hydrostatic pressure at each step, after oil pressure and strain gauge readings reach equilibrium. The bulk volume strain can be calculated from the three normal strain gauge measurements ($\varepsilon_v = \varepsilon_{xx} + \varepsilon_{yy} + \varepsilon_{zz}$). After the jacketed test, the membrane is removed while retaining the strain gauges to be properly attached, allowing fluid to penetrate the pores. Consequently, the stepwise loading and unloading procedures are repeated for the unjacketed compression test, where 10 minutes are taken at each 2 MPa increment step. The unjacketed boundary condition is attained where the external pressure becomes equal to the pore pressure ($\Delta P = \Delta p^f$).

For the uniformity of deformation in the unjacketed compression test, it is essential to confirm that the pore pressure is equal to the mean stress at each point inside the specimen. The characteristic time to reach equilibration of the pore pressure can be estimated as $t_{char} \sim H_{dr}^2/c$, where H_{dr} is the maximum drainage distance for the fluid equal to the half of the minimum

specimen dimension in case of the drainage on all sides. The diffusion coefficient c is estimated to be $\sim 10^{-2}$ m²/s for Berea sandstone, $\sim 10^{-4}$ m²/s for Apulian limestone, and $\sim 10^{-3}$ m²/s for Indiana limestone (Tarokh and Makhnenko, 2019). Thus, the characteristic time is calculated to be on the order of a few seconds, assuring 10 minutes per loading step is sufficient to reach equilibrium at each stage. For both jacketed and unjacketed tests, the loading-unloading procedures are repeated at least two times to confirm the repeatability of the experiment and these parameters are reported with 5% accuracy.

5.3.5. Time-dependent response

Measurements of the time-dependent behavior of reservoir rock are conducted in the conventional triaxial compression system at room temperature (22°C) (GDS Instruments, UK). The system consists of a 50kN load frame, a 4.0 MPa capacity triaxial cell, and three 4.0 MPa capacity pressure/volume controllers for the confining pressure, and the upstream and downstream pressures. For both confining and pore fluids, deionized water is utilized. Additional pore pressure transducers are installed at the upstream and downstream pressure lines to measure the pore pressure next to the specimen. With the two axial and one lateral LVDTs attached to the viton membrane around the specimen, its deformation can be monitored (Tarokh et al., 2020). Adopting deionized water as the pore fluid may affect the clay particles and dissolve the calcite minerals in reservoir rock (Sjöberg and Rickard, 1984; Zhang and Spiers, 2005a). Since all materials for this study contain an insignificant portion of clay particles, this effect is considered to be negligible, which is confirmed by repeated measurements. For calcite-rich rock, we assume that the pore fluid reaches an equilibrium state for mineral dissolution, as the saturation process before any measurements usually takes at least a week. Therefore, for both sandstone and

limestones, the chemical reaction due to CO₂ injection is the dominant factor affecting the poromechanical properties.

The poroviscoelastic model parameter – bulk viscosity η_ϕ can be determined under the drained boundary condition by measuring the volume deformation of the specimen with time (equation 5.1). Alternatively, it has been observed that after achieving full saturation from the back pressure saturation method, all the air bubbles are dissolved in the pore water, and a pore pressure buildup dp^f/dt occurs as the porous rock is compacting with time after application of constant total mean stress under the undrained boundary condition (equation 5.2). This indirect measurement of the time-dependent response possesses a significant advantage against the direct measurement of the viscous deformation regarding accuracy and time, where the effective bulk viscosity η_ϕ can be calculated as (Makhnenko and Podladchikov, 2018):

$$\eta_\phi = \frac{BK}{\alpha(1-\phi)} \frac{P - p^f}{dp^f / dt} \quad (5.13)$$

The lower value of η_ϕ corresponds to more pronounced time-dependent deformation. Calculation of the bulk viscosity then requires knowledge of the other poroelastic properties (K , B , and α) that need to be measured at the corresponding values of the effective mean stress. The bulk viscosity values are reported with 10% accuracy.

5.4. Poromechanical properties

5.4.1. Undrained response

The Skempton's B coefficient is measured in the core flooding device for pristine and CO_2 treated specimens. The undrained loading for Berea sandstone and Indiana limestone is conducted up to 10 MPa effective mean stress. Considering the low yield limit for Apulian limestone, the effective mean stress is only increased up to 4.5 MPa to avoid any inelastic deformation caused by the deviatoric loading applied due to the presence of passive restraint in axial direction (Kim et al., 2018).

For Berea sandstone, the B value decreases from 0.98 to 0.67 with the increase of the effective mean stress from 0.5 MPa to 10.0 MPa for the pristine specimen (Figure 5.2). The B values become lower after CO_2 treatment, with the new range being from 0.87 to 0.62. For Apulian limestone, the B values are in the range of 0.70 to 0.48 for the pristine specimen as the effective mean stress increases from 0.5 MPa to 4.5 MPa, while these values increase to the range of 0.90 to 0.55 after CO_2 treatment. The Skempton's B coefficient for Indiana limestone increases due to CO_2 treatment: from 0.80 to 0.82 at 0.5 MPa and from 0.18 to 0.23 at 10 MPa, though the chemical effect is less pronounced than for Apulian limestone (Figure 5.2).

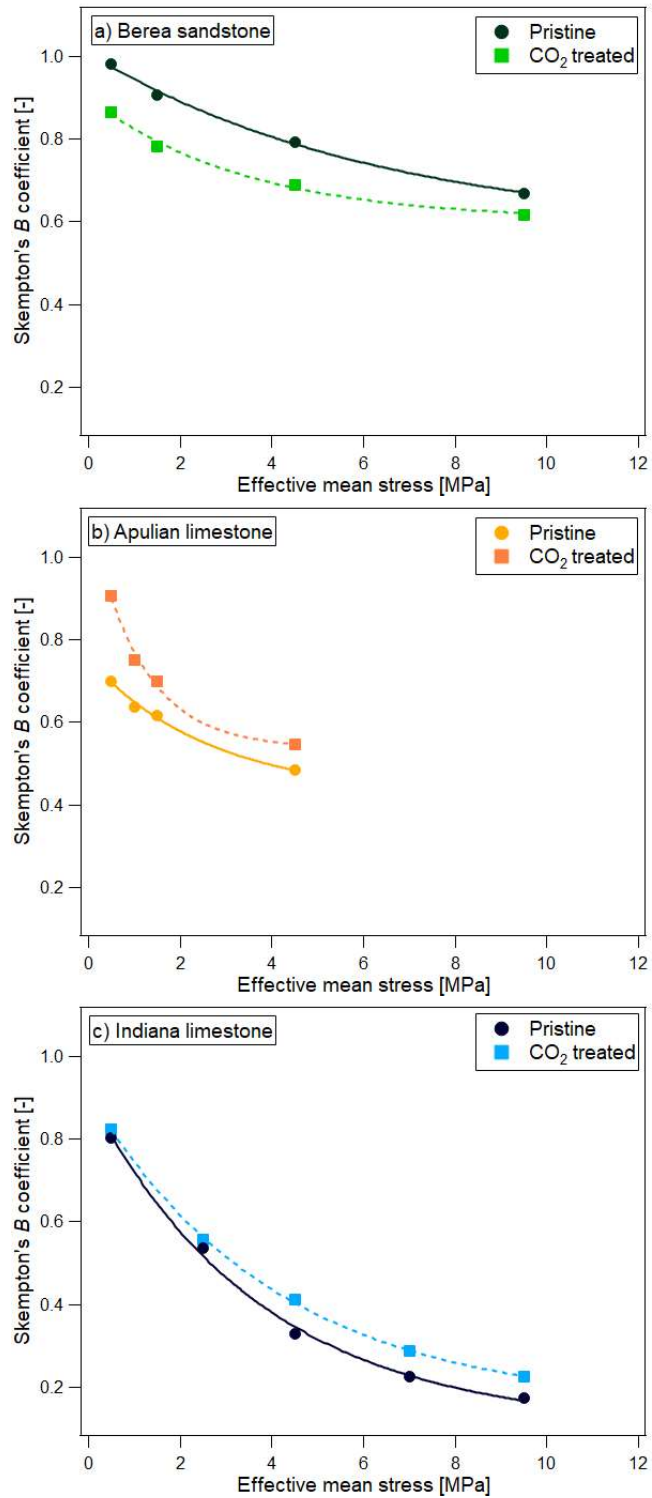


Figure 5.2. Effective mean stress-dependent Skempton's B coefficient measured for pristine and CO_2 treated a) Berea sandstone, b) Apulian limestone, and c) Indiana limestone.

5.4.2. Dry andunjacketed response

The effect of CO₂ treatment on reservoir rock bulk and solid compressibilities is investigated in the jacketed and unjacketed hydrostatic compression tests. The loading-unloading procedure is repeated up to 50 MPa to verify the reproducibility of the results as the normal (directional) strains are recorded on the specimen surfaces. For Apulian limestone, the jacketed compression test is conducted only up to 30 MPa, since pore collapse for this soft material is observed when exceeding the yield point at around 39 MPa (Tarokh and Makhnenko, 2019). Although it is not reported in this study, anisotropy is observed for both the jacketed and unjacketed responses of Berea sandstone, where the normal strain in one direction is 15-20% larger than in the other two directions. For limestones, it is observed that minor differences exist in the initial slopes of the jacketed and unjacketed normal strain measurements, but they eventually become identical, implying isotropy.

The bulk moduli of the pristine and CO₂ treated materials are determined from the volume strain vs the hydrostatic pressure plots shown only for the unloading part of the tests (Figures 5.3-5.5). The jacketed response indicates the increase in bulk moduli with pressure caused by partial pore and crack closure and linear response at higher pressures (above 20 MPa). On the other hand, the unjacketed response presents a constant slope during the whole loading-unloading procedure. For Berea sandstone, the jacketed bulk modulus decreases slightly from 12.1 GPa to 10.3 GPa (or by 15%) due to CO₂ treatment. The unjacketed response is measured to be identical for pristine and treated Berea sandstone, with K_s' being constant and equal to 30.0 GPa, indicating no observable effect from the CO₂ injection.

For the jacketed response of Apulian limestone, the bulk modulus K decreases due to CO₂ treatment from 6.3 GPa to 5.0 GPa (by 20%). The unjacketed bulk modulus K_s' for pristine

Apulian limestone is calculated to be 42.7 GPa. For the CO₂ treated specimen, $K_s' = 34.2$ GPa, so a similar to the dry case 20% decrease in stiffness is observed. The values of K and K_s' for Indiana limestone are the highest among the tested rock, where K is measured to be 29.5 GPa for the pristine specimen and it decreases to 23.1 GPa due to CO₂ treatment (by 21%). It is also noted that the treatment decreases theunjacketed bulk modulus of the limestone from 65.9 GPa to 54.9 GPa (by 17%). In summary, CO₂ treatment decreases the bulk and solid moduli of limestones by approximately 20% and decreases the bulk modulus of Berea sandstone by 15%, while its solid response remains unchanged.

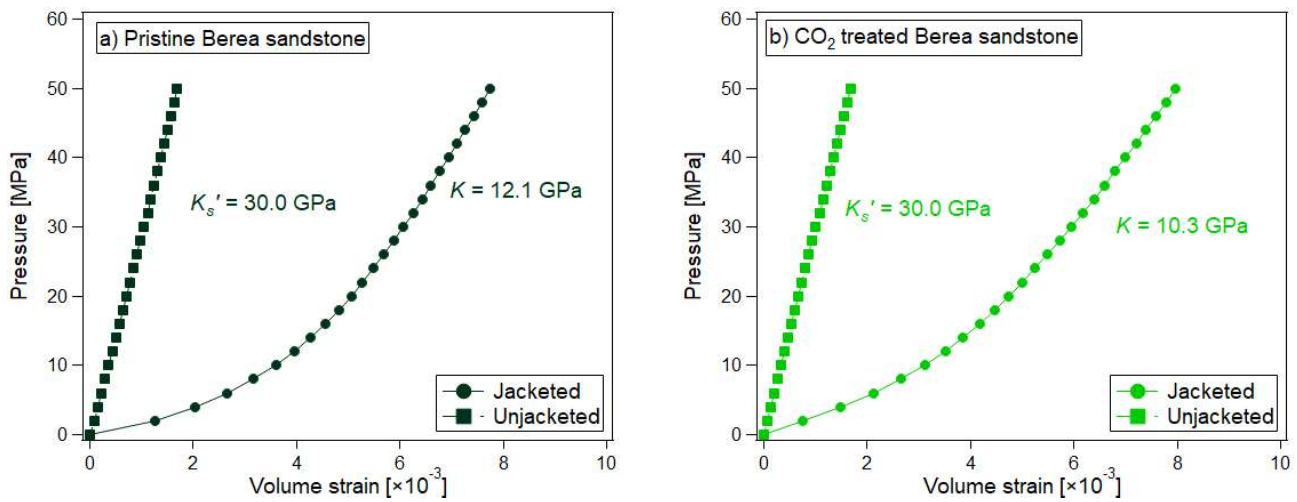


Figure 5.3. Results of the jacketed (dry) andunjacketed (oil-saturated) hydrostatic compression tests on a) pristine and b) CO₂ treated Berea sandstone.

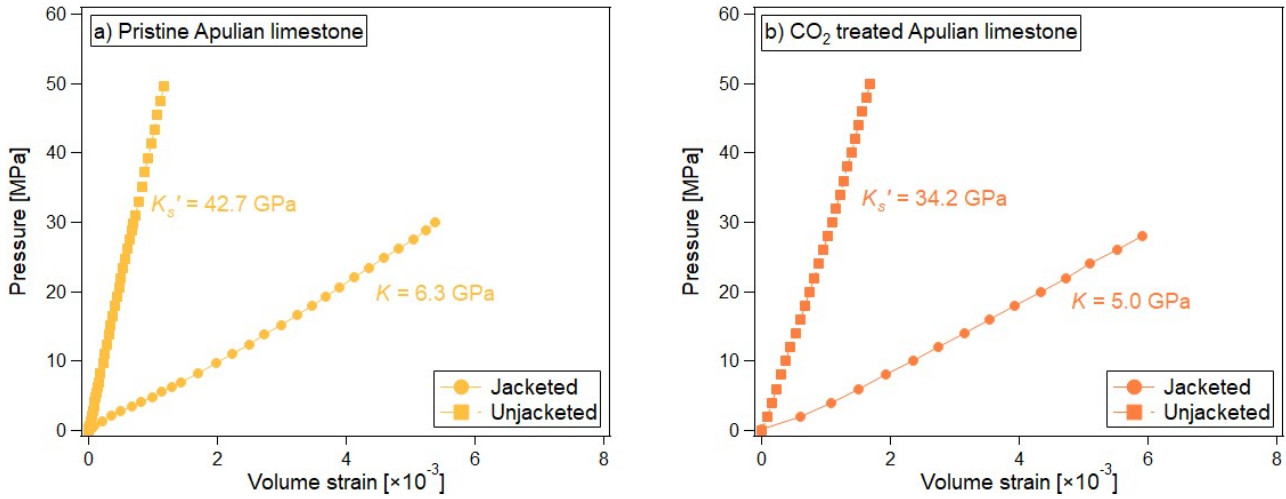


Figure 5.4. Results of the jacketed (dry) andunjacketed (oil-saturated) hydrostatic compression tests on a) pristine and b) CO₂ treated Apulian limestone.

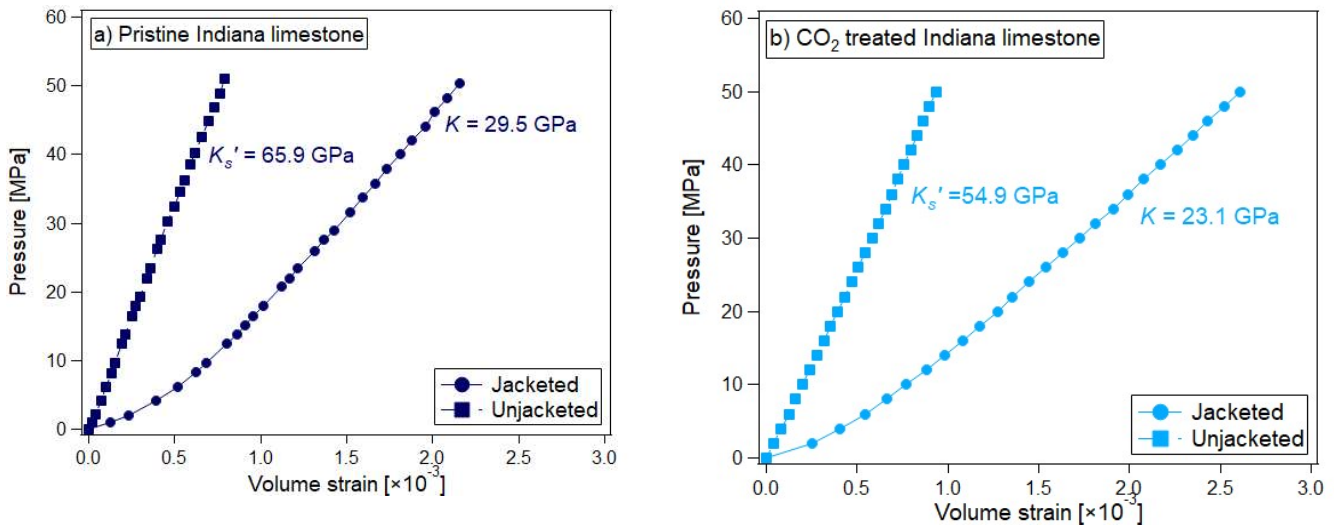


Figure 5.5. Results of the jacketed (dry) andunjacketed (oil-saturated) hydrostatic compression tests on a) pristine and b) CO₂ treated Indiana limestone.

5.4.3. Time-dependent behavior

Considering the timescale of CO₂ storage operations, understanding the long-term response of reservoir rock becomes crucial for successful implementation of the GCS projects. In order to quantify the time-dependent behavior, the ‘indirect method’ is adopted to evaluate the bulk viscosity η_ϕ , which describes the degree of viscous response within the elastic regime (equations 5.1-5.2). For Berea sandstone, Apulian limestone, and Indiana limestone, the bulk viscosity values are calculated for the water-saturated specimens from the pore pressure buildup measured before and after the CO₂ treatment. The total mean stress is fixed at $P = 3.5$ MPa while the pore pressure buildup is monitored at different levels of initial pore pressure, usually following the measurements of the Skempton’s B coefficient. The pore pressure buildup is observed for at least ten thousand seconds (3 hours), and the linear part of the pressure buildup is taken to calculate η_ϕ .

For $P' = 2$ MPa, the calculated bulk viscosity values before and after CO₂ treatment change from 1.6×10^{16} Pa·s to 7.8×10^{15} Pa·s for Berea sandstone, from 4.9×10^{15} Pa·s to 2.4×10^{15} Pa·s for Apulian limestone, and from 4.4×10^{16} Pa·s to 1.7×10^{16} Pa·s for Indiana limestone (Figure 5.6). CO₂ treatment causes the decrease in bulk viscosities by 50-60% for all reservoir rocks, which indicates the significant increase in time-dependent deformation. It appears that the effect of CO₂ treatment on the long-term response could be significantly more pronounced than the effect on the short-term response. It is to be noted that the term viscoelasticity presumes that the material deforms in the elastic domain. At the same time, along with the elastic (or recoverable) deformation, the irrecoverable (viscous) component is also present due to the time-dependent response (Yarushina and Podladchikov, 2015).

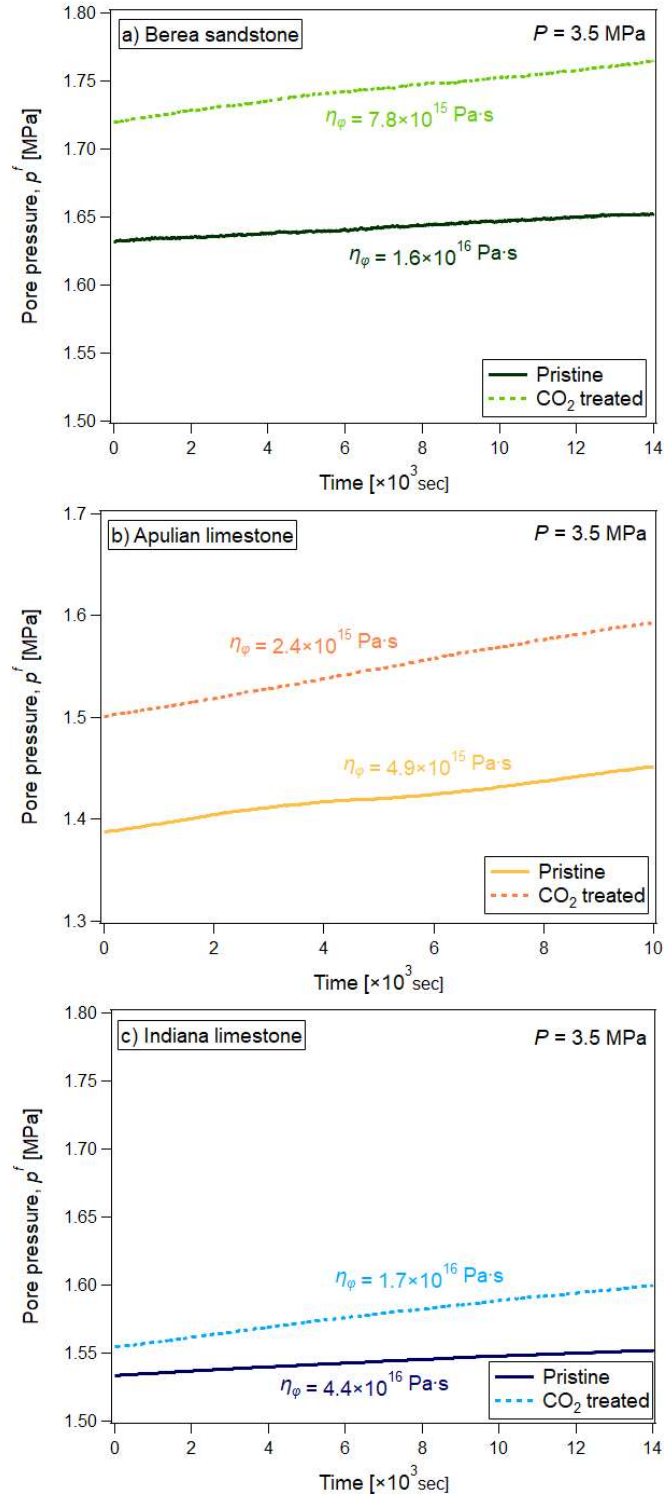


Figure 5.6. Pore pressure buildup under the constant loading and undrained boundary condition for pristine and CO₂ treated: a) Berea sandstone, b) Apulian limestone, and c) Indiana limestone.

5.5. Flow properties

5.5.1. Stress-dependent permeability

The permeabilities of the reservoir rock are reported to be on the order of 10^{-13} m^2 , 10^{-15} m^2 , and 10^{-14} m^2 , for Berea sandstone, Apulian limestone, and Indiana limestone, respectively. The permeability increases due to CO_2 treatment by approximately 10-15% for all the materials, while the effect is slightly more pronounced for the limestones (Figure 5.7). This implies that calcite dissolution in limestones increases their permeability, while apparent creation of new crack-like pores also contributes to the increase in permeability of Berea sandstone. It is to be noted that the stress-dependency of the permeability has a similar trend even after the CO_2 treatment. Apulian limestone appears to be an order of magnitude less permeable than Indiana limestone because its dominant pore size is an order of magnitude smaller.

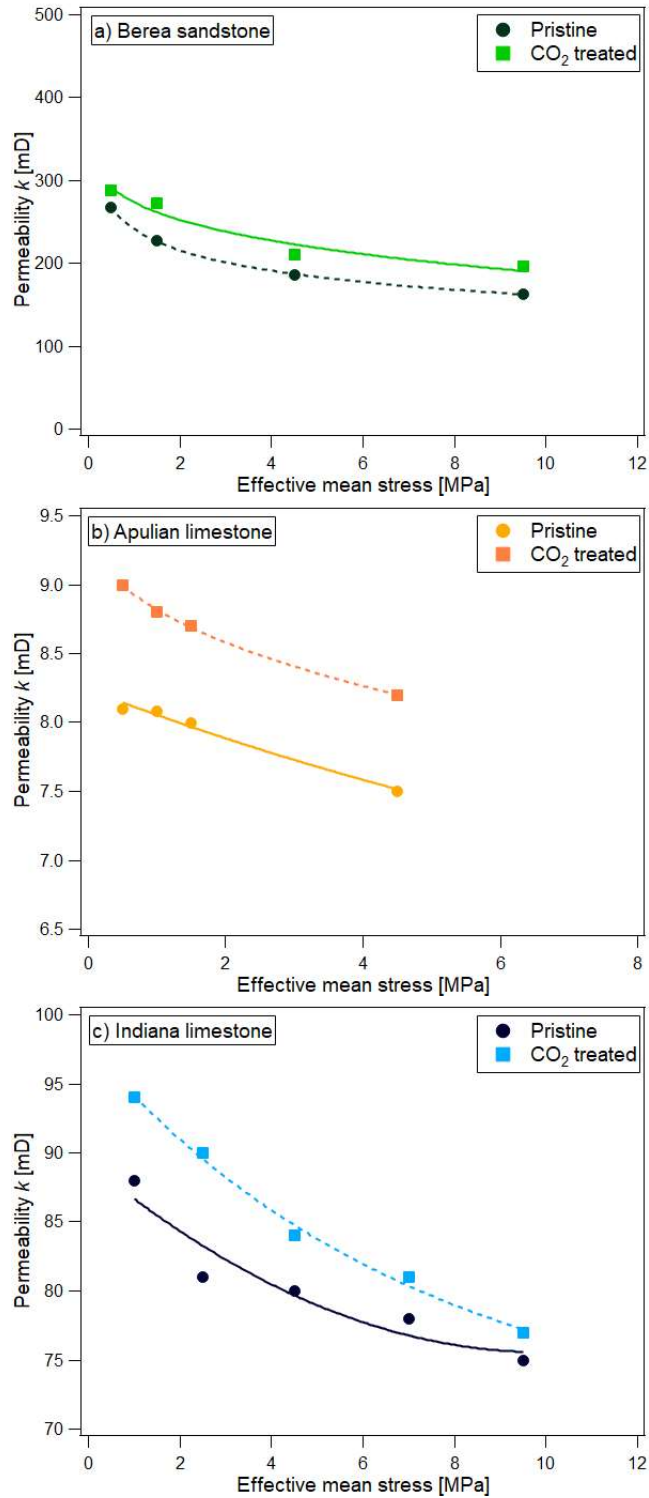


Figure 5.7. Effective mean stress-dependent permeability k measured for pristine and CO₂ treated: a) Berea sandstone, b) Apulian limestone, and c) Indiana limestone.

5.5.2. Porosity calculation

Establishing a porosity-permeability relationship for reservoir rock possesses significant advantages for geoengineering projects where oftentimes assumptions on either hydraulic or mechanical properties have to be made (Bernabé et al., 2003). Since precise measurements of the changes of rock porosity at elevated pressures are challenging, it can be determined from the poroelastic parameters and initial (unconfined) porosity values under the assumption of isotropic linear poroviscoelasticity (Makhnenko and Podladchikov, 2018):

$$\frac{\partial\phi}{\partial t} = \left(\frac{1-\phi}{K} - \frac{1}{K_s'} \right) \frac{\partial P'}{\partial t} - \phi \left(\frac{1}{K_s'} - \frac{1}{K_s''} \right) \frac{\partial p^f}{\partial t} + \frac{P-p^f}{\eta_\phi} \quad (5.14)$$

Here K_s'' is theunjacketed pore modulus (Detournay and Cheng, 1993). If measurements of permeability at different values of the effective mean stress are performed at a fixed value of the pore pressure, the contribution of the second term on the right-hand side of equation (5.14) is neglected. Similarly, the third term is neglected because the time scale for permeability measurement is on the order of hundreds of seconds, making the contribution of the time-dependent deformation at least three orders of magnitude smaller than the deformation caused by the changes in the effective mean stress. As a result, only the first term on the right-hand side of equation (5.14) is considered for calculations of the porosity change.

Measurements of the unconfined values of the interconnected porosities and pore size distributions of pristine and CO₂ treated reservoir rock are conducted using the mercury intrusion porosimetry (MIP) device. Small pieces of each material are collected during the sample preparation, that are utilized for the MIP experiments. At least three samples for each rock in each state have been tested, and the average values are presented in Figure 5.8. The porosity of Berea sandstone is reported to be $\phi = 0.219 \pm 0.001$ for both pristine and CO₂ treated samples. The

porosity of Apulian limestone increased due to treatment from 0.371 ± 0.004 to 0.388 ± 0.004 , and the porosity of Indiana limestone increased from 0.127 ± 0.001 to 0.136 ± 0.001 . Here, we assume that application of 416 MPa mercury pressure was enough to reach all the interconnected pores in the tested rock (down to 3.6 nm size). The dominant pore size for Berea sandstone (20 μm) and Indiana limestone (0.7-0.8 μm) remained approximately the same after CO_2 treatment. At the same time, the dominant pore size for Apulian limestone increased from 0.7 μm to 2-4 μm because dissolution has mainly affected micron-scale pores that mainly comprise this material's pore space (Kim and Makhnenko, 2021).

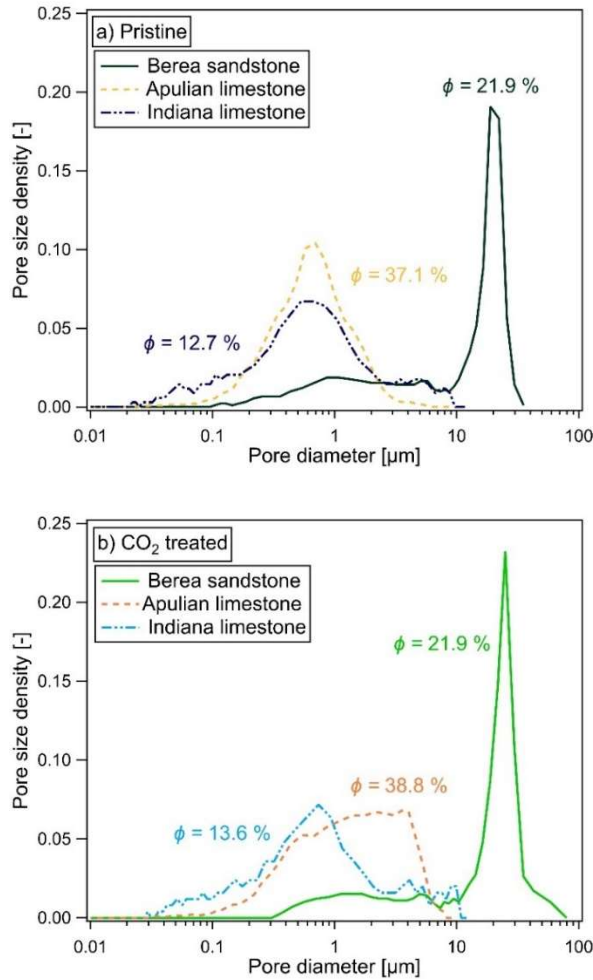


Figure 5.8. Pore size distribution and porosity values measured via Mercury Intrusion Porosimetry on Berea sandstone, Apulian limestone, and Indiana limestone samples in a) pristine and b) CO₂ treated states.

5.5.3. Porosity-permeability relationship

Once the dependence of porosity and permeability on the applied effective mean stress is known, the porosity-permeability relationship can be established. For this study, the Kozeny-Carman equation adopting the percolation threshold porosity ϕ_c is utilized (Bernabe et al., 1982; Bourbié et al., 1987; Gueguen and Dienes, 1989; Mavko and Nur, 1997). The percolation threshold porosity is the minimum required porosity to be filled to initiate the connectivity of flow paths (Kirkpatrick, 1973). In general, the percolation threshold porosity depends on the pore geometry,

where crack-like pores can be fully connected at almost zero porosity, while spherically shaped pores require a more significant threshold porosity for the onset of macroscopic connectivity. Previous studies reported ϕ_c to be in the range of 0.01 to 0.03 (Mavko and Nur, 1997; Ghasemi and Bayuk, 2020). Thus, the Kozeny-Carman relationship with percolation can be presented by replacing the interconnected porosity ϕ with $\phi - \phi_c$.

$$k = S \frac{(\phi - \phi_c)^3}{(1 - (\phi - \phi_c))^2} d^2 \quad (5.15)$$

Since two parameters, geometric factor S and percolation threshold porosity ϕ_c are the unknowns, a numerical calculation using an optimization algorithm is conducted to search for solutions that minimize the sum of squared errors between the experimental data and model prediction. The dominant pore size is selected as the characteristic pore diameter d (Figure 5.8). The fitting results show that a converging curve cannot be determined for any value of the percolation porosity ϕ_c between 0.001 and 0.03 (Figure 5.9). Therefore, a modified power-law relationship introducing the porosity sensitivity exponent n is adopted (David et al., 1994; Doyen, 1988).

$$k = k_0 \left(\frac{\phi}{\phi_0} \right)^n \quad (5.16)$$

The porosity sensitivity exponent is calculated to be $n = 7$ for Berea sandstone and Indiana limestone and $n = 6$ for Apulian limestone (Figure 5.9), being significantly higher than $n \approx 3$ from the Kozeny-Carman equation. Moreover, it is to be noted that the CO₂ treatment of the reservoir rock does not significantly affect the porosity sensitivity exponent value suggesting that the power-law relationship obtained for the pristine rock can be utilized in the reservoir simulations predicting the flow properties of the formation before and after the treatment.

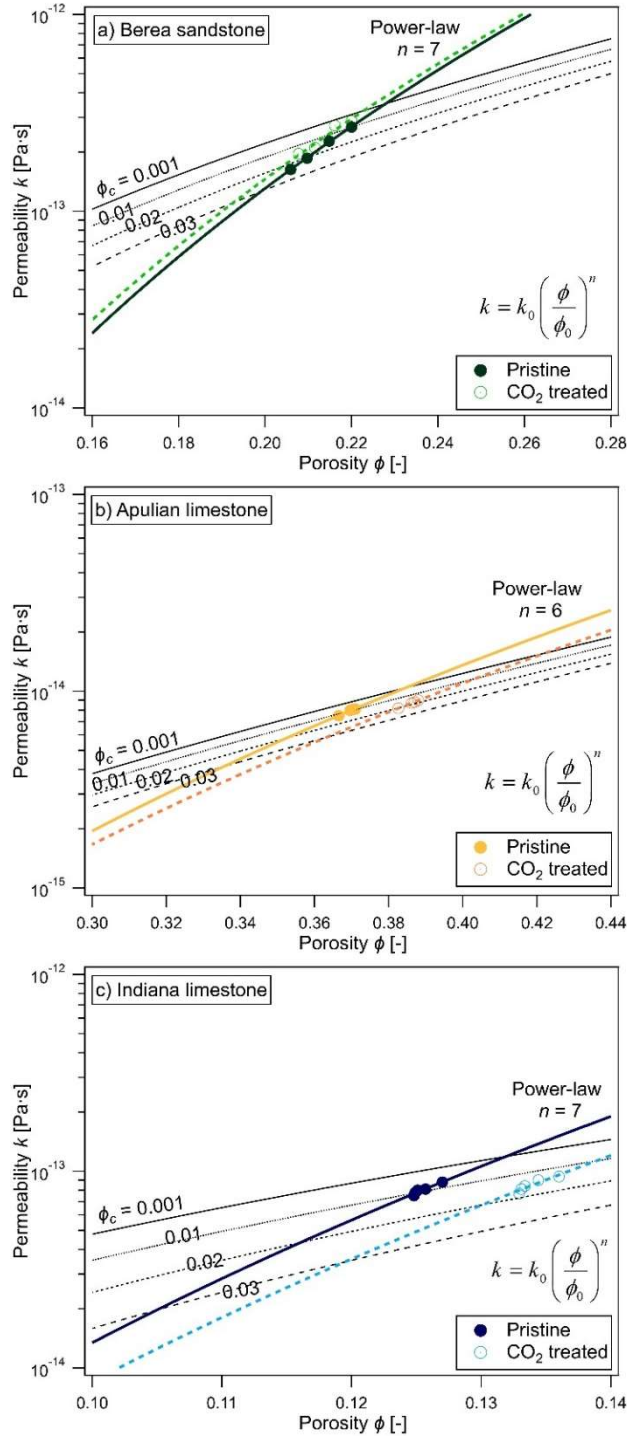


Figure 5.9. Porosity-permeability relationship for a) Berea sandstone, b) Apulian limestone, and c) Indiana limestone calculated using Kozeny-Carman equation with percolation threshold porosity ϕ_c and power-law relationship with the exponent value n .

5.6. Discussion

5.6.1. Poroelastic response

Laboratory experiments are performed to measure the stress-dependent poroelastic properties of water-saturated reservoir rock before and after treatment with liquid CO₂. The porosity of Berea sandstone remains constant, while it increases for Apulian and Indiana limestone by 4-6%. The Skempton's B coefficient decreases for the sandstone by 7%, and increases for both limestones by 10% (at effective mean stress $P' = 10$ MPa). The bulk modulus decreases for all three rock types by 15-20% (compared at $P' > 30$ MPa where it becomes approximately constant for all materials). Theunjacketed bulk modulus decreases for the limestones by 20%, but remains unaffected for Berea sandstone (Table 5.1). This observation is in general agreement with other tests performed on fluid-saturated reservoir rock (Rohmer et al., 2016; Vilarrasa et al., 2019). The parameter responsible for the coupling of mechanical and hydraulic loading - Biot coefficient α can be calculated from the measured drained and unjacketed bulk moduli of the rock before and after the CO₂ treatment. In general, α appears to decrease with increasing effective mean stress as the drained bulk modulus converges to a constant value, while for more compressible Apulian limestone, this effect is less pronounced as the drained bulk modulus is almost constant throughout the pressure increase (Figure 5.10). For Berea sandstone, a minor increase in the Biot coefficient due to CO₂ treatment (from $\alpha = 0.60$ to 0.65 at $P' = 50$ MPa) is observed due to the slight decrease in the drained bulk modulus. For the limestones, CO₂ treatment does not significantly change the Biot coefficient, where α is calculated to be 0.83 (at 30 MPa) for Apulian limestone, and $\alpha = 0.56$ (at 50 MPa) for Indiana limestone.

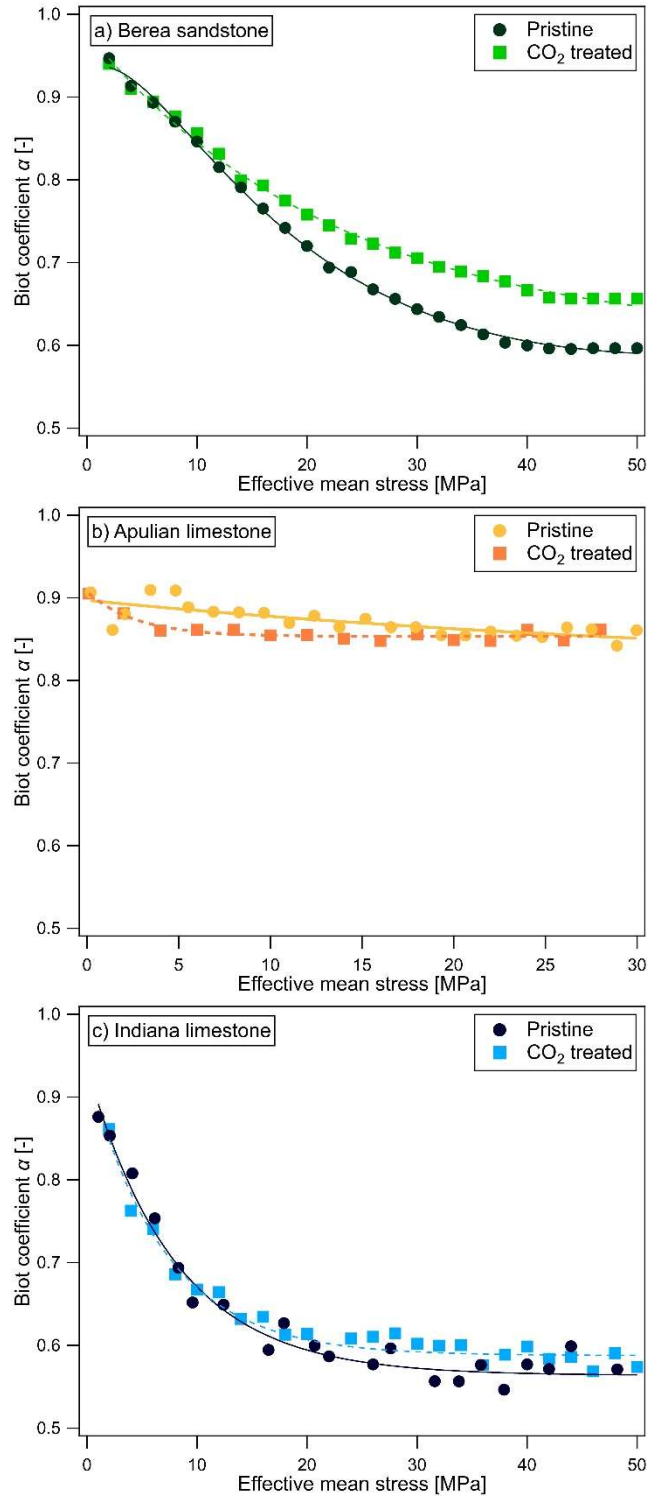


Figure 5.10. Stress-dependent Biot coefficient α values calculated for pristine and CO₂ treated a) Berea sandstone, b) Apulian limestone, and c) Indiana limestone.

Microimaging analysis show changes in the structure at a microscale level for all materials after the CO₂ treatment (Figure 5.11). Dissolution of calcite appears to be the main factor for the alteration in the bulk and solid moduli of the limestones. Disolution happens over the entire body of the specimen being just slightly more pronounced in the upstream part. This leads to higher Skempton's B values, not only because of the decrease in K and K_s' , but also because of the increase in the rock's porosity that makes the undrained response more compliant. At the same time, the compressibility of calcite itself remains constant, and it is argued that the decrease in theunjacketed modulus is caused by the creation of new non-connected pores (Kim and Makhnenko, 2021). As the dissolution and precipitation in calcite-rich rock are usually used as the explanation of changes in material properties (c.f., Rohmer et al., 2016), the authors acknowledge that rearrangement of the calcite particles following the dissolution can provide a better argument. Mangane et al. (2013) reported that a migration of the calcite particles was monitored during the CO₂ flow test in Oolitic limestone, as clogging was verified by microimaging analysis and permeability measurements. Therefore, the particle migration within the pores of the specimen can also be responsible for the creation of new non-connected pores.

Considering Berea sandstone, the drained modulus and Skempton's B value decrease after the CO₂ treatment. Conversely, the unjacketed modulus and solid modulus of quartz remain unchanged (Kim and Makhnenko, 2021). It is argued that the CO₂ injection promotes creation or enlargement of crack-like pores in water-saturated sandstone, which is reflected in more compliant drained response at low effective mean stresses. The measured Skempton's B values are lower, since the undrained bulk modulus K_u could also decrease and $B=(K_u - K)/\alpha K_u$ (Tarokh et al., 2020). At the same time, crack-like pores are still connected to the sandstone's pore structure, and the increase in crack density does not affect the value of K_s' . Due to this and the

decrease in K , the reported increase in the value of Biot coefficient α for the sandstone is more pronounced compared to the limestones, where both the drained and unjacketed bulk moduli decrease by approximately the same percentage (Figure 5.10).

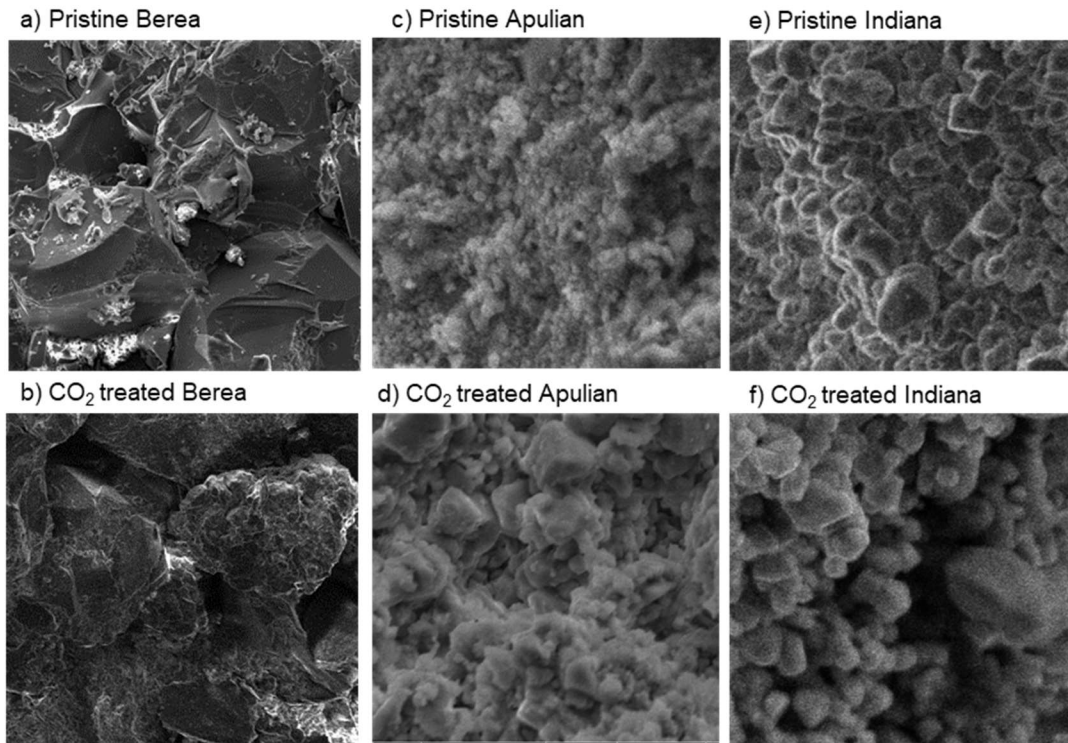


Figure 5.11. ESEM images of reservoir formations for pristine and CO₂ treated Berea sandstone (a) and b)), Apulian limestone (c) and d)), and Indiana limestone (e) and f)).

Table 5.1. Summary of the poroviscoelastic (Skempton's B coefficient, drained bulk modulus K ,unjacketed bulk modulus K_s' , and bulk viscosity η_ϕ) and hydraulic (permeability k and porosity ϕ) properties of Berea sandstone, Apulian limestone, and Indiana limestone.

		Berea sandstone	Apulian limestone	Indiana limestone
ϕ [-]	Pristine	0.219	0.371	0.127
	CO ₂ treated	0.219	0.388	0.136
k [mD] ($P'=4.5$ MPa)	Pristine	186	7.5	80
	CO ₂ treated	210	8.2	84
B [-] ($P'=4.5$ MPa)	Pristine	0.79	0.48	0.33
	CO ₂ treated	0.69	0.55	0.41
K [GPa] ($P'=4.5$ MPa)	Pristine	2.9	4.5	18.5
	CO ₂ treated	2.8	4.2	13.5
K_s' [GPa]	Pristine	30.0	42.7	65.9
	CO ₂ treated		34.2	54.9
α [-] ($P'=4.5$ MPa)	Pristine	0.9	0.9	0.75
	CO ₂ treated	0.91		
η_ϕ [Pa·s] ($P'=2.0$ MPa)	Pristine	1.6×10^{16}	4.9×10^{15}	4.4×10^{16}
	CO ₂ treated	7.8×10^{15}	2.4×10^{15}	1.7×10^{16}

5.6.2. Bulk viscosity

Further investigation is conducted on the stress-dependency of the bulk viscosity (Figure 5.12). Analysis of the measured η_ϕ values shows that the time-dependent response is governed by both the pore pressure p^f and the total mean stress P . It has been observed that bulk viscosity has a tendency to decrease with the increase in the ratio between the pore pressure p^f and the total mean stress P rather than just being a function of the effective mean stress (Makhnenko and Podladchikov, 2018). The CO₂ treatment leads to the decrease of the bulk viscosity for all materials for a given p^f/P ratio. For Berea sandstone and Apulian limestone, η_ϕ values are measured to be $\sim 10^{15}$ Pa·s and decreasing due to CO₂ treatment by 50%. For Indiana limestone, η_ϕ values are in the order of 10^{16} Pa·s and decrease by 60% due to the treatment at low p^f/P values.

The dissolution of calcite is argued to be the main cause of the bulk viscosity decrease in limestones since newly created pores can serve as points for microscale stress concentration and promote time-dependent deformation of the calcite-rich rock (Zhang and Spiers, 2005b). For Berea sandstone, minor alterations of the quartz grains and intergranular material are observed but apparently do not affect the solid response of the material. At the same time, the crack density in the sandstone increases, possibly due to stress corrosion cracking. If the pore fluid becomes chemically active, stress corrosion cracking, describing rock–fluid interactions at the crack tip, can increase the rate of time-dependent deformation by increasing the length of existing cracks and weakening bonds between the grains (Atkinson and Meredith, 1987, Tang et al., 2018). The stress corrosion cracking is related to Si-O bonds becoming weaker (activated) due to the strain-induced reduction in the overlap of atomic orbitals, which can become broken at lower stresses than the strained bonds (Michalske and Freiman, 1982). This process has been

shown to be affected by the level of pore fluid pH, which implies that the CO₂ treatment may promote crack propagation (Atkinson and Meredith, 1987). The dissolution kinetics directly related to stress corrosion is significantly promoted at lower pH values, which can also explain the stress corrosion cracking in the sandstone (Krauklis et al., 2019). Stress corrosion can also induce the microseismic activity in sandstones, sometimes without really affecting their elastic and strength characteristics (Brantut et al., 2013; Makhnenko et al., 2020). Also, as the stress corrosion affects the cracks at the nanoscale (Bonamy et al., 2006), it can explain the observed small increase in the permeability, while the measured porosity does not change due to the resolution of the MIP device (4 nm). As crack growth is a combination of the chemical process and pure mechanical bond rupture, an explanation of the crack propagation under hydrostatic loading needs to be provided (Atkinson and Meredith, 1987). At a microscale level, a small anisotropy of the reservoir rock may still induce shear stresses, which can also contribute to the crack propagation. This effect is expected to be inhibited with increasing effective mean stress due to the crack closure, which would require further analysis.

While the existing studies reported that time-dependent deformation rates increase with the increase in deviatoric loading (cf., Brantut et al., 2013), here we observe that the time-dependent deformation of reservoir rock is accelerated with the increase in p'/P (or decrease in P') under the hydrostatic loading. Compression loading induced processes combined with the decrease in the effective mean stress can promote local stress concentration and eventually accelerate the time-dependent response, which is reflected in reduced values of the bulk viscosity (Makhnenko and Podladchikov, 2018). In addition, the local chemical effects, induced by CO₂ injection in water and subsequent decrease in pore fluid pH, can noticeably influence the long-term behavior. A range of microscale mechanisms, including atomic diffusion, dissolution, ion exchange,

microplasticity, and stress corrosion, could be responsible for subcritical crack growth and subsequent time-dependent deformation (Atkinson and Meredith, 1987). In general, creep strain rates are reported to be very sensitive to environmental conditions, such as differential and mean stresses, temperature, and pore fluid composition, as well as water saturation and pore pressure (Bernabe et al., 1994; Brantut et al., 2013). The effect of pore pressure and chemical (in our case - CO₂) treatment on the rates of time-dependent deformation is confirmed by the presented experimental data.

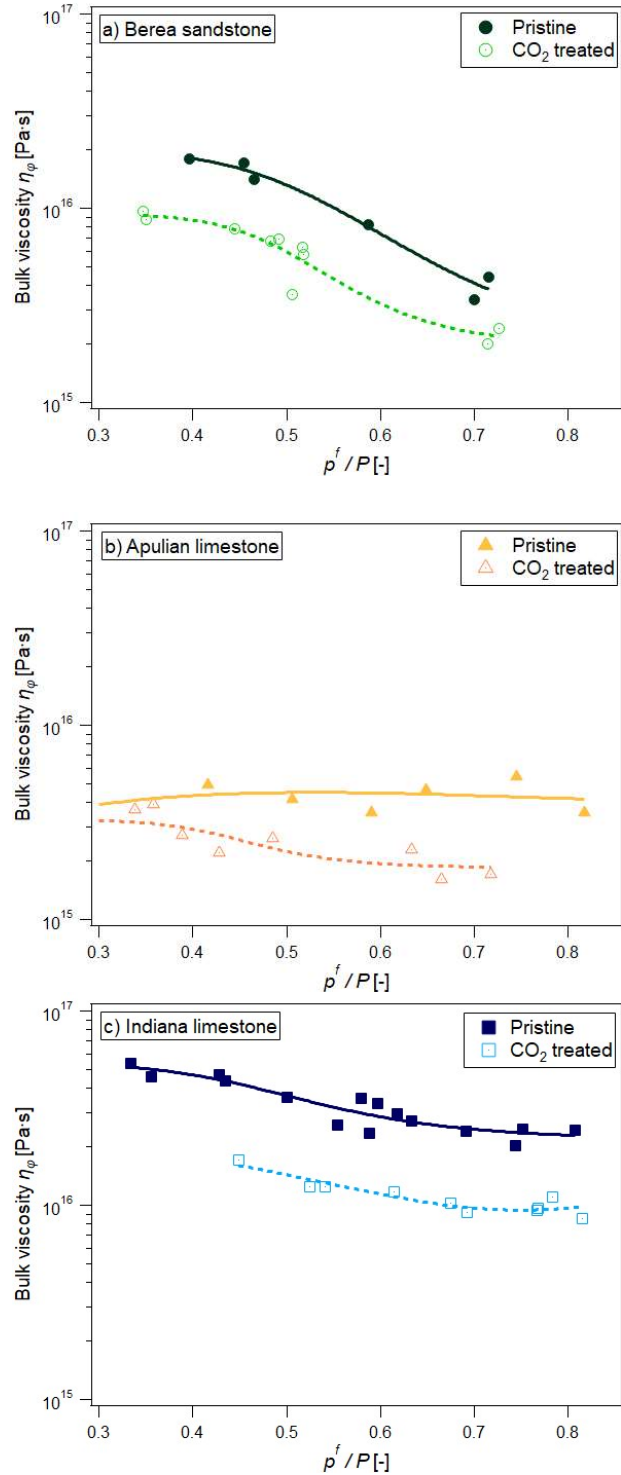


Figure 5.12. Bulk viscosity calculated from undrained pore pressure buildup at different levels of pore pressure to mean stress ratio p^f/P for a) Berea sandstone, b) Apulian limestone, and c) Indiana limestone.

5.6.3. Poroviscoelastic model validation

Measured volume strains can be compared with the model prediction based on equation (5.1) where the poroviscoelastic parameters of the pristine and CO₂ treated materials are adopted for $P' = 2$ MPa. For all materials, the poroviscoelastic model with input parameters measured during the undrained pressure buildup presents a good agreement with the directly measured volume strain (with the accuracy of 10^{-5}). In addition, a significant effect of CO₂ treatment on the volume strain evolution is observed, as the time-dependent deformation rate increases by 40-80% (Figure 5.13). While increasing pore pressure generally accompanies expansion, in case of our experiments conducted under the constant hydrostatic load and undrained boundary conditions, the specimens are compacting during the pore pressure buildup. Time-dependent deformation of a rock saturated by acidic fluid is a complex process where pore-scale processes including mineral dissolution, subcritical crack growth, and stress corrosion contribute to the observed acceleration of material compaction caused by CO₂ treatment.

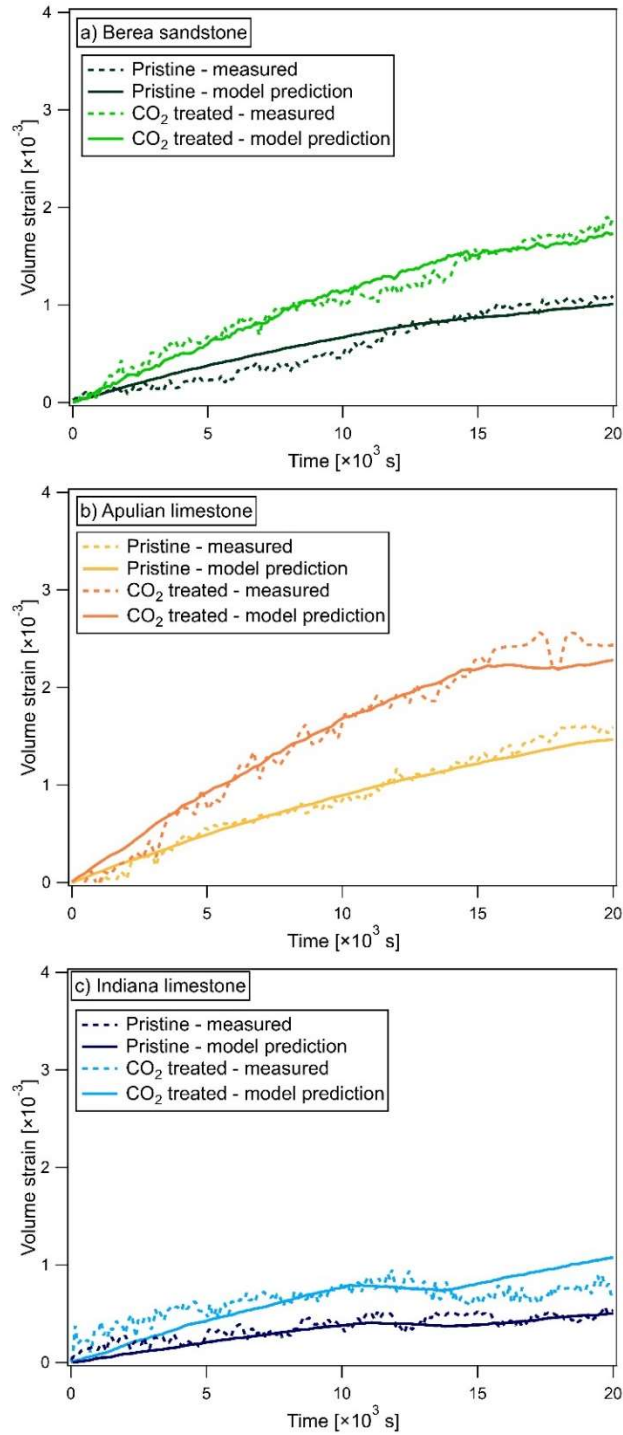


Figure 5.13. Comparison of volume strain as a function of time (directly measured and predicted by the model) for pristine and CO₂ treated a) Berea sandstone, b) Apulian limestone, and c) Indiana limestone.

5.6.4. Limitations of the model

For this study, Biot poroelastic model combined with Maxwell's viscoelasticity is selected to describe the short- and long-term response of water-saturated reservoir rock to CO₂ injection. Compared to other constitutive models, linear poroviscoelasticity relationships provide a significant advantage in terms of simplifying the time-dependent behavior by introducing only one parameter – bulk viscosity η_ϕ (Huang and Ghassemi, 2017; Simakin and Ghassemi, 2005). This parameter is directly related to the rate of time-dependent deformation and can be measured via straightforward experiments (Makhnenko and Podladchikov, 2018). Nevertheless, the potential limitations of the model should be discussed.

Firstly, the performed measurements of bulk viscosity are based on the condition where the specimens are taken out of the equilibrium state. This quasi-dynamic loading effect (on the order of minutes) can be extended to influence the consequential pore pressure buildup and affect the measurements. Longer term observations (lasting from days to weeks) could possibly indicate larger values of η_ϕ , hence smaller deformation rates. At the same time, in two-month long experiment performed on clayey material, continuous pressure buildup has been observed. Even though the pressure change was decreasing with time – it still corresponded to approximately the same value of the bulk viscosity (Makhnenko and Podladchikov, 2018). The experimental procedure used in this study implies that the time-dependent response may affect the measurements of poroelastic parameters. Particularly, as the experiments show that the viscous response of reservoir rock is promoted due to CO₂ treatment, this effect is expected to be important for accurately assessing the bulk modulus and Skempton's B values for the treated rock. Thus, their measurements are conducted for 1 minute for all specimens to minimize this inaccuracy.

Secondly, the important contribution of the shear stress to time-dependent deformation of geomaterials is not considered here, while only hydrostatic loading is applied. Subsurface materials at depths typical for CO₂ storage (1-3 km) can be subjected to relatively large (tens of MPa) deviatoric in-situ stresses (van der Meer, 1992). Many experimental studies were conducted to explore the effect of shear stress on the time-dependent behavior of subsurface formations, as deviatoric loading was applied at different boundary conditions (Hangx et al., 2010; Li and Xia, 2000; Sone and Zoback, 2014; Yang et al., 1999). While it is oftentimes reported that the deviatoric stress promoted the time-dependent response (Brantut et al., 2013), the conclusions for water-saturated rock are not consistent (Rohmer et al., 2016). Our preliminary experiments with the application of the shear stress also indicate that if deformation of the rock is kept within the viscoelastic range – the effect could be the opposite: the higher is the deviatoric loading – the smaller is the time-dependent deformation, and the higher is the bulk viscosity. A further accurate study with a range of applied mean and shear stresses and pore pressures is needed to address this phenomenon.

Another critical concern is related to the scale effect on the bulk viscosity. We report the laboratory measurements of the bulk viscosity to be on the order of 10¹⁵-10¹⁶ Pa·s. Typical viscosity of solid Earth materials is estimated to be in the range of 10¹⁹-10²² Pa·s (Karato, 2010), but smaller values are expected for porous and fluid-saturated rock (Renshaw and Schulson, 2017). This discrepancy can be related to the measuring method where extra pore pressure cannot dissipate in sealed rock specimens, but at reservoir scale, the formations could be much more permeable and significantly more compressible due to the presence of fractures, lessening the compaction effect on time-dependent deformation. Hence, one should use the reported values carefully trying to predict long-term reservoir response to CO₂ injection. At the same time, the

presented results are important for indicating the time-dependent deformation of fluid-saturated rock and changes in its behavior caused by CO₂ treatment.

5.7. Conclusions

This study investigates the effect of CO₂ treatment on reservoir rock's short- and long-term behavior. Berea sandstone, Apulian limestone, and Indiana limestone are selected as representative materials for silica-rich and calcite-rich formations. CO₂ treatment at elevated pressure conditions is conducted using the core flooding device, and the poromechanical properties (short- and long-term) are measured in hydrostatic and triaxial compression experiments performed on fluid-saturated rock specimens before and after the treatment. For the jacketed (dry) andunjacketed (solid) response, the CO₂ treatment leads to a decrease of corresponding bulk moduli of limestones by approximately 20%. For Berea sandstone, the jacketed bulk modulus decreased by around 15%, while no change is observed for the unjacketed bulk modulus. The time-dependent behavior measurements show that the CO₂ treatment decreases the bulk viscosity by 50-60% for all materials, promoting more rapid viscous deformation. It appears that the permeability of all tested rock increases due to CO₂ treatment by 10-15%, while the power-law porosity-permeability relationship remains unchanged.

We argue that the explanation of the observed phenomena can be provided via observing the microstructural changes in the tested rock. Surface electron microscopy and mercury intrusion porosimetry indicate dissolution happening in both limestones and increasing the fraction of micron scale pores. At the same time, the porosity of the sandstone does not change while its drained and apparently undrained responses become more compliant. We believe that it can be explained by the promotion of stress-corrosion cracking in the material that becomes saturated

with acidic mixture of water and CO₂. While the adopted poroviscoelastic model has a number of limitations, this approach highlights the importance of properly characterizing the short-term and time-dependent behavior of reservoir rock in CO₂ storage projects.

References

- Abousleiman, Y., Cheng, A.D., Jiang, C., Roegiers, J.C. (1996) Poroviscoelastic analysis of borehole and cylinder problems. *Acta Mech.* 119(1): 199-219.
- Akono, A.T., Dávila, G., Druhan, J., Shi, Z., Jessen, K., Tsotsis, T. (2020) Influence of geochemical reactions on the creep behavior of Mt. Simon sandstone. *Int J Greenh Gas Con.* 103: 103183.
- Alam, M.M., Hjuler, M.L., Foged, H., Lykke, I., Christensen, H.F., Fabricius, I.L. (2014) Petrophysical and rock-mechanics effects of CO₂ injection for enhanced oil recovery: experimental study on chalk from south Arne field, North Sea. *J Petrol Sci Eng.* 122: 468-487.
- Aman, M., Espinoza, D.N., Ilgen, A.G., Major, J.R., Eichhubl, P., Dewers, T.A. (2018) CO₂-induced chemo-mechanical alteration in reservoir rocks assessed via batch reaction experiments and scratch testing. *Greenh Gases.* 8(1): 133-49.
- Atkinson, B.K., Meredith, P.G. (1987) The theory of subcritical crack growth with applications to minerals and rocks. In B. K. Atkinson (Ed.), *Fracture mechanics of rock* (pp. 111–116). London: Academic Press.
- Bachu, S. (2003) Screening and ranking of sedimentary basins for sequestration of CO₂ in geological media in response to climate change. *Environ Geol.* 44: 277–289.

- Bachu, S. (2004) Sequestration of CO₂ in geological media: criteria and approach for site selection in response to climate change. *Energy Convers Manage.* 41(9): 953–970.
- Bachu, S. (2008) CO₂ storage in geological media: Role, means, status and barriers to deployment. *Prog Energy Combust Sci.* 34(2): 254-273.
- Baisch, S., Vörös, R. (2010) Reservoir induced seismicity: Where, when, why and how strong. In *Proceedings World Geothermal Congress.* 3160.
- Bao, T., Burghardt, J., Gupta, V., Edelman, E., McPherson, B., White, M. (2021) Experimental workflow to estimate model parameters for evaluating long term viscoelastic response of CO₂ storage caprocks. *Int J Rock Mech Min.* 146: 104796.
- Bemer, E., Lombard, J.M. (2010) From injectivity to integrity studies of CO₂ geological storage: chemical alteration effects on carbonates petrophysical and geomechanical properties. *Oil Gas Sci Technol.* 65: 445-459.
- Bernabé, Y., Brace, W.F., Evans, B. (1982) Permeability, porosity and pore geometry of hot-pressed calcite. *Mech Mater.* 1(3): 173-183.
- Bernabé, Y., Fryer, D.T., Shively, R.M. (1994) Experimental observations of the elastic and inelastic behaviour of porous sandstones. *Geophys J Int.* 117(2): 403-418.
- Bernabé, Y., Mok, U., Evans, B. (2003) Permeability–porosity relationships in rocks subjected to various evolution processes. *Pure Appl Geophys.* 160: 937–960.
- Biot, M.A. (1941) General theory of three-dimensional consolidation, *J Appl Phys.* 12: 155-164.
- Biot, M.A. (1956) Theory of deformation of a porous viscoelastic anisotropic solid. *J Appl Phys.* 27(5): 459-467.
- Biot, M.A., Willis, D.G. (1957) The elastic coefficients of the theory of consolidation. *J Appl Mech.* 24: 594-601.

- Biot, M.A. (1962) Mechanics of deformation and acoustic propagation in porous media. *J Appl Phys.* 33(4): 1482-1498.
- Bishop, A.W. (1976) The influence of an undrained change in stress on the pore pressure in porous media of low compressibility. *Géotechnique.* 26: 371-375.
- Bonamy, D., Prades, S., Rountree, C.L., Ponson, L., Dalmas, D., Bouchaud, E., Ravi-Chandar, K., Guillot, C. (2006) Nanoscale damage during fracture in silica glass. *Int J Fracture.* 140(1): 3-14.
- Bourbié, T., Coussy, O., Zinszner, B. (1987) *Acoustics of Porous Media*: Gulf. Houston, TX 56.
- Brantut, N., Heap, M.J., Meredith, P.G., Baud, P. (2013) Time-dependent cracking and brittle creep in crustal rocks: A review. *J Struct Geol.* 52: 17-43.
- Chadwick, R.A., Williams, G.A., Williams, J.D., Noy, D.J. (2012) Measuring pressure performance of a large saline aquifer during industrial-scale CO₂ injection: The Utsira Sand, Norwegian North Sea. *Int J Greenh Gas Con.* 10: 374-388.
- Choens II, R.C., Ilgen, A.G., Espinoza, D.N., Aman, M., Wilson, J., Dewers, T.A. (2020) Impacts on mechanical strength of chemical reactions induced by hydrous supercritical CO₂ in Boise Sandstone. *Int J Greenh Gas Con.* 95: 102982.
- Cleary, M.P. (1978) Elastic and dynamic regimes of fluid-impregnated solids with diverse micro-structure. *Int J Solids Struct.* 14: 795-819.
- Collins, H.C. (1979) *The Mississippian and Pennsylvanian (Carboniferous) systems in the United States.* Ohio, United States Geological Survey.

- David, C., Wong, T-F., Zhu, W., Zhang, J. (1994) Laboratory measurement of compaction-induced permeability change in porous rock: implications for the generation and maintenance of pore pressure excess in the crust. *Pure Appl Geophys.* 143: 425-456.
- Detournay, E., Cheng, A.H.-D. (1993) Fundamentals of poroelasticity. In: Fairhurst C, editor. *Comprehensive rock engineering, Vol. II.* Oxford: Pergamon 113–171.
- Doyen, P.M. (1988) Permeability, conductivity, and pore geometry of sandstone. *J Geophys Res.* 93: 7729–7740.
- Eisner, L., Williams-Stroud, S., Hill, A., Duncan, P., Thornton, M. (2010) Beyond the dots in the box: Microseismicity-constrained fracture models for reservoir simulation. *The Leading Edge.* 29(3): 326-333.
- Ellsworth, W.L. (2013) Injection-induced earthquakes. *Science.* 341(6142): 1225942.
- Espinoza, D.N., Jung, H., Major, J.R., Sun, Z., Ramos, M.J., Eichhubl, P., Balhoff, M.T., Choens, R.C., Dewers, T.A. (2018) CO₂ charged brines changed rock strength and stiffness at Crystal Geyser, Utah: Implications for leaking subsurface CO₂ storage reservoirs. *Int J Greenh Gas Con.* 73: 16-28.
- Foroutan, M., Ghazanfari, E., Amirlatifi, A. (2021) Variation of failure properties, creep response and ultrasonic velocities of sandstone upon injecting CO₂-enriched brine. *Geomech Geophys Geo-Energy and Geo-Resources.* 7(2): 1-30.
- Ghasemi, M.F., Bayuk, I.O. (2020) Bounds for pore space parameters of petroelastic models of carbonate rocks. *Izv Phys Solid Earth.* 56(2): 207-224.

- Goertz-Allmann, B.P., Gibbons, S.J., Oye, V., Bauer, R., Will, R. (2017) Characterization of induced seismicity patterns derived from internal structure in event clusters. *J Geophys Res: Solid Earth*. 122(5): 3875-3894.
- Gor, Y.G., Elliot, T.R., Prévost, J.H. (2013) Effects of thermal stresses on caprock integrity during CO₂ storage. *Int J Greenh Gas Con*. 12: 300-309.
- Grgic, D. (2011) Influence of CO₂ on the long-term chemomechanical behavior of an oolitic limestone. *J Geophys Res: Solid Earth*. 116: B07201.
- Griggs, D. (1939) Creep of rocks. *J Geol*. 47(3): 225-251.
- Grombacher, D., Vanorio, T., Ebert, Y. (2012) Time-lapse acoustic, transport, and NMR measurements to characterize microstructural changes of carbonate rocks during injection of CO₂-rich water. *Geophysics*. 77(3): WA169-WA179.
- Gueguen, Y., Dienes, J. (1989) Transport properties of rocks from statistics and percolation. *Math Geol*. 21: 1-13.
- Hangx, S.J., Spiers, C.J., Peach, C.J. (2010) Creep of simulated reservoir sands and coupled chemical-mechanical effects of CO₂ injection. *J Geophys Res: Solid Earth*. 115(B9).
- Hangx, S., Van der Linden, A., Marceils, F., Bauer, A. (2013) The effect of CO₂ on the mechanical properties of the Captain Sandstone: geological storage of CO₂ at the Goldeneye field (UK). *Int J Greenh Gas Con*. 19: 609-619.
- Hansen, O., Gilding, D., Nazarian, B., Osdal, B., Ringrose, P., Kristoffersen, J.B., Eiken, O., Hansen, H. (2013) Snøhvit: The history of injecting and storing 1 Mt CO₂ in the fluvial Tubåen Fm. *Energy Proced*. 37: 3565-3573.

- Hsieh, P.A., Bredehoeft, J.D. (1981) A reservoir analysis of the Denver earthquakes: A case of induced seismicity. *J Geophys Res: Solid Earth*. 86(B2): 903-920.
- Huang, J., Ghassemi, A. (2017) Poro-viscoelastic modeling of production from shale gas reservoir: An adaptive dual permeability model. *J Petrol Sci Eng*. 158: 336-350.
- IEA (International Energy Agency) (2004) *Prospects for CO₂ Capture and Storage*. IEA/OECD, Paris 249.
- IPCC (Intergovernmental Panel on Climate Change) (2005) *IPCC special report on carbon dioxide capture and storage*. In: Metz B, Davidson O, de Coninck HC, Loos M, Mayer LA (eds) Cambridge University Press, Cambridge 442.
- Johnson, J.W., Nitao, J.J., Morris, J.P., Benson, S. (2005) Reactive transport modeling of cap-rock integrity during natural and engineered CO₂ storage. *Carbon dioxide capture for storage in deep geologic formations 2*: 787.
- Jung, H., Espinoza, D.N. (2017) Chemo-Poromechanical Properties of Tuscaloosa Sandstone: Implications on CO₂ Geological Storage. In: 51st US Rock Mech/Geomech Symposium.
- Karato, S. (2010) Rheology of the Earth's mantle: A historical review. *Gondwana Res*. 18(1): 17-45.
- Kim, K., Vilarrasa, V., Makhnenko, R.Y. (2018) CO₂ injection effect on geomechanical and flow properties of calcite-rich reservoirs, *Fluids*. 3(3): 66.
- Kim, K., Makhnenko, R.Y. (2020) Coupling Between Poromechanical Behavior and Fluid Flow in Tight Rock. *Transport Porous Med*. 135(2): 487-512.
- Kim, K., Makhnenko, R.Y. (2021) Changes in rock matrix compressibility during deep CO₂ storage. *Greenh Gases Sci Tech*. 0: 0-20.

- Kirkpatrick, S. (1973) Percolation and conduction. *Rev Mod Phys.* 45(4): 574.
- Le Guen, Y., Renard, F., Hellmann, R., Brosse, E., Collombet, M., Tisserand, D. (2007) Enhanced deformation of limestone and sandstone in the presence of high fluids. *J Geophys Res: Solid Earth.* 112(B5).
- Lei, X., Xue, Z. (2009) Ultrasonic velocity and attenuation during CO₂ injection into water-saturated porous sandstone: measurements using difference seismic tomography. *Phys Earth Planet In.* 176: 224-234.
- Li, Y., Xia, C. (2000) Time-dependent tests on intact rocks in uniaxial compression. *Int J Rock Mech Min Sci.* 37(3): 467-475.
- Liteanu, E., Spiers, C.J. (2009) Influence of pore fluid salt content on compaction creep of calcite aggregates in the presence of supercritical CO₂. *Chem Geol.* 265(1-2): 134-147.
- Liteanu, E., Niemeijer, A., Spiers, C.J., Peach, C.J., De Bresser, J.H. (2012). The effect of CO₂ on creep of wet calcite aggregates. *J Geophys Res: Solid Earth.* 117(B3).
- Liteanu, E., Spiers, C.J., De Bresser, J.H.P. (2013) The influence of water and supercritical CO₂ on the failure behavior of chalk. *Tectonophysics.* 599: 157-169.
- Lowe, J., Johnson, T.C. (1960) Use of back pressure to increase degree of saturation of triaxial test specimens. In: *Proceedings of the Research Conference on Shear Strength of Cohesive Soils*, Boulder, Colorado, ASCE. 819-836.
- Luquot, L., Gouze, P. (2009) Experimental determination of porosity and permeability changes induced by injection of CO₂ into carbonate rocks. *Chem Geol.* 265: 148-159.
- Makhnenko, R.Y., Labuz, J.F. (2016) Elastic and inelastic deformation of fluid-saturated rock. *Phil T R Soc A.* 374: 20150422.

- Makhnenko, R.Y., Podladchikov, Y.Y. (2018) Experimental poroviscoelasticity of common sedimentary rocks. *J Geophys Res: Solid Earth*. 123(9): 7586-7603.
- Makhnenko, R.Y., Ge, C., Labuz, J.F. (2020) Localization of deformation in fluid-saturated sandstone. *Int J Rock Mech Min Sci*. 134: 104455.
- Marbler, H., Erickson, K.P., Schmidt, M., Lempp, C., Pöllmann, H. (2013) Geomechanical and geochemical effects on sandstones caused by the reaction with supercritical CO₂: an experimental approach to in situ conditions in deep geological reservoirs. *Environ Earth Sci*. 69(6): 1981-1998.
- Mangane, P.O., Gouze, P., Luquot, L. (2013) Permeability impairment of a limestone reservoir triggered by heterogeneous dissolution and particles migration during CO₂-rich injection. *Geophys Res Lett*. 40(17):4614-9.
- Mavko, G., Nur, A. (1997) The effect of a percolation threshold in the Kozeny-Carman relation. *Geophysics*. 62: 1480-1482.
- Michalske, T.A., Freiman, S.W. (1982) A molecular interpretation of stress corrosion in silica. *Nature*. 295(5849): 511-2.
- Oikawa, Y., Takehara, T., Tosha, T. (2008) Effect of CO₂ injection on mechanical properties of Berea sandstone. In: *Proceedings of 42nd US Rock Mechanics Symposium and 2nd US-Canada Rock Mechanics Symposium, San Francisco, CA*.
- Orr Jr, F.M. (2004) Storage of carbon dioxide in geologic formations. *J Pet Technol*. 56(9): 90-97.

- Paterson, L., Lu, M., Connell, L., Ennis-King, J.P. (2008) Numerical modeling of pressure and temperature profiles including phase transitions in carbon dioxide wells. In: SPE Annual Technical Conference and Exhibition, Society of Petroleum Engineers.
- Patton, J.B., Carr, D.D. (1982) The Salem limestone in the Indiana building-stone district. Indiana Geological Survey.
- Rayward-Smith, W.J., Woods, A.W. (2011) Some implications of cold CO₂ injection into deep saline aquifers. *Geophys Res Lett.* 38(6).
- Renard, F., Gundersen, E., Hellmann, R., Collombet, M., Le Guen, Y. (2005) Numerical modeling of the effect of carbon dioxide sequestration on the rate of pressure solution creep in limestone: Preliminary results. *Oil Gas Sci Technol.* 60(2): 381-399.
- Renshaw, C.E., Schulson, E.M. (2017) Strength-limiting mechanisms in high-confinement brittle-like failure: Adiabatic transformational faulting. *J Geophys Res: Solid Earth.* 122: 1088-1106.
- Rimmelé, G., Barlet-Gouédard, V., Renard, F. (2010) Evolution of the petrophysical and mineralogical properties of two reservoir rocks under thermodynamic conditions relevant for CO₂ geological storage at 3 km depth. *Oil Gas Sci Technol.* 65(4): 565-580.
- Rohmer, J., Pluymakers, A., Renard, F. (2016) Mechano-chemical interactions in sedimentary rocks in the context of CO₂ storage: weak acid, weak effects? *Earth Sci Rev.* 157: 86-110.
- Rutqvist, J. (2012) The geomechanics of CO₂ storage in deep sedimentary formations. *Geotech Geol Eng.* 30(3): 525–551.

- Schimmel, M.T., Hangx, S.J., Spiers, C.J. (2019) Impact of chemical environment on compaction creep of quartz sand and possible geomechanical applications. *J Geophys Res: Solid Earth*. 124(6): 5584-5606.
- Shi, Z., Sun, L., Haljasmaa, I., Harbert, W., Sanguinito, S., Tkach, M., Goodman, A., Tsotsis, T., Jessen, K. (2019) Impact of Brine/CO₂ exposure on the transport and mechanical properties of the Mt Simon sandstone. *J Petro Sci Eng*. 177: 295-305.
- Simakin, A., Ghassemi, A. (2005) Modelling deformation of partially melted rock using a poroviscoelastic rheology with dynamic power law viscosity. *Tectonophysics*. 397(3-4): 195-209.
- Sjöberg, E.L., Rickard, D.T. (1984) Temperature dependence of calcite dissolution kinetics between 1 and 62 C at pH 2.7 to 8.4 in aqueous solutions. *Geochim Cosmochim Acta*. 48(3): 485-493.
- Smith, V., Jaques, P. (2016) Illinois Basin–Decatur Project pre-injection microseismic analysis. *Int J Greenh Gas Control*. 54: 362-377.
- Sone, H., Zoback, M.D. (2014) Time-dependent deformation of shale gas reservoir rocks and its long-term effect on the in situ state of stress. *Int J Rock Mech Min*. 69: 120-132.
- Tang, S.B., Yu, C.Y., Heap, M.J., Chen, P.Z., Ren, Y.G. (2018) The influence of water saturation on the short- and long-Term mechanical behavior of Red Sandstone. *Rock Mech Rock Eng*. 51: 2669–2687.
- Terzaghi, K. (1923) Die berechnung der durchlassigkeitszifer des tones aus dem verlauf der hydrodynamischen spannungsercheinungen. *Sitzungsber Akad Wissen Wien Math Naturwiss Kl Abt Iia* 132: 105-124.

- Tarokh, A., Makhnenko, R.Y. (2019) Remarks on the solid and bulk responses of fluid-filled porous rock. *Geophysics*. 84(4): WA83-WA95.
- Tarokh, A., Makhnenko, R.Y., Kim, K., Zhu, X., Popovics, J.S., Segvic, B., Sweet, D.E. (2020) Influence of CO₂ injection on the poromechanical response of Berea sandstone. *Int J Greenh Gas Control*. 95: 102959.
- U.S. Department of Energy (2010) Carbon Sequestration Atlas of the United States and Canada, 3rd ed., US DOE, Washington, D.C.
- Van der Meer, L.G.H. (1992) Investigations regarding the storage of carbon dioxide in aquifers in the Netherlands. *Energ Convers Manage*. 33(5-8): 611-618.
- Vandamme, M., Ulm, F.J. (2009) Nanogranular origin of concrete creep. *P Natl A Sci*. 106(26): 10552-10557.
- Vanorio, T., Nur, A., Ebert, Y. (2011) Rock physics analysis and time-lapse rock imaging of geochemical effects due to the injection of CO₂ into reservoir rocks. *Geophysics*. 76(5): O23-O33.
- Vasco, D.W., Rucci, A., Ferretti, A., Novali, F., Bissell, R.C., Ringrose, P.S., Mathieson, A.S., Wright, I.W. (2010) Satellite-based measurements of surface deformation reveal fluid flow associated with the geological storage of carbon dioxide. *Geophys Res Lett*. 37(3).
- Verdon, J.P., Kendall, J.M., White, D.J., Angus, D.A. (2011) Linking microseismic event observations with geomechanical models to minimise the risks of storing CO₂ in geological formations. *Earth Planet Sci Lett*. 305(1-2): 143-152.

- Verdon, J.P., Kendall, J.M., Stork, A.L., Chadwick, R.A., White, D.J., Bissell, R.C. (2013) Comparison of geomechanical deformation induced by megatonne-scale CO₂ storage at Sleipner, Weyburn, and In Salah. *P Natl A Sci.* 110(30): E2762-2771.
- Vialle, S., Vanorio, T. (2011) Laboratory measurements of elastic properties of carbonate rocks during injection of reactive CO₂-saturated water. *Geophys Res Lett.* 38: 1-5.
- Vilarrasa, V., Silva, O., Carrera, J., Olivella, S. (2013) Liquid CO₂ injection for geological storage in deep saline aquifers. *Int J Greenh Gas Control.* 14: 84-96.
- Vilarrasa, V., Makhnenko, R.Y., Rutqvist, J. (2019) Field and laboratory studies of geomechanical response to the injection of CO₂. In: *Science of Carbon Storage in Deep Saline Formations.* Elsevier, Oxford, UK. 209-236.
- Wang, H.F. (2000) *Theory of linear poroelasticity with applications to geomechanics and hydrogeology.* Princeton, NJ: Princeton University Press.
- Will, R., El-Kaseeh, G., Jaques, P., Carney, M., Greenberg, S., Finley, R. (2016) Microseismic data acquisition, processing, and event characterization at the Illinois Basin–Decatur Project. *Int J Greenh Gas Control.* 54: 404-420.
- Williams-Stroud, S., Bauer, R., Leetaru, H., Oye, V., Stanek, F., Greenberg, S., Langet, N. (2020) Analysis of Microseismicity and Reactivated Fault Size to Assess the Potential for Felt Events by CO₂ Injection in the Illinois Basin. *B Seismol Soc A.* 110(5): 2188-2204.
- Yang, C., Daemen, J.J., Yin, J.H. (1999) Experimental investigation of creep behavior of salt rock. *Int J Rock Mech Min Sci.* 36(2): 233-242.
- Yarushina, V.M., Podladchikov, Y.Y. (2015) (De)compaction of porous viscoelastoplastic media: model formulation. *J Geophys Res: Solid Earth.* 120(6): 4146-4170.

- Zhang, Q., Le Roy, R., Vandamme, M., Zuber, B. (2014) Long-term creep properties of cementitious materials: Comparing microindentation testing with macroscopic uniaxial compressive testing. *Cement Concrete Res.* 58: 89-98.
- Zhang, W., Li, Y., Xu, T., Cheng, H., Zheng, Y., Xiong, P. (2009) Long-term variations of CO₂ trapped in different mechanisms in deep saline formations: A case study of the Songliao Basin, China. *Int J Greenh Gas Control.* 3(2): 161-180.
- Zhang, X., Spiers, C.J. (2005a) Compaction of granular calcite by pressure solution at room temperature and effects of pore fluid chemistry. *Int J Rock Mech Min Sci.* 42(7-8): 950-60.
- Zhang, X., Spiers, C.J. (2005b) Effects of phosphate ions on inter-granular pressure solution in calcite: an experimental study, *Geochim Cosmochim Acta.* 69(24): 5681-5691.

CHAPTER 6: DEVELOPMENT OF HYDRO-MECHANICAL-CHEMICAL MODEL DESCRIBING RESERVOIR ROCK RESPONSE DURING CO₂ STORAGE

6.1 Introduction

Multiphysical processes occurring during CO₂ injection affect the mechanical stress, pore pressure, temperature, and chemistry of the adjacent reservoir formation. Moreover, as each physical aspect can mutually influence the others and vice versa, this complex phenomenon requires a fully coupled analysis rather than just discrete observations of the chemical effect on the rock properties. Thus, hydro-mechanical-chemical (HMC) coupling studies have been suggested for isothermal conditions, where the change in the material's chemistry is considered with the rock porosity and compressibility (Jun et al., 2013; Emmanuel et al., 2015; Gajo et al., 2015). Furthermore, additional investigations have been conducted to establish an HMC coupled constitutive model, as most studies adopted the chemical reaction to the governing equations (Hu et al., 2012; Ciantia and Hueckel, 2013; Malvoisin et al., 2015; Omlin, 2016; Schmalholz et al., 2020; Cai et al., 2021; Kadeethum et al., 2021). However, as the existing studies introduce conceptual parameters such as the free energy of the solid and fluid phase, the application of these models is very limited because they require the knowledge of fluid and solid properties (e.g., concentration of cations) that are difficult to be measured directly (Hu et al., 2012). Therefore, a number of studies have been limited to pure numerical simulations (Hurter et al., 2007; Malvoisin et al., 2015; Omlin, 2016; Cai et al., 2019; Fan et al., 2019; Tao et al., 2019).

Another important question that arises is how the poromechanical behavior of reservoir formations may be affected by the duration of CO₂ treatment. Al-Ameri et al. (2016) conducted CO₂ treatment experiments to observe the effect of CO₂ storage time on the mechanical properties of Pink Desert limestone. The Young's modulus, Poisson's ratio, and uniaxial

compression strength gradually decreased with time, as the results agree with other experiments (Vialle and Vanorio, 2011; Marbler et al., 2013). Shi et al. (2019) also compared the porosity change between one and two weeks of CO₂ aging time, reporting the increase in the porosity with the treatment duration. In general, most of the experimental studies are limited to reporting the change in the poromechanical properties with the duration of CO₂ treatment.

Here we attempt to extend the preceding findings by adopting a coupled HMC model based on previously introduced poroviscoelastic relationships with the aim of including the effect of the duration of CO₂ treatment on the poroviscoelastic properties of the reservoir rock. We introduce a novel experimental setup that allows measurements of the poroviscoelastic properties at high-pressure conditions with CO₂ treatment. Since sandstone and limestone are the two most common reservoir rock types, Berea sandstone and Indiana limestone are selected as the representative materials. The short- and long-term poroviscoelastic properties of reservoir rocks are measured for the pristine, 1-week, 2-weeks- 3-weeks CO₂ treated samples. Accordingly, the effect of the CO₂ treatment time on the poromechanical properties is included in the HMC model via the variation of rock's porosity. For further validation of the suggested model, the effect of CO₂ treatment on another monomineralic rock – Apulian limestone, is adopted for its poroviscoelastic properties.

6.2 Hydro- Mechanical-Chemical Model

Chemo-poro-visco-elastic model that considers a porous and viscous system with volatilization reaction is selected to describe the hydro-mechanical-chemical coupling (Malvoisin et al., 2015; Omlin, 2016). The stress state of the porous media can be addressed by the Terzaghi effective mean stress $P' = P - p^f$, where P is the total mean stress, and p^f is the pore fluid pressure. Subsequently, for the two dynamic variables P and p^f , the corresponding kinematic parameters: volume strain ε and increment of fluid content ζ are introduced (Biot, 1941; 1957). Biot's poroelastic model is then extended to include Maxwell's viscoelasticity at a macroscopic scale (Yarushina and Podladchikov, 2015; Makhnenko and Podladchikov, 2018). In addition to the poroviscoelastic response, the chemical effect of CO₂ injection is included by adopting the volatilization reaction to the system (Malvoisin et al., 2015; Omlin, 2016). As the reactive model considers the exchange of volatile species between the fluid and solid, chemo-poro-visco-elastic constitutive relationships are introduced, where equations for the increment of fluid content (fluid mass conservation) and porosity are extended for the chemical reaction.

$$\frac{d\varepsilon}{dt} = \frac{d}{dt} \left(\frac{P}{K} - \left(\frac{1}{K} - \frac{1}{K_s'} \right) p^f \right) + \frac{P - p^f}{(1 - \phi) \eta_\phi} \quad (6.1)$$

$$\frac{d\zeta}{dt} = \left(\frac{1}{K} - \frac{1}{K_s'} \right) \left(\frac{dP}{dt} - \frac{1}{B} \frac{dp^f}{dt} \right) + \frac{P - p^f}{(1 - \phi) \eta_\phi} + R_{X\zeta} \frac{\partial X}{\partial t} \quad (6.2)$$

$$\frac{d\phi}{dt} = \left(\frac{1 - \phi}{K} - \frac{1}{K_s'} \right) \frac{dP'}{dt} - \phi \left(\frac{1}{K_s'} - \frac{1}{K_s''} \right) \frac{\partial p^f}{\partial t} + \frac{P - p^f}{\eta_\phi} - R_X \frac{\partial X}{\partial t} \quad (6.3)$$

The time derivatives of ε , ζ , and ϕ are expressed in terms of a number of parameters (K , K_s' , B , η_ϕ , $R_{X\zeta}$, R_X , and X) that need to be thoroughly understood.

As all the poroviscoelastic properties are introduced in Chapters 4 and 5, here we focus on the parameters describing the chemical coupling. Assuming that the only chemical reaction during CO₂ treatment is dissolution/precipitation, $R_{X\zeta}$ and R_X – the reaction parameters, and X – the mass fraction of the volatile species are introduced. The reaction parameter can be defined for the increment of fluid content $R_{X\zeta}$ and porosity R_X , as the ratio of the change in the increment of fluid content and porosity to the alteration of the volatile species, respectively (Omlin, 2016). As the CO₂ treatment is conducted under the undrained condition for this study, parameter X refers to the mass fraction of the bicarbonate dissolved in the pore fluid, that would react with calcite. It is to be noted that the chemical reaction only affects the mass conservation for the increment of fluid content ζ and porosity ϕ (equations 6.2 and 6.3), while it is not directly reflected in the volume deformation (equation 6.1).

Previous studies reported that the pressure controlling kinetics of the chemical reaction is the fluid pressure under isothermal conditions, and the initial mass fraction of the volatile species X can be expressed as a function of fluid pressure p^f : $X = X_0 + dX/dp^f \cdot p^f$ (Holdaway and Goodge, 1990; Llana-Fúnez S et al., 2012). This expression can be simplified to a linear relationship by applying Henry's law, where $p^f_1/p^f_2 = X_1/X_2$. As the CO₂ treatment is conducted at an identical stress state ($P = 11.5$ MPa, $p^f = 7$ MPa), this initial mass fraction of bicarbonate is constant for this study as 0.06, as the dissolution of CO₂ is a function of pressure and temperature (Perry and Chilton, 1973; Ma et al., 2017; Kim and Makhnenko, 2021). As the chemical kinetics towards equilibrium generally follows the non-linear fitting curve, $X(t) = a \cdot e^{-bt} + c$ is utilized to estimate X , where a , b , and c are fitting parameters and time t is an independent parameter (Eatough et al., 1974; Connors, 1987). It is to be noted that the chemical reactions affect the fluid mass

conservation equation and the porosity, but does not directly impact the bulk deformation, as the chemical part is not included in equation 6.1.

6.3. Experimental Methods

The modified hydrostatic compression system is developed and utilized to accurately measure the poroviscoelastic properties of reservoir rock. The system consists of a hydrostatic compression cell and two pore fluid vessels, where water or CO₂ can be filled. Pristine specimens are prepared in prismatic shapes with a diameter of 23×23×30 mm and sets of resistive strain gages are installed on the surfaces to monitor the deformation in three perpendicular directions. Then, the specimen and the pore platens are thoroughly covered with polyurethane to prevent the confining oil from intruding into the pores while connected to the pore fluid cylinder. The confining and pore pressures are controlled by syringe pumps (Teledyne ISCO, USA) with 25.8 MPa capacity, and external pressure transducers (Omega, USA) are installed to allow independent pore pressure measurements at undrained conditions. To resume isothermal conditions, the modified hydrostatic compression system is located inside a temperature-controlled air bath (Figure 6.1).

The drained andunjacketed bulk moduli are measured after reaching full water saturation. In the drained test, the initial pore pressure is set as 1.5 MPa, and the confining pressure is increased from 1.6 MPa to 25.6 MPa in 2 MPa steps. Although the pore pressure is relatively low, full saturation is assured by applying the by the back saturation method. The unjacketed bulk modulus is measured by increasing both the confining and pore pressure in 2 MPa steps up to $P = 25.6$ MPa and $p^f = 25.5$ MPa. The bulk deformation is monitored during the loading-unloading procedure, and the experiment is duplicated to confirm repeatability. As the modified hydrostatic

compression system allows determining the bulk moduli after achieving full saturation, the measurements are compared with those under zero initial pore pressure conditions (dry). The presence of pore water is found not to affect the bulk and solid deformation of the tested reservoir rock, similar to the findings of Tarokh and Makhnenko (2019). The modified hydrostatic compression system is also capable of determining the time-dependent behavior at high-pressure conditions. After reaching full saturation, the pore pressure buildup is monitored for more than six hours under the undrained condition after measuring the Skempton's B coefficient. As the time-dependent deformation may affect the measured B values, those are reported from the short-term loading experiments that last just for one minute.

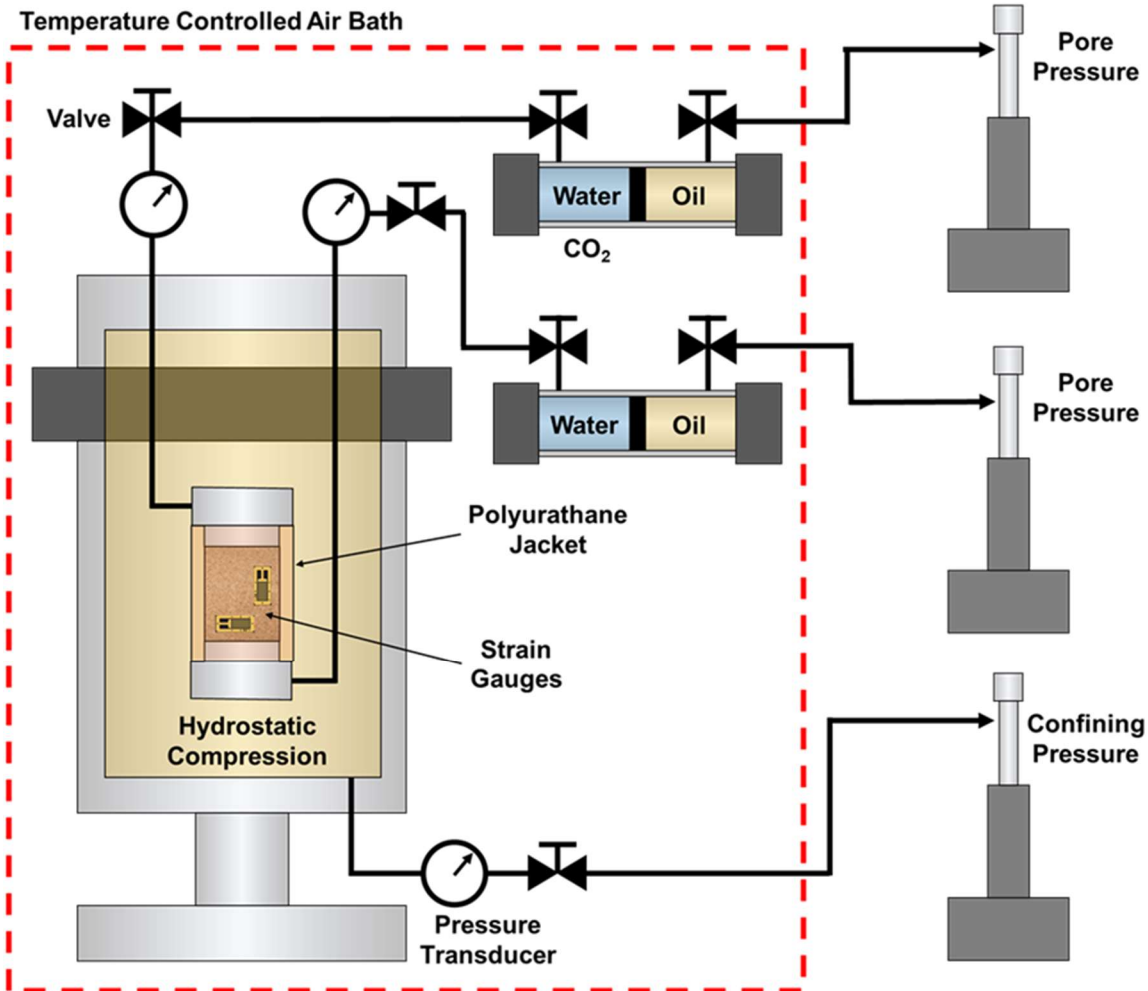


Figure 6.1. Sketch of the modified hydrostatic compression system where the deformation of prismatic rock specimens can be monitored with sets of strain gages. The confining pressure controller is used to apply all-around oil pressure up to 53 MPa and two pore pressure controllers allow injection of water and CO₂ at pressures up to 37.5 MPa.

As the main objective of this study is to characterize the effect of CO₂ treatment time on the poroviscoelastic properties, the experiments are conducted in the following procedure. First, a pristine specimen is installed in the device, and the backpressure saturation technique is utilized to reach full saturation indicated by no change in the Skempton's *B* coefficient values at fixed effective mean stress (Makhnenko and Labuz, 2016). Then, the drained and unjacketed bulk moduli are measured by changing the confining and pore pressures. Consequently, the time-

dependent response is assessed by monitoring the pore pressure buildup under the undrained condition.

After accurately measuring one set of the poroviscoelastic properties, the CO₂ injection is conducted to monitor the chemical effect of CO₂ treatment. With the downstream valve closed (undrained), liquid CO₂ at 7 MPa is injected from the upstream side, while the effective mean stress is maintained at 4.5 MPa. After injecting 4-5 mL of CO₂, the volume of the upstream CO₂ pump remains constant, indicating an equilibrium state of the dissolution of CO₂ into water. Then, the upstream valve is closed, and the CO₂ treatment is conducted for 7 days under the undrained condition, as the time-dependent deformation is recorded. The pore fluid pressure is also monitored during this process to ensure that it does not decrease.

After a week of CO₂ treatment, the CO₂ in the pores is flushed sufficiently with deionized water at low pressure (~1 MPa) conditions. The release of pressure and relatively large pore sizes of the tested materials allow to assume that CO₂ is completely removed from the pores after flushing them with water exceeding the pore volume by more than one hundred times. Consequently, the measurements of the poroviscoelastic properties after 1-week of CO₂ treatment are repeated after reaching full saturation with deionized water, and the above procedures are repeated after the second and third weeks of the treatment. Although the time-dependent response can be monitored during the CO₂ treatment process, the poroviscoelastic properties (K , K_s' , B , and η_ϕ) for each period (1, 2, and 3 weeks) are measured after completely removing CO₂ from the pores (at full water saturation) to exclude the chemical impact that presence of CO₂ may have on them during the experimental procedure.

For Berea sandstone and Indiana limestone, the poroviscoelastic properties are measured at the pristine, 1 week, 2 weeks, and 3 weeks treatment state. An additional material is considered for

the model validation – Apulian limestone is tested in the core flooding device and its poroviscoelastic properties are reported only for the pristine and 3-days CO₂ treated specimens.

6.4 Results

The poroviscoelastic properties of Berea sandstone and Indiana limestone are measured after 0-weeks, 1-week, 2-weeks, and 3-weeks CO₂ treatment. The results of stress-dependent Skempton's B coefficient measurements are presented in Figure 6.2. For Berea sandstone, it is observed that no significant change in this parameter happens during the three weeks of treatment, as the measured values all fall within the error range of ± 0.01 . In contrast, the results for Indiana limestone show that the Skempton's B coefficient increases with the duration of CO₂ treatment at all effective mean stresses. Also, it can be seen that changes in the B values are more pronounced at the initial stage (from pristine to 1-week), as the effect becomes less pronounced with time.

The compressibilities of the reservoir formations under drained andunjacketed conditions are also measured, while increasing the CO₂ treatment time (Figure 6.3). For all experiments, the initial pore pressure is set as 1.5 MPa, as the confining and pore pressures are controlled to determine the bulk moduli. The results for Berea sandstone show that for both drained and unjacketed bulk moduli, no effect of CO₂ treatment is observed with time, as all the bulk responses are reported to be almost identical. The drained bulk modulus changes at the initial stage of loading due to crack closure in the sandstone and becomes constant and equal to 12.1 GPa after exceeding $P' = 15$ MPa. The unjacketed bulk modulus is determined to be stress-independent and equal to 30.2 GPa. On the other hand, both drained and unjacketed moduli of Indiana limestone are significantly affected by the CO₂ treatment. For the drained response, K is

measured to be 30.2 GPa when the response of the pristine limestone becomes linear at $P' > 15$ MPa. However, as CO₂ treatment duration increases, the K values in the linear region decrease gradually to 23.0 GPa. Theunjacketed bulk modulus shows a similar trend decreasing from 64.5 GPa for pristine Indiana limestone down to 53.0 GPa after three weeks of CO₂ treatment. It is to be noted that the trends that the bulk moduli K and K_s' are following are similar to the changes in the B values, where the effect of CO₂ treatment on the parameters is more pronounced at the initial stage but reduces with time.

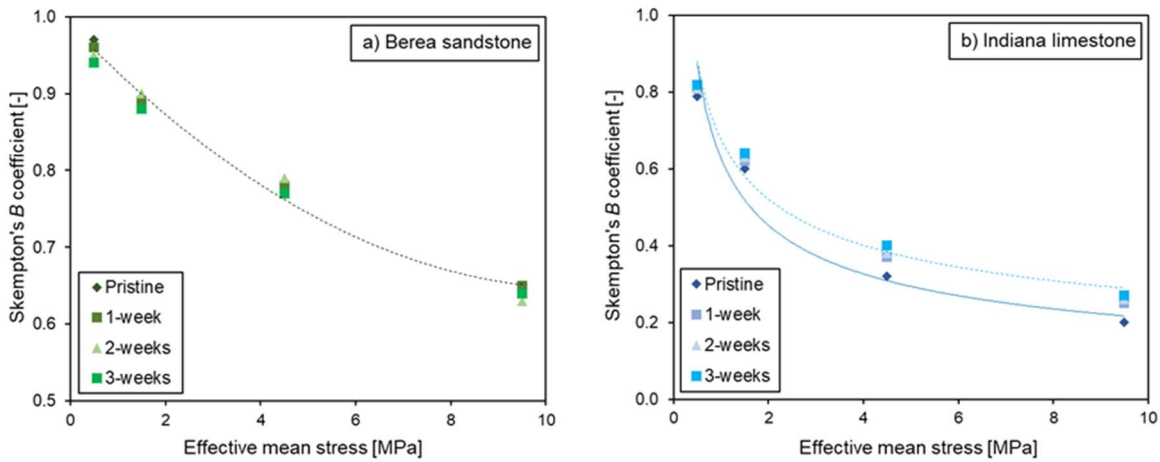


Figure 6.2. Change in the stress-dependent Skempton's B coefficient of a) Berea sandstone and b) Indiana limestone due to CO₂ treatment for up to 3 weeks.

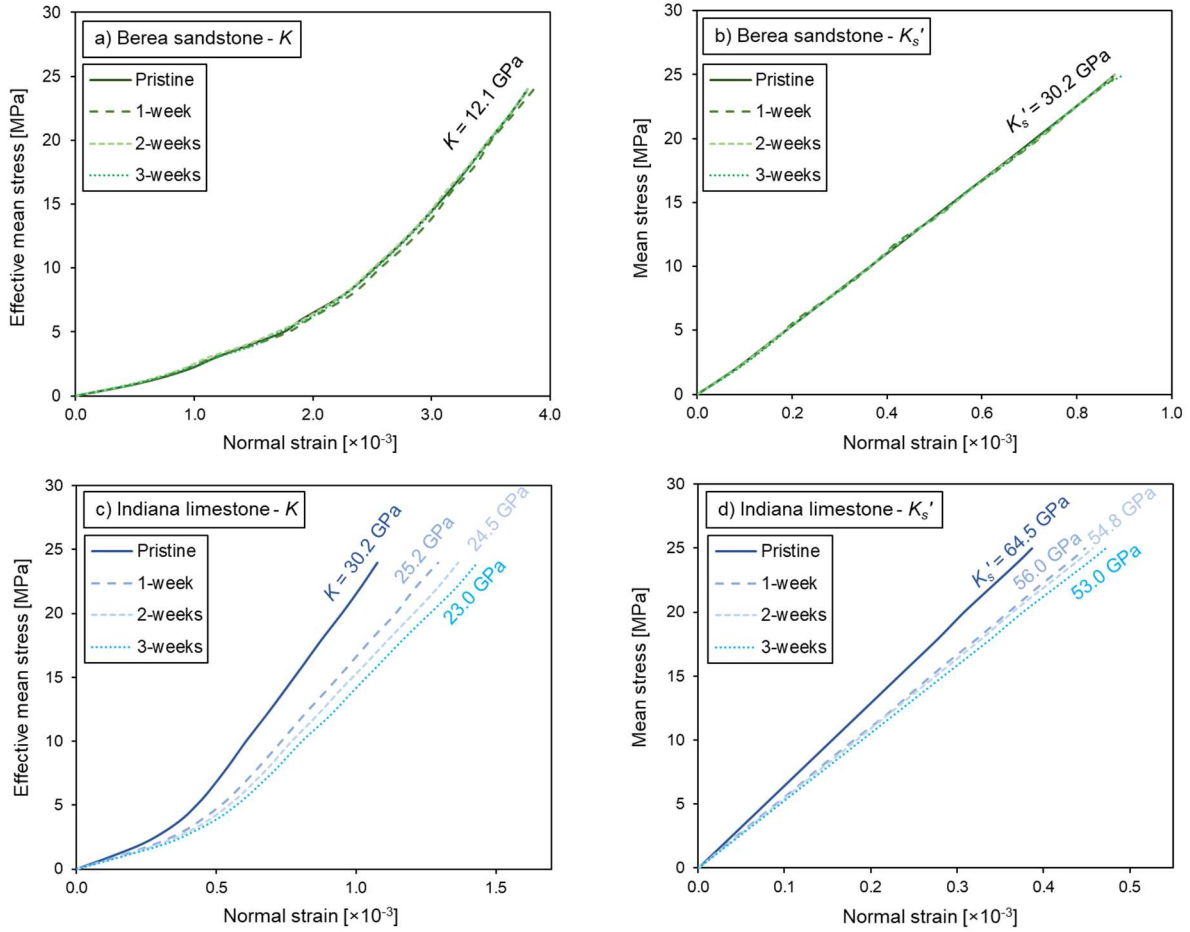


Figure 6.3. Change in (a) drained (K) and (b)unjacketed (K_s') bulk moduli of Berea sandstone and (c) drained and (d)unjacketed bulk moduli of Indiana limestone due to CO_2 treatment for up to 3 weeks.

The pore pressure buildup for Berea sandstone and Indiana limestone at $P' = 4.5$ MPa are monitored after different CO_2 treatment durations (Figure 6.4). For pristine Berea sandstone, the bulk viscosity η_ϕ is calculated as 1.6×10^{16} Pa·s. With the increasing CO_2 treatment time, the η_ϕ values decrease gradually, reaching 5.3×10^{15} Pa·s after 3-weeks of treatment. Similarly, the bulk viscosity values for Indiana limestone also reduce from 5.2×10^{16} Pa·s to 8.5×10^{15} Pa·s, implying that the length of CO_2 treatment plays the role in changes of the time-dependent response. The changes in poroviscoelastic response for both rocks are most pronounced between the pristine and 1-week specimens. Interestingly, it is to be noted that the long-term time-dependent

deformations of both rocks are promoted by the CO₂ treatment, while it is previously presented that the short-term poroelastic properties of sandstone do not change during the same treatment procedure. An explanation for this phenomenon is provided in Chapter 5, where the mechanisms for the chemical effect of CO₂ treatment on the limestones (chemical dissolution) and sandstones (subcritical crack growth and stress corrosion) are proposed to be significantly different.

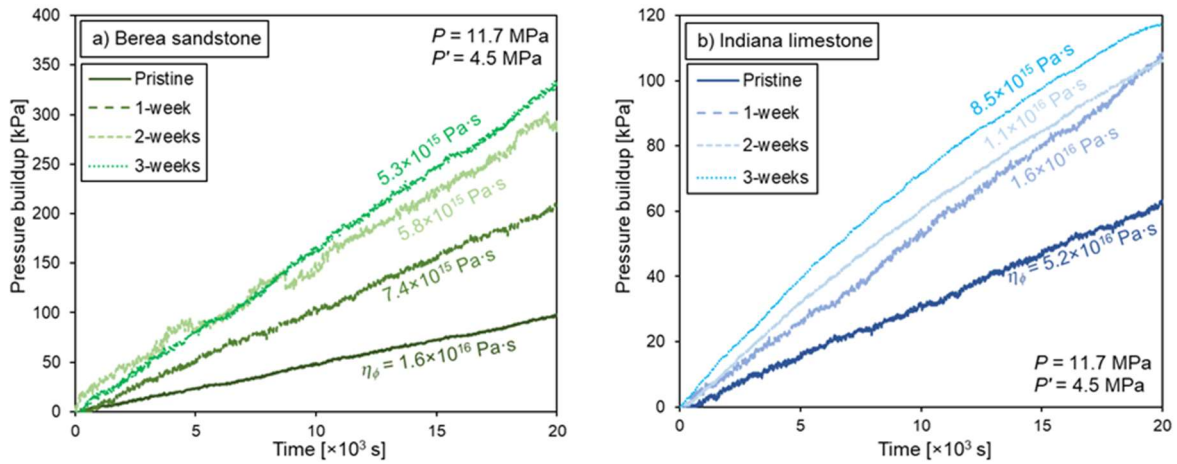


Figure 6.4. Changes in the pressure buildup of a) Berea sandstone and b) Indiana limestone due to CO₂ treatment for up to 3 weeks. The bulk viscosity η_ϕ is reported for each experiment.

The relative errors for all reported properties are determined from the relationships provided in Chapter 2. The relative error in porosity determination is 3%, the Skempton's B coefficient - 5%, drained and unjacketed bulk moduli - 3%, and it is 10% for the bulk viscosity due to the errors of all the parameters that contribute to its calculation.

6.5 Discussion

The poroviscoelastic properties of Berea sandstone and Indiana limestone are accurately measured every week during a three week-long CO₂ treatment process. The stress-dependent poroelastic properties B , K , and K_s' are reported. No effect of CO₂ treatment is observed on Berea sandstone, while for Indiana limestone, measurements indicate that the compressibility increases due to chemical dissolution. Similarly, the stress-dependent bulk viscosity is measured at three different stress states, as η_ϕ has been reported to be affected by both p^f and P , showing a tendency to decrease with the increasing p^f/P ratio (Makhnenko and Podladchikov, 2018).

The bulk viscosity values determined from the modified hydrostatic compression system are combined with those reported in Chapter 5 and presented in Figure 6.5. For both Berea sandstone and Indiana limestone, the decrease in the bulk viscosity values is observed at different p^f/P ratios, with the strongest effect happening during the first week of CO₂ injection. In addition, the stress-dependent bulk viscosity values for the pristine and CO₂ treated Apulian limestone are adopted from Chapter 5, where it is shown that the CO₂ treatment also promotes time-dependent deformation.

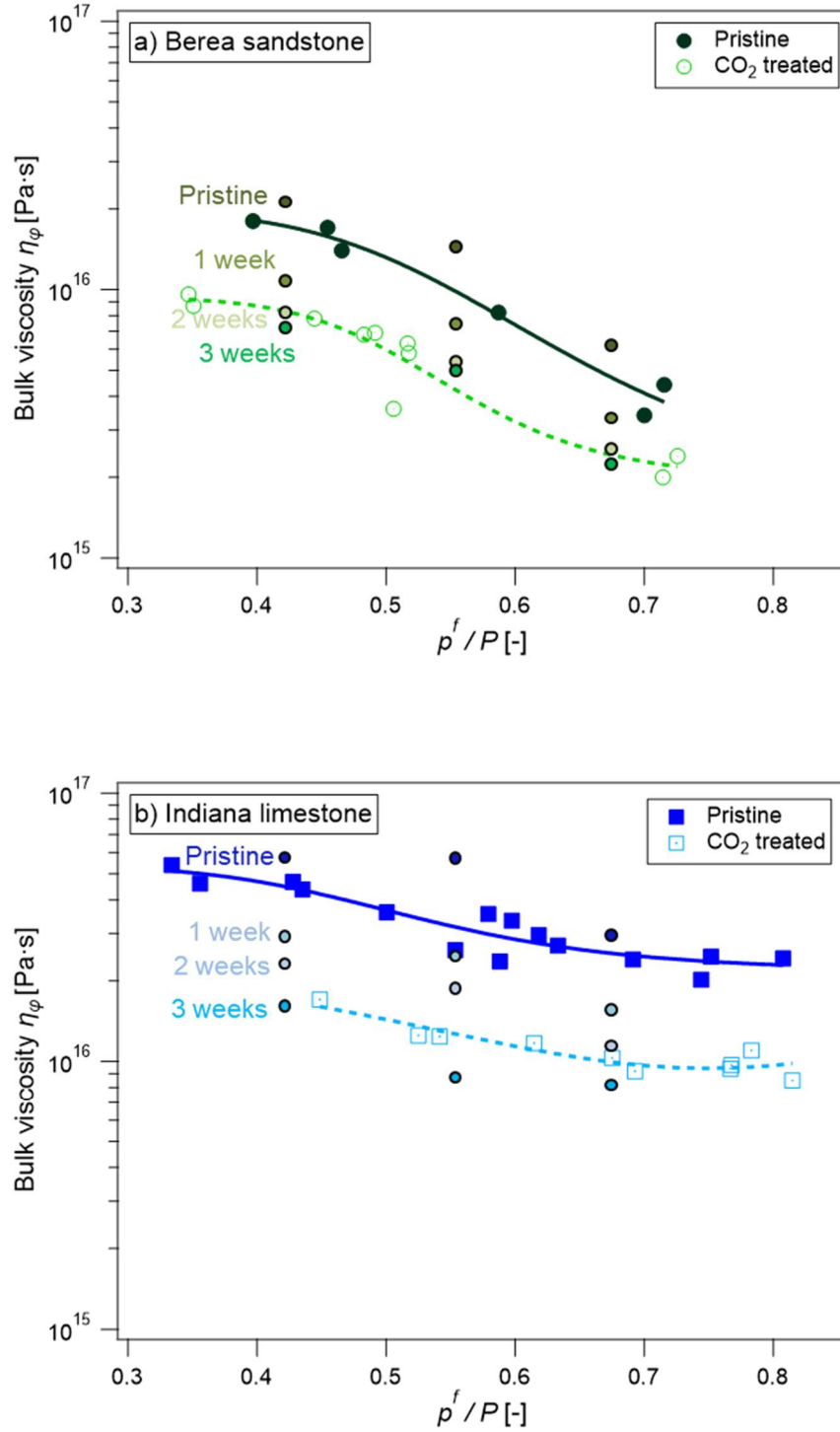


Figure 6.5. Stress-dependent bulk viscosity η_ϕ measured for pristine, 1-week, 2-weeks, and 3-weeks treated a) Berea sandstone and b) Indiana limestone.

The chemo-poro-visco-elastic model is then adopted to determine the chemical reaction parameters, as the poroviscoelastic properties are expressed as a function of time. Since the experimental setup for this study cannot accurately measure the changes in porosity during the CO₂ treatment, the porosity values of the pristine and 3-week treated samples are taken from the previous study conducted with the same materials (Kim and Makhnenko, 2021).

As no effect of CO₂ treatment is observed for Berea sandstone and its time-dependent porosity variation is negligible, the results for the HMC coupled model are expected to be identical to that of the HM model. Moreover, as the HMC coupling assumes calcite dissolution as the only chemical reaction, it implies these constitutive equations can only be adopted for the rock that contains a significant amount of calcite, i.e., the limestones and shale. Verification of this method is conducted for Apulian limestone, where the poroviscoelastic properties (K , K_s' , B , and η_ϕ) for pristine and 3-days CO₂ treated specimens are adopted from the measurements reported in Chapter 5. It is to be noted that both Indiana and Apulian limestones are mostly composed of calcite (>97%), and it can be assumed that calcite dissolution is the dominant chemical reaction. The poroviscoelastic properties are introduced in Table 6.1. Assumptions are made for the chemical reaction rate for calcite dissolution, where they are identical for both Apulian and Indiana limestone. Presuming that the porosity variation follows the non-linear curve with the same degradation exponent for calcite dissolution ($b = 0.07$), its change during three weeks of CO₂ treatment can be estimated. Then, the contribution of the chemical dissolution to the porosity change can be calculated by comparing the HM coupling (neglecting the chemical part in equation 6.3) and HMC coupling (Figure 6.6).

Results for all materials show that the porosity decreases with time in the HM model due to compaction during the time-dependent deformation. The chemical reaction is the most

pronounced on Apulian limestone, as the porosity change is more significant. The chemical parameters R_X and X can be determined from equation 6.3 (Figure 6.7). A single relationship for mass fraction of the volatile species X is assumed for both limestones, where the slope dX/dt gradually reduces, implying that the chemical reaction rate decreases. Also, by assuming the initial mass solubility is linearly related to the fluid pressure, the expression for X as a function of t (in hours) and p^f (in MPa) can be provided

$$X(t, p^f)_{Indiana} = 0.008 \cdot p^f \cdot e^{-0.07 \cdot t} \quad (6.4)$$

As parameter R_X explains how much porosity has altered due to changes in mass fraction of the volatile species X , the results reveal that the dissolution effect is larger for Apulian limestone than for Indiana limestone. This indicates that R_X is more than merely a ratio of the porosity change to the mass solubility change, as it also provides information on the rate of the dissolution of porosity. Furthermore, since R_X increases with dissolution during the treatment, it can be related to the changes in specific surface area S and porosity ϕ (Vanorio et al., 2011). The specific surface area can be obtained from the mercury intrusion porosimetry measurements. It is reported to increase from 0.9 to 1.6 m²/g, 0.4 to 0.6 m²/g, for Apulian and Indiana limestones, respectively. Also, the significant difference in the porosity of the two materials implies that the specific surface area for Apulian limestone is much larger, meaning more surface is in contact with the carbonate acid for dissolution. Further detailed analysis is required to quantitatively relate R_X to the specific surface area. Thus, understanding the dissolution effect on the porosity of limestones involves a coupled analysis regarding the fluid pressure, mass solubility, and potentially the reactive surface area.

Although previous studies present that the time-dependent deformation with the chemical effect matches the poroviscoelastic model, this study emphasizes that the chemo-poro-visco-elastic

constitutive model needs to be adopted for the variation in porosity during CO₂ treatment, since the chemical dissolution of the pore volume itself is mainly responsible for the porosity change.

The chemical effect of CO₂ treatment on the behavior of limestone can be estimated from poromechanical measurements during the treatment procedure and needs to be included in the constitutive model for the change in porosity. However, some limitations may exist regarding the verification and calibration of the model, which require further discussion. As the chemical aspect in the constitutive model is attributed to only calcite dissolution, the application of the model is limited to the materials where Ca is the only reactive element with acidic CO₂-water mixture. At the same time, previous studies reported that other minerals, such as K-feldspar, albite, and anorthite, can also be chemically affected by CO₂ treatment (Law and Bachu, 1996; Gunter et al., 1993; 1997). While it is acceptable for this study where the tested limestones are mostly composed of calcite, it becomes important for other materials containing a considerable portion of the other minerals that would simultaneously affect the concentration of the volatile species. Moreover, characterization of $R_{X\zeta}$ in equation 6.2 needs to be conducted, as the chemical effect on the increment of fluid content is also important regarding the mass conservation. Regarding these issues, the limitations may be overcome by directly measuring the ion concentration of the pore fluid, utilizing the ion-selective microelectrodes, where calibration and modification of this model can be conducted for extensive types of rock. Although there are difficulties in measuring the chemical responses at high-pressure conditions, this would also verify the constitutive equation for the fluid mass conservation law (equation 6.2).

Lastly, limitation regarding the boundary condition for CO₂ treatment needs to be discussed. As the undrained CO₂ treatment procedure utilized in this study is not often the case in field applications, the provided findings may be only applicable to the areas where dissolved CO₂

exists. Future work may be proposed by extending this research to the open system, where continuous flow is introduced.

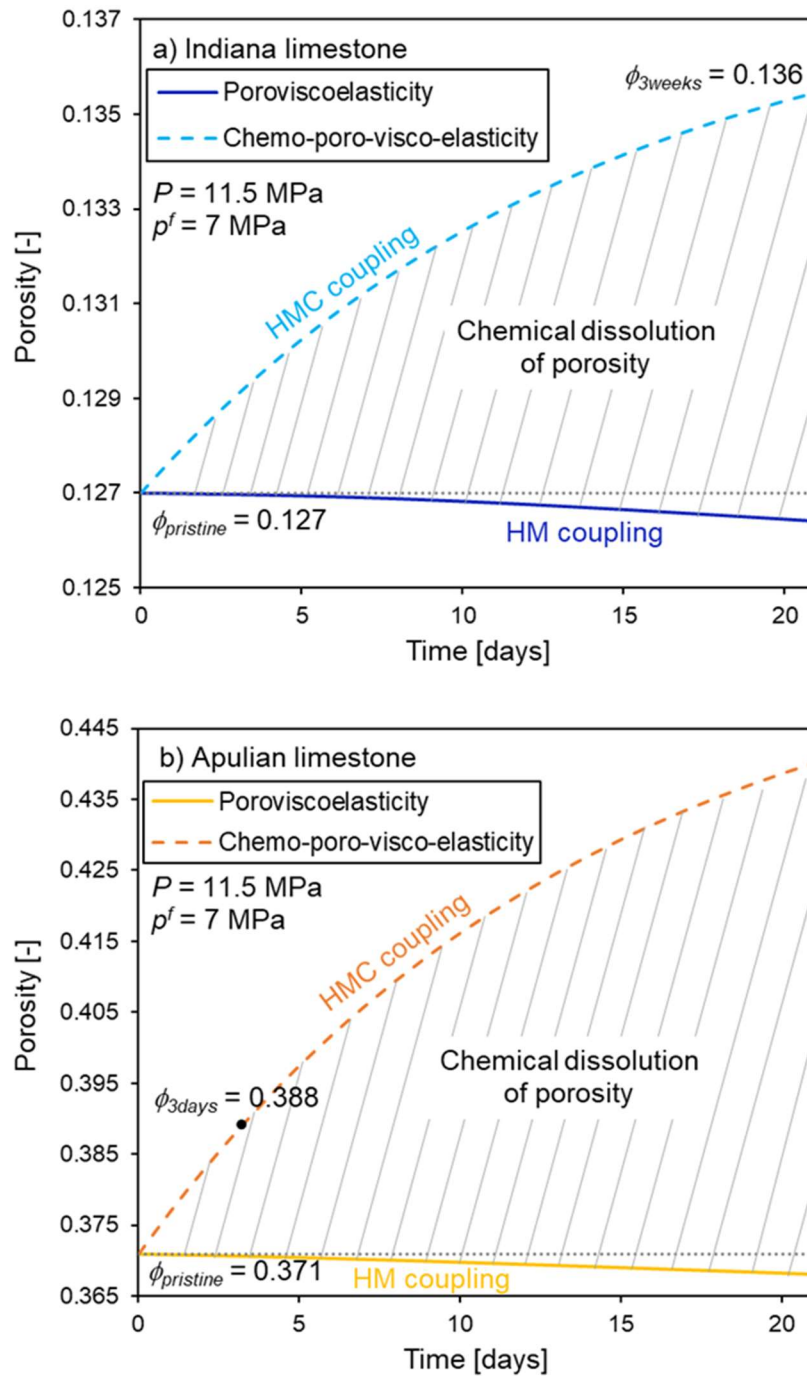


Figure 6.6. Comparison of the HM and HMC coupling model predictions of the porosity variation for a) Indiana limestone and b) Apulian limestone.

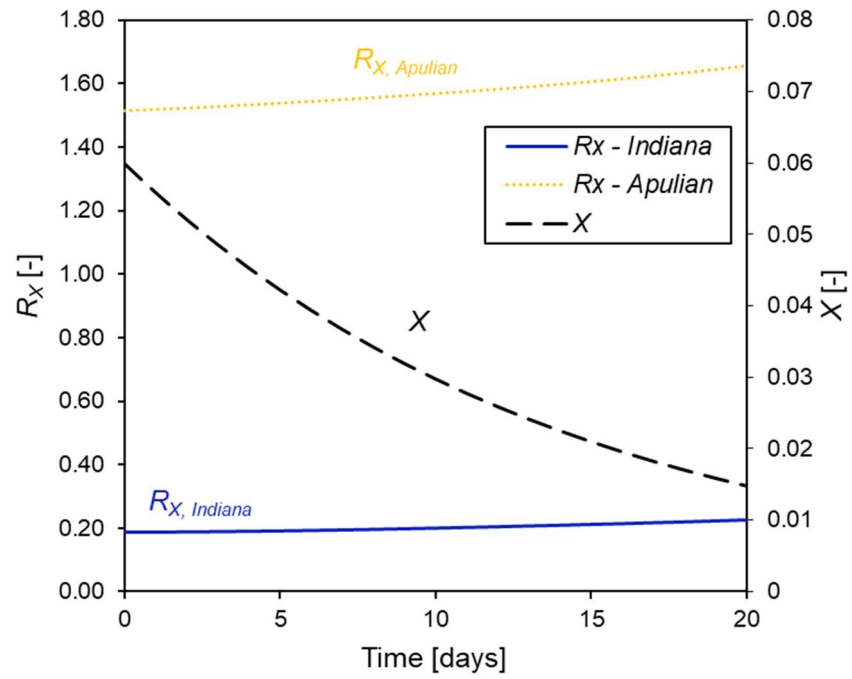


Figure 6.7. Results for $R_{X,Indiana}$, $R_{X,Apulian}$, and X with time, calculated from HMC model.

Table 6.1. Summary of the measured values of the chemo-poro-visco-elastic properties (B , K , K_s' , η_ϕ , and R_X) and specific surface area S at different CO₂ treatment times (reported at $P' = 4.5$ MPa). The values of R_X provided for Apulian limestone are based on the calculations that adopt the measurements reported in Chapter 5.

	Berea sandstone				Indiana limestone				Apulian limestone	
Weeks of treatment	0	1	2	3	0	1	2	3	0	3
ϕ [%]	21.9				12.7	-	-	13.6	37.1	38.8
B [-]	0.78				0.32	0.36	0.38	0.40	0.48	0.55
K [GPa]	5.0				23.5	18.2	17.7	17.1	4.5	4.2
K_s' [GPa]	30.2				64.5	56.0	54.8	53.0	42.7	34.2
η_ϕ [$\times 10^{15}$ Pa·s]	16	7.4	5.8	5.3	52	16	11	8.5	4.9	2.4
R_X [-]	0				0.18	0.19	0.21	0.23	1.51	1.66
S [m ² /g]	0.6				0.4	-	-	0.6	0.9	1.6
Calcite content [%]	0				97	-		97	98	98

6.6 Conclusions

The multiphysical processes that occur during CO₂ injection are investigated by adopting a coupled hydro-mechanical-chemical model. Short- and long-term responses of Berea sandstone and Indiana limestone to CO₂ treatment are explored. The modified hydrostatic compression system allows characterization of the poroviscoelastic properties at high-pressure conditions, while also allowing controlled CO₂ injection process. The injection is performed for three weeks, while the Skempton's B coefficient, drained bulk modulus, unjacketed bulk modulus, and the bulk viscosity are measured after every week of treatment. While no significant effect is observed for Berea sandstone, the observations of dissolution in Indiana limestone allow evaluation of its chemo-poro-visco-elastic properties. The hydro-mechanical-chemical coupling

model is validated by introducing another calcite-rich rock – Apulian limestone. Comparison of the hydro-mechanical response to the hydro-mechanical-chemical model prediction for porosity changes during CO₂ storage indicates the complexity of the process, where the time-dependent compaction is competing with calcite dissolution. Moreover, the chemical parameter R_X is assumed to depend on the specific surface and porosity, which requires further investigation. Indeed, the chemical effect of CO₂ injection into water-saturated limestones should be included in the constitutive equations to properly evaluate the changes in their response during long-term storage operations.

References

- Alam, M.M., Hjuler, M.L., Foged, H., Lykke, I., Christensen, H.F., Fabricius, I.L. (2014) Petrophysical and rock-mechanics effects of CO₂ injection for enhanced oil recovery: experimental study on chalk from south Arne field, North Sea. *J Petrol Sci Eng.* 122: 468-487.
- Al-Ameri, W.A., Abdurraheem, A., Mahmoud, M. (2016) Long-term effects of CO₂ sequestration on rock mechanical properties. *J Energy Resour Technol.* 138(1).
- Bachu, S. (2008) CO₂ storage in geological media: role, means, status and barriers to deployment. *Prog Ener Combust Sci.* 34(2): 254–273.
- Bemer, E., Lombard, J.M. (2010) From injectivity to integrity studies of CO₂ geological storage: chemical alteration effects on carbonates petrophysical and geomechanical properties. *Oil Gas Sci Technol.* 65: 445-459.
- Biot, M.A. (1941) General theory of three-dimensional consolidation. *J Appl Physics.* 12(2): 155-64.

- Biot, M.A., Willis, D.G. (1957) The elastic coefficients of the theory of consolidation. *J Appl Mech.* 24: 594-601.
- Cai, M., Su, Y., Elsworth, D., Li, L., Fan, L. (2021) Hydro-mechanical-chemical modeling of sub-nanopore capillary-confinement on CO₂-CCUS-EOR. *Energy.* 225: 120203.
- Ciantia, M.O., Hueckel, T. (2013) Weathering of submerged stressed calcarenites: chemo-mechanical coupling mechanisms. *Géotechnique.* 63(9): 768-85.
- Connors, K.A. (1987) *The measurement of molecular complex stability*, John Wiley & Sons, New York. 50-65.
- Eatough, D.J., Christensen, J.J., Izatt, R.M. (1974) *Experiments in thermometric titrimetry and titration calorimetry*. Utah, Brigham Young University Press.
- Emmanuel, S., Anovitz, L.M., Day-Stirrat, R.J. (2015) Effects of coupled chemo-mechanical processes on the evolution of pore-size distributions in geological media. *Rev Mineral Geochem.* 80(1): 45-60.
- Fan, C., Elsworth, D., Li, S., Zhou, L., Yang, Z., Song, Y. (2019) Thermo-hydro-mechanical-chemical couplings controlling CH₄ production and CO₂ sequestration in enhanced coalbed methane recovery. *Energy.* 173: 1054-77.
- Foroutan, M., Ghazanfari, E., Amirlatifi, A. (2021) Variation of failure properties, creep response and ultrasonic velocities of sandstone upon injecting CO₂-enriched brine. *Geomech Geophys Geo-Energy Geo-Resources.* 7(2): 1-30.
- Gajo, A., Cecinato, F., Hueckel, T. (2015) A micro-scale inspired chemo-mechanical model of bonded geomaterials. *Int J Rock Mech Min Sci.* 80: 425-38.
- Gunter, W.D., Perkins, E.H., McCann, T.J. (1993) Aquifer disposal of CO₂-rich gases: reaction design for added capacity. *Energy Convers Manag.* 34(9-11): 941-8.

- Gunter, W.D., Wiwehar, B., Perkins, E.H. (1997) Aquifer disposal of CO₂-rich greenhouse gases: extension of the time scale of experiment for CO₂-sequestering reactions by geochemical modelling. *Mineral Petrol.* 59(1): 121-40.
- Grombacher, D., Vanorio, T., Ebert, Y. (2012) Time-lapse acoustic, transport, and NMR measurements to characterize microstructural changes of carbonate rocks during injection of CO₂-rich water. *Geophysics.* 77(3): WA169-WA179.
- Hangx, S.J., Spiers, C.J., Peach, C.J. (2010) Creep of simulated reservoir sands and coupled chemical-mechanical effects of CO₂ injection. *J Geophys Res: Solid Earth.* 115(B9).
- Holdaway, M.J., Goodge, J.W. (1990) Rock pressures vs. fluid pressure as a controlling influence on mineral stability; an example from New Mexico. *Am Min.* 75(9-10): 1043-58.
- Hu, D., Zhou, H., Hu, Q., Shao, J., Feng, X., Xiao, H. (2012) A hydro-mechanical-chemical coupling model for geomaterial with both mechanical and chemical damages considered. *Acta Mech Solida Sin.* 25(4): 361-76.
- IPCC (Intergovernmental panel on climate change) (2007) *Climate change 2007: The physical science basis. Fourth assessment report, IPCC Secretariat, Geneva, Switzerland.*
- Jun, Y.S., Giammar, D.E., Werth, C.J. (2013) Impacts of geochemical reactions on geologic carbon sequestration. *Environ Sci Technol.* 47: 3-8.
- Jung, H., Espinoza, D.N. (2017) Chemo-Poromechanical Properties of Tuscaloosa Sandstone: Implications on CO₂ Geological Storage. In: 51st US Rock Mech/Geomech Symposium.
- Kadeethum, T., Lee, S., Ballarin, F., Choo, J., Nick, H.M. (2021) A locally conservative mixed finite element framework for coupled hydro-mechanical–chemical processes in heterogeneous porous media. *Comput Geosci.* 152: 104774.

- Kim, K., Vilarrasa, V., Makhnenko, R.Y. (2018) CO₂ injection effect on geomechanical and flow properties of calcite-rich reservoirs. *Fluids*. 3(3): 66.
- Kim, K., Makhnenko, R.Y. (2021) Changes in rock matrix compressibility during deep CO₂ storage. *Greenh Gases: Sci Technol*. 11(5): 954-73.
- Law, D.H.-S., Bachu, S. (1996) Hydrogeological and numerical analysis of CO₂ disposal in deep aquifers in the Alberta sedimentary basin. *Energy Convers Manag*. 37: 1167-1174.
- Le Guen, Y., Renard, F., Hellmann, R., Brosse, E., Collombet, M., Tisserand, D. (2007) Enhanced deformation of limestone and sandstone in the presence of high fluids. *J Geophys Res: Solid Earth*. 112(B5).
- Liteanu, E., Spiers, C.J. (2009) Influence of pore fluid salt content on compaction creep of calcite aggregates in the presence of supercritical CO₂. *Chem Geol*. 265(1-2): 134-147.
- Liteanu E, Niemeijer A, Spiers CJ, Peach CJ, De Bresser JH (2012). The effect of CO₂ on creep of wet calcite aggregates. *J Geophys Res: Solid Earth*. 117(B3).
- Llana-Fúnez, S., Wheeler, J., Faulkner, D.R. (2012) Metamorphic reaction rate controlled by fluid pressure not confining pressure: implications of dehydration experiments with gypsum. *Contrib Mineral Petrol*. 164(1): 69-79.
- Ma, X., Abe, Y., Kaneko, A., Fujimoto, S., Murakami, C. (2017) Study on dissolution process of liquid CO₂ into water under high pressure condition for CCS. *Energy Procedia*. 114: 5430-7.
- Makhnenko, R.Y., Labuz, J.F. (2016) Elastic and inelastic deformation of fluid-saturated rock. *Philos Trans A: Math Phys Eng Sci*. 374(2078): 20150422.
- Makhnenko, R.Y., Podladchikov, Y.Y. (2018) Experimental poroviscoelasticity of common sedimentary rocks. *J Geophys Res: Solid Earth*. 123(9): 7586-603.

- Malvoisin, B., Podladchikov, Y.Y., Vrijmoed, J.C. (2015) Coupling changes in densities and porosity to fluid pressure variations in reactive porous fluid flow: Local thermodynamic equilibrium. *Geochem Geophys.* 16(12): 4362-87.
- Marbler, H., Erickson, K.P., Schmidt, M., Lempp, C., Pöllmann, H. (2013) Geomechanical and geochemical effects on sandstones caused by the reaction with supercritical CO₂: an experimental approach to in situ conditions in deep geological reservoirs. *Environ Earth Sci.* 69(6): 1981-98.
- Omlin S. (2016) Development of massively parallel near peak performance solvers for three-dimensional geodynamic modelling (Doctoral dissertation, Université de Lausanne, Faculté des géosciences et de l'environnement).
- Perry, R.H., Chilton, C.H. (1973) *Chemical Engineer's Handbook*. McGraw-Hill Book Company, New York.
- Rohmer, J., Pluymakers, A., Renard, F. (2016) Mechano-chemical interactions in sedimentary rocks in the context of CO₂ storage: weak acid, weak effects? *Earth Sci Rev.* 157: 86-110.
- Schmalholz, S.M., Moulas, E., Plümper, O., Myasnikov, A.V., Podladchikov, Y.Y. (2020) 2D Hydro-Mechanical-Chemical Modeling of (De) hydration Reactions in Deforming Heterogeneous Rock: The Periclase-Brucite Model Reaction. *Geochem Geophys.* 21(11): e2020GC009351.
- Shi, Z., Sun, L., Haljasmaa, I., Harbert, W., Sanguinito, S., Tkach, M., Goodman, A., Tsotsis, T.T., Jessen, K. (2019) Impact of Brine/CO₂ exposure on the transport and mechanical properties of the Mt Simon sandstone. *J Pet Sci Eng.* 177: 295-305.

- Tao, J., Wu, Y., Elsworth, D., Li, P., Hao, Y. (2019) Coupled thermo-hydro-mechanical-chemical modeling of permeability evolution in a CO₂-circulated geothermal reservoir. *Geofluids*.
- Tarokh, A., Makhnenko, R.Y. (2019) Remarks on the solid and bulk responses of fluid-filled porous rock. *Geophysics*. 84(4): WA83-95.
- Tarokh, A., Makhnenko, R.Y., Kim, K., Zhu, X., Popovics, J.S., Segvic, B., Sweet, D.E. (2020) Influence of CO₂ injection on the poromechanical response of Berea sandstone. *Int J Greenh Gas Control*. 95: 102959.
- Vanorio, T., Nur, A., Ebert, Y. (2011) Rock physics analysis and time-lapse rock imaging of geochemical effects due to the injection of CO₂ into reservoir rocks. *Geophysics*. 76(5): O23-O33.
- Vialle, S., Vanorio, T. (2011) Laboratory measurements of elastic properties of carbonate rocks during injection of reactive CO₂-saturated water. *Geophys Res Lett*. 38(1).
- Vilarrasa, V., Makhnenko, R.Y., Rutqvist, J. (2019) Field and laboratory studies of geomechanical response to the injection of CO₂. In: *Science of Carbon Storage in Deep Saline Formations*. Elsevier, Oxford, UK. 209-236.
- Yarushina, V.M., Podladchikov, Y.Y. (2015) (De) compaction of porous viscoelastoplastic media: Model formulation. *J Geophys Res: Solid Earth*. 120(6): 4146-70.

CHAPTER 7: EFFECT OF CO₂ INJECTION ON THE MULTIPHASE FLOW RESPONSE OF RESERVOIR ROCK

A manuscript submitted to Transport in Porous Media

Kim, K., Kundzicz P.M., Makhnenko, R.Y.

Abstract

Geologic carbon storage (GCS) has recently been drawing attention as an effective and sustainable method to reduce CO₂ emission to the atmosphere. The injection of CO₂ is mainly conducted into brine-saturated reservoir formations, and assessment of the multiphase flow properties becomes essential to evaluate the injectivity and storage capacity for carbon storage. Characterization of the CO₂/water flow system requires comprehensive knowledge on the rock's relative permeability, capillary pressure, and wettability, that are coupled to each other. Moreover, the chemical reactions between the mineral grains and the acidic mixture of CO₂ and water may significantly affect the multiphase flow properties. In this study, a comprehensive experimental approach to characterize the effect of CO₂ treatment on the multiphase flow of CO₂ in water-saturated reservoir rock is presented. One silica-rich formation - Berea sandstone, and two calcite-rich formations - Apulian and Indiana limestones, are selected to represent the reservoir materials. We introduce a robust experimental method to measure the relative permeability and degree of saturation based on the changes in poroelastic response. The relative permeability curves are determined, as it is shown that the curvatures and maximum degree of CO₂ saturation change after CO₂ treatment, especially for the limestones. In addition, contact

angle and surface roughness measurements are conducted to investigate the effect of CO₂ injection on the microscale properties. Finally, discussions regarding the validation of the relative permeability curves with porosimetry measurements are presented.

7.1. Introduction

Climate change is accelerated by CO₂ among different greenhouse gases, highlighting the importance of mitigating its atmospheric emission (IPCC, 2021). As a solution, geologic carbon storage (GCS) has been widely recognized as a sustainable and effective method to reduce the discharge of CO₂, aiming to collect CO₂ from stationary sources and inject it into subsurface formations for permanent sequestration (IPCC, 2005). The injection is generally conducted into brine-filled porous reservoir rocks with potentially large storage capacities, mainly comprising of sandstones and limestones located at depths of at least 800 m (Orr, 2004; US DOE, 2010).

As CO₂ is injected into the reservoir, the distribution of the aqueous fluid is rearranged laterally, followed by the shift of CO₂ upwards due to its lower density (Johnson et al., 2005). It was observed that CO₂ injected into Utsira sandstone in the North Sea propagated laterally over an area of ~10 km², while the plume was also rising due to buoyancy (Chadwick et al., 2006). This transposition of the fluid can be described by understanding the hydraulic behavior of participating rock - one of the most important factors in assessing the formation's suitability for most geo-energy projects. However, as CO₂ injection is generally conducted into brine-saturated reservoir formations, the concept of permeability for single-phase flow cannot be directly applied for the multiphase fluid system (Figure 7.1). Therefore, the relative permeability needs to be evaluated considering the interaction between the wetting and non-wetting fluids (Kopp et al., 2009; Bachu, 2013). Characterization of the multiphase flow response for GCS projects involves

assessment of viscous and capillary forces at the pore-scale and the interfacial and wetting properties of the involved fluids (Fulcher et al., 1985). Moreover, as the injection of high-pressure CO₂ introduces poromechanical deformation and chemical reaction, proper description of relative CO₂ permeability in reservoir rock requires a comprehensive understanding of the multi-physical processes (Rutqvist, 2012; Rohmer et al., 2016; Vilarrasa et al., 2019).

The significance of accurately assessing the two-phase flow behavior has been highlighted by many laboratory-scale experiments, where the relative permeabilities were measured with various methods. Civan and Donaldson (1989) suggested a semianalytic approach to calculate the relative permeability for the immiscible displacement of two incompressible fluids based on the fractional-flow equation and an integro-differential equation (Donaldson et al., 1988). Bennion and Bachu (2005; 2008) and Bachu and Bennion (2008) reported a series of core-scale experiments to evaluate the two-phase flow characteristics of brine and CO₂ for various rock types, using the mass balance method to determine the degree of saturation and the relative permeability curve. Krevor et al. (2012; 2015) conducted a series of tests on reservoir rock to measure the relative permeability under in-situ conditions. The X-ray computed tomography (CT) method was utilized to determine the degree of saturation by scanning the fluid distribution in the pores, as other studies have also adopted this method (Perrin et al., 2009; Pini et al., 2012). A different approach to evaluating the degree of CO₂ saturation is based on accurate measurements of the ultrasonic wave velocities during the multiphase flow experiments (Shi et al., 2017; Falcon-Suarez, 2020). In general, the changes in velocities and wave attenuation are shown to be correlated with the degree of saturation of the pore fluid (Winkler and Plona, 1982; Amalokwu et al., 2014). Akbarabadi and Piri (2013) conducted unsteady- and steady-state flow tests and determined the relative permeability curves, while the effect of hysteresis on capillary

trapping was also examined for both supercritical and gaseous CO₂. Despite the existing number of studies focused on measuring the CO₂ relative permeability in porous rock, the reported experimental data remains to be dependent on the experimental setup and interpretation (Müller, 2011; Chen et al., 2014; Pini and Krevor, 2019).

Many numerical simulations have also been conducted to predict the multiphase flow during CO₂ injection (Chen et al., 1994; Juanes et al., 2006; Martinez et al., 2013). Pruess et al. (1999) introduced a multiphase fluid and heat flow code TOUGH2, and presented simulations of CO₂ flow in brine aquifer considering the losses through fault discharge (Pruess and Garcia, 2002). As TOUGH2 could not consider the effect of chemical reactions and mechanical stress, the code was expanded to include a nonisothermal reactive geochemical transport relationship and became TOUGHREACT (Xu and Press, 2001; Xu et al., 2006). The analytical relationship between relative permeability and saturation were proposed by Brooks and Corey (1964), van Genuchten (1980), and Burdine (1953) and Mualem (1976). However, comparing their prediction for CO₂ relative permeability, saturation, and capillary pressure, a significant discrepancies have been reported, noticing that they be can partially addressed by performing proper experimental measurements (Oostrom et al., 2016).

CO₂ injection causes the non-wetting fluid (CO₂) to displace the wetting fluid (brine or water), so understanding the wettabilities of the participating fluids is extremely important since it affects the capillary pressure and degree of saturation (Anderson, 1986). Wettability is the preference of a solid to be in contact with one fluid than the other, and depending on the fluid's contact angle to the surface, the material can be classified as water/CO₂/intermediate-wet (Abdallah et al., 1986). Different approaches to measuring the wettability of the multi-fluid system have been reported, as both the quantitative (contact angle measurement, Amott method, and USBM

method) and qualitative methods (imbibition rates, relative permeability curves, microscope examination, and capillary pressure curves) have been introduced (Amott, 1959; Craig, 1971; Donaldson et al., 1969; Ionescu and Maini, 1983). Among the suggested techniques, measurements of the contact angle can be selected as one of the most consistent method for reporting the wettability since it is not affected by surfactants or other compounds, and is determined by the balance of the interfacial forces of the multi-fluid system and the surface (Anderson, 1986). Thus, many different methods such as the tilting plate method, sessile drop and bubble method, vertical rod method, and cylinder method have been proposed to perform accurate contact angle measurements (Adamson and Gast, 1967; Johnson, 1969; Good, 1979; Neumann and Good, 1979; Drelich et al., 1996). These techniques have been already implemented to report the contact angles for the water/brine-CO₂-mineral system at high pressure (Espinoza and Santamarina, 2010) and even inside the rock pores using micro-CT images (Tudek et al., 2017).

Wettability explains the distribution of multiphase fluids in the pore space but does not directly describe the saturation state of the system and needs to be considered along with the hydromechanical behavior of the system (Marsden, 1965; Falode and Manuel, 2014). Moreover, several factors such as the pore geometry, surface roughness, and heterogeneity can increase the complexity of assessing the wettability of the porous rock, as previous studies reported a wide range of contact angles for various materials (Drelich et al., 1996; Sarmadivaleh et al., 2015). Particularly, since reservoir formations are composed of micro-sized and rough mineral grains, the surface roughness should also be analyzed to accurately determine the wettability (Morrow, 1990; Amirfazli et al., 1998; Baldacchini et al., 2006). Kaveh et al. (2014) performed laboratory experiments at representative reservoir conditions to establish a relationship between the surface

roughness and contact angle, where it was found that the CO₂ injection did not significantly affect the surface roughness, although its increase caused the contact angles to become slightly larger. Haeri et al. (2020) and proposed that the contact angle increased with the surface roughness based on a series of tests with various sandstones. In contrast to the previous results, Al-Yaseri (2016) reported that for the CO₂/brine/quartz system, the contact angles decreased with surface roughness in accordance with the Wenzel theory (1936). Moreover, from contact angle measurements on several solid surfaces, the contact angle decreased with the increase in the surface roughness can be inferred (Wang et al., 2013). To investigate these discrepancies, the effect of CO₂ injection on the surface roughness and its relationship with the wettability requires further investigation.

Another important factor to be considered is the chemical reaction from CO₂ injection, as it alters the pore structure and directly affects mechanical and flow characteristics of the reservoir rock (Mazumder and Wolf, 2008; Luquot and Gouze, 2009; Grombacher et al., 2012; Su et al., 2019; Tarokh et al., 2020). Due to the challenges with direct experimental measurements, only a few recent studies have been focused on the chemical effect on the multiphase flow behavior, reporting the change in relative permeability curves due to dissolution of calcite in limestones (Kim et al., 2018; Niu and Krevor, 2020).

In this study, we present the experimental work to assess the multiphase flow characteristics of reservoir formations during CO₂ injection. Berea sandstone, Apulian limestone, and Indiana limestone are selected as representative materials, and the properties of pristine and CO₂ treated specimens are compared. The relative permeability curves are determined by adopting a novel technique, where the poroelastic measurements are utilized to calculate the degree of saturation. Maximum and residual degree of saturation and the entry pressure for CO₂ are evaluated, and the

chemical effect of CO₂ treatment is observed. The relative permeability curve measurements are compared with the predictions based on the application of the mercury intrusion porosimetry (MIP). In addition, microscopic measurements are conducted for the wettability and surface roughness, and further discussions on the potential implications for CO₂ storage are provided.

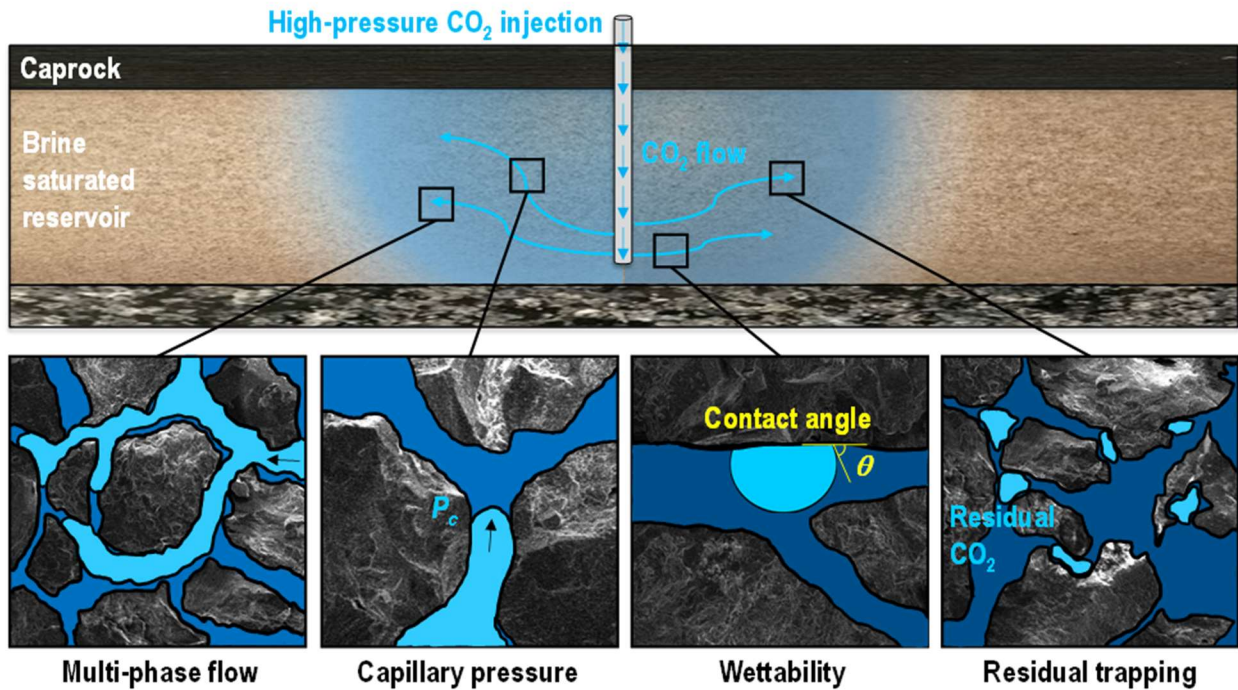


Figure 7.1. Schematic illustration of the multiphase flow aspects during CO₂ injection for geologic carbon storage (GCS).

7.2. Methods

7.2.1. Materials

Three isotropic and homogeneous porous materials – Berea sandstone, Apulian limestone, and Indiana limestone, are selected for this study. Berea sandstone is a sedimentary formation that overlies the Bedford and Ohio shale and underlies Sunbury shale, also known as Berea grit (Newberry, 1874). It was formed in the late Devonian period and primarily consists of fine to medium-sized grains, being well known as the host rock for oil and natural gas and one of the most tested rock-like materials (Collins, 1979). The gray-colored sandstone dominantly consists of quartz (around 90% by mass), with minor inclusions of kaolinite, K-feldspar, and muscovite. The porosity ϕ is measured to be 0.22.

Apulian limestone is a glauconitic fossiliferous carbonate rock, formed in the mid-Cretaceous era, and originated from the Apulia region of Southern Italy. This formation mainly comprises calcite (more than 95%) with a small portion of plagioclase, glauconite, and iron oxide, representing the soft calcite-rich rock for this study. The matrix of Apulian limestone is constructed with 0.05-1 mm size fragmental calcitic foraminifera, which are calcitic mud (micrite) cementations with allochems. For this soft limestone, the porosity is measured to be the largest among the tested rock: $\phi = 0.37$.

Indiana limestone is versatile for buildings and public structures, as it is widely recognized for its durability and stability (Shaffer, 2020). It is formed with uniform carbonate grainstones during the Mississippian Subperiod of the Carboniferous, and is composed mainly of calcite (more than 97%), with quartz, aluminum oxide, and sulfur. This light-grey to bluish-grey rock has the porosity equal to 0.13.

For this study, deionized water is selected as the pore fluid instead of brine. Thus, we neglect the influence of salinity and only focus on the chemical effect of the acidic mixture of CO₂ and water on the rock minerals and pore structure. CO₂ is injected and maintained in the liquid state throughout all the tests to disregard any phase transitions and associated thermal effects on the rock properties. In addition, injection of liquid CO₂ is energetically more efficient comparing to the supercritical fluid and should be investigated for near-wellbore multi-phase flow (Rayward-Smith and Woods, 2011; Vilarrasa et al., 2013). The capillary pressure – saturation curves and porosities for all materials are measured using the mercury intrusion porosimetry (MIP) method, with mercury being a non-wetting fluid in air-saturated samples (Figure 7.2). The dominant pore sizes are determined as 20 μm, 2 μm, and 1 μm for Berea sandstone, Apulian limestone, and Indiana limestone, respectively. At least three samples are tested for each material and the results appear to be very consistent.

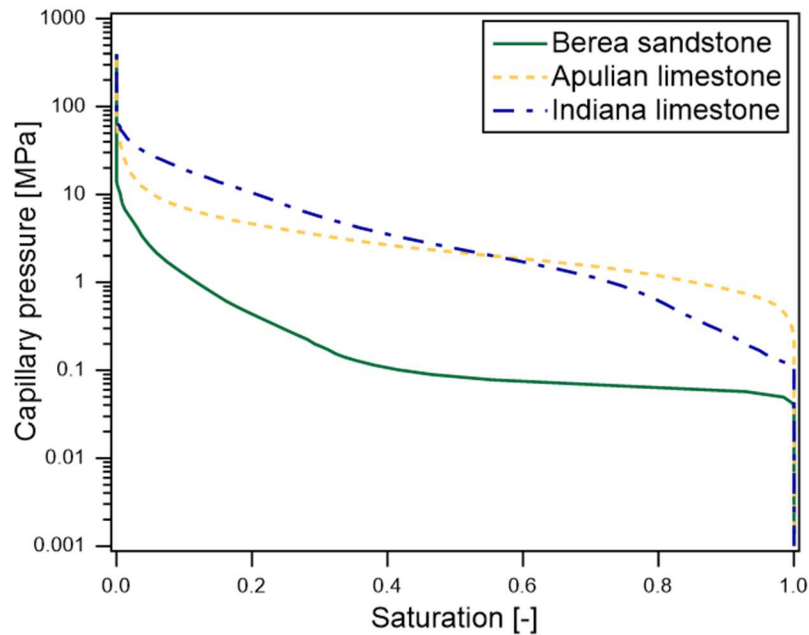


Figure 7.2. Capillary pressure (mercury) – saturation curves for Berea sandstone, Apulian limestone, and Indiana limestone measured using mercury intrusion porosimetry.

7.2.2. Multiphase flow test

The multiphase flow is defined as the simultaneous flow of more than one fluid through a porous media, as it becomes the case for CO₂ injection in water-saturated rock in geologic carbon storage. Although multiple fluids exist, characterizing the multiphase flow behavior triggers from defining the concept of intrinsic permeability. Permeability describes the capacity of the interconnected porous medium to allow fluid to penetrate, and can be introduced based on the law of conservation of mass. If it is written in Darcy's form for laminar and steady-state conditions, the flow rate q can be expressed as a function of viscosity of the fluid μ_f and the differential pressure dp^f along the differential distance x_i .

$$q_i = -\frac{k}{\mu_f} \frac{\partial p^f}{\partial x_i} \quad (7.1)$$

The parameter k in this equation can be measured when a constant differential pressure Δp^f between the upstream and downstream sides of a specimen is applied: $p_{up}^f - p_{down}^f = \Delta p^f$. The flow rate is calculated as the volume of the fluid ΔV exiting the specimen over time Δt . If the viscosity of the fluid is known ($\mu^f = 0.001$ Pa·s for pure deionized water at 22°C), L is the length of the specimen, and A is the cross-sectional area perpendicular to the flow, then permeability can be calculated as

$$k = \frac{\mu^f \cdot L \cdot \Delta V}{A \cdot \Delta t \cdot \Delta p^f} \quad (7.2)$$

For the multiphase fluid flow, relative permeability $k_{ri} = k_i / k$ is introduced to describe the flow capability of the i -th fluid. By extending equation (7.2), the relative permeability can be calculated from the knowledge of the viscosity μ_i^f , as well as the flow rate $\Delta V_i / \Delta t$ and differential pressure Δp_i^f in the i -th fluid (Bear, 1988).

$$k_{ri} = \frac{\mu_i^f \cdot L \cdot \Delta V_i}{k \cdot A \cdot \Delta t \cdot \Delta p_i^f} \quad (7.3)$$

The two-phase flow test of water and CO₂ can be conducted utilizing the core flooding device with the high-pressure CO₂ injection setup, assuming that flow of the two fluids in the rock is steady-state and laminar. Right cylindrical specimens with diameter $D = 50.8$ mm and length $L = 100$ - 110 mm are inserted in the rubber viton membrane installed inside the device. The core holder allows imitation of high in situ stress conditions and is connected to four pressure controllers: the Stigma 500/700 controller (Sanchez Technologies, France, 70 MPa capacity) for the confining pressure, and three syringe pumps (Teledyne ISCO, USA, 25.9 MPa capacity) for the CO₂ upstream, water upstream, and downstream pressures. Accurate measurements of the pore pressure are performed via two pore pressure transducers (Honeywell, USA, capacity 34.5 MPa) installed at the upstream and downstream sides of the specimen. As two syringe pumps are connected to the upstream for CO₂ and water for the flow rate and pressure control, this setup allows two-phase flow experiments, while the CO₂ treatment test can also be conducted by only having the CO₂ syringe pump valve open (Kim and Makhnenko, 2021).

The deformation of the specimen is assumed to be poroelastic and the total mean stress P can be determined from calculating the induced axial stress σ_{ax} applied via the passive restraint installed in the axial direction. By knowing the applied confining pressure σ_{lat} and the pore pressure p^f , and measuring the Poisson's ratio ν and Biot coefficient α from the mechanical tests, P can be calculated as (Kim and Makhnenko, 2020a).

$$P = \frac{\sigma_{ax} + 2\sigma_{lat}}{3} = \frac{2(1+\nu)}{3}\sigma_{lat} - \frac{(1-2\nu)\alpha}{3}p^f \quad (7.4)$$

Full saturation with water is achieved before each flow test by adopting the back pressure saturation method (Lowe and Johnson, 1960; Makhnenko and Labuz, 2016). Then, the pore

water is exposed to liquid CO₂ for at least 4 hours to guarantee that it becomes CO₂-rich under the testing conditions. In the flow test, the two upstream pumps for water and CO₂ are operated in the flow control regime with the prescribed rate of injection, while the downstream pump is maintained in constant pressure control. The ratio of the flow rates (water:CO₂) for the upstream pumps are prescribed to be 100:0%, 80:20%, 50:50%, 20:80%, and 0:100%. As the two fluids are injected from the upstream, the pressure of each pump fluctuates at the beginning, while it eventually reaches a constant value that allows calculation of the differential pressure Δp_i^f for each fluid ($i=w$ for water and $i=c$ for CO₂ in equation 7.3). The two-phase flow tests for reservoir rock are conducted for not more than an hour after reaching the steady state flow condition to assure that the chemical effects from the relative permeability measurements are minimal on the material properties. Moreover, as the relative permeability experiment starts from injection of water only and then increases the rate of CO₂ injection, it is to be noted that this study focuses solely on the drainage process. After treating the specimens with CO₂, it is completely removed from the pores by flushing the deionized water at low pressure before conducting any relative permeability measurements. Considering the pore size of the tested rock, and resaturating the treated specimens with water via the back pressure saturation technique (Makhnenko and Labuz, 2016), we affirm that the subsequent measurements of the mechanical and hydraulic properties are performed with presence of only the wetting fluid (Kim and Makhnenko, 2021).

7.2.3. Saturation calculation

In order to assess the storage efficiency for CO₂ injection projects, a proper understanding of the degree of saturation for the two fluids (water and CO₂) is required. In addition, as the pore compressibility can be affected due to CO₂ injection, the poromechanical response needs to be

coupled with the multiphase flow. The materials selected for this study all represent monomineralic and isotropic rock (the sandstone is silica-rich and limestones consist mainly of calcite) allowing to adopt the poroelastic theory introduced by Biot (1941) for the description of their mechanical behavior. In this study, a novel method to determine the degree of saturation is introduced based on the measurements of the fluid-saturated rock compressibility during the CO₂ injection. After running a two-phase flow test and assuring that the total injected fluid volume of CO₂ and water exceeds five times the pore volume of the specimen, both the upstream and downstream valves are closed simultaneously, imposing the undrained boundary condition. Then, the Skempton's B coefficient is directly measured in the experiment as an increase in pore pressure Δp^f due to the application of the increment in the mean stress ΔP . At the same time, it can be expressed through other poroelastic parameters and the bulk modulus of the pore fluid that represents a mixture of water and CO₂ - $K_{f,mix}$ (Detournay and Cheng, 1993).

$$B = \left. \frac{\Delta p^f}{\Delta P} \right|_{\zeta=0} = \frac{\left(1 - \frac{K}{K_s'}\right)}{\left(1 - \frac{K}{K_s'}\right) + \phi K \left(\frac{1}{K_{f,mix}} - \frac{1}{K_s''}\right)} \quad (7.5)$$

Here, K is the drained bulk modulus, K_s' is theunjacketed bulk modulus, K_s'' is theunjacketed pore modulus, and ϕ is the interconnected porosity. The drained bulk modulus K (equation 7.6) and unjacketed bulk modulus K_s' (equation 7.7) are measured using the hydrostatic compression device, with strain gauges installed on a prismatic specimen with a linear dimeonsion of at least 30 mm in three perpendicular directions. The bulk deformation is monitored during the loading/unloading steps, as the slope for the pressure versus volume strain ($\varepsilon_v = \varepsilon_1 + \varepsilon_2 + \varepsilon_3$) is taken as the bulk modulus (Tarokh and Makhnenko, 2019).

$$K = V \left. \frac{\Delta p^f}{\Delta V} \right|_{\Delta p^f = 0} \quad (7.6)$$

$$K_s' = V \left. \frac{\Delta p^f}{\Delta V} \right|_{\Delta p^f = \Delta P} \quad (7.7)$$

Theunjacketed pore modulus K_s'' is assumed to be equal to K_s' for ideal porous media, so $K_s' = K_s''$ is adopted in this study regarding the isotropy of the tested reservoir formations (Detournay and Cheng, 1993). We acknowledge though that this assumption might be violated for Berea sandstone that has minor inclusions of other minerals (Makhnenko and Labuz, 2016) and Apulian limestone that contains some non-connected pores (Tarokh and Makhnenko, 2019).

With the knowledge of the poroelastic properties, the bulk modulus for the mixture of two fluids (water and CO₂) - $K_{f,mix}$ can be calculated from equation 5. Then, from the Wood's (1930) equation, the degree of saturation for each fluid can be determined, while the bulk modulus of CO₂ is calculated to be $K_c = 0.07$ GPa at the testing conditions (Achenbach, 1984) and bulk modulus of pure water $K_w = 2.24$ GPa.

$$\frac{1}{K_{f,mix}} = \frac{S_w}{K_w} + \frac{1-S_w}{K_c} \quad (7.8)$$

The procedure to determine the saturation of the two fluids are repeated for each flow rate of H₂O:CO₂, where the relative permeabilities of the wetting and non-wetting fluids are measured. The relative permeability curve can be obtained by plotting the measured values of k_{rw} and k_{rCO_2} versus the degree of saturation for each of the fluids. This approach overcomes the limitations of other methods, such as the X-ray CT scanning, regarding the resolution, discretization effect, and testing conditions (Cnudde and Boone, 2013) and can be used with the materials where pore sizes fall below the imaging resolution.

For the discrete data points obtained from the multiphase flow measurements, the fitting is performed using the analytical relationships. The Brooks and Corey (1964) power-law model is adopted, where the effective saturation parameter S_e is introduced. Then, with the fitting exponent parameters for water and CO₂, N_w and N_c , the relative permeabilities can be expressed as:

$$k_{rw} = (S_e)^{N_w} \quad k_{rc} = (1 - S_e)^{N_c} \quad (7.9)$$

The parameter S_e can be calculated from the knowledge of liquid saturation S_l , the residual liquid saturation S_{rl} , and the maximum liquid saturation S_{max} , that is equal to 1 for the case of full water-saturation.

$$S_e = \frac{S_l - S_{rl}}{S_{max} - S_{rl}} = \frac{S_l - S_{rl}}{1 - S_{rl}} \quad (7.10)$$

The effective saturation parameter S_e allows estimation of the capillary pressure P_c through Brooks-Corey fitting parameters: CO₂ entry pressure P_e and pore size distribution index λ (Dullien, 1992).

$$P_c = P_e \cdot S_e^{-\frac{1}{\lambda}} \quad (7.11)$$

Although the Brooks-Corey model provides intuitive fitting of the relative permeability curves and information on the CO₂ entry pressure, it cannot be directly connected to the saturation characteristics of a porous material. Therefore, van Genuchten model (1980) is utilized, since it adopts the same fitting parameters α , m , and n , for both capillary pressure and relative permeability curves.

$$S_e = \frac{1}{\left(1 + (\alpha P_c)^n\right)^m} \quad (7.12)$$

$$k_r(S_e) = S_e^{\frac{1}{2}} \cdot \left[1 - \left(1 - S_e^{\frac{1}{m}} \right)^m \right]^2 \quad (7.13)$$

Use of this model enables validation of the two different methods presented in this study - relative permeability and capillary pressure measurements. For van Genuchten model, certain restrictions can be imposed on the fitting parameters based on Mualem's (1976) approach, where m can be expressed in terms of n as $m = 1-1/n$, while m stays in the range of $0 < m < 1$. However, for this study, we utilize three parameters independently to obtain a more accurate fitting.

7.2.4. CO₂ treatment test

In this study, the effect of CO₂ treatment on the multiphase flow behavior is explored by comparing the characteristics of the pristine and treated rock specimens. After reaching full saturation with deionized water, the pressure conditions are controlled to maintain 4.5 MPa effective mean stress and 6.9 MPa pore pressure. Then, liquid CO₂ is injected from the upstream side at 7 MPa with the downstream valve closed. The upstream valve is being closed after injecting 40-50 mL of liquid CO₂ to maintain an undrained condition, and the pore pressures at the upstream and downstream sides of the specimen are monitored. The readings on the pressure transducers indicated that the pore pressure slowly decreases to 6.2 MPa – the boundary value between liquid and gaseous CO₂. Therefore, additional liquid CO₂ is injected daily at the pressure of 7 MPa once the decrease of the pore pressure is observed.

Previous studies reported that the duration time of CO₂ treatment correlates with the degree of the change in the material properties (Kim et al., 2020b; Shi et al., 2019). For this study, 21 days are selected as the treatment period, as we intend not to introduce any macroscopic damage to the materials (Tarokh et al., 2020). Furthermore, since Apulian limestone is recognized as a

softer material that highly reacts with the acidic mixture of water and CO₂, the treatment period is reduced to 3 days (Luquot and Gouze, 2009; Kim et al., 2018).

7.2.5. Mercury intrusion porosimetry

The capillary pressure P_c for the CO₂-water-rock system can be determined by utilizing the mercury intrusion porosimetry (MIP) to measure the porosity and pore size distribution. Quantachrome Poremaster 60 from Anton Paar© is used to inject mercury in the pores of dry reservoir rock samples with a mass of approximately 1 gram. As liquid mercury has a high cohesive force, its volume can be accurately measured, while it is forced to intrude the pores by increasing the pressure up to 413.7 MPa. After reaching full saturation with mercury, the weight of the sample cell is accurately measured to calculate the bulk density of the rock sample. Then, with the knowledge of the density ($\rho = 13.54 \text{ g/cm}^3$), contact angle ($\theta = 140^\circ$), and surface tension ($\gamma = 480.0 \text{ erg/cm}^2$) of mercury, the pore size distribution can be determined as the function of the pore throat diameter d using the Young-Laplace equation.

$$P_c = -\frac{4\gamma \cos \theta}{d} \quad (7.14)$$

The degree of saturation for each corresponding pressure is calculated as the ratio of the injected mercury to the total interconnected pore volume. Finally, the capillary pressure curve can be obtained by plotting the capillary pressure vs the degree of saturation. The application of the capillary pressure curves for CO₂ injection requires converting the MIP data from the mercury/air/rock system to the CO₂/water/rock system. The abbreviation n/w describes the non-wetting/wetting system for CO₂/water, while m/a represents the mercury-air system. As a result, the capillary pressure for the CO₂-water-rock system can be calculated as:

$$P_{c,n/w} = P_{c,m/a} \frac{\sigma_{n/w} \cos \theta_{n/w}}{\sigma_{m/a} \cos \theta_{m/a}} \quad (7.15)$$

For this study, we employ the findings of Espinoza and Santamarina (2010), where the average interfacial tension and contact angle for CO₂/water are measured as 32 mN/m and 20° for silica-rich materials and 32 mN/m and 40° for calcite-rich materials, respectively. Although some previous studies reported different contact angles for porous rock to that of its composing mineral (Lv et al., 2017; Scanziani et al., 2017; Tudek et al., 2017), we presume that the contact angle and interfacial tension of the tested rocks follow their dominant composing minerals. Nevertheless, based on the direct measurements of the apparent contact angle, further discussion regarding the effect of CO₂ injection on wettability is presented in this study.

7.2.6. Wettability

The wettability of the system can be assessed by measuring the contact angle θ , which is formed at an equilibrium state of the interfacial forces in the multiphase fluid system. Although in-situ measurements of the wettability may differ to that from ambient conditions (Lv et al., 2017; Tudek et al., 2017), a simple method to evaluate the effect of CO₂ treatment on the contact angle is adopted by doing the direct imaging with a microgoniometer MCA-3 (Kyowa, Japan). The device is capable of accurately controlling the size of the microscopic droplets to be as small as 100 μm , and can detect the droplet from both the top and the side for its movement and wettability. A high magnification lens is installed with the ability to monitor the droplet in a 12-fold zoom, that allows a field of view from 75×56 μm to 910×680 μm , with a fast image capture system for accurate measurements. The drop deposition can be automatically recognized with the FAMAS software, and the apparent contact angle can be measured in the range of 0.1° to 180° with 0.01° resolution.

The specimens are prepared by cutting slices from rock cores with a 1-2 cm length and width and 0.5 cm depth, and then polishing their surface to maintain a uniform roughness. Then, after washing with deionized water, the rock is being completely dried before the contact angle measurements. The sessile drop method is used for this study as the microscopic droplets are applied to the flat and polished surface (McCaffery et al., 1970; Anderson, 1986), after which the contact angles are measured using the microgoniometer.

7.2.7. Surface roughness

Characterization of the wettability is crucial for understanding the multiphase flow in porous rock, while the contact angle could also depend on the surface roughness (Wenzel, 1949; Tamai and Aratani, 1972; Morrow, 1975). A qualitative approach to evaluate the effect of CO₂ treatment on rock's surface roughness is adopted, where the Sloan Dektak3ST Profilometer provides repeatable and accurate measurements of the height and 2D profile of the surface, ranging from a few nanometers to one hundred microns. With a 2.5-micron radius diamond-tipped conical stylus, the contact technique is utilized to measure the surface topography without any damage, as it scans across the surface of the specimen. All specimens are precisely ground to take a shape of a disk with 2 cm in diameter and 1cm thickness. Each measurement is conducted by scanning 1000 μm along the specimen surface, with $N = 2000$ data points collected per scan. Then, 12 scans are performed per specimen to obtain average representative data by selecting different starting positions for the stylus. The profilometer is set to the highest scanning resolution with 12 seconds scanning time duration for each measurement. The root-mean-square (RMS) method is utilized to calculate the surface roughness, where Z_i is the measured height value and Z_{avg} is the arithmetic mean for all height values.

$$RMS = \left[\frac{1}{N} \sum_{i=1}^N |Z_i - Z_{avg}|^2 \right]^{1/2} \quad (7.16)$$

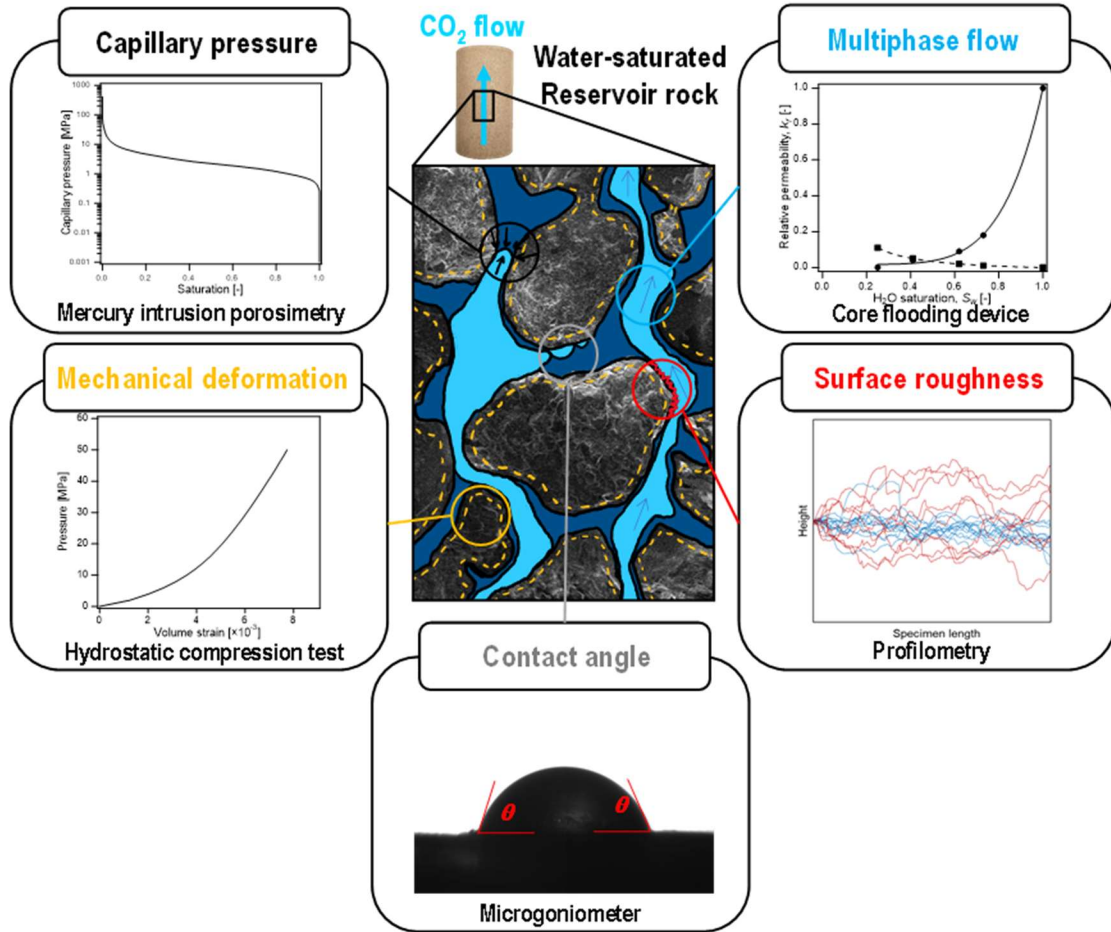


Figure 7.3. Illustration of the experimental methods utilized to characterize the multiphase flow behavior of reservoir rock upon CO₂ injection.

7.3. Results

7.3.1. Poroelastic properties

The knowledge on the poroelastic properties of reservoir rock is needed to calculate their degree of saturation with CO₂ and report the relative permeability curve. Pristine and CO₂ treated specimens are tested in the hydrostatic compression cell under the jacketed andunjacketed conditions to report the corresponding bulk moduli measured during the unloading stage (Figure 7.4). For the jacketed test on Apulian limestone, the pressure is increased up to 30 MPa, since preceding studies reported pore collapse of this material around 39 MPa (Tarokh and Makhnenko, 2019). For the other two materials, the jacketed compression test is conducted up to 50 MPa. The results for all materials show that the drained bulk moduli increase gradually to reach a constant value, indicating that all the microcracks and oblique pores at the early compression stage are being closed. For Berea sandstone, the drained bulk modulus decreases from 12.1 GPa to 10.3 GPa. For Apulian limestone, the jacketed bulk modulus K decreases (e.g., from 6.3 GPa to 5.0 GPa at $P = 30$ MPa), meaning the material is getting more compressible due to the treatment process. The measurements for Indiana limestone show a similar result to Apulian limestone in terms of CO₂ treatment – the decrease in drained bulk modulus by 20%, from 29.5 GPa to 23.1 GPa (at $P = 30$ MPa pressure).

Accurate measurements of the unjacketed bulk modulus K_s' are also required to calculate the degree of saturation and the results of unjacketed experiments are reported in Kim and Makhnenko (2021). All the unjacketed moduli are measured to be constant during the loading and unloading stages. K_s' for Berea sandstone remained identical after CO₂ treatment, and being equal to 30 GPa. For Apulian limestone, the unjacketed bulk modulus decreased from 42.7 GPa to 34.2 GPa, and for Indiana limestone, K_s' also decreased by 20%, from 65.9 GPa to 54.9 GPa

(Table 7.1). The decrease in theunjacketed moduli of limestones is explained by the observed dissolution and precipitation of calcite caused by the chemical reaction with the acidic mixture of water and CO₂. However, it is to be noted that apparent precipitation may be related to the particle migration and rearrangement of calcite particles, which can be suggested as another reason for the creation of the new non-connected pores (Mangane et al., 2013), as it appears that CO₂ treatment causes increases in the total porosity, as well as in the non-connected porosity in calcite-rich rock, making the overall solid matrix response more compliant (Kim and Makhnenko, 2021).

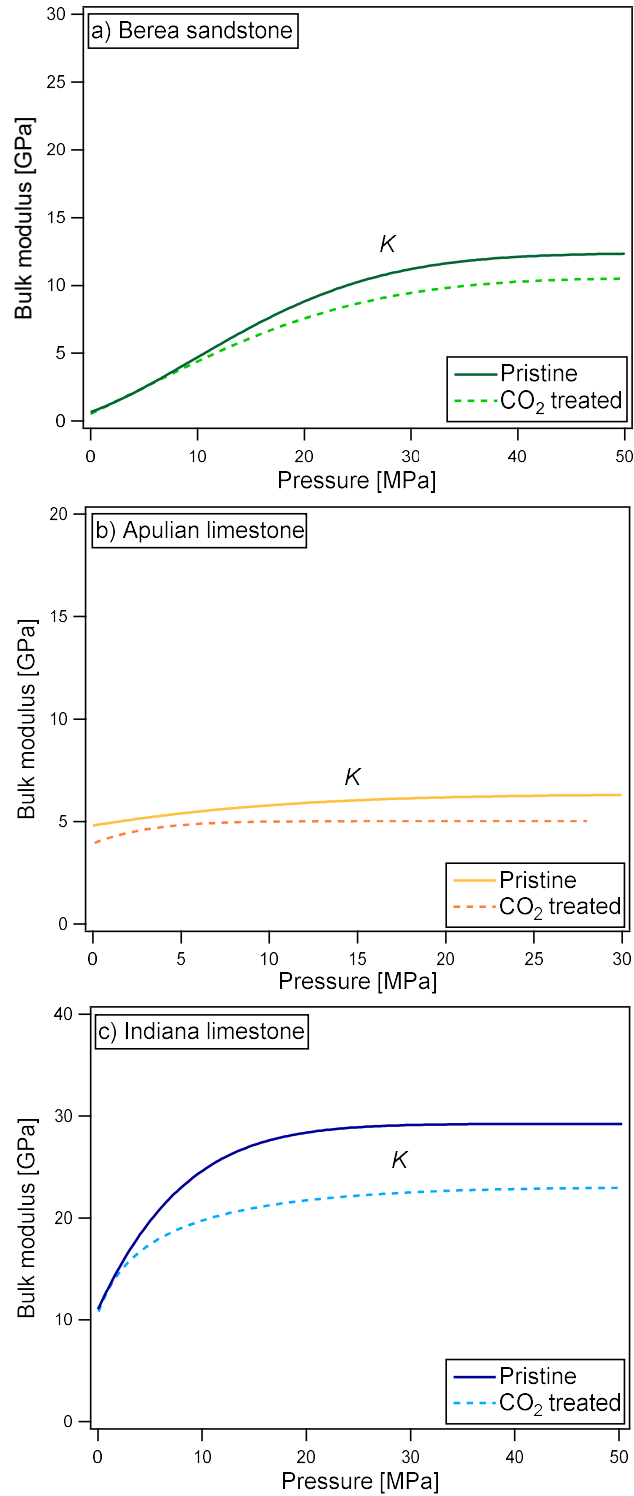


Figure 7.4. Drained bulk modulus K measurements for pristine and CO₂ treated a) Berea sandstone, b) Apulian limestone, and c) Indiana limestone.

For this study, the measurements of the Skempton's B coefficient are utilized to calculate the degree of saturation for the relative permeability curves. The B values are measured for the pristine and CO_2 treated reservoir rock specimens at $P' = 4.5$ MPa and are reported as functions of the degree of saturation, that is calculated from equation 7.5. The Skempton's B coefficient for Berea sandstone decreases from 0.77 to 0.67, while it increases from 0.47 to 0.53 for Apulian limestone and 0.32 to 0.40 for Indiana limestone. For limestones, calcite dissolution has been reported to be the main reason for the increase in the B values, since the porosity increases and rock becomes more compliant (Kim and Makhnenko, 2021). On the other hand, for Berea sandstone, the reduction in the undrained bulk modulus K_u along with the drained bulk modulus K is observed and explained by the stress corrosion cracking, hence $B = (K_u - K) / (1 - K / K_s) / K_u$ can decrease (Tarokh et al., 2020).

7.3.2. Relative permeability

Understanding the flow properties of reservoir rock in the water/ CO_2 system is crucial for CO_2 injection, as it is closely related to the injectivity and storage efficiency. For the multiphase flow behavior, the capillary pressure and relative permeability are essential factors that describe the two-phase fluid displacement in the pore space. This section examines the effect of CO_2 treatment on the multiphase characteristic curves of the reservoir rock. The relative permeability is measured using the core flooding apparatus via the novel method that allows assessing the CO_2 saturation from changes in the undrained compressibility of rock upon CO_2 injection.

The relative permeability curves are determined before and after CO_2 treatment. Before conducting the multiphase flow experiments, the intrinsic permeabilities for pristine and CO_2 treated specimens are accurately measured at $P' = 4.5$ MPa. For Berea sandstone, the intrinsic

permeability is $1.9 \times 10^{-13} \text{ m}^2$ for the pristine state, and it increases slightly to $2.1 \times 10^{-13} \text{ m}^2$ after the CO_2 treatment. The permeability of pristine Apulian limestone is measured to be $7.5 \times 10^{-15} \text{ m}^2$, changing to $8.2 \times 10^{-15} \text{ m}^2$ for the treated specimen. Similarly, for Indiana limestone, the intrinsic permeability increases from $8.0 \times 10^{-14} \text{ m}^2$ to $8.4 \times 10^{-14} \text{ m}^2$ after CO_2 treatment. For all tested materials, the intrinsic permeability slightly increases due to CO_2 treatment, while the interpretation is different for the sandstone and limestones. For the limestones, calcite dissolution appears to increase the porosity, and hence the permeability – similar results are reported in a number of studies (Bennion and Bachu, 2008; Luquot and Gouze, 2009; Kim and Makhnenko, 2021). For Berea sandstone, the stress corrosion cracking is assumed to be the main mechanism affecting the permeability without any significant increase in porosity (Tarokh et al., 2020).

The values of Skempton's B coefficient are measured during the two-phase flow experiments at each injection rate (10:0, 8:2, 5:5, 2:8, 0:10 for $\text{H}_2\text{O}:\text{CO}_2$), and the degree of CO_2 saturation is calculated from equation 5. The pristine and CO_2 treated poroelastic properties measured at the same effective mean stress ($P' = 4.5 \text{ GPa}$) are adopted for the calculations for each corresponding material. At the same time, we assume that the poroelastic parameters (K , K_s' , and ϕ) remain constant at different flow rates. The measured Skempton's B coefficients decrease significantly right after starting CO_2 injection, also being different for the pristine and CO_2 treated rock (Table 7.2).

Then, the intrinsic permeability value is taken for each pristine and CO_2 treated material to calculate the relative permeability from equation 7.3. Finally, with the degree of saturation calculated from the measurements of the poroelastic parameters and changes in Skempton's B values (equations 7.5 and 7.8), the relative permeability curves are reported (Figures 7.5-7.7). The results are then fitted to the power-law functions in terms of the degree of saturation, similar

to the Brooks-Corey model. The fitting parameter N_w is determined using the least-squares method for all materials. The additional fitting is provided for van Genuchten model (equations 7.12 and 7.13), where the set of fitting parameters (α , n , and m) is reported in Table 7.1.

For Berea sandstone, CO₂ treatment does not seem to significantly affect the relative permeability curves, with the exponent N_w remaining constant at 2.9 and slight increase in the maximum degree of CO₂ saturation from 0.70 to 0.73 (Figure 7.5). For Apulian limestone, the maximum degree of CO₂ saturation increases from 0.68 to 0.80, while the exponent N_w decreases from 3.8 to 1.3, indicating that the shape of the relative permeability curve turned from a power law to a quasi-linear function (Figure 7.6). The relative permeability curves for Indiana limestone are presented in Figure 7.7, showing N_w decreasing from 6.3 to 5.2 and the maximum degree of CO₂ saturation increasing from 0.69 to 0.75 after the treatment. The values of S_w are reported with 5% accuracy where the main error comes from the determination of the Skempton's B coefficient with the core flooding apparatus at high degree of CO₂ saturation (Kim and Makhnenko, 2021). Each experiment is duplicated and very similar results are obtained (with less than 3% variation), while the average results are provided in the figures and tables. This study suggests that the multiphase flow response for sandstones is not affected by CO₂ injection, while for limestones, the exponent parameter N_w decreases as the maximum degree of saturation for CO₂ increases slightly.

In addition to the Brooks-Corey model, the van Genuchten model is applied for fitting the relative permeability curves for all materials. The α values are reported to increase due to CO₂ injection, as they are mostly related to the CO₂ entry pressure. Although, when the relative permeability relationship gets closer to a linear one after the CO₂ treatment of Apulian limestone

(Figure 7.6 b), - the van Genuchten model fails to provide a good fit, unlike the Brooks-Corey model.

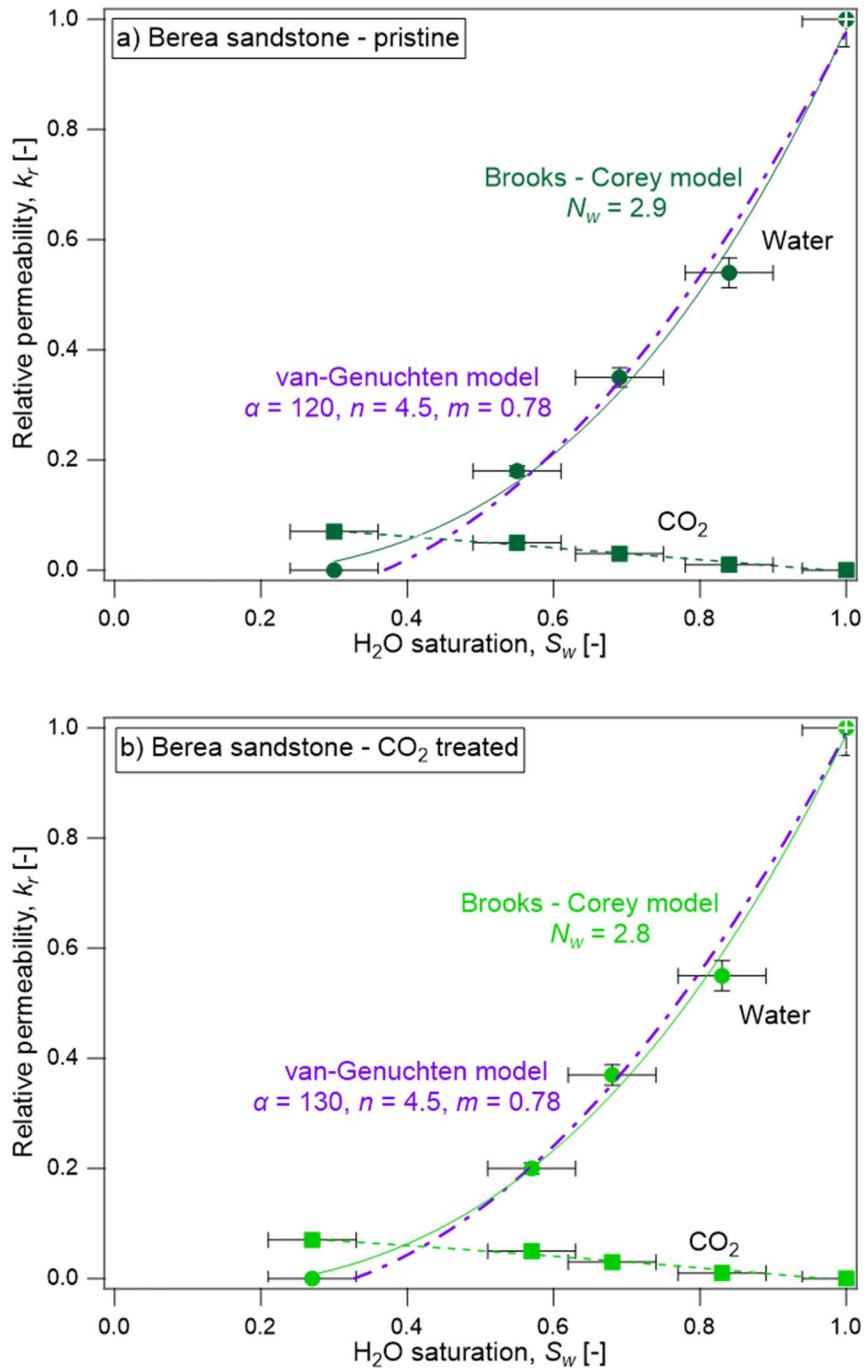


Figure 7.5. Relative permeability curves for a) pristine and b) CO₂ treated Berea sandstone.

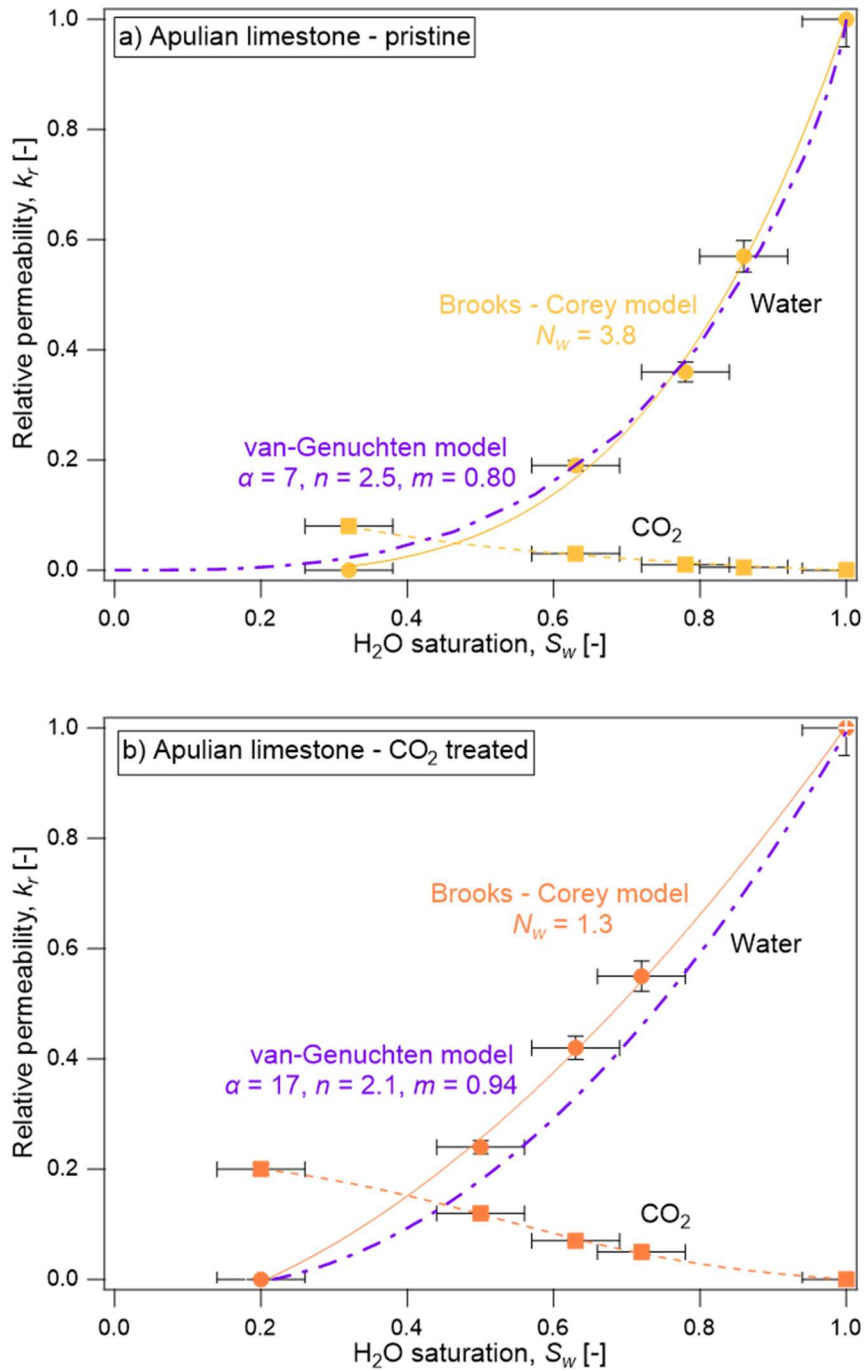


Figure 7.6. Relative permeability curves for a) pristine and b) CO₂ treated Apulian limestone.

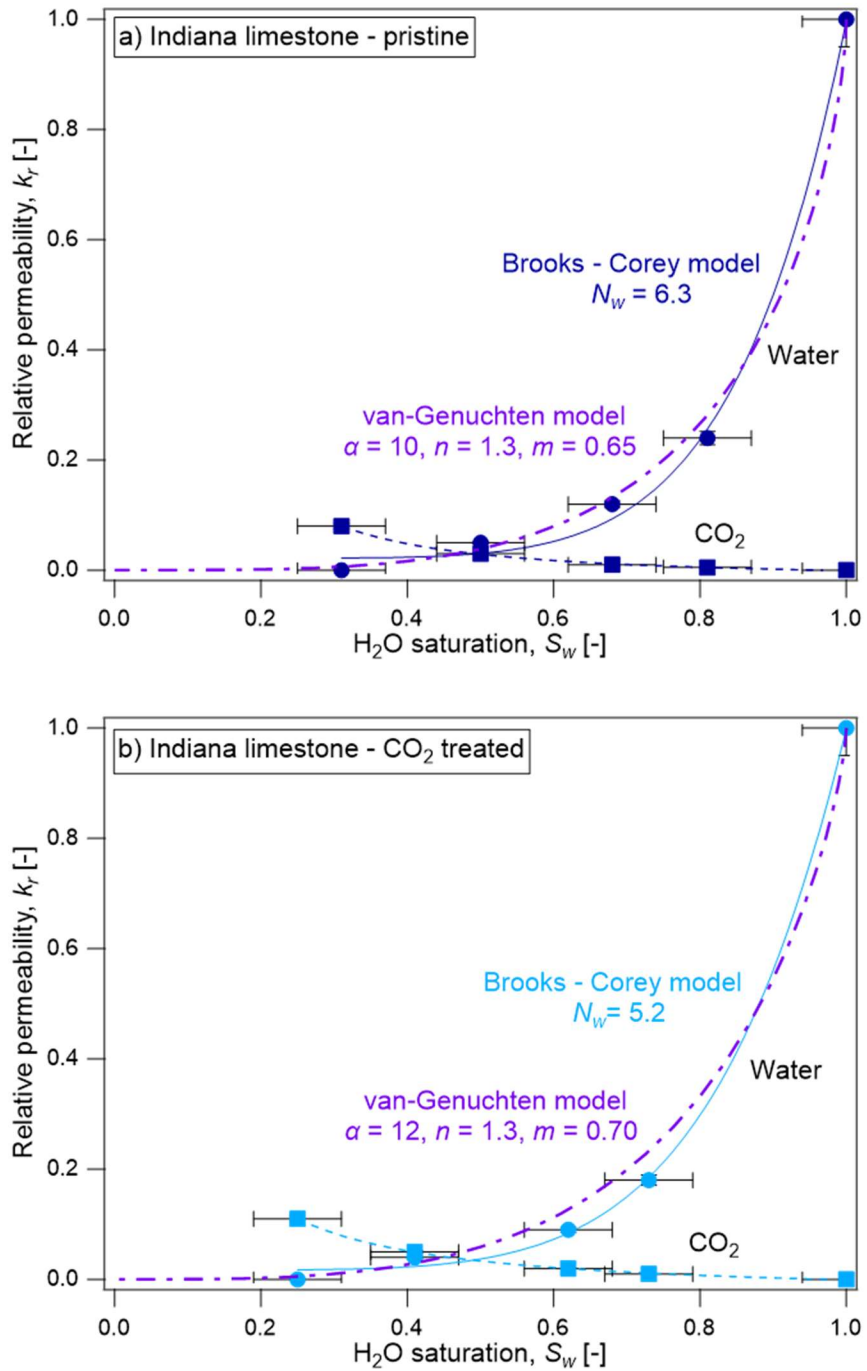


Figure 7.7. Relative permeability curves for a) pristine and b) CO₂ treated Indiana limestone

CO₂ treatment appears to cause an increase in the maximum degree of CO₂ saturation for all tested materials, although it requires more detailed analyses on the elements that may affect the capillary pressure, such as the wettability and the surface roughness. Further investigations and validation of the measured relative permeability curves are presented in the discussion section, where the capillary pressure curves are coupled with the relative permeability measurements.

Table 7.1. Summary of the results for the porosity (ϕ), poroelastic properties: K (drained bulk modulus), K_s' (unjacketed bulk modulus), and multiphase flow parameters: k (intrinsic permeability), N_w (Brooks-Corey exponent), $\alpha/n/m$ (van Genuchten fitting parameters) and S_{CO_2} (maximum degree of water saturation). The drained bulk modulus is reported at $P' = 30.0$ MPa, and the intrinsic permeability is measured at $P' = 4.5$ MPa).

		ϕ [-]	K [GPa]	K_s' [GPa]	K [m ²]	N_w [-]	van Genuchten fitting parameters			S_{CO_2} [-]
							α [MPa ⁻¹]	n [-]	m [-]	
Berea sandstone	Pristine	0.219	12.1	30.0	1.9×10^{-13}	2.9	120	4.5	0.78	0.70
	CO ₂ treated	0.219	10.3	30.0	2.1×10^{-13}	2.8	130	4.5	0.78	0.73
Apulian limestone	Pristine	0.371	6.3	42.7	7.5×10^{-15}	3.8	7	2.5	0.80	0.68
	CO ₂ treated	0.388	5.0	34.2	8.2×10^{-15}	1.3	17	2.1	0.94	0.80
Indiana limestone	Pristine	0.127	29.5	65.9	8.0×10^{-14}	6.3	10	1.3	0.65	0.69
	CO ₂ treated	0.136	22.6	54.9	8.4×10^{-14}	5.2	12	1.3	0.70	0.75

Table 7.2. Summary of the Skempton's B coefficient measurements during the multiphase flow test at different flow rates of H_2O and CO_2 ($P' = 4.5$ MPa).

		Skempton's B coefficient [-] ($H_2O : CO_2$ flow rate)				
		10:0	8:2	5:5	2:8	0:10
Berea sandstone	Pristine	0.77	0.14	0.08	0.06	0.04
	CO_2 treated	0.67	0.15	0.09	0.07	0.04
Apulian limestone	Pristine	0.47	0.17	0.12	0.08	0.05
	CO_2 treated	0.53	0.13	0.10	0.07	0.05
Indiana limestone	Pristine	0.32	0.10	0.07	0.05	0.03
	CO_2 treated	0.40	0.09	0.06	0.04	0.03

7.4. Microscopic Measurements

Characterization of the multiphase flow in rock oftentimes relies on the assumption that the microscale properties generally remain constant after CO_2 treatment. However, a number of studies have reported the chemical effect of CO_2 at a microscale (Farokhpoor et al., 2013; Al-Ansari et al., 2017). Thus, the parameters that directly affect the relative permeability – wettability and surface roughness, have to be measured before and after CO_2 treatment (Kaveh et al., 2014; Haeri et al., 2020).

7.4.1. Wettability

Experiments are conducted to assess the effect of CO_2 treatment on the wettability of reservoir rock, as it is directly related to the changes in capillary pressure and relative permeability. For reservoir formations, the pores on the surface may affect the contact angle measurements as they can be considered as deflection or surface rugosity. By using the microgoniometer, the apparent contact angles for the air/water system are measured for the pristine and CO_2 treated reservoir rock (Figure 7.8). More than twenty measurements are taken for each sample at different locations, and the average values are reported in this study with the overall variations being

within $\pm 5^\circ$ for each material. For Berea sandstone, the CO_2 treatment causes a slight increase in the contact angle from 31° to 34° , so the effect is minor staying within the accuracy range. However, the contact angle increases from 52° to 75° for Apulian limestone and from 55° to 83° for Indiana limestone, revealing a significant effect of CO_2 treatment. It is to be noted that the measured contact angles are apparent angles that are based on the average plane of the surface for air/water system, as it does not quantitatively characterize the true contact angle in the microscale pores for the CO_2 -water-rock system. However, it can be argued that these measurements provide a qualitative understanding on the effect of CO_2 treatment on the wettability of the reservoir rock.

Additionally, as the tested materials in this study are mainly composed of quartz or calcite, the contact angles of the pristine and CO_2 treated mineral crystals are measured (Figure 7.9). The contact angle for pristine quartz is 40° , and it increases to 42° after the treatment. For calcite, the contact angle changes from 78° to 83° , indicating that the effect of CO_2 treatment on the contact angle of minerals is significantly smaller than that for the porous rock that is composed of these minerals. This implies that the change in the contact angle for reservoir rock cannot result only from that of the minerals, but should also be attributed to the changes in the surface roughness. Detailed procedures for the CO_2 treatment of crystal minerals are elaborated in Kim and Makhnenko (2021).

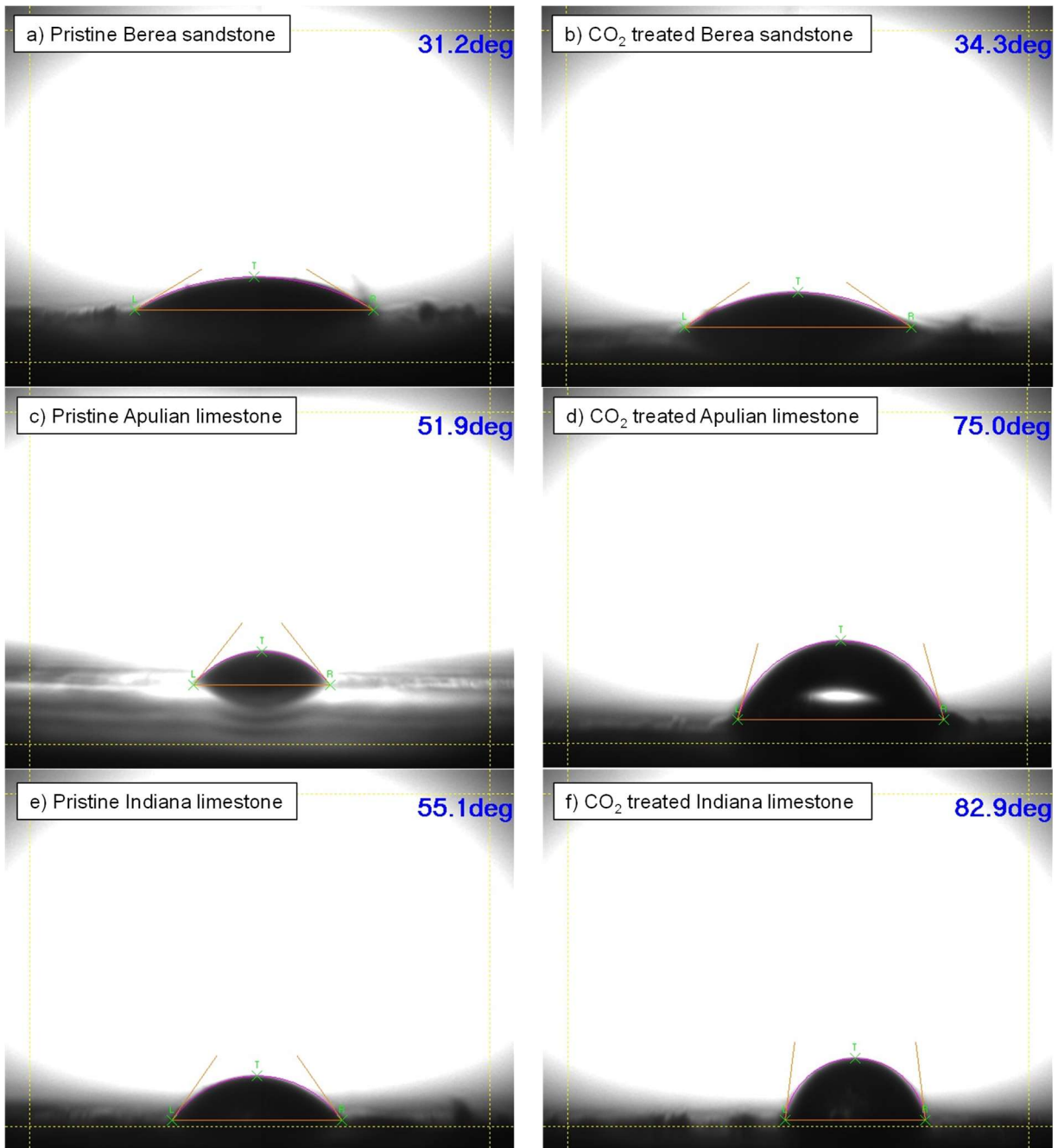


Figure 7.8. Apparent contact angle measurements for (a) pristine and (b) CO₂ treated Berea sandstone, (c) pristine and (d) CO₂ treated Apulian limestone, and (e) pristine and (f) CO₂ treated Indiana limestone. All measurements are conducted for the air/water/rock interface at ambient room temperature (22°C) and pressure.

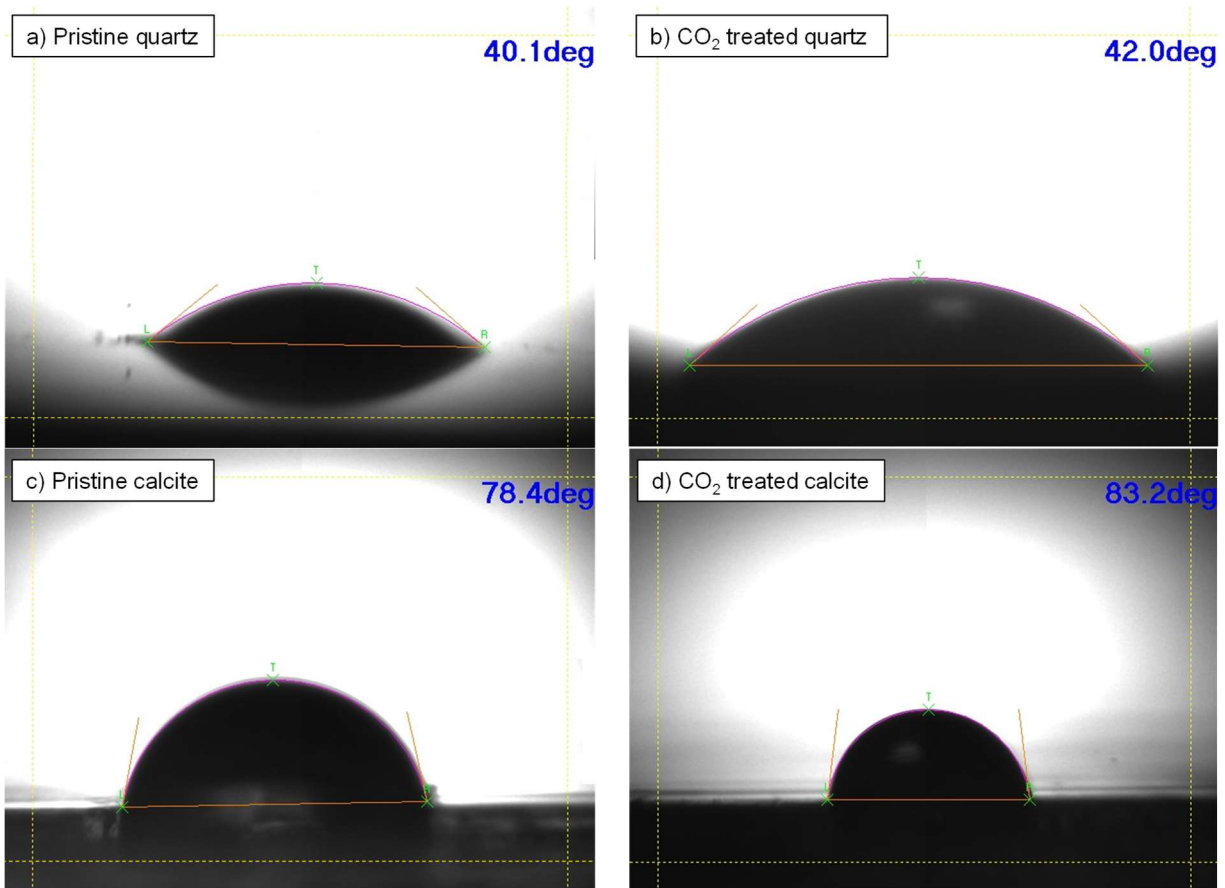


Figure 7.9. Apparent contact angle measurements of (a) pristine and (b) CO₂ treated quartz, and (c) pristine and (d) CO₂ treated calcite.

7.4.2. Surface roughness

One of the main reasons the apparent contact angle differs from the true contact angle is the surface roughness. Particularly, for porous rock formations, the pores contribute to surface rugosity, which requires thorough investigation (Cassie and Baxter, 1944). As the surface roughness is highly dependent on the specimen preparation, for this study, it is evaluated through the parameter R_q - the root mean square (RMS) average of the profile heights over the evaluation length of 1000 μm . Moreover, to investigate the effect of CO₂ treatment on the surface roughness, the ratio of the R_q values of the pristine and CO₂ treated samples ($R_{q,pris}/R_{q,CO_2}$) is reported. Ten to twelve scans are made for each specimen, and the average value of $R_{q,pris}/R_{q,CO_2}$

is calculated, while only the surface variation for a single measurement is presented in Figure 10. $R_{q,pris}/R_{q,CO_2}$ values appear to be larger than 1 for all materials, indicating that CO₂ treatment smoothens the surface at the microscale. It appears that the chemical effect is more pronounced for the limestones, where the $R_{q,pris}/R_{q,CO_2}$ values are reported as 2.4 and 2.2 for Apulian and Indiana limestones, while the value for Berea sandstone is 1.1.

Wenzel's relation predicts that a decrease in surface roughness would lead to a reduction in wettability, hence the increase in contact angle, as it is observed in this study for the CO₂ treated specimens (Wenzel, 1936). Considering Young's equation (equation 7.14), this effect can be intuitively verified, as the capillary pressure curve for water shifts down - towards smaller capillary pressure if the contact angle increases. Moreover, as the preceding study showed that the dominant pore sizes for the tested limestones increased after the CO₂ treatment (Kim and Makhnenko, 2021), the surface roughness measurements are in agreement with the theory of Cassie and Baxter (1944), stating that the apparent contact angles for porous surfaces should increase with the pore size (Figure 7.10).

In summary, the results align with the previous analyses on the wettability and surface roughness, indicating that the CO₂ treatment smoothens the rock surface, resulting in larger apparent contact angles for the wetting fluid. Therefore, this implies that the surface becomes more wet with respect to the non-wetting phase, which causes the increase in the maximum CO₂ saturation.

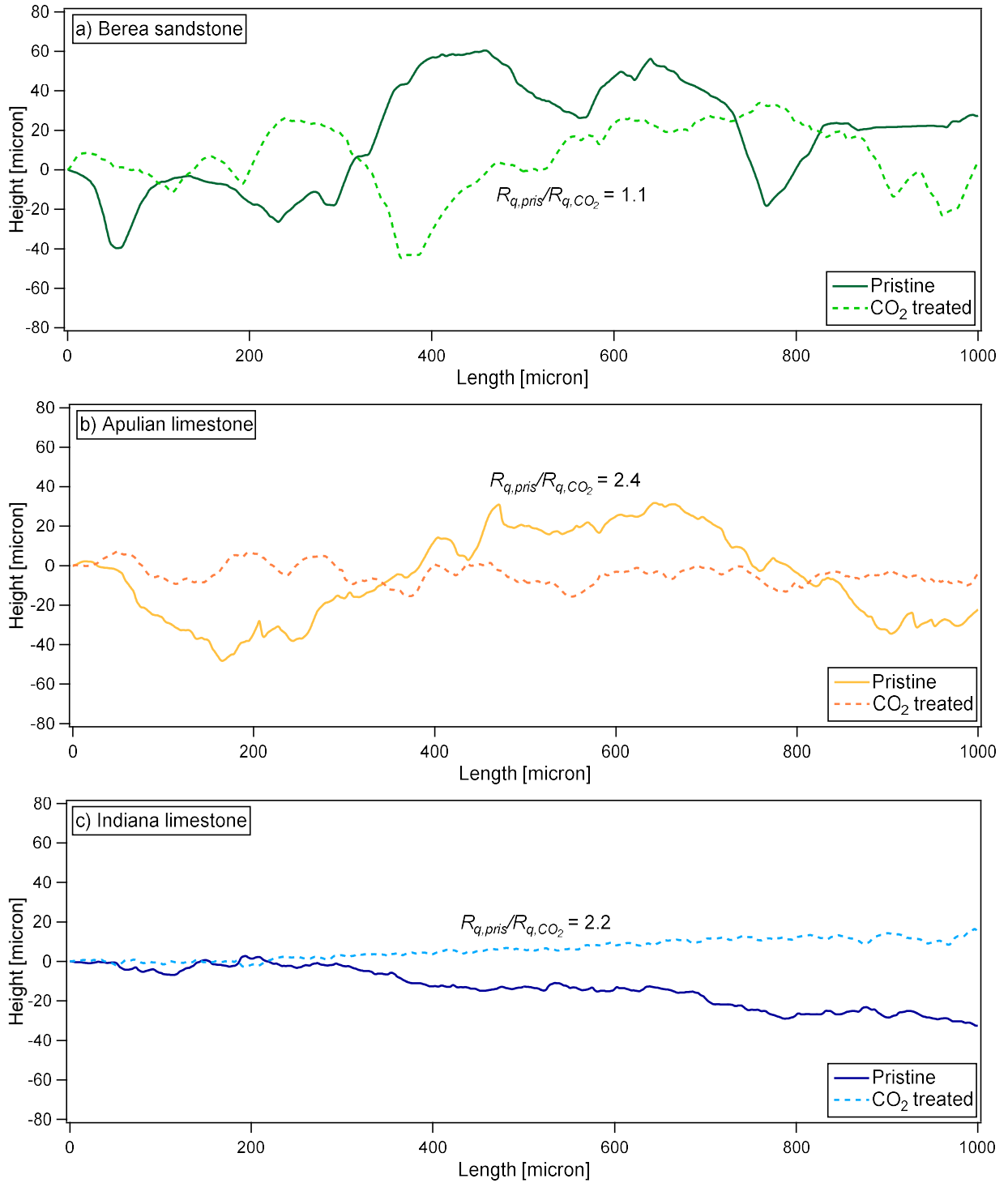


Figure 7.10. Surface roughness measurements of pristine and CO₂ treated: a) Berea sandstone, b) Apulian limestone, and c) Indiana limestone.

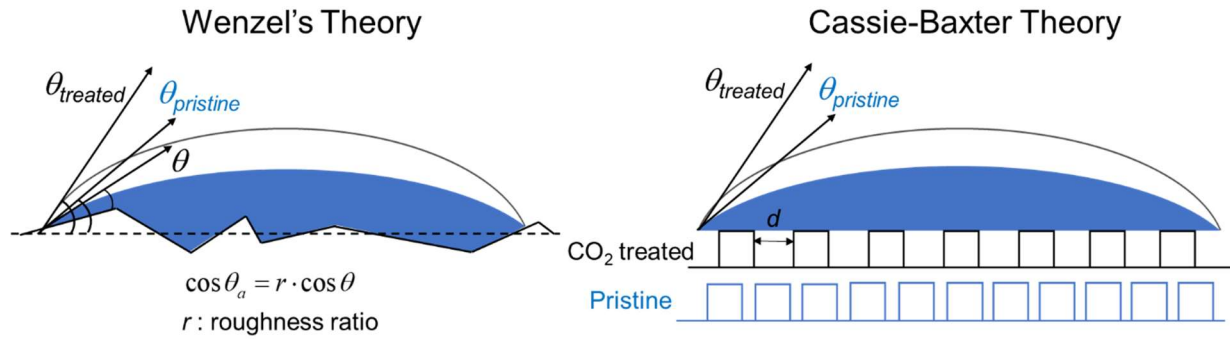


Figure 7.11. Illustrative comparison between the Wenzel's and Cassie-Baxter models for the apparent contact angles of pristine and CO₂ treated specimens.

7.5. Discussion

In the previous sections, the effect of CO₂ treatment on the poroelastic and multiphase flow response is experimentally determined, indicating that the compressibilities of limestones increase due to CO₂ treatment, while for the sandstone the effect is less pronounced. The relative permeability measurements suggest that the maximum degree of CO₂ saturation increases for all materials. The evaluation of the fitting parameters for the relative permeability curves shows that the Brooks-Corey exponents decrease for limestones, implying that the CO₂ treatment increases the relative permeability of CO₂ at the same degree of saturation. In this section, further analyses on the capillary pressure – saturation curves are presented. The capillary pressure curves for pristine and CO₂ treated specimens are reported by adopting the information on the residual water saturation that can be obtained from the relative permeability measurements. Lastly, a discussion on the limitations of the presented approach is presented.

7.5.1. Residual water saturation – capillary pressure curve

Although accurate measurements from the MIP method allow characterizing the capillary pressure for the mercury/air system, it cannot be directly applied to the water/CO₂ system (equation 7.15), because the residual CO₂ saturation also needs to be considered (Bennion and Bachu, 2005). The residual liquid saturation S_{rl} is the irreducible degree of saturation for the wetting phase, indicating the amount of the latter one that remains in the pores whichever are the pressure and flow rate of the non-wetting fluid. While the existing studies on CO₂ relative permeability and saturation mostly rely on X-ray computed tomography (CT) (Krevor et al., 2012, 2015; Akbarabadi and Piri, 2013), this technique has a number of limitations in terms of the possibility to simulate the in-situ stress conditions, as well as in terms of the available image resolution that neglects the presence of submicron scale pores (Elkhoury et al., 2019). In this study, a simple method to estimate the residual saturation from the relative permeability curve is adopted. As the selected reservoir formations have relatively large pores and almost no inclusions of clay minerals, it is assumed that the effect of hysteresis is minor, which is confirmed via the experimental observations. Thus, the fitting curves for the discrete measurements of relative permeabilities are utilized to determine the residual saturation.

From the relative permeability measurements, the equation for the fitting curves can be obtained by the least-squares method, which allows the calculation of the effective saturation parameter S_e at zero relative permeability. Subsequently, the residual water saturation S_{rl} can be obtained using equation (7.10) for S_e . For Berea sandstone, S_{rl} is equal to 0.1 for pristine and CO₂ treated specimens. The residual water saturation is calculated to be 0.08 and 0.07 for pristine Apulian limestone and Indiana limestone, respectively, and these values decrease to almost zero (≈ 0.01) after CO₂ treatment. These observations are in accordance with the previous studies, where the

residual saturation is reported to be in the range of 0.05-0.11 for reservoir rock (Bennion and Bachu, 2008; Krevor et al., 2012; Pini and Krevor, 2019; Niu and Krevor, 2020). The decrease in the S_{rl} values for limestones implies that higher CO₂ saturation can be achieved after the CO₂ treatment. As the residual liquid saturation values are obtained, the capillary pressure – saturation curves for the CO₂/water system can now be determined. By changing the minimum value of water saturation with respect to the measured residual saturation of CO₂, the capillary pressure – saturation curve can be proportionally reformed.

For Berea sandstone, the water saturation decreases at 0.004 MPa capillary pressure, and no significant effect of the CO₂ treatment is observed. The CO₂ entry pressure of Apulian limestone significantly decreases due to the treatment from 0.04 MPa to 0.01 MPa. This indicates that the non-wetting fluid (liquid CO₂ in this case) can more easily intrude into the pores. However, the effect is less pronounced for Indiana limestone, as its CO₂ entry pressure decreases only slightly from 0.009 to 0.008 MPa.

The van Genuchten parameters (α , m , and n) assessed from the relative permeability measurements (Table 7.1) are utilized to validate the capillary pressure – saturation curves obtained from the MIP tests (Figure 7.12). The two methods show an excellent agreement, so it can be argued that the introduced approach for reporting the relative permeability curve is acceptable. The only discrepancy is observed at low water saturation for Berea sandstone, which may be caused by a few factors. Firstly, it is the difference between specimen sizes for the core flooding (10 cm long) and MIP (<1 cm linear dimension) tests. Berea sandstone contains grains with sizes 70-400 μm and pores and cracks with sizes up to 0.1 mm, while for the limestones they are an order of magnitude smaller. The small size of MIP specimens with relatively large pores and cracks on its surface may affect the saturation curve measurements (Churcher et al.,

1991). Secondly, errors in determining the fitting curves can provide another explanation for the disagreement between the two methods. The relative permeability curve is highly sensitive to the value of the entry pressure of the non-wetting fluid, where a major decrease in the degree of saturation occurs. However, as few studies have reported, van Genuchten model has some limitations in accurately assessing the capillary pressure and saturation at low saturation conditions (Krevor et al., 2012; Pini and Krevor, 2019). The pore distribution results obtained from MIP experiments cannot always be directly used to evaluate the relative permeability curves, and direct capillary pressure measurements at low saturation levels are suggested (Oostrom et al., 2016).

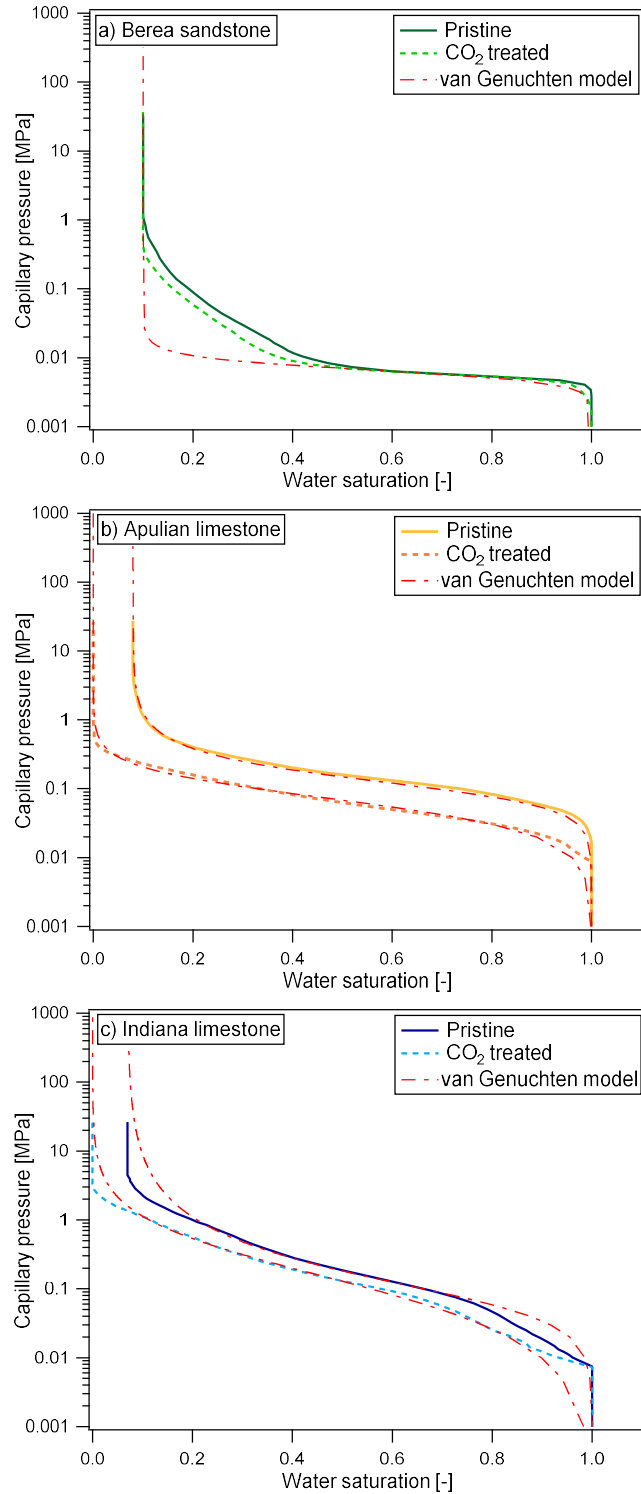


Figure 7.12. Analysis for the capillary pressure versus water saturation for CO₂/water system of pristine and CO₂ treated a) Berea sandstone, b) Apulian limestone, and c) Indiana limestone.

Table 7.3. Summary of the measurements of residual water saturation S_{rl} , breakthrough pressure, measured apparent contact angle, and ratio of the pristine to CO₂ treated surface roughness.

		Residual water saturation S_{rl} [-]	Breakthrough pressure [MPa]	Apparent contact angle [°]	Surface roughness $R_{q,pris}/R_{q,CO_2}$ [-]
Berea sandstone	Pristine	0.10	0.004	31.2	1.1
	CO ₂ treated			34.3	
Apulian limestone	Pristine	0.08	0.040	51.9	2.4
	CO ₂ treated	0.01	0.010	75.0	
Indiana limestone	Pristine	0.07	0.009	55.1	2.2
	CO ₂ treated	0.01	0.008	82.9	

7.5.2. Limitations of the approach

In this study, a novel method is introduced to characterize the relative permeability curve by estimating the degree of saturation of the two fluids as the poromechanical responses are accurately measured. Although this method offers significant advantages, there are some limitations that need to be discussed.

The degree of saturation for the multiphase flow experiment is calculated by measuring the Skempton's B coefficient, where it is assumed that the pore fluid is evenly distributed in the pores (equation 7.5). However, few studies reported that the CO₂ saturation could be larger in the upstream and gradually decrease towards the downstream (Krevor et al., 2012; Chen et al., 2014). Although the undrained condition is maintained for a sufficient time (10 minutes) to redistribute the fluids before the measurements are performed, this may affect the measured B values and cause errors in evaluating the degree of saturation of CO₂.

The novel method introduced in this study calculates the degree of water/CO₂ saturation by measuring the poroelastic properties, as the accuracy and validation of this technique need to be discussed. From the measurement of Skempton's B coefficient, the bulk modulus of the mixed fluid of CO₂ and water ($K_{f,mix}$) is calculated (equation 7.5). Since the B values significantly

decrease as CO₂ is injected, the uncertainty in reported $K_{f,mix}$ values increases, resulting in larger errors for the reported degree of saturation. Also, for the non-wetting fluid saturation above 20%, the wetting fluid may not exist as a continuous phase in the pores, limiting the application of the Wood's formula and potentially causing uneven pore pressure distribution (Dullien, 1992). The applicability of this method for anisotropic materials that contain multiple minerals may also be an issue, as it provides uncertainty in calculating the applied mean stress (equation 7.4) and may violate the ideal porous media assumption of $K_s' = K_s''$ increasing the errors in calculated Skempton's B coefficients (equation 7.5).

By duplicating the experiments and considering the accuracy of the experimental devices, the relative errors in determining the material properties are calculated as follows: 3% for the porosity, 5% for permeability, 3% for Skempton's B coefficient, 3% for the bulk moduli, and 10% for the degree of saturation. It is to be noted that the fitting parameters for the relative permeability curve (e.g., Brooks-Corey exponent) may differ by up to 50% due to the error range in the degree of saturation, so the average value is taken for comparison.

The hysteresis of the CO₂/water relative permeability curve for drainage and imbibition is another potential issue that has been reported in a few studies (Juanes et al., 2006; Bennion and Bachu, 2007; 2008). This effect is argued to be minor for the tested reservoir rock, where we only concentrate on the drainage procedure (injection of the non-wetting fluid), assuming no hysteresis for the capillary pressure and relative permeability.

Lastly, the difference between the lab- and the field-scales needs to be considered. Despite accurate laboratory measurements of relative permeability and characterization of the microscopic properties, these findings cannot be directly applied for field-scale problems, as the preferential flow paths such as wormholes, cracks, and faults may affect the hydraulic behavior

(Szymczak and Ladd, 2009; Elkhoury et al., 2013). Thus, future work may be suggested to characterize the upscaling effect for reservoir characterization (Saad et al., 1995). As no direct measurements of relative permeability have been performed at the field-scale, efforts to upscale the laboratory measurements have been introduced for the large-scale simulations (Crotti and Cobeñas, 2001; Benson and Doughty, 2006; Kamali and Hussain, 2017) but further research needs to be conducted regarding validation of the proposed methods.

7.6. Conclusions

This study characterizes the effect of CO₂ treatment on the multiphase flow characteristics of reservoir rock, by comprehensively considering various factors such as poroelastic deformation, capillary pressure, wettability, and surface roughness. By selecting one silica-rich and two calcite-rich porous rocks, the chemical effect on the type of the dominant mineral is examined. Different experimental methods – core flooding, mercury intrusion porosimetry, microgoniometry, and profilometry are introduced to characterize the changes in relative permeability, capillary pressure, wettability, and surface roughness of reservoir formations during CO₂ injection. A robust technique is implemented to evaluate the relative permeability curve from the measurements of the changes in poroelastic response upon CO₂ flow in the rock, and the results are compared with independent evaluations based on the direct capillary pressure measurements. The capillary pressure curves are affected due to the chemical effect caused by CO₂ injection in water-saturated limestones, where the exponent values for the Brooks-Corey model decrease, implying that the relative CO₂ permeability increases with maximum CO₂ saturation. On the other hand, the exponent value is reported to remain constant for the sandstone, while its maximum CO₂ saturation slightly increases. A qualitative analysis of the

contact angle and the surface roughness is conducted, showing that the CO₂ treatment smoothens the surface for limestones and increases their CO₂ wettability, while the effect is almost unnoticeable for the sandstone. This implies that CO₂ treatment may affect the relative permeability and wettability, highlighting the importance of adopting accurate multiphase flow parameters for reservoir models, that are often assumed to be constant. In conclusion, this study thoroughly investigates the effect of CO₂ treatment on the multiphase flow characteristics of reservoir rock and suggests that the chemical effect can increase the CO₂ injectivity in calcite-rich rock.

References

- Abdallah, W., Buckley, J.S., Carnegie, A., Edwards, J., Herold, B., Fordham, E., Graue, A., Habashy, T., Seleznev, N., Signer, C., Hussain, H. (1986) Fundamentals of wettability. Technology. 38: 1125-1144.
- Achenbach, J. (2012) Wave propagation in elastic solids. Elsevier.
- Adamson, A.W., Gast, A.P. (1967) Physical chemistry of surfaces (Vol. 15). New York: Interscience publishers.
- Akbarabadi, M., Piri, M. (2013) Relative permeability hysteresis and capillary trapping characteristics of supercritical CO₂/brine systems: An experimental study at reservoir conditions. Adv Water Resour. 52: 190-206.
- Al-Anssari, S., Arif, M., Wang, S., Barifcani, A., Lebedev, M., Iglauer, S. (2017) Wettability of nano-treated calcite/CO₂/brine systems: Implication for enhanced CO₂ storage potential. Int J Greenh Gas Control. 66: 97-105.

- Al-Yaseri, A.Z., Lebedev, M., Barifcani, A., Iglauer, S. (2016) Receding and advancing (CO₂+ brine+ quartz) contact angles as a function of pressure, temperature, surface roughness, salt type and salinity. *J Chem Thermodyn.* 93: 416-423.
- Amalokwu, K., Best, A.I., Sothcott, J., Chapman, M., Minshull, T., Li, X.Y. (2014) Water saturation effects on elastic wave attenuation in porous rocks with aligned fractures. *Geophys J Int.* 197(2): 943-7.
- Amirfazli, A., Kwok, D.Y., Gaydos, J., Neumann, A.W. (1998) Line tension measurements through drop size dependence of contact angle. *J Colloid Interface Sci.* 205(1): 1-1.
- Amott, E. (1959) Observations relating to the wettability of porous rock. *Transactions of the AIME.* 216(01): 156-162.
- Anderson, W. (1986) Wettability literature survey-part 2: Wettability measurement. *J Pet Technol.* 38(11): 1246-1262.
- Bachu, S. (2013) Drainage and imbibition CO₂/brine relative permeability curves at in situ conditions for sandstone formations in western Canada. *Energy Procedia.* 37: 4428-4436.
- Bachu, S., Bennion, B. (2008) Effects of in-situ conditions on relative permeability characteristics of CO₂-brine systems. *Environ Geol.* 54(8): 1707-1722.
- Baldacchini, T., Carey, J.E., Zhou, M., Mazur, E. (2006) Superhydrophobic surfaces prepared by microstructuring of silicon using a femtosecond laser. *Langmuir.* 22(11): 4917-4919.
- Bear, J. (1988) *Dynamics of fluids in porous media.* Courier Corporation.
- Bennion, B., Bachu, S. (2005) Relative permeability characteristics for supercritical CO₂ displacing water in a variety of potential sequestration zones. In *SPE Annual Technical Conference and Exhibition.* Society of Petroleum Engineers.

- Bennion, D.B., Bachu, S. (2007) Permeability and relative permeability measurements at reservoir conditions for CO₂-water systems in ultra low permeability confining caprocks. In EUROPEC/EAGE Conference and Exhibition. SPE 106995.
- Bennion, B., Bachu, S. (2008) Drainage and imbibition relative permeability relationships for supercritical CO₂/brine and H₂S/brine systems in intergranular sandstone, carbonate, shale, and anhydrite rocks. SPE Reserv Evaluation Eng. 11: 487-496.
- Benson, S.M., Doughty, C. (2006) Estimation of field-scale relative permeability from pressure transient tests. In Proceedings, EPA CO₂SC Workshop, Berkeley, CA: Lawrence Berkeley National Laboratory.
- Biot, M.A. (1941) General theory of three-dimensional consolidation. J Appl Phys. 12: 155-164.
- Brooks, R.H., Corey, A.T. (1964) Hydraulic Properties of Porous Media. Hydrology Papers 3. Colorado State University, Fort Collins, CO.
- Burdine, N.T. (1953) Relative permeability calculations from pore size distribution data. Trans Am Inst Mining Metall Eng. 198: 71–78.
- Cassie, A.B.D., Baxter, S. (1944) Wettability of porous surfaces. Trans Faraday Soc. 40: 546-51.
- Chadwick, A., Arts, R., Eiken, O., Williamson, P., Williams, G. (2006) Geophysical monitoring of the CO₂ plume at Sleipner, North Sea. In Advances in the Geological Storage of Carbon Dioxide. Springer, Dordrecht. 303–314.
- Chen, Z., Ewing, R.E., Espedal, M. (1994) Multiphase flow simulation with various boundary conditions. Comput Meth Water Res. 925-32.
- Chen, X., Kianinejad, A., DiCarlo, D.A. (2014) An experimental study of CO₂-brine relative permeability in sandstone. Society of Petroleum Engineers, Richardson, TX, US. SPE-169137-MS.

- Churcher, P.L., French, P.R., Shaw, J.C., Schramm, L.L. (1991) Rock properties of Berea sandstone, Baker dolomite, and Indiana limestone. Society of Petroleum Engineers, Anaheim, CA, US. SPE 21044.
- Civan, F., Donaldson, E.C. (1989) Relative permeability from unsteady-state displacements with capillary pressure included. SPE Formation Evaluation. 4(02): 189-193.
- Cnudde, V., Boone, M.N. (2013) High-resolution X-ray computed tomography in geosciences: A review of the current technology and applications. Earth-Sci Rev. 123: 1-17.
- Collins, H.C. (1979) The Mississippian and Pennsylvanian (Carboniferous) systems in the United States. Ohio, United States Geological Survey.
- Craig, F.F. (1971) The reservoir engineering aspects of waterflooding, Monograph Series. Society of Petroleum Engineers of AIME.
- Crotti, M.A., Cobeñas, R.H. (2001) Scaling Up of Laboratory Relative Permeability Curves. An Advantageous Approach Based on Realistic Average Water Saturations. In SPE Latin American and Caribbean Petroleum Engineering Conference.
- Detournay, E., Cheng, A.H-D. (1993) Fundamentals of poroelasticity. In: Fairhurst C, editor. Comprehensive rock engineering, Vol. II. Oxford: Pergamon. 113-71.
- Donaldson, E.C., Thomas, R.D., Lorenz, P.B. (1969) Wettability determination and its effect on recovery efficiency. Soc Pet Eng J. 9(01): 13-20.
- Donaldson, E.C., Civan, F., Ul Alam, M.W. (1988) Relative permeabilities at simulated reservoir conditions. SPE Reserv Eng. 3(04): 1323-1327.
- Drelich, J., Miller, J.D., Good, R.J. (1996) The effect of drop (bubble) size on advancing and receding contact angles for heterogeneous and rough solid surfaces as observed with sessile-drop and captive-bubble techniques. J Colloid Interface Sci. 179(1): 37-50.

- Dullien, F.A.L. (1992) Porous Media Fluid Transport and Pore Structure. Acad Press Inc, San Diego, California.
- Elkhoury, J.E., Ameli, P., Detwiler, R.L. (2013) Dissolution and deformation in fractured carbonates caused by flow of CO₂-rich brine under reservoir conditions. *Int J Greenh Gas Control*. 16: S203-15.
- Elkhoury, J.E., Shankar, R., Ramakrishnan, T.S. (2019) Resolution and limitations of X-ray micro-CT with applications to sandstones and limestones. *Trans Porous Media*. 129(1).
- Espinoza, D.N., Santamarina, J.C. (2010) Water-CO₂-mineral systems: Interfacial tension, contact angle, and diffusion—Implications to CO₂ geological storage. *Water Resour Res*. 46(7).
- Falcon-Suarez, I.H., Papageorgiou, G., Jin, Z., Muñoz-Ibáñez, A., Chapman, M., Best, A.I. (2020) CO₂-brine substitution effects on ultrasonic wave propagation through sandstone with oblique fractures. *Geophys Res Lett*. 47(16): e2020GL088439.
- Falode, O., Manuel, E. (2014) Wettability effects on capillary pressure, relative permeability, and irreducible saturation using porous plate. *J Pet Eng*.
- Farokhpoor, R., Bjørkvik, B.J., Lindeberg, E., Torsæter, O. (2013) CO₂ wettability behavior during CO₂ sequestration in saline aquifer-An Experimental study on minerals representing sandstone and carbonate. *Energy Procedia*. 37: 5339-51.
- Fulcher, R.A., Ertekin, T., Stahl, C.D. (1985) Effect of capillary number and its constituents on two phase relative permeability curves. *J Pet Technol* 37: 249–260.
- Good, R.J. (1979) Contact angles and the surface free energy of solids. In *Surface and colloid science*. Springer, Boston, MA.

- Grombacher, D., Vanorio, T., Ebert, Y. (2012) Time-lapse acoustic, transport, and NMR measurements to characterize microstructural changes of carbonate rocks during injection of CO₂-rich water. *Geophys.* 77(3): WA169-WA179.
- Haeri, F., Tapriyal, D., Sanguinito, S., Shi, F., Fuchs, S.J., Dalton, L.E., Baltrus, J., Howard, B., Crandall, D., Matranga, C., Goodman, A. (2020) CO₂-Brine contact angle measurements on Navajo, Nugget, Bentheimer, Bandera Brown, Berea, and Mt. Simon sandstones. *Energy Fuels.* 34(5): 6085-6100.
- Ionescu, E., Maini, B.B. (1983) A review of laboratory techniques for measuring wettability of petroleum reservoir rocks. US Department of Energy, Technical Report.
- IPCC. (2005) IPCC Special Report on Carbon Dioxide Capture and Storage. Cambridge University Press.
- IPCC. (2021) Climate Change 2021: The Physical Science Basis. Contribution of Working Group I to the Sixth Assessment Report of the Intergovernmental Panel on Climate Change. Cambridge University Press.
- Johnson, R.E. (1969) Wettability Contact Angles. *Surface Colloid Sci.* 2: 85-153.
- Johnson, J.W., Nitao, J.J., Morris, J.P. (2005) Reactive transport modeling of caprock integrity during natural and engineered CO₂ storage. *Carbon Dioxide Capture for Storage in Deep Geologic Formations.* Elsevier, Oxford, UK. 787-813.
- Juanes, R., Spiteri, E.J., Orr Jr, F.M., Blunt, M.J. (2006) Impact of relative permeability hysteresis on geological CO₂ storage. *Water Resour Res.* 42: W12418.
- Kamali, F., Hussain, F. (2017) Field-scale simulation of CO₂ enhanced oil recovery and storage through SWAG injection using laboratory estimated relative permeabilities. *J Pet Sci Eng.* 156: 396-407.

- Kaveh, N.S., Rudolph, E.S.J., Van Hemert, P., Rossen, W.R., Wolf, K.H. (2014) Wettability evaluation of a CO₂/water/bentheimer sandstone system: contact angle, dissolution, and bubble size. *Energy Fuels*. 28(6): 4002-4020.
- Kim, K., Vilarrasa, V., Makhnenko, R.Y. (2018) CO₂ injection effect on geomechanical and flow properties of calcite-rich reservoirs. *Fluids*. 3(3): 66.
- Kim, K., Makhnenko, R.Y. (2020a) Coupling between poromechanical behavior and fluid flow in tight rock. *Trans Porous Media*. 135(2): 487-512.
- Kim, K., Makhnenko, R.Y. (2020b) Evolution of poroviscoelastic properties of silica-rich rock after CO₂ injection. *InE3S Web of Conferences*. EDP Sciences. 205: 08007.
- Kim, K., Makhnenko, R.Y. (2021) Changes in rock matrix compressibility during deep CO₂ storage. *Greenh Gas: Sci Tech*. 0: 1-20.
- Kopp, A., Class, H., Helmig, R. (2009) Investigations of CO₂ storage capacity in deep saline aquifers. Part 1: Dimensional analysis of flow processes and reservoir characteristics. *Int J Greenh Gas Control*. 3(3): 263-276.
- Krevor, S.C., Pini, R., Zuo, L., Benson, S.M. (2012) Relative permeability and trapping of CO₂ and water in sandstone rocks at reservoir conditions. *Water Resour Res*. 48(2).
- Krevor, S., Blunt, M.J., Benson, S.M., Pentland, C.H., Reynolds, C., Al-Menhali, A., Niu, B. (2015) Capillary trapping for geologic carbon dioxide storage—From pore scale physics to field scale implications. *Int J Greenh Gas Control*. 40: 221-237.
- Lowe, J., Johnson, T.C. (1960) Use of back pressure to increase degree of saturation of triaxial test specimens. In: *Proceedings of the Research Conference on Shear Strength of Cohesive Soils*, Boulder, Colorado, ASCE. 819–836.

- Luquot, L., Gouze, P. (2009) Experimental determination of porosity and permeability changes induced by injection of CO₂ into carbonate rocks. *Chem Geol.* 265: 148–159.
- Lv, P., Liu, Y., Wang, Z., Liu, S., Jiang, L., Chen, J., Song, Y. (2017) In situ local contact angle measurement in a CO₂–brine–sand system using microfocused X-ray CT. *Langmuir.* 33(14): 3358-66.
- Makhnenko, R.Y., Labuz, J.F. (2016) Elastic and inelastic deformation of fluid-saturated rock. *Phil Trans R Soc A.* 374: 20150422.
- Marsden, S.S. (1965) Wettability-Its measurement and application to waterflooding. *J Jap Assoc Pet Tech.* 30(1): 1-10.
- Martinez, M.J., Newell, P., Bishop, J.E., Turner, D.Z. (2013) Coupled multiphase flow and geomechanics model for analysis of joint reactivation during CO₂ sequestration operations. *Int J Greenh Gas Control.* 17: 148-60.
- Mazumder, S., Wolf, K.H. (2008) Differential swelling and permeability change of coal in response to CO₂ injection for ECBM. In *SPE Asia Pacific Oil and Gas Conference and Exhibition.*
- McCaffery, F.G., Mungan, N. (1970) Contact angle and interfacial tension studies of some hydrocarbon-water-solid systems. *J Can Pet Technol.* 9(03).
- Morrow, N.R. (1975) The effects of surface roughness on contact: angle with special reference to petroleum recovery. *J Can Pet Technol.* 14(04).
- Morrow, N.R. (1990) Wettability and its effect on oil recovery. *J Pet Technol.* 42(12): 1476-1484.
- Mualem, Y. (1976) New model for predicting hydraulic conductivity of unsaturated porous media. *Water Resour Res.* 12(3): 513–522.

- Müller, N. (2011) Supercritical CO₂-brine relative permeability experiments in reservoir rocks— literature review and recommendations. *Trans Porous Media*. 87(2): 367-383.
- Neumann, A.W., Good, R.J. (1979) Techniques of measuring contact angles. In *Surface and colloid science* (pp. 31-91). Springer, Boston, MA.
- Newberry, J.S. (1874) Report of the Geological Survey of Ohio. Nevins & Myers. 2: 1.
- Niu, B., Krevor, S. (2020) The Impact of Mineral Dissolution on Drainage Relative Permeability and Residual Trapping in Two Carbonate Rocks. *Trans Porous Media*. 131(2): 363-380.
- Oostrom, M., White, M.D., Porse, S.L., Krevor, S.C., Mathias, S.A. (2016) Comparison of relative permeability–saturation–capillary pressure models for simulation of reservoir CO₂ injection. *Int J Greenh Gas Control*. 45: 70-85.
- Orr Jr, F.M. (2004) Storage of carbon dioxide in geologic formations. *J Pet Technol*. 56(9): 90-97.
- Patton, J.B., Carr, D.D. (1982) The Salem limestone in the Indiana building-stone district. Indiana Geological Survey.
- Perrin, J.C., Krause, M., Kuo, C.W., Miljkovic, L., Charoba, E., Benson, S.M. (2009) Core-scale experimental study of relative permeability properties of CO₂ and brine in reservoir rocks. *Energy Procedia*. 1(1): 3515-22.
- Pini, R., Krevor, S.C., Benson, S.M. (2012) Capillary pressure and heterogeneity for the CO₂/water system in sandstone rocks at reservoir conditions. *Adv Water Resour*. 38: 48-59.
- Pini, R., Krevor, S. (2019) Laboratory Studies to Understand the Controls on Flow and Transport for CO₂ Storage. In *Science of Carbon Storage in Deep Saline Formations*, Elsevier. 145-180.
- Pruess, K., Oldenburg, C.M., Moridis, G. (1999) TOUGH2 User's Guide, Version 2.0. Report LBNL-43134. Lawrence Berkeley National Laboratory, Berkeley, CA, USA.

- Pruess, K., Garcia, J. (2002) Multiphase flow dynamics during CO₂ disposal into saline aquifers. *Environ Geol.* 42: 282–295.
- Rayward-Smith, W.J., Woods, A.W. (2011) Some implications of cold CO₂ injection into deep saline aquifers. *Geophys Res Lett.* 38(6).
- Rohmer, J., Pluymakers, A., Renard, F. (2016) Mechano-chemical interactions in sedimentary rocks in the context of CO₂ storage: weak acid, weak effects? *Earth Sci Rev.* 157: 86-110.
- Rutqvist, J. (2012) The geomechanics of CO₂ storage in deep sedimentary formations. *Geotech Geol Eng.* 30(3): 525–551.
- Saad, N., Cullick, A.S., Honarpour, M.M. (1995) Effective relative permeability in scale-up and simulation. In *Low Permeability Reservoirs Symposium*.
- Sarmadivaleh, M., Al-Yaseri, A.Z., Iglauer, S. (2015) Influence of temperature and pressure on quartz–water–CO₂ contact angle and CO₂–water interfacial tension. *J Colloid Interface Sci.* 441: 59-64.
- Scanziani, A., Singh, K., Blunt, M.J., Guadagnini, A. (2017) Automatic method for estimation of in situ effective contact angle from X-ray micro tomography images of two-phase flow in porous media. *J Colloid Interface Sci.* 496: 51-9.
- Sedaghatinasab, R., Kord, S., Moghadasi, J., Soleymanzadeh, A. (2021) Relative permeability hysteresis and capillary trapping during CO₂ EOR and sequestration. *Int J Greenh Gas Control.* 106: 103262.
- Shaffer, N.R. (2020) *Indiana Limestone: America's building stone*. Geological Society, London, Special Publications. 486(1): 77-101.

- Shi, J.Q., Xue, Z., Durucan, S. (2007) Seismic monitoring and modelling of supercritical CO₂ injection into a water-saturated sandstone: Interpretation of P-wave velocity data. *Int J Greenh Gas Control*. 1(4): 473-80.
- Shi, Z., Sun, L., Haljasmaa, I., Harbert, W., Sanguinito, S., Tkach, M., Goodman, A., Tsotsis, T.T., Jessen, K. (2019) Impact of Brine/CO₂ exposure on the transport and mechanical properties of the Mt Simon sandstone. *J Pet Sci Eng*. 177.
- Su, E., Liang, Y., Zou, Q., Niu, F., Li, L. (2019) Analysis of effects of CO₂ injection on coalbed permeability: implications for coal seam CO₂ sequestration. *Energy Fuels*. 33(7): 6606-6615.
- Szymczak, P., Ladd, A.J. (2009) Wormhole formation in dissolving fractures. *J Geophys Res: Solid Earth*. 114(B6).
- Tamai, Y., Aratani, K. (1972) Experimental study of the relation between contact angle and surface roughness. *J Phys Chem*. 76(22): 3267-71.
- Tarokh, A., Makhnenko, R.Y. (2019) Remarks on the solid and bulk responses of fluid-filled porous rock. *Geophysics*. 84(4): WA83-WA95.
- Tarokh, A., Makhnenko, R.Y., Kim, K., Zhu, X., Popovics, J.S., Segvic, B., Sweet, D.E. (2020) Influence of CO₂ injection on the poromechanical response of Berea sandstone. *Int J Greenh Gas Control*. 95: 102959.
- Tudek, J., Crandall, D., Fuchs, S., Werth, C.J., Valocchi, A.J., Chen, Y., Goodman, A. (2017) In situ contact angle measurements of liquid CO₂, brine, and Mount Simon sandstone core using micro X-ray CT imaging, sessile drop, and Lattice Boltzmann modeling. *J Pet Sci Eng*. 155: 3-10.
- U. S. Department of Energy. (2010) Carbon Sequestration Atlas of the United States and Canada, 3rd ed., US DOE, Washington, D.C.

- van Genuchten, M.T. (1980) A closed-form equation for predicting the hydraulic conductivity of unsaturated soils. *Soil Sci Soc Am J.* 44(5): 892-898.
- Vilarrasa, V., Makhnenko, R.Y., Rutqvist, J. (2019) Field and laboratory studies of geomechanical response to the injection of CO₂. In: *Science of Carbon Storage in Deep Saline Formations*. Elsevier, Oxford, UK. 209-236.
- Wang, S., Edwards, I.M., Clarens, A.F. (2013) Wettability phenomena at the CO₂-brine-mineral interface: implications for geologic carbon sequestration. *Environ Sci Tech.* 47(1): 234-241.
- Wenzel, R.N. (1936) Resistance of solid surfaces to wetting by water. *Ind Eng Chem Res.* 28(8): 988-994.
- Winkler, K.W., Plona, T.J. (1982) Technique for measuring ultrasonic velocity and attenuation spectra in rocks under pressure. *J Geophys Res: Solid Earth.* 87(B13): 10776-80.
- Wood, A.B. (1930) *A textbook of sound*. G. Bell and Sons, London.
- Xu, T., Pruess, K. (2001) Modeling multiphase non-isothermal fluid flow and reactive geochemical transport in variably saturated fractured rocks: 1 Methodology. *Am J Sci.* 301: 16-33.
- Xu, T., Sonnenthal, E.L., Spycher, N., Pruess, K. (2006) TOURGHREACT: a simulation program for non-isothermal multiphase reactive geochemical transport in variably saturated geologic media. *Comput Geosci.* 32: 145-165.

CHAPTER 8: COUPLING BETWEEN POROMECHANICAL BEHAVIOR AND FLUID FLOW IN TIGHT ROCK

Based on a manuscript published in Transport in Porous Media

Kim, K., Makhnenko, R.Y. (2020) Coupling between poromechanical behavior and fluid flow in tight rock. Transport in Porous Media. 135(2): 487-512.

Abstract

Proper characterization of the mechanical and flow properties of participating rock formations is crucial for subsurface geo-energy projects, including hydrocarbon extraction, geologic carbon storage, and enhanced geothermal systems. Application of mechanical and hydraulic pressures changes the porosity of rock and modifies flow paths. For low-permeable or “tight” rock that mainly contains nanoscale pores and serves as the confining layer for underground storage operations, a significant change in permeability may occur due to a small change in porosity. The pore volume changes in nanoporous geomaterials are extremely difficult to measure directly, but can be assessed from the knowledge of the hydromechanical response. Experimental methods to measure the stress-dependent permeability and poroelastic parameters of fluid-saturated tight rock are introduced. Eau Claire shale, Opalinus clay (claystone), and Charcoal granite are selected as representative materials for tight rock and their pore structure and material properties are carefully investigated. The porosity-permeability relationship for tight rock is established by adopting a power-law dependence with the exponent value in the range of 15-17, thus being significantly larger than that for a porous reservoir rock. Consequently, even small perturbations

of porosity can cause orders of magnitude changes in permeability, possessing a risk on the sealing capacity of the tight formations.

8.1. Introduction

Establishment of porosity-permeability relationship for rock provides a straightforward way to couple its mechanical and hydraulic behavior thus being a topic of investigation in geophysical and petroleum engineering research. Fluid flow through the subsurface rock is affected by the external stress and internal pore pressure that affect the pore structure and modify the flow paths (Bear, 1972; Biot, 1973). Porosity and permeability are well-known as essential properties that can be selected to represent the pore space and hydro-mechanical behavior of subsurface rocks (Quintard, 1993). For petroleum engineering and sustainable geo-energy applications, such as enhanced geothermal systems (EGS), geological carbon storage (GCS), and radioactive waste disposal, understanding these characteristics is of great interest because corresponding reservoir formations require adequate storage capacity and flow efficiency, while the stability in terms of leakage should be carefully evaluated for the tight sealing layers (Tsang et al., 2005; Ezekwe, 2010; Rutqvist, 2012; Song and Zhang, 2012). Therefore, finding a relationship between porosity and permeability possesses a considerable advantage for geoengineering projects (Ahmed, 2006; Bernabé et al., 2003), especially in the cases where measurements of material properties are limited (Cui et al., 2009; Trimmer, 1981).

Various approaches have been proposed to introduce a relationship between porosity and permeability, including the notable Kozeny-Carman equation. Kozeny (1927) and Carman (1938, 1956) derived an analytical relationship for porous rock by representing the porous media as a set of parallel and uniform pipe conduits with spherical particles. Generalized parameters

such as porosity ϕ , grain size d , and tortuosity τ , defined as the ratio of the length of the path traveled by a fluid to the domain unit length, are adopted to correlate the structure of a porous material with its permeability k :

$$k = \frac{d^2}{72\tau^2} \frac{\phi^3}{(1-\phi)^2} \quad (8.1)$$

Although, subsequent studies questioned the ability of the Kozeny-Carman equation to accurately characterize the porosity-permeability relationship for natural tight rock and stated that it required some modifications (Coyner, 1984; Wyllie and Gardner, 1958a, b; Nelson, 1994; Civan, 2019). It was argued that the power law dependence ($k \sim \phi^m$) suggested by Rose (1948) is more accurate than the Kozeny-Carman equation for low-permeable materials (Civan, 1996). Bourbié et al. (1987) modified the general power law relationship by adopting the average material's grain size d : $k/d \sim \phi^m$. Another way of expressing this relationship is through the sensitivities of porosity and permeability:

$$k = k_0 \left(\frac{\phi}{\phi_0} \right)^n \quad (8.2)$$

where k_0 is a reference permeability at reference porosity ϕ_0 and n is a porosity sensitivity exponent calculated when k and ϕ are expressed in an exponential relationship (Doyen, 1988; David et al., 1994).

Detailed experimental studies emphasized a number of difficulties in establishing a uniform porosity-permeability relationship for all subsurface rock (Bernabé et al., 2003), and usually separate analyses are carried out for porous reservoir rocks and tight sealing layers. For the reservoir rock, direct measurements of porosity and permeability are viable due to the relatively large pore sizes ($\sim 10^{-6}$ - 10^{-4} m). The reported exponent values for the power law relationship

range from 2 to 7 and are mostly centered at 3 (Bourbié and Zinszner, 1985; David et al., 1994; Dong et al., 2010). Thus, the results are compatible with the commonly used cubic law and the Kozeny-Carman equation (Bear, 1972).

In contrast to high permeable reservoir rock, low porous (<10%) and low permeable (<10⁻¹⁶ m²) formations are classified as “tight” rock (Law and Spencer, 1993) and include clay-rich sedimentary rock (mudstones), igneous rock (e.g., granite and gabbro), and metamorphic rock (e.g., gneiss and quartzite). A few experimental studies were aimed at proposing a porosity-permeability relationship for tight rock. Extensive review on the flow properties of mudstones and shales with porosities ranging from 0.2 to 0.8 and permeabilities from ~10⁻²¹ m² to 10⁻¹⁶ m² is presented by Neuzil (1994) and concluded that the Kozeny-Carman equation did not provide an accurate fit for the porosity-permeability relationship. Revil and Cathles (1999) studied the ϕ - k relationship for the shale-sand mixtures and reported the porosity sensitivity exponent values for kaolinite, illite, and smectite to be 7-9, 10, and 12, respectively. Dong et al. (2010) reported the increase of the permeability of silty shale from ~10⁻¹⁹ m² to ~10⁻¹⁵ m² as the porosity increased from 0.10 to 0.13, which resulted in the porosity sensitivity exponent value varying from $n = 30$ up to 55. On the other side, values of n between 2 to 5 are reported by Zhang et al. (2015) for the shale from Sichuan basin in China with permeability ~10⁻¹⁹ m² and porosity of 0.03. Yang and Aplin (2010) suggested a porosity-permeability relationship for the mudstones with an additional parameter, the clay content, that seemed to provide a good fit for fine-grained clastic sedimentary rocks from North Sea and Gulf of Mexico but required an involved non-linear fitting.

In crystalline rock, the permeability is usually considered only for the fractured states where existing fractures act as dominant flow paths for fluid (Raven and Gale, 1985; Plümper et al.,

2017) and the cubic law is used for the porosity-permeability relationship in fractured media (Ge, 1997; Witherspoon, 1986). Consistent measurements of intact crystalline rock permeability are rarely reported. Brace et al. (1968) conducted laboratory experiments to evaluate the permeability of Westerly granite via the transient method. Changes in the porosity are estimated from the measurements of the electrical resistivity and the porosity sensitivity exponent n was found to be equal to 3. Alternatively, Morrow and Lockner (1997) reported the relationship for seven granite cores from Illinois by measuring the permeability with the steady-state method and evaluating the porosity change indirectly from the fluid volume discharge, which resulted in the porosity sensitivity exponent values ranging from 12 to 43. For the purposes of the underground storage projects, discontinuous fractures in the tight sealing layers are unfavorable and need to be avoided. So, the hydraulic properties of the matrix should be characterized to estimate the characteristic times for the linear and non-linear diffusion processes (Berchenko et al., 2004; Plümper et al., 2017; Räss et al., 2017).

Use of the Kozeny-Carman equation for tight rock may result in underestimation of the permeability change due to the variations in porosity. The pore structure of a tight rock is usually more complex than an assembly of spherical grains (Bustin et al., 2008; Ross and Bustin, 2009). For example, Opalinus claystone contains relatively long pores (up to a few microns in length) with the dominant pore throat diameters of just 0.02 μm and tortuosity significantly larger than 1 (Figure 8.1).

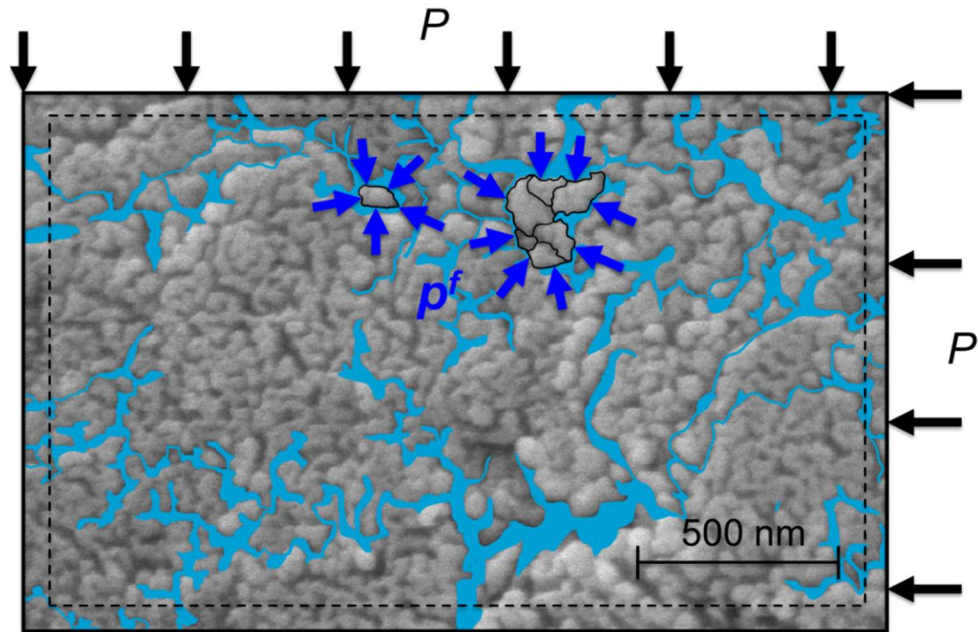


Figure 8.1. Surface Electron Microscopy (SEM) image of Opalinus clay with illustration of applied hydro-mechanical loading and tortuous flow path.

The existing experimental studies stated difficulties in accurately assessing small variations of porosity and have limitations in providing reliable parameters for numerical models that involve coupling between fluid flow and mechanical behavior (e.g., Bower and Zyvoloski, 1997; Noorishad et al., 1984; Vilarrasa et al., 2010; Schulz et al., 2019). Therefore, the establishment of a more appropriate porosity-permeability relationship for tight rock needs serious consideration. In this study, we present an experimental method aimed at direct measurements of the stress-dependent permeability and poromechanical parameters of saturated tight rock. Subsequently, the change in porosity can be calculated and the porosity-permeability relationship for tight rock is established. Shale, claystone, and granite are selected as representative geomaterials and their properties are measured and analyzed.

8.2. Background

In geo-energy applications, the elastic deformation of participating formations is usually preferable to avoid unrecoverable deformations, failure, seismicity, and loss of integrity (Rutqvist et al., 2010; Chen, 2011; Salimzadeh et al., 2017). Therefore, we focus on the poroelastic response and measurements of the corresponding material properties. Porous rock consists of the solid matrix and pore space that is usually filled with fluids. Porosity ϕ is used as an index property to efficiently characterize the porous media, where it is defined as the ratio of the pore volume V_p to the total volume of the material V : $\phi = V_p/V$. Porosity changes due to the variations in external and internal pressures, and therefore it is essential to understand the poromechanical behavior of fluid-filled porous rock. For a representative elementary volume (REV) of a saturated rock, the applied total mean stress $P = \sigma_{kk} = (\sigma_1 + \sigma_2 + \sigma_3)/3$ and pore fluid pressure p^f can be taken as the dynamic parameters that govern its behavior, where σ_1 , σ_2 , and σ_3 are the three principal stresses ($\sigma_1 \geq \sigma_2 \geq \sigma_3$). Then, the Terzaghi effective mean stress can be expressed as $P' = P - p^f$ (Terzaghi, 1923).

The kinematic parameters associated with the total mean stress P and pore fluid pressure p^f can be introduced as the volume strain ε_v and the increment of fluid content ζ (Biot, 1941). Volume strain is the sum of three normal strains: $\varepsilon_v = \varepsilon_1 + \varepsilon_2 + \varepsilon_3$ and describes the bulk deformation of the rock element. The increment of fluid content is defined as the fluid volume ΔV_f entering the solid frame per unit volume of the element: $\zeta = -\Delta V_f/V$. The adopted sign convention is compression positive, meaning that the principal stresses are positive in compression and negative in tension, volume strain is positive when the rock element is compacting, and the increment of the fluid content is positive when fluid exits the porous material (Rice and Cleary, 1976).

Biot (1941) introduced a general constitutive relationship for an isotropic fluid-saturated porous media using a set of poroelastic constants. In this work, we adopt the poroelastic constants that are defined under the three boundary conditions:unjacketed, drained, and undrained (Detournay and Cheng, 1993). Under the unjacketed condition, the variation in the mean stress P is equal to that of the pore pressure p^f : $\Delta P = \Delta p^f$. Unjacketed bulk modulus K_s' and unjacketed pore modulus K_s'' can be defined as:

$$K_s' = V \left. \frac{\Delta p^f}{\Delta V} \right|_{\Delta p^f = \Delta P} \quad (8.3)$$

$$K_s'' = V_p \left. \frac{\Delta p^f}{\Delta V_p} \right|_{\Delta p^f = \Delta P} \quad (8.4)$$

Under the drained condition, fluid can freely move in or out of the pores while the pore fluid pressure is set to be constant ($\Delta p^f = 0$). Drained bulk modulus K can be calculated from the change in the volume of the material due to the applied mean stress:

$$K = V \left. \frac{\Delta P}{\Delta V} \right|_{\Delta p^f = 0} \quad (8.5)$$

Biot coefficient α is introduced as the ratio between the volume of fluid expelled from the element during the drained loading and the change in the element volume. In addition, the relationship for α can be expressed through the ratio between the drained and unjacketed bulk moduli:

$$\alpha = \left. \frac{\Delta V_\phi}{\Delta V} \right|_{\Delta p^f = 0} = 1 - \frac{K}{K_s'} \quad (8.6)$$

The undrained condition is defined by zero change in the increment of fluid content: $\zeta = 0$, indicating that the fluid cannot move in or out of the porous material causing changes in the pore

pressure if external loading is applied. Skempton's (1954) B coefficient is introduced to characterize the undrained loading, where it is defined as the change in the pore pressure due to the change in the mean stress:

$$B = \frac{\Delta p^f}{\Delta P} \Big|_{\zeta=0} \quad (8.7)$$

The elastic change in the porosity ϕ caused by the application of the effective mean stress P' and pore pressure p^f can be expressed using the introduced poroelastic constants (Detournay and Cheng, 1993):

$$\phi_0 - \phi = \Delta\phi = \left(\frac{1-\phi}{K} - \frac{1}{K'_s} \right) P' - \phi \left(\frac{1}{K'_s} - \frac{1}{K''_s} \right) p^f \quad (8.8)$$

The increment of fluid content ζ in the porous element is linked to the fluid flux q through the fluid continuity equation:

$$\frac{\partial \zeta}{\partial t} + \nabla \cdot \vec{q} = 0 \quad (8.9)$$

For the laminar and steady-state flow in a fully saturated element, Darcy's law relates fluid flux to the change in pore pressure dp^f through the permeability k and viscosity of the fluid μ_f (Bear, 1972):

$$q_i = -\frac{k}{\mu_f} \frac{\partial p^f}{\partial x_i} \quad (8.10)$$

The permeability characterizes the degree of fluid movement through the rock and, for tight rock, it appears to strongly depend on the effective mean stress, $k = k(P')$ (Neuzil, 1994; Bernabé, 1986). Subsequently, by measuring the stress-dependent permeability and calculating variations in porosity with the effective mean stress P' (through the measured poroelastic parameters in Equation 8.8), the porosity-permeability relationship can be established.

8.3. Experimental methods

Measurements of hydraulic and poromechanical properties of porous rock can be conducted in a single test performed on a fluid-saturated specimen subjected to external loading (Wang, 2000). However, accurate assessment of tight rock properties is a challenging task that requires weeks to months due to the time scales of saturation and pore pressure diffusion processes (Section 8.4). For example, conventional triaxial compression test on fluid-saturated rock is conducted in a load frame that needs to be operating continuously for a few weeks, demanding considerable energy consumption and continuous monitoring. In this work, a more time and energy efficient approach is used. Drained (dry) and unjacketed bulk responses of tight rock are measured in the hydrostatic cell (Section 8.3*b*), while the fluid flow and the undrained response are characterized in the core flooding device (Section 8.3*c*).

8.3.1. Material

Three materials are utilized for this study: Eau Claire shale, Opalinus clay, and Charcoal granite. The pore size distribution is measured via mercury intrusion porosimetry (MIP) method. Maximum intrusion pressure of 400 MPa can be applied to force the mercury to penetrate in a rock sample with a pore size diameter as low as 4 nm. The results of the pore size distribution measurements are presented in Figure 8.2.

Eau Claire shale is a heterolithic carbonate and fine siliciclastic unit present across west-central Illinois, where it overlies high permeable reservoir sandstone and is considered to serve as the caprock for the CO₂ storage in Illinois Basin (Bauer et al., 2019). Tested Eau Claire shale contains 42% quartz, 40% K-feldspar, 16% dolomite, and 2% mica. The dominant pore size is

between 30 and 60 nm. Despite being named "shale," the rock contains a small portion of clay minerals and is not fissile, so its drained properties change insignificantly with fluid saturation.

Opalinus clay is a potential host rock for nuclear waste storage and caprock for CO₂ storage in Switzerland. Shaly facies extracted from the Mont Terri underground rock laboratory represent a ductile Jurassic shale with an excellent retention ability (Bossart and Thury, 2008). Tested material contains 50% clay (illite, kaolinite, chlorite, and smectite), 24% calcite, 20% quartz, 5% organic matter and traces of other minerals. The dominant pore throat diameter for Opalinus clay is 15 nm.

Charcoal granite, quarried in Cold Spring, Minnesota, is a medium-grained (0.2 to 8 mm), crystalline, Precambrian granodiorite. The material contains 15% quartz, 15% plagioclase, 47% feldspar, 10% biotite, and 13% hornblende (Althaus et al., 1994). Even after 3 months of fluid injection, the flow through the intact cores of Charcoal granite could not be established and its permeability is evaluated to be below 10^{-22} m². Therefore, the thermal treatment method is used to induce microstructural changes in the rock in a consistent way. The pristine granite specimens are heated to 300°C for 72 hours, before cooling it back to the room temperature. For the damaged granite, the dominant pore size is equal to 8 nm.

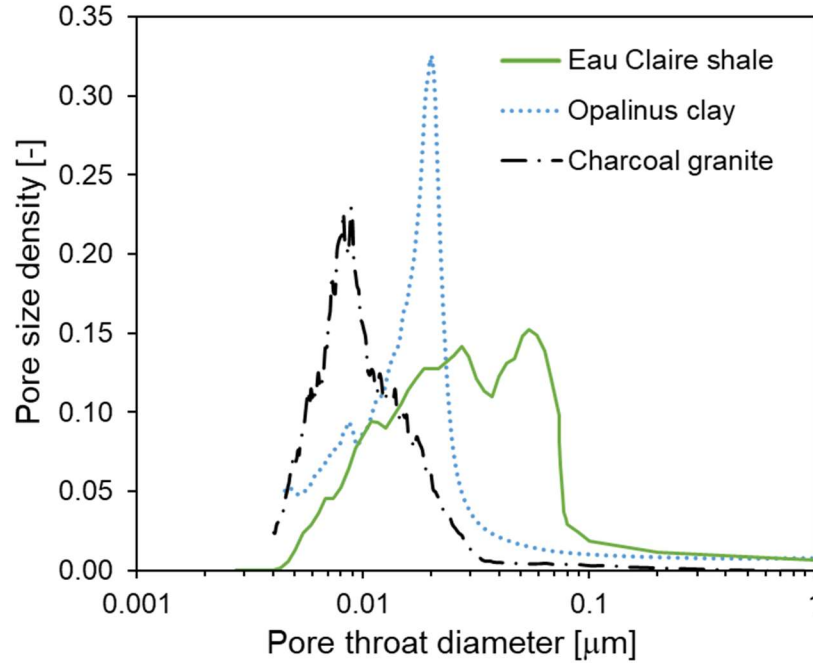


Figure 8.2. Pore size density distribution of Eau Claire shale, Opalinus clay, and Charcoal granite.

The pore volume of a tight rock mainly consists of nanoscale pores, which makes it difficult to measure accurately. Mercury Intrusion Porosimetry allows determination of the porosity by measuring the cumulative pore volume. As the applied pressure increases, pores with a smaller throat diameters are getting filled, and the cumulative mercury volume at the maximum pressure can be taken as the total pore volume. Thus, the porosity can be calculated with the measurement of the total specimen volume (at zero mercury pressure). The disadvantage of the method is that it utilizes specimens of a size smaller than 1 cm^3 , and the measured porosity values can vary by 2-5% due the specimen surface preparation (Kuila and Prasad, 2013). For the validation of reported porosity values, the mass of fully water-saturated cylindrical specimens (diameter $D = 50.8 \text{ mm}$ and length $L = 102 \text{ mm}$) is measured after the permeability tests. By knowing the density of the pore fluid ρ_f , the porosity can be calculated from the difference between the saturated and dry mass. The two methods show agreement within 3% and the porosity of Eau

Claire shale, Opalinus clay, and Charcoal granite are reported as 0.10, 0.13, and 0.02, respectively.

8.3.2. Hydrostatic compression tests

The hydrostatic compression test provides a robust way to determine jacketed (dry) and unjacketed bulk moduli of rock (Tarokh and Makhnenko, 2019). It is performed in a pressure vessel filled with hydraulic oil, where pressure is controlled by a hydraulic pump with 70 MPa capacity (Figure 8.3a). The pressure transducer measures the hydrostatic pressure, whereas the deformation is obtained locally on the rock specimen surfaces with the sets of resistive strain gages. For Eau Claire shale, a cylindrical specimen ($D = 30$ mm and $L = 60$ mm) is used with installed axial (ε_{ax}) and lateral (ε_{lat}) strain gages. The specimen is cored perpendicular to the bedding planes and it is assumed that the lateral strain is equal to the radial one, so the volume strain ε_v can be calculated as:

$$\varepsilon_v = \varepsilon_{ax} + 2\varepsilon_{lat} \quad (8.11)$$

For Charcoal granite and Opalinus clay, three normal perpendicular strains: ε_{xx} , ε_{yy} , and ε_{zz} are measured on the prismatic specimens ($50 \times 35 \times 35$ mm) and the volume strain is calculated as the sum of three orthogonal normal strains:

$$\varepsilon_v = \varepsilon_{xx} + \varepsilon_{yy} + \varepsilon_{zz} \quad (8.12)$$

After the specimens are instrumented with the strain gages, they are covered with polyurethane liquid membrane that solidifies after a few days and prevents confining fluid penetration into the rock. The hydrostatic pressure is applied after the membrane-coated specimens are submerged in the confining fluid, and the strain gage readings are recorded. Loading and unloading are repeated at least two times for validation of the accuracy of the measurements. By plotting the

mean stress (or hydrostatic pressure) versus the volume strain, the jacketed (dry or drained) bulk modulus K can be determined.

After the jacketed test, the membrane is removed carefully by retaining the strain gages attached, and the loading-unloading procedure is repeated under theunjacketed conditions. During the loading, the confining fluid intrudes into the pores and the equilibration between the hydrostatic pressure and the pore fluid pressure ($P = p^f$) can take up to tens of hours due to the low permeability of the tight rock. The pore pressure is assumed to be equal to the applied hydrostatic pressure when the strain gage readings become constant for at least 3-4 hours. For each specimen, full saturation with hydraulic oil can be assured by applying the cell pressure higher than the capillary pressure for the fluid to intrude the pores of the smallest size. Consequently, unloading in the unjacketed test is performed in steps of a few MPa with a few hours to a few days equilibration time between each step, depending on the pore pressure diffusion time for each particular material. Further detailed discussion on saturation and the diffusion times for each tested rock are elaborated in Section 3*d* Eventually, measurements of volume strain versus the hydrostatic pressure under the unjacketed conditions provide the unjacketed bulk modulus K_s' .

Shaly facies of Opalinus clay become fissile when the pore fluid dries out, so they are tested with the in-situ fluid (brine) inside with the initial saturation after specimens' recovery from a borehole being about 85-90%. The unjacketed test on Opalinus clay is conducted by gradually applying 60 MPa pore pressure with hydraulic oil ($P = p^f$) for 15 days and then unloading the specimen for 30 days to assure full pore fluid pressure dissipation. It is assumed that the full liquid saturation (no air bubbles) of the shale is reached by oil pushing the pre-existing brine into the smaller pores and filling the remaining pore space. Instead of conducting a dry jacketed test,

a drained compression test is performed on Opalinus clay to obtain its drained bulk modulus $K_{drained}$. The test is conducted in the high-pressure (70 MPa) triaxial cell with pore pressure control pumps and measurements of axial/lateral deformations (Makhnenko and Podladchikov, 2018).

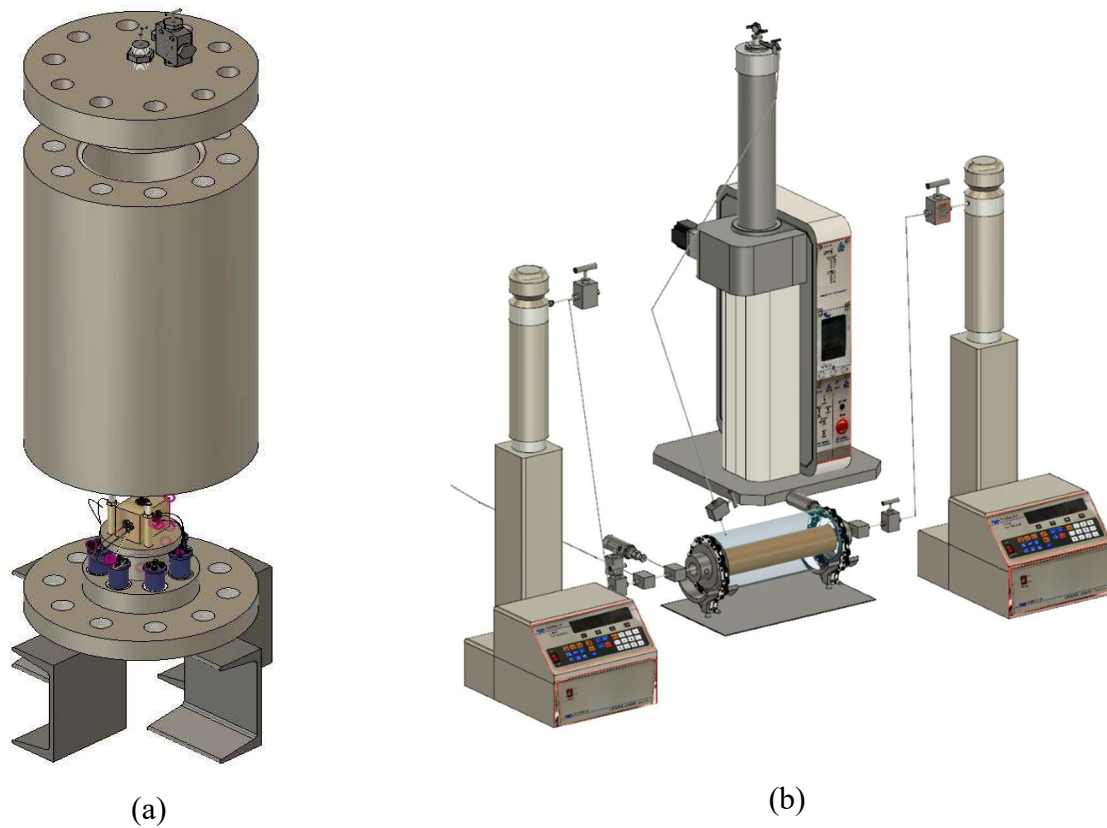


Figure 8.3. Sketches of the experimental devices: (a) Hydrostatic compression cell used for jacketed (dry) and unjacketed (oil-saturated) experiments, and (b) core flooding device used for flow and undrained compression experiments.

8.3.3. Flow tests

Under the assumption of Darcy's flow, the permeability of rock can be measured by two common techniques: steady state method and transient method. The steady state method involves creating a constant pressure gradient through a specimen subjected to external stresses by applying the upstream pore pressure higher than the downstream one. Thus, the permeability can be calculated after the flow stabilizes, which requires long experimental times for tight rock (Suri et al., 1997).

As an effort to overcome this drawback, the transient method (also known as the pulse decay method) was introduced by Brace et al. (1968). The transient pulse decay method estimates the permeability from the pressure diffusion across the specimen after applying an instant pulse pressure at the upstream. The two ends of the rock sample are initially subjected to equal fluid pressure and the pulse induced pressure difference of the upstream and downstream channels is monitored as it decreases with time. Further works of Hsieh et al. (1981) and Neuzil et al. (1981) indicated the practicality of the method for crystalline rock and shale, but also the dependence of the results on the boundary conditions and accurate knowledge of the storage capacity of tested materials, measurements of which are challenging for the tight rock (Hart et al., 2005) and, in general, require the knowledge of the compressibilities of the mineral phase, pore, and the fluid (Zimmerman, 2017). Boulin et al. (2012) compared the use of the steady state method and the transient method for tight rock and concluded that the former one would provide more accurate results for permeabilities as low as 10^{-22} m^2 .

Selection of the pore fluid for measuring the permeability of tight rock is also crucial in terms of accuracy and experimental time, where use of inert gas with low viscosity has been suggested as an alternative for liquid based permeability measurements (Klinkenberg, 1941; Bloomfield and

Williams, 1995). Despite shorter time scales for saturation and flow tests with a gas, the permeability measurements can be affected by numerous issues: type of the gas used (Sakhae-Pour and Bryant, 2012; Alnoaimi and Kovscek, 2019), gas slippage which requires correction factors (Klinkenberg, 1941; Rose, 1948), potentially uneven gas pressure distribution in the pores (Mehmani et al., 2013), presence of other fluids in the pore space (e.g., brine in the case of in-situ shales), and small variations in temperature and pressure in the controllers that can significantly affect the recorded inflow and outflow volumes, and hence, the accuracy of the results.

Therefore, due to the complexities associated with the use of the transient method and gases as the working fluids, we adopt a more intuitive steady state method with water as the pore fluid to determine the permeability of rock without any additional assumptions. The tests are performed on right cylindrical specimens ($D = 50.8$ mm and $L = 102$ mm) using the core flooding device and three syringe pumps (Figure 8.3b). The confining pressure is applied via 70 MPa capacity pump filled with hydraulic oil. Two 25 MPa capacity syringe pumps are connected to the core holder: one - for the upstream pressure control and the other one - for the downstream pressure. All the pumps can be operated in pressure, volume, and flow control modes. From Darcy's law, the flow rate q_i can be expressed as $\Delta V/\Delta t$ in a single direction, and once reaching steady state condition, dp^f/dx_i becomes $\Delta p^f/L$ in the direction of flow, where Δp^f is the pore pressure difference along a distance L . The expression for calculating the permeability k [m^2] of a specimen with a cross-sectional area A takes the following form:

$$k = \frac{\mu_f \cdot L \cdot \Delta V_f}{A \cdot \Delta t \cdot \Delta p^f} \quad (8.13)$$

In the core flooding test, the confining pressure is only applied in the lateral direction and the lateral stress is the major principal stress. In the axial direction, the stainless-steel platens provide

passive restraint and inhibit the deformation of the specimen. From the generalized Hooke's law, the induced axial stress becomes $\sigma_{ax} = 2\nu\sigma_{lat}$, and the total mean stress can be expressed as $P = 2\sigma_{lat}(1 + \nu)/3$ (Kim et al., 2018).

Pure deionized water is used as the pore fluid for Eau Claire shale and Charcoal granite, while for Opalinus clay – the in-situ brine is utilized. The tests are performed at constant room temperature (22°C) and the viscosity of the pore fluid μ_f is taken as 0.001 Pa·s. While preserving the total mean stress constant, the differential pore pressure $\Delta p^f = p_{up}^f - p_{down}^f = 2$ MPa (upstream minus downstream pressure) is applied to induce the flow through the fluid-saturated specimen. Changes in the volumes of both pumps are observed over time, and as the absolute volume change rates ($\Delta V_f / \Delta t$) of these pumps become identical, steady-state flow is assumed and the permeability of the rock can be calculated from Equation 8.13. Measurements of permeability are repeated at different effective mean stress levels by preserving constant average pore pressure $p^f = (p_{up}^f + p_{down}^f)/2$, while the total mean stress P is varied. As a result, the permeability - effective mean stress relationship ($k - P'$) can be obtained.

Figures 8.4a and 8.4b demonstrate the results of flow tests performed on the most permeable rock under consideration - Eau Claire shale and the least permeable rock - Opalinus clay. For Eau Claire shale, approximately 400 mm³ is collected at the outflow controller for two hours. Opalinus clay appears to be much less permeable: reaching steady-state flow and collecting 200 mm³ of brine at the downstream controller (with the accuracy of 1 mm³) takes at least two days for a single flow test. Measurements of permeability - effective mean stress relationship for a tight rock require a few weeks to assure reporting the precise numbers at each step. In addition, for Opalinus clay and Eau Claire shale, the flow tests are repeated in the reverse direction to check for a potential pore throat clogging. The measured permeability values are within 5% of

those observed for the reverse direction indicating that the clogging effect can be neglected considering the accuracy of reported results. Charcoal granite is a crystalline rock that does not contain any clay and calcite, so clogging is not expected and reverse flow tests are not performed.

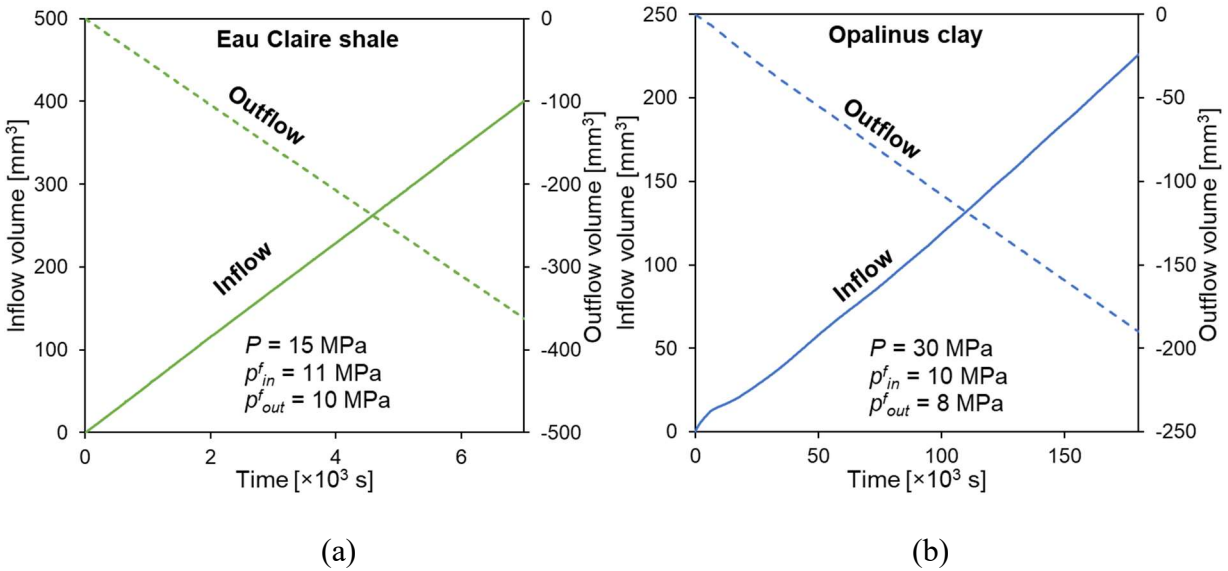


Figure 8.4. Volume change of the inflow and outflow controllers during a permeability test on (a) Eau Claire shale and (b) Opalinus clay.

8.3.4. Saturation

The poroelastic parameters of rock should be measured under the condition of full saturation, meaning that all interconnected pore space is occupied by one pore fluid. For the unjacketed tests, full saturation needs to be confirmed to guarantee even distribution of the pore pressure and homogeneous deformation. Hydraulic oil is used as the pore fluid because it has neither chemical effect on the rock nor electrical effect on the strain gages. During the unjacketed test, the cell pressure is gradually increased to 50-60 MPa within a few days to ensure full saturation with the confining fluid (oil). Achievement of full saturation can be validated by evaluating the values of

required capillary pressures to overcome for replacing another fluid. This can be done by interpreting the results of MIP tests via the Young-Laplace equation:

$$p^f = -\frac{4\sigma_{oa} \cos \theta_{oa}}{d} \quad (8.14)$$

The interfacial tension between the hydraulic oil and air is taken as $\sigma_{oa} = -0.036$ N/m - the most conservative case for hydraulic oils (Blinks and Clint, 2002), and the pore throat diameter d can be calculated from the MIP test. The oil-air-rock contact angle θ_{oa} is assumed to be 0° , based on the values from previous studies and direct measurements for smooth surfaces (Wenzel, 1936; Ethington, 1990). Thus, the calculation of capillary pressure provides the saturation curve for the hydrostatic compression test using hydraulic oil as the confining fluid (Figure 8.5a). Full oil saturation can be achieved for Eau Claire shale and Charcoal granite at pressures above 15 MPa, and it could require more than 60 MPa to access the smallest pores in Opalinus clay. However, the clay specimen is tested with 85% of initial brine (wetting fluid) saturation and after 15 days of 60 MPa oil pressure application, it is stated that it becomes 100% liquid saturated (Makhnenko and Podladchikov, 2018).

The pore pressure diffusion process needs to be taken into account at each step of loading or unloading to assure that pressure equilibrium has been reached before strain measurements. For the hydrostatic compression tests on tight rock, enough time is given at each step for pressure diffusion: 30 minutes to 3 hours for Eau Claire shale, 6 to 48 hours for Opalinus clay, and 6 to 24 hours for Charcoal granite. This can be confirmed by calculating the diffusion coefficient c as a function of permeability k , fluid viscosity μ_f , and measured poroelastic constants (Detournay and Cheng, 1993):

$$c \approx \frac{k}{\mu_f \left(\frac{\phi}{K_{oil}} + \frac{1}{K} - \frac{1+\phi}{K'_s} \right)} \quad (8.15)$$

Given viscosity $\mu_{oil} = 0.07 \text{ Pa}\cdot\text{s}$ and bulk modulus $K_{oil} = 1.3 \text{ GPa}$ of the hydraulic oil, the c values for oil-saturated specimens can be determined. For Opalinus clay, the fluid properties of water ($\mu_{water} = 0.001 \text{ Pa}\cdot\text{s}$ and $K_{water} = 2.24 \text{ GPa}$) are used to calculate c . The corresponding characteristic diffusion time t_{char} for specimens of linear size L with drained boundary conditions on all sides can be calculated by $t_{char} \sim L^2/4c$, where it is determined as $\sim 20 \text{ min}$ for Eau Claire shale, $\sim 5 \text{ hours}$ for Opalinus clay, and $\sim 2 \text{ hours}$ for Charcoal granite (see Table 8.1), implying that the experimental times for each step of our tests are sufficient to reach pore pressure equilibrium.

For the tests conducted in the core flooding device, full saturation is achieved by applying the back pressure technique (Lowe and Johnson, 1960; Makhnenko and Labuz, 2016). Its purpose is to achieve 100% saturation by forcing any gas into the solution of the pore water. Measurements of Skempton's B coefficient are performed at gradually increasing back pressures while keeping the Terzaghi effective mean stress P' constant. When the rock is not fully saturated, the B value increases with pore pressure, as more air is forced into solution and the value of pore fluid bulk modulus K_f increases (Equation 8.16). A measured B value that is constant and independent of the magnitude of the back pressure indicates full saturation (Figure 8.5b). Once the air is driven into the solution, the air-water mixture behaves as a fluid with a bulk modulus equal to that of pure water, $K_{water} = 2.24 \text{ GPa}$.

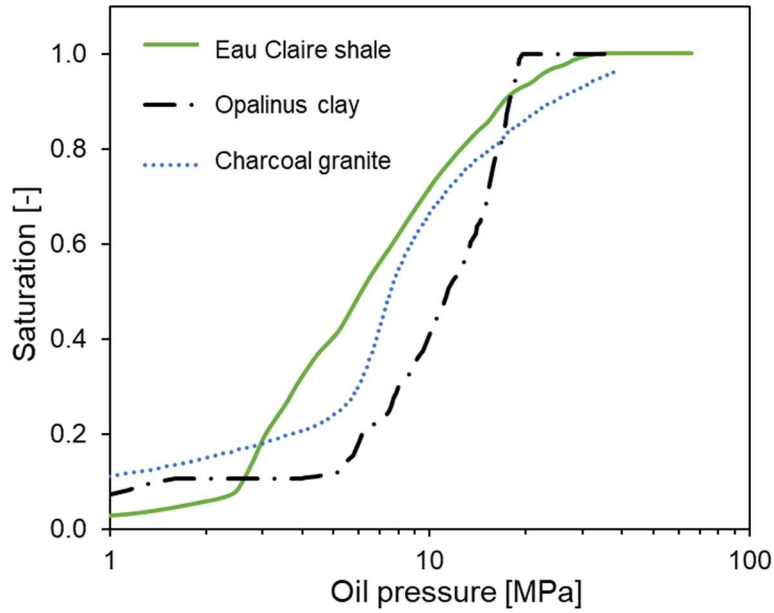
The change in the mean stress during the undrained test can be calculated from generalized Hooke's law as $\Delta P = 2\Delta\sigma_{lat}(1 + \nu_u)/3$, where ν_u is the undrained Poisson's ratio of rock since the

specimen is deforming under the undrained condition. The Skempton's B coefficient is then calculated from the change in pore pressure Δp^f caused by the increase in the mean stress ΔP .

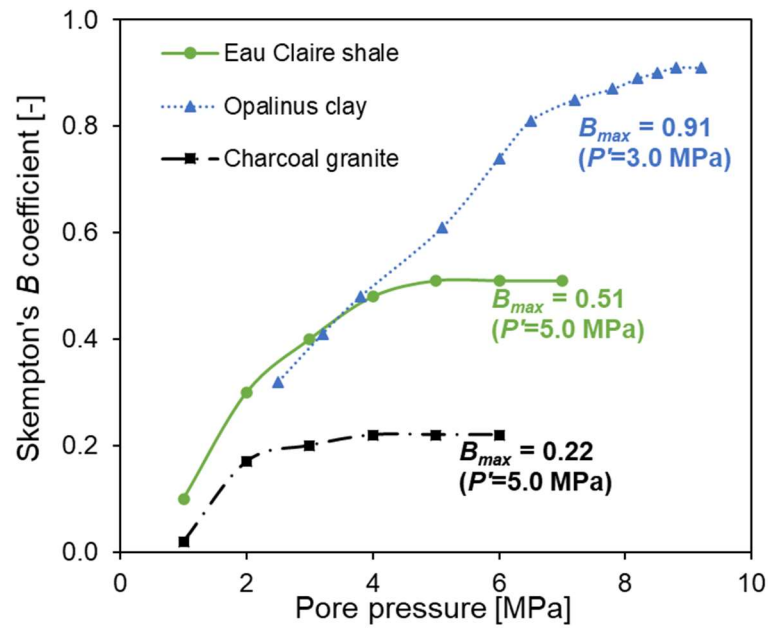
$$B = \frac{1}{\frac{\Delta P}{\Delta p^f} - C_{cor}} = \frac{1}{\frac{2(1+\nu_u) \cdot \Delta \sigma_{lat}}{3 \cdot \Delta p^f} - C_{cor}} = \frac{\alpha}{\alpha + \phi K \left(\frac{1}{K_f} - \frac{1}{K_s''} \right)} \quad (8.16)$$

Measured Skempton's B coefficient needs to be corrected because the pore water lines (that connect the specimen and pore pressure transducers) are compressible and provide an extra volume for the pore fluid to dissipate (Bishop, 1976). This effect is considered through the correction factor C_{cor} , which appears to be very small for the core flooding device ($C_{cor} = 0.5 \times 10^{-2}$) and its contribution to the measured B values is within 0.005. The undrained Poisson's ratio ν_u needed for calculation of ΔP is not measured in this study, but can be calculated from other poroelastic constants as (Rice and Cleary, 1976)

$$\nu_u = \frac{3\nu + B(1-2\nu)(1 - K/K_s')}{3 - B(1-2\nu)(1 - K/K_s')} \quad (8.17)$$



(a)



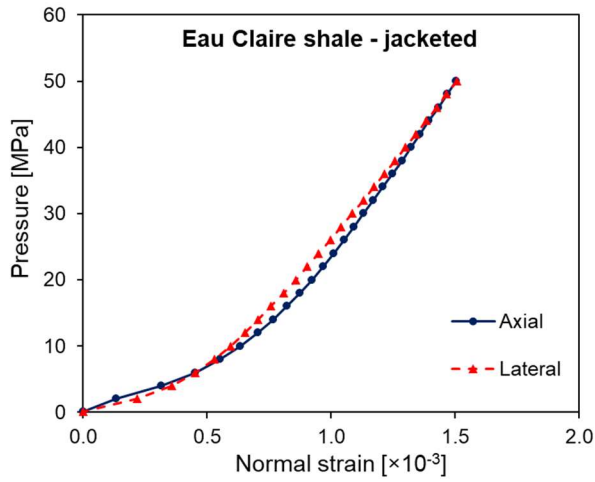
(b)

Figure 8.5. (a) Saturation curves indicating oil pressures needed for achievement of full saturation in the hydrostatic compression tests. (b) Increase of the Skempton's B values with applied pore pressure during the application of back pressure saturation technique in the core flooding device.

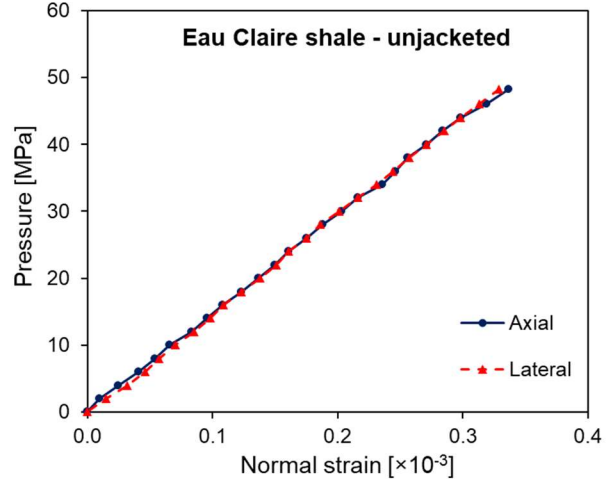
8.4. Results

8.4.1. Hydrostatic compression tests

Jacketed andunjacketed hydrostatic compression tests are conducted on Eau Claire shale, Opalinus clay, and Charcoal granite (Figures 8.6-8.8). The loading-unloading procedure is duplicated to check the repeatability of the test, and the unloading response is used for the determination of the bulk moduli (K and K_s). Results for jacketed tests performed on Eau Claire shale and Charcoal granite show that the slope of the hydrostatic pressure - volume strain curve increases until it becomes constant at pressures above 20 MPa, most likely due to the closure of crack-like pores (Walsh, 1965). On the other hand, the results for the unjacketed tests show a linear response throughout the whole loading-unloading procedure. For Eau Claire shale, measured axial and lateral strains are almost identical, indicating the validity of isotropic deformation assumption (Figure 8.6). The drained response from the triaxial test on Opalinus clay does not appear to be strongly stress-dependent, but shows pronounced differences in axial and lateral deformations, which is hindered in the unjacketed test where the role of the orientation of cracks and pores in the material is diminished (Figure 8.7). For Charcoal granite, we observe anisotropy for both the drained (dry) and unjacketed response. The normal strain in one direction is 30% different from the two other directions. This difference decreases to 20% in the unjacketed test, but does not disappear indicating the solid matrix anisotropy for the granite (Figure 8.8). Even though the degree of anisotropy can decrease at elevated pressures due to the crack closure (Carvalho et al., 1997), the intrinsic matrix anisotropy can still play an important role in bulk and solid response of rock (Hart and Wang, 2010; Tarokh and Makhnenko, 2019).

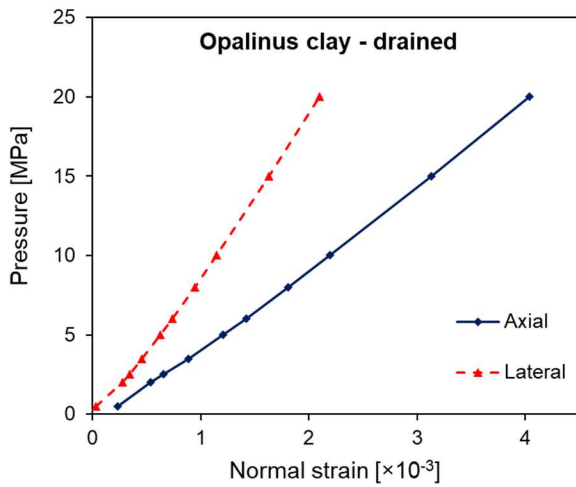


(a)

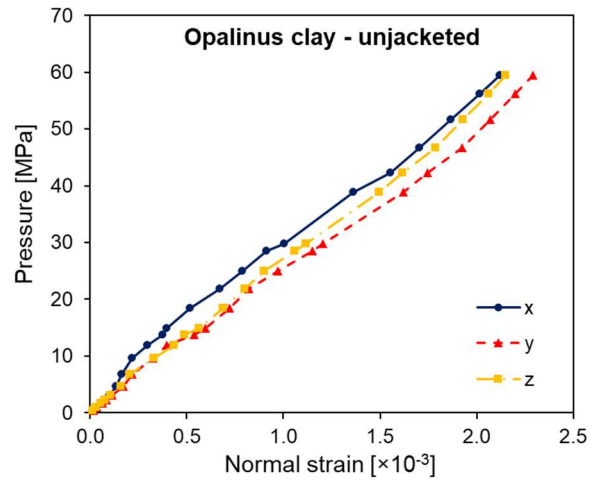


(b)

Figure 8.6. Results of hydrostatic compression tests performed on Eau Claire shale under (a) jacketed (dry) and (b) unjacketed conditions.



(a)



(b)

Figure 8.7. Results of hydrostatic compression tests performed on Opalinus clay under (a) drained (brine-saturated) and (b) unjacketed conditions (fully saturated with brine and oil).

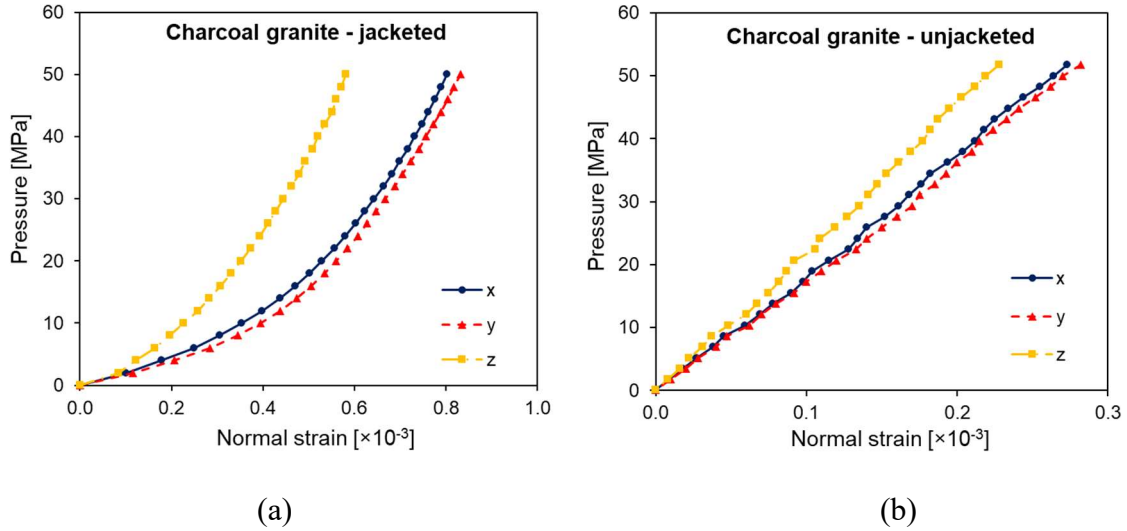


Figure 8.8. Results of hydrostatic compression tests performed on Charcoal granite under (a) jacketed (dry) and (b) unjacketed conditions.

For Eau Claire shale, K and K_s' are measured as 17.0 GPa (at $P' > 30$ MPa) and 49.3 GPa, respectively. Drained and unjacketed bulk moduli of Opalinus clay are measured to be the lowest among the three tested materials: $K = 1.8$ -2.7 GPa and $K_s' = 8.9$ GPa. Charcoal granite demonstrates the stiffest response among three rocks with $K = 46.4$ GPa (at $P' > 30$ MPa) and $K_s' = 63.2$ GPa. Measurements of K and K_s' provide calculation of Biot coefficient $\alpha = 1 - K/K_s'$, which is found to vary from above 0.9 for Eau Claire shale at low pressures to 0.27 for Charcoal granite at elevated pressures. The results of hydrostatic compression tests for all three materials are shown in Figure 8.9 and are summarized in Table 8.1.

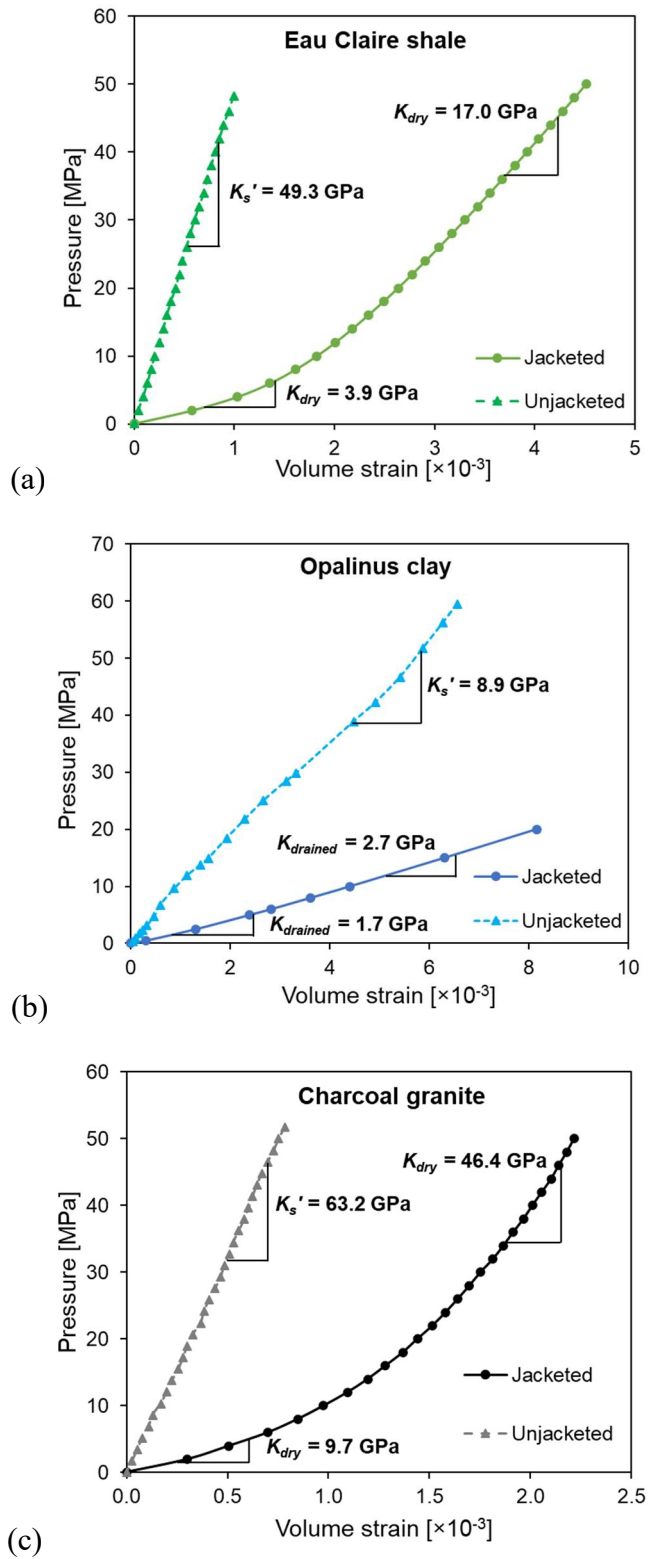


Figure 8.9. Drained (dry) and unjacketed behavior of (a) Eau Claire shale, (b) Opalinus clay, and (c) Charcoal granite.

8.4.2. Flow and undrained compression tests

Permeability k and Skempton's B coefficient are measured for Eau Claire shale, Opalinus clay, and Charcoal granite. Constant and pore pressure independent values of B are confirmed before conducting permeability tests to secure the achievement of full saturation. During the subsequent permeability measurements, the difference between the input and output pore pressures are maintained at a constant value of 2 MPa, and the inflow and outflow volume changes are recorded at each step for 2 hours for Eau Claire shale, 15 hours for Charcoal granite, and at least 50 hours for Opalinus clay. While maintaining constant average pore pressure, the confining pressure is controlled to measure the permeability and Skempton's B coefficient at different effective mean stress values. For Eau Claire shale, the permeability is measured in the range of $2-3 \times 10^{-18} \text{ m}^2$, while B decreases from 0.68 to 0.30 with increasing pressure. Opalinus clay shows the lowest permeability in the range of $4-15 \times 10^{-21} \text{ m}^2$, while the B value is the largest among the three tested rocks varying from 0.91 to 0.81. Permeability measurements for Charcoal granite provide k in the range of $1-5 \times 10^{-19} \text{ m}^2$ and the Skempton's B coefficient values are the smallest among the three materials, changing from 0.26 to 0.06. The results for stress-dependent B and k are demonstrated in Figures 8.10a and 8.10b and all measurements are summarized in Table 8.1.

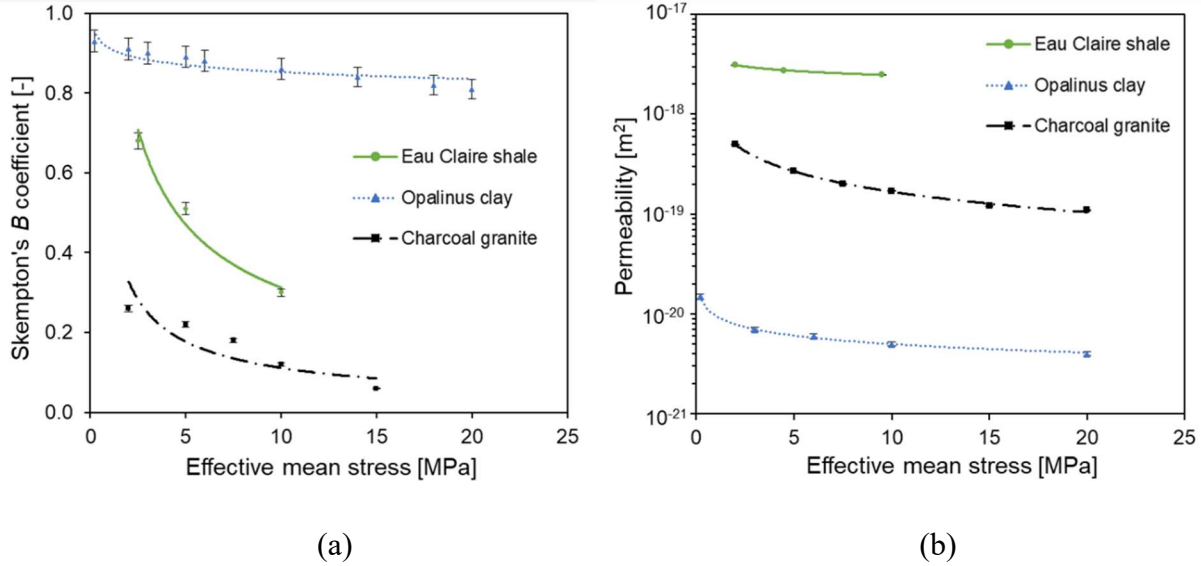


Figure 8.10. (a) Skempton's B coefficient and (b) permeability as functions of effective mean stress for Eau Claire shale, Opalinus clay, and Charcoal granite.

Table 8.1. Summary of measured and calculated proelastic and flow properties for Eau Claire shale, Opalinus clay, and Charcoal granite (stress-dependent parameters are reported at $P' = 10$ MPa).

	Material	Eau Claire shale	Opalinus clay	Charcoal granite
Measured parameters	ϕ [-]	0.10	0.13	0.02
	ν [-]	0.18	0.30	0.22
	k [m^2]	2.8×10^{-18}	6.5×10^{-21}	2.7×10^{-19}
	B [-]	0.51	0.89	0.22
	K [GPa]	10.0	2.7	18.3
	K_s' [GPa]	49.3	8.9	63.2
Calculated parameters	α [-]	0.80	0.70	0.71
	ν_u [-]	0.27	0.42	0.23
	c [m^2/s]	2.3×10^{-7}	1.7×10^{-8}	4.6×10^{-8}
	n [-]	15	16	17
	β [-]	13	13	18

The absolute errors of the reported parameters can be evaluated from the precision of the experimental devices. The syringe pumps utilized for both hydrostatic compression and flow tests have the accuracy of 1 mm^3 for the volume and 5 kPa for the pressure, and the strain

measurements are consistent with the accuracy of a few microstrain (10^{-6}). Some errors, however, are associated with calculation of the applied mean stress from the knowledge of drained and undrained Poisson's ratios in the core flooding device. Based on the provided accuracies and the repeatability of test results, the relative errors are determined as: 3% for porosity ϕ , 5% for drained Poisson's ratio ν , 2% for permeability k (5% for Opalinus clay), 3% for Skempton's B coefficient (5-10% for Charcoal granite), 2% for dry bulk modulus K (5% for Opalinus clay), 2% forunjacketed bulk modulus K_s' , 4% for Biot coefficient α (7% for Opalinus clay), 10% for undrained Poisson's ratio ν_u , 10-15% for the diffusion coefficient c , and 10% for porosity sensitivity exponent n .

8.5. Discussion

The solid (unjacketed) compressibility of the tested rock is found to be stress independent, while the drained moduli gradually increase and Skempton's B coefficient values decrease with applied pressure until reaching constant values due to the closure of pre-existing crack-like pores. The flow properties also change with the effective mean stress, with the strongest effect being observed for Charcoal granite (k decreases from 5×10^{-19} to 1×10^{-19} m²) and Opalinus clay (k decreases from 10×10^{-21} to 4×10^{-21} m²), while the permeability of Eau Claire shale changes from 3×10^{-18} to 2×10^{-18} m² with the increase of P' from 2 to 20 MPa. The data reported data is within the order of magnitude of typical values reported for Charcoal granite ($\sim 10^{-20}$ - 10^{-21} m² by South and Daemen, 1986), shaly facies of Opalinus clay ($\sim 10^{-21}$ - 10^{-20} m² by Croisé et al., 2004; Marschall et al., 2005; Romero et al., 2012), and Eau Claire shale with porosity of about 0.1 and 10% of clay content (10^{-18} - 10^{-17} m² by Neufelder et al., 2012).

Considering the anisotropy of the tested rock, we acknowledge that the reported permeabilities could take slightly different values if the applied loading would be isotropic during the core flooding tests. In addition, the permeabilities reported in this work correspond to the flow in the direction perpendicular to apparent bedding planes in Opalinus clay and Eau Claire shale cores and the vertical direction for the extracted block of Charcoal granite. The vertical (perpendicular to the bedding planes) flow direction is considered in the context of tight rock being a sealing layer for geo-energy problems. Measurements of the flow in the other directions are limited by the size of the cores for shales and time constraints in case of the granite. The permeability anisotropy in granites is reported to be relatively small – about 20% for Chelmsford and Barre granites (Bernabe, 1986) and up to 200% for Inada granite (Kiyama et al., 1996). The directional dependence of flow properties in shales could be significantly more pronounced with the ratio of vertical to horizontal permeability taking the values up to 100 (Grainger, 1984; Armitage et al., 2010; Loucks et al., 2012; Bhandari et al., 2015). For Opalinus clay, the reported permeabilities for parallel vs perpendicular to the bedding planes directions can vary from a factor of 3 (Romero et al., 2012) up to 10 (Marschall et al., 2005). It has to be noted that the permeability anisotropy might not affect the power law relationship between ϕ and k , since the permeability in different directions often change in the same manner with applied effective mean stress (Bernabe, 1986; Kiyama et al., 1996; Romero et al., 2012).

Measurements of theunjacketed moduli are challenging for the tight rock because of the difficulties associated with assuring its full saturation and pore pressure diffusion at each stage of loading. The validity of the reported results can be examined by calculating the upper and lower bounds for the mineral moduli proposed by Voigt (1889) and Reuss (1929). The Voigt average (upper bound) can be calculated as: $K_s = \sum \phi_i \cdot K_{si}$ where K_{si} is the solid modulus and ϕ_i is the

volume fraction of the i -th constituent. The Reuss average (lower bound) is introduced as: $1/K_s = \sum \phi_i/K_{si}$. The values of mineral moduli are adopted from Mavko et al. (2009) as $K_{quartz} = 37.0$ GPa, $K_{feldspar} = 63.0$ GPa, $K_{dolomite} = 95.0$ GPa, $K_{mica} = 58.2$ GPa, $K_{clay} = 2.0$ GPa, $K_{calcite} = 73.3$ GPa, $K_{organic} = 1.0$ GPa, $K_{plagioclase} = 75.6$ GPa, $K_{biotite} = 59.7$ GPa, and $K_{hornblende} = 90.0$ GPa. The measured K_s' value for Eau Claire shale is 49.3 GPa and it falls within the calculated bounds of 48.0 GPa and 54.5 GPa. Opalinus clay also satisfies the calculated lower 3.5 GPa and upper 26.1 GPa boundaries, with the measured $K_s' = 8.9$ GPa. Interestingly, measured $K_s' = 63.4$ GPa for Charcoal granite is close to the calculated upper boundary of 64.2 GPa for the mineral modulus of the material. It can be caused by the low porosity of the rock, but also may be due to the lack of knowledge of the exact mineral composition of the tested specimen. Given the linear response of all three rocks during theunjacketed unloading, measured K_s' values are assumed to be valid. We acknowledge that bulk moduli of some clays and organic matter can be larger than the adopted values, but it has a little effect on the provided estimate of the upper and lower boundaries.

Evaluation of the stress-dependent porosity is a requisite for establishing the porosity-permeability relationship. However, directly measuring the change in the porosity of tight rock is remarkably challenging due to the pore volume variations on the order of microstrain. It is proposed instead that the poroelastic parameters of the rock are accurately determined for the fully-saturated specimens, thus providing the calculation of the change in porosity (Equation 8.8) with the initial porosity value ϕ_0 measured via Mercury Intrusion Porosimetry. Calculation of the change in porosity requires the knowledge of the unjacketed pore modulus K_s'' . Direct measurement of K_s'' is very sensitive to the small pore volume variations (Tarokh et al., 2018), hence this parameter is estimated only for Opalinus clay by using a pore pressure controller with

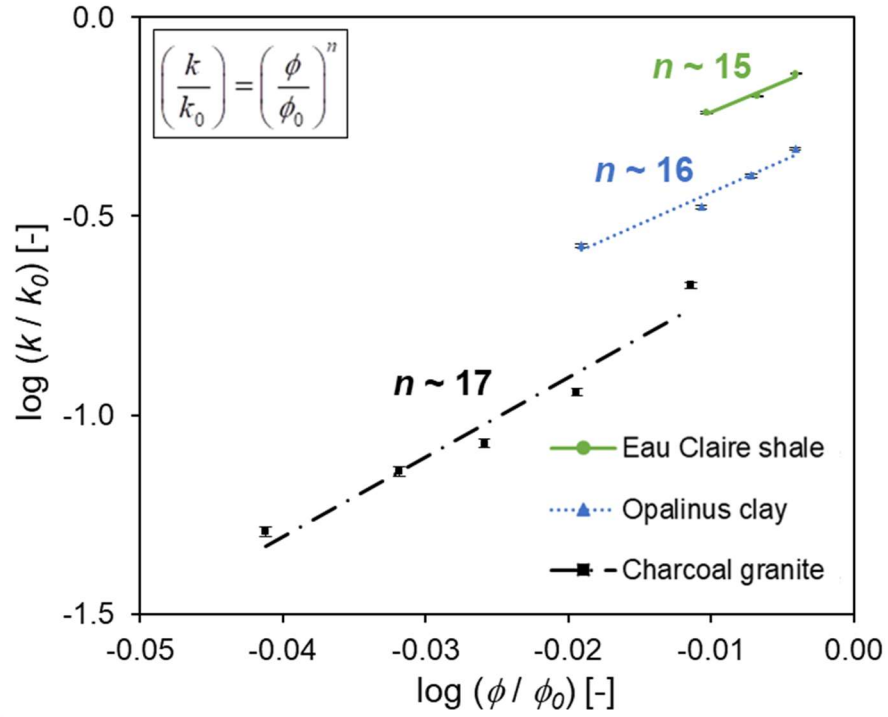
a capacity of 4 MPa and an accuracy of pressure measurements of 0.4 kPa and volume measurements of 1 mm³. K_s'' is evaluated to be 7 ± 2 GPa, so $K_s' \approx K_s''$ can be assumed (Makhnenko et al., 2017). For Eau Claire shale and Charcoal granite, theunjacketed pore modulus has not been measured. Given that pore pressure in the flow tests is around 8 MPa and assuming that K_s'' can take values as low as $0.5 K_s'$, it can be estimated that the second term on the right hand side of Equation 8.8 could contribute to 20% of overall porosity variation. However, in this work, the main interest is in the change of porosity with the effective mean stress P' , while the pore pressure p^f is preserved constant. Hence, the second term in Equation 3.8 remains constant once we reach the testing conditions and contributes by less than 0.1% (within the accuracy of our measurements) to the total porosity value. Therefore, only the first term on the righthand side of Equation 8.8 is utilized for calculation of porosity variations.

The porosity-permeability relationship can be established by adopting the power law with the porosity sensitivity exponent n (Figure 8.11a). For all the tested rocks, a linear fit with R^2 values above 0.98 can be observed between the logarithms of permeability and porosity. The porosity sensitivity exponent values are determined as 15, 16, and 17 for Eau Claire shale, Opalinus clay, and Charcoal granite, respectively. The exponent values for tight rock (15-17) are significantly larger than those for sandstones (~3-5) (Mavko et. al, 2009), indicating that in the former materials, small perturbations of porosity may result in a substantial changes in permeability.

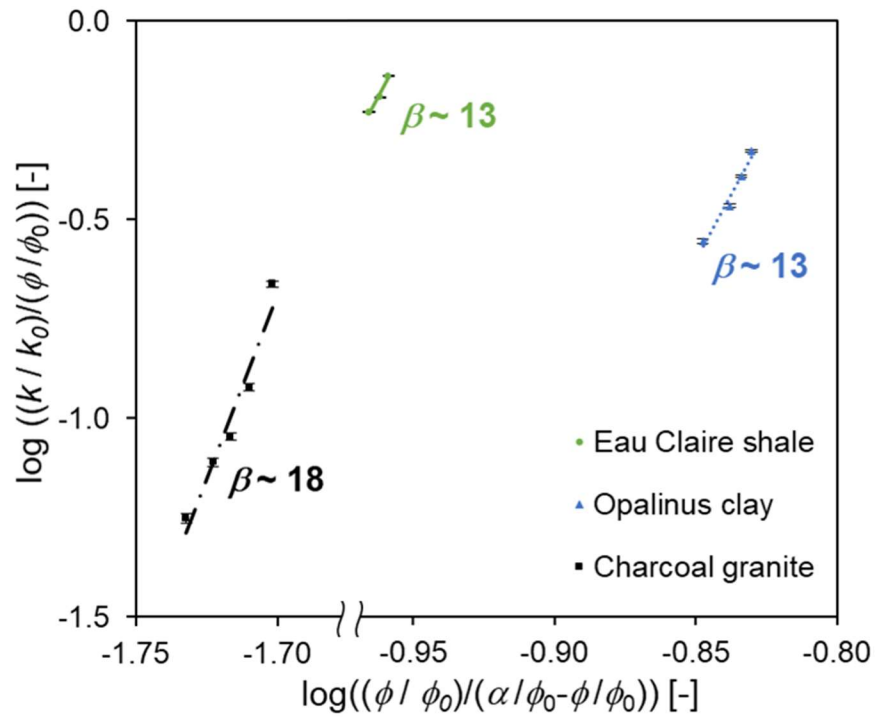
Additionally, the Kozeny-Carman equation can be rearranged in a form of power-law flow-units function that includes the nonzero-transport threshold, cementation effects, and the gate or valve effect for the isolated pores (Civan, 1996; 2000). Empirical parameters β - the effect of the pore connectivity on the pore to solid volume ratio and γ - the interconnectivity are adopted along with assumption of the cement exclusion factor being equal to 1 (Civan, 2001) to write:

$$\sqrt{\frac{k/k_0}{\phi/\phi_0}} = \gamma \sqrt{\frac{\phi_0}{k_0} \left(\frac{\phi/\phi_0}{1/\phi_0 - \phi/\phi_0} \right)^\beta} \quad (8.18)$$

The parameter β can be obtained by plotting the relationship between $\log[(k/k_0)/(\phi/\phi_0)]$ vs $\log [(\phi/\phi_0)/(1/\phi_0 - \phi/\phi_0)]$. Figure 8.11b shows that the experimental data fits well ($R^2 \approx 0.97$) with the Civan's (2000) equation with β values calculated as $\beta \sim 13, 13,$ and 18 for Eau Claire shale, Opalinus clay, and Charcoal granite, respectively. It can be stated that the parameter β is analogous to the porosity sensitivity exponent n and takes similar values for the tested tight rock.



(a)



(b)

Figure 8.11. Porosity-permeability relationships for tight rock with reported values of (a) porosity sensitivity exponent n (Equation 8.2), and (b) pore connectivity parameter β (Equation 3.18).

A fraction of small pores in tight rock that does not participate to the fluid flow could significantly influence the reported data. Percolation theory characterizes the fluid flow in a random porous media and is based on mathematical and statistical calculations where the pores are assumed to be pipes or cracks (Broadbent and Hammersley, 1957; Gueguen and Dienes, 1989). The fraction of connected pores is introduced in the equations for permeability to explain the random distribution of pores, where the percolation threshold porosity ϕ_c is considered (Stauffer, 1985). Below ϕ_c , k is equal to zero, meaning that no flow would occur, while as ϕ increases over ϕ_c , the corresponding k values increase. Mavko and Nur (1997) included the percolation threshold porosity ϕ_c to the Kozeny-Carman relation by replacing ϕ by $(\phi - \phi_c)$, which notably improved the fit for porous and well-sorted rocks.

$$k = \frac{1}{72\tau^2} \frac{(\phi - \phi_c)^3}{(1 - (\phi - \phi_c))^2} d^2 \quad (8.19)$$

The major drawbacks of the percolation theory are that the employed parameters cannot be experimentally determined, leading to limitations in practical applications. Moreover, the oversimplification of the pore structure and hydraulic behavior may not be applicable for tight rock, where the pore sizes are incredibly smaller and the morphology of the pores is much more complex.

We employ the theoretically derived Kozeny-Carman relationship with the percolation threshold porosity and compare it with the data for Opalinus clay based on the procedure introduced by Mavko and Nur (1997). The tendency curves are calculated for four different percolation threshold porosity ϕ_c values (0.001, 0.01, 0.03, 0.05), while the effect of tortuosity τ is evaluated by comparing $\tau \approx 2.5$ for tight rock (Ghanbarian et al., 2013) to $\tau \approx 1.0$. As ϕ_c and τ increase, the tendency curves move downwards, but the sensitivity of permeability from porosity change

remains to be strongly underestimated (Figure 8.12), independently of the value of τ . Therefore, we state that a power-law type relationship with a higher exponent value provides a significantly better fit, while the Kozeny-Carman relationship is unable to capture the strong dependence of permeability on the little changes in porosity for tight rock.

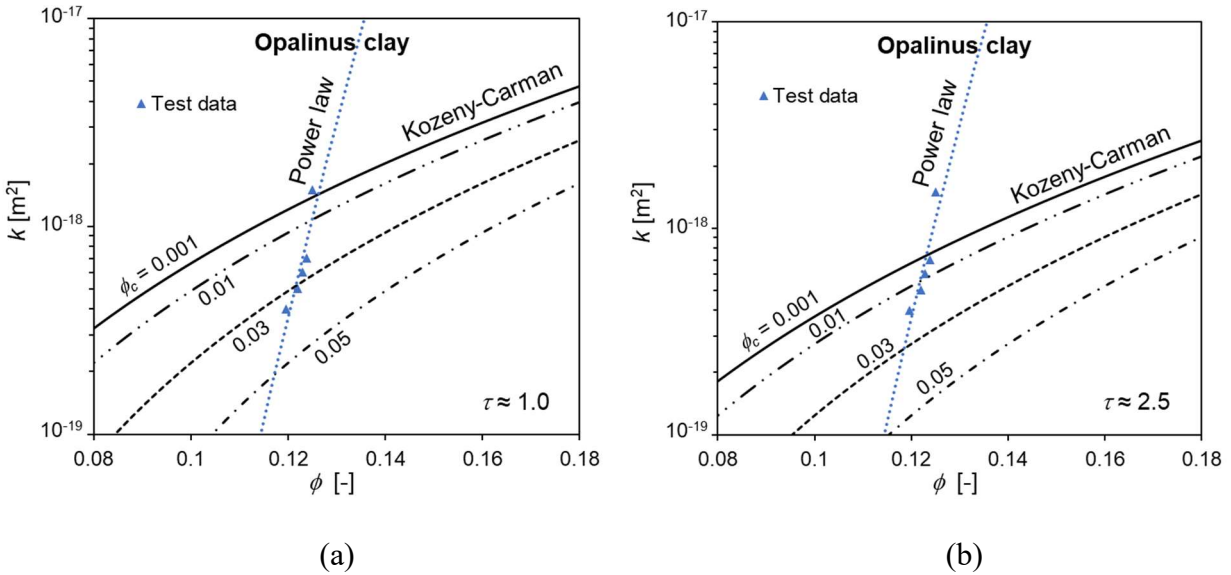


Figure 8.12. Comparison of Kozeny-Carman and power law porosity-permeability relationship for Opalinus clay with tortuosity τ as (a) $\tau \approx 1.0$ and (b) $\tau \approx 2.5$.

Measurements of tight rock poromechanical properties and permeability are essential for the success of geo-energy applications. Mechanisms controlling fluid flow through the low-permeable barriers and pore fluid dissipation in them dictate the capacity and efficiency of geologic storage of CO₂ and radioactive waste (Tsang et al., 2005; Angeli et al., 2009). Flow properties that are highly dependent on porosity are important for creation of dynamic permeability pathways in reservoir and barrier formations (Räss et al., 2018) and may lead to undesirable CO₂ leakage to the near surface (Tian and Ague, 2014). In addition, fluid flow

initiation in deforming Earth crust needs to be properly understood (Bredehoeft and Norton, 1990), because of its importance for crustal pore pressure development (Walder and Nur, 1984) and triggering of intermediate depth subduction zone seismicity (Plümper et al., 2017). This study shows that small variations in tight rock porosity can be accompanied by large variations in permeability meaning that porosity-permeability relationship with low exponent values (such as Kozeny-Carman) may mislead the assessment of the subsurface flow. Instead, the ϕ - k relationship for tight rock needs to be measured for each participating formation to properly assess the integrity of the sealing layers (Angeli et al., 2009) and avoid the induced seismicity (National Research Council, 2012).

8.6. Conclusions

In this study, we propose an experimental method to evaluate the porosity-permeability relationship for tight rock by coupling its mechanical and flow responses. We select Eau Claire shale, Opalinus clay, and Charcoal granite as the representative materials. Flow and mechanical tests are conducted simultaneously by utilizing the core flooding device that allows measurements of permeability and undrained parameters, and the hydrostatic cell, where jacketed and unjacketed compression tests are performed. A special effort is taken to achieve full saturation of the rock that often times requires elevated pressures (above 8 MPa) and long pore fluid pressure diffusion times (days to weeks). In addition, for Opalinus clay, a drained triaxial test is conducted instead of the jacketed test, because the in-situ pore fluid plays a crucial role in material integrity and it could not be tested dry.

Due to the nanoscale size of the dominant pores in the tight rock, small variation of porosity cannot be measured directly, but is calculated as a function of effective mean stress via measurements of the poroelastic rock properties. By integrating the experimental results, the

porosity-permeability relationship can be established with a porosity sensitivity exponent n . Our measurements demonstrate that the relationship for tight rock has a significantly larger exponent value $n \sim 15-17$, as compared to the porous rock such as sandstones with $n \sim 3-5$. This implies that a small porosity change may induce a significant change in permeability for tight rock, potentially causing undesired consequences such as fluid channeling and leakage.

References

- Ahmed, T. (2006) Reservoir Engineering Handbook. Elsevier.
- Alnoaimi, K.R., Kovscek, A.R. (2019) Influence of microcracks on flow and storage capacity of gas shales at core scale. *Transp Porous Med.* 127: 53-84.
- Althaus, E., Friz-Töpfer, A., Lempp, Ch., Natau, O. (1994) Effects of water on strength and failure mode of coarse-grained granites at 300°C. *Rock Mech Rock Eng.* 27: 1-21.
- Angeli, M., Soldal, M., Skurtveit, E., Aker, E. (2009) Experimental percolation of supercritical CO₂ through a caprock. *Energy Procedia.* 1: 3351-3358.
- Armitage, P.J., Worden, R.H., Faulkner, D.R., Aplin, A.C., Butcher, A.R., Iliffe, J. (2010) Diagenetic and sedimentary controls on porosity in Lower Carboniferous fine-grained lithologies, Krechba field, Algeria: A petrological study of a caprock to a carbon capture site. *Mar Pet Geol.* 27: 1395–1410.
- Bauer, R.A., Will, R., Greenberg, S., Whittaker, S.G. (2019) Illinois Basin-Decatur project. In *Geophysics and Geosequestration*, eds. T.M. Davis, M. Landrø, and M. Wilson, 339-369.
- Bear, J. (1972) *Dynamics of Fluids in Porous Media*. Elsevier.
- Berchenko, I., Detournay, E., Chandler, N., Martino, J. (2004) An in-situ thermo-hydraulic experiment in a saturated granite I: design and results. *Int J Rock Mech Min Sci.* 41: 1377-94.

- Bernabé, Y. (1986) The effective pressure law for permeability in Chelmsford granite and Barre granite. *Int J Rock Mech Min Sci Geomech Abstr.* 23: 267-275.
- Bernabé, Y., Mok, U., Evans, B. (2003) Permeability–porosity relationships in rocks subjected to various evolution processes. *Pure Appl Geophys.* 160: 937–960.
- Bhandari, A.R., Flemings, P.B., Polito, P.J., Cronin, M.B., Bryant, S.L. (2015) Anisotropy and Stress Dependence of Permeability in the Barnett Shale. *Trans Porous Med.* 108: 393-411.
- Biot, M.A. (1941) General theory of three-dimensional consolidation. *J Appl Phys.* 12: 155-164.
- Biot, M.A. (1973) Nonlinear and semilinear rheology of porous solids. *J Geophys Res.* 78: 4924-4937.
- Bishop, A.W. (1976) The influence of an undrained change in stress on the pore pressure in porous media of low compressibility. *Géotechnique.* 26: 371–375.
- Blinks, B.P., Clint, J.H. (2002) Solid wettability from surface energy components: relevance to pickering emulsions. *Langmuir.* 18: 1270–1273.
- Bloomfield, J.P., Williams, A.T. (1995) An empirical liquid permeability-gas permeability correlation for use in aquifer properties studies. *Q J Eng Geol.* 28: 143–150.
- Bossart, P., Thury, M. (2008) Mont Terri Rock Laboratory—Project, programme 1996 to 2007 and results (Vol. 3). Wabern: Swiss Geological Survey.
- Boulin, P., Bretonnier, P., Gland, N., Lombard, J.-M. (2012) Contribution of the steady state method to water permeability measurement in very low permeability porous media. *Oil Gas Sci Technol. –Rev. IFP Energies Nouvelles.* 67: 387–401.
- Bourbié, T., Zinszner, B. (1985) Hydraulic and acoustic properties as a function of porosity in Fontainebleau sandstone. *J Geophys Res.* 90: 11524–11532.
- Bourbié, T., Coussy, O., Zinszner, B. (1987) *Acoustics of porous media*: Gulf Publ. Co.

- Bower, K.M., Zyvoloski, G. (1997) A numerical model for thermo-hydro-mechanical coupling in fractured rock. *Int J Rock Mech Min Sci.* 34: 1201-1211.
- Brace, W.F., Walsh J.B., Frangos, W.T. (1968) Permeability of granite under high pressure. *J Geophys Res.* 73: 2225–2236.
- Bredehoeft, J.D., Norton, D.L. (1990) Mass and energy transport in a deforming Earth's crust. In *NRC Study in Geophysics (Ed.), The Role of Fluids in Crustal Processes (27e41)*. Washington D.C: National Academy Press.
- Broadbent, S.E., Hammersley, J.M. (1957) Percolation Processes I. Crystals and Mazes: *Proc Cambridge Philos Soc.* 63: 629-641.
- Bustin, R.M., Bustin, A.M.M., Cui, X., Ross, D.J.K., Murthy Pathi, V.S. (2008) Impact of shale properties on pore structure and storage characteristics. *Soc Petrol Eng.* 119892.
- Carman, P.C. (1938) The determination of the specific surface of powders. *J Soc Chem Ind Trans.* 57, 225.
- Carman, P.C. (1956) *Flow of gases through porous media*. Butterworths Scientific Publications, London.
- Carvalho, F.C.S., Chen, C.-N., Labuz, J.F. (1997) Measurements of effective elastic modulus and microcrack density. *J Rock Mech Min Sci.* 34: 3-4.
- Chen, Z.R. (2011) Poroelastic model for induced stresses and deformation in hydrocarbon and geothermal reservoirs. *J Petro Sci Eng.* 80: 41-52.
- Civan, F. (1996) A multi-purpose formation damage model, *Formation Damage Symposium*. Proceedings: *Soc Petrol Eng.* 31101: 311-326.

- Civan, F. (2000) Predictability of Porosity and Permeability Alterations by Geochemical and Geomechanical Rock and Fluid Interactions, Paper SPE 58746, Proceedings of the SPE International Symposium on Formation Damage, Lafayette, Louisiana.
- Civan, F. (2001) Scale Effect on Porosity and Permeability- Kinetics, Model, and Correlation. *AICHE J.* 47: 271-287.
- Civan, F. (2019) Stress-dependent porosity and permeability of porous rocks represented by a mechanistic elastic cylindrical pore-shell model. *Transp Porous Med.* 129: 885-899.
- Croisé, J., Schlickenrieder, L., Marschall, P., Boisson, J. Y., Vogel, P., Yamamoto, S. (2004) Hydrogeological investigations in a low permeability claystone formation: the Mont Terri Rock Laboratory. *Phys Chem Earth.* 29(1): 3-15.
- Coyner, K.B. (1984) Effects of Stress, Pore Pressure, and Pore-fluids on Bulk Strain, Velocity and Permeability in Rocks (Ph.D. Thesis, Massachusetts Institute of Technology).
- Cui, X., Bustin, A.M.M., Bustin, R.M. (2009) Measurements of gas permeability and diffusivity of tight reservoir rocks: different approaches and their applications. *Geofluids.* 9: 208-223.
- David, C., Wong, T.-f., Zhu, W., Zhang, J. (1994) Laboratory Measurement of Compaction-induced Permeability Change in Porous Rock: Implications for the Generation and Maintenance of Pore Pressure Excess in the Crust. *Pure Appl Geophys.* 143: 425–456.
- Detournay, E., Cheng, A.H.-D. (1993) Fundamentals of poroelasticity. In: Fairhurst C, editor. *Comprehensive rock engineering, Vol. II.* Oxford: Pergamon. 113–71.
- Dong, J.J., Hsu, J.Y., Wu, W.J., Shimamoto, T., Hung, J.H., Yeh, E.C., et al. (2010) Stress dependence of the permeability and porosity of sandstone and shale from TCDP Hole-A. *Int J Rock Mech Min Sci.* 47: 1141–1157.

- Doyen P.M. (1988) Permeability, conductivity, and pore geometry of sandstone. *J Geophys Res.* 93: 7729–7740.
- Ethington, E.F. (1990) Interfacial contact angle measurements of water, mercury, and 20 organic liquids on quartz, calcite, biotite, and Ca-montmorillonite substrates. U. S. Department of the interior Geological Survey. Open File Report. 90-409.
- Ezekwe, N. (2010) *Petroleum Reservoir Engineering Practice*. Prentice Hall, United States.
- Ge, S. (1997) A governing equation for fluid flow in rough fractures, *Water Resour Res.* 33: 53-61.
- Ghanbarian, B., Hunt, A.G., Ewing, R.P., Sahimi, M. (2013) Tortuosity in porous media: a critical review. *Soil Sci Soc Am J.* 77: 1461-1477.
- Grainger, P. (1984) The classification of mudrocks for engineering purposes. *Q J Eng Geol.* 17: 381–387.
- Gueguen, Y., Dienes, J. (1989) Transport properties of rocks from statistics and percolation. *Math Geol.* 21: 1-13.
- Hart, D.J., Wang, H.F. (1995) Laboratory measurements of a complete set of poroelastic moduli for Berea sandstone and Indiana limestone. *J Geophys Res.* 100: 17741-17751.
- Hart, D.J., Bradbury, K.R., Feinstein, D.T. (2005) The vertical hydraulic conductivity of an aquitard at two spatial scales. *Ground Water.* 44: 201-211.
- Hsieh, P.A., Tracy, J.V., Neuzil, C.E., Bredehoeft, J.D., Silliman, S.E. (1981) A Transient Laboratory Method for Determining the Hydraulic Properties of ‘Tight’ Rocks - I. Theory. *Int J Rock Mech Min Sci Geomech Abstr.* 18: 245-252.
- Kim, K., Vilarrasa, V., Makhnenko, R. Y. (2018) CO₂ injection effect on geomechanical and flow properties of calcite-rich reservoirs. *Fluids.* 3: 3.

- Kiyama, T., Kita, H., Ishijima, Y., Yanagidani, T., Aoki, K., and Sato, T. (1996) Permeability in anisotropic granite under hydrostatic compression and triaxial compression including post-failure region. *Rock mechanics: Tools and Techniques, Proceedings of the 2nd North American Rock Mechanics Symposium*. 2: 1161-1168.
- Klinkenberg, L.J. (1941) The permeability of porous media to liquids and gases. *Am Petrol Inst Drilling Production Pract*. 2: 200-213.
- Kozeny, J. (1927) Ueber kapillare Leitung des Wassers im Boden. *Wien. Akad Wiss*. 136(2a): 271.
- Kuila, U., Prasad, M. (2013) Specific surface area and pore-size distribution in clays and shales. *Geophys Prospect*. 61(2): 341-362.
- Law, B.E., Spencer, C.W.: Gas in tight reservoirs-an emerging major source of energy, in David G. Howell (ed.) (1993) *The Future of Energy Gasses*. US Geological Survey, Professional Paper. 1570: 233-252.
- Loucks, R.G., Reed, R.M., Ruppel, S.C., Hammes, U. (2012) Spectrum of pore types and networks in mudrocks and a descriptive classification for matrix-related mudrock pores. *AAPG Bulletin*. 96(6): 1071–1098.
- Lowe, J., Johnson, T.C. (1960) Use of back pressure to increase degree of saturation of triaxial test specimens. *Proceedings of the research conference on shear strength of cohesive soils*. Boulder, Colorado, ASCE. 819-836. June.
- Makhnenko, R.Y., Labuz, J.F. (2016) Elastic and inelastic deformation of fluid-saturated rock. *Phil Trans R Soc A*. 374: 20150422.
- Makhnenko, R.Y., Tarokh, A., Podladchikov, Y. (2017). On theunjacketed moduli of sedimentary rock (pp. 897–904). In M. Vandamme, P. Dangla, J.-M. Pereira, & S. Ghabezloo

- (Eds.), *Poromechanics VI—Proceedings of the 6th Biot Conference on Poromechanics*. Reston, VA: American Society of Civil Engineers.
- Makhnenko, R.Y., Podladchikov, Y.Y. (2018) Experimental poroviscoelasticity of common sedimentary rocks. *J Geophys Res Sol Earth*. 123(9): 7586–7603.
- Marschall, P., Horseman, S., Gimmi, T. (2005) Characterisation of gas transport properties of the Opalinus Clay, a potential host rock formation for radioactive waste disposal. *Oil Gas Sci Technol*. 60(1): 121-139.
- Mavko, G., Nur, A. (1997) The effect of a percolation threshold in the Kozeny-Carman relation. *Geophysics*. 62: 1480-1482.
- Mavko, G., Mukerji, T., Dvorkin, J. (2009) *The Rock Physics Handbook: Tools for Seismic Analysis in Porous Media*. Cambridge Univ. Press, Cambridge, U. K.
- Mehmani, A., Prodanović, M., Javadpour, F. (2013) Multiscale, multiphysics network modeling of shale matrix gas flows. *Transp Porous Med*. 99: 377-390.
- Morrow C.A., and Lockner D.A. (1997) Permeability and porosity of the Illinois UPH 3 drillhole granite and a comparison with other drillhole rocks. *J Geophys Res*. 102: 3067–3075.
- National Research Council (2012) *Induced seismicity potential in energy technologies*. National Academies Press. Washington, D.C.
- Nelson, P.H. (1994) Permeability-porosity relationships in sedimentary rocks. *The Log Analyst*. 35: 38-62.
- Neufelder, R.J., Bowen, B.B., Lahann, R.W., Rupp, J.A. (2012) Lithologic, mineralogical, and petrophysical characteristics of the Eau Claire Formation: complexities of a carbon storage system seal. *Environ Geosci*. 19: 81–104.

- Neuzil, C.E., Cooley, C., Silliman, S.E., Bredehoeft, J.D., Hsieh, P.A. (1981) Transient Laboratory Method for Determining the Hydraulic Properties of 'Tight' Rocks - II. Application. *Int J Rock Mech Min Sci Geomech Abstr.* 18: 253-258.
- Neuzil, C.E. (1994) How permeable are clays and shales? *Water Resour Res.* 30: 145-150.
- Noorishad, J., Tsang, C.F., Witherspoon, P.A. (1984) Coupled thermal-hydraulic-mechanical phenomena in saturated fractured porous rocks: numerical approach. *J Geophys Res.* 89: 365-373.
- Pearson, F.J. (2002) PC experiment: Recipe for artificial pore water (Tech. Note 2002-17). Mont Terri Project, St-Ursanne, Switzerland.
- Plümper, O., John, T., Podladchikov, Y.Y., Vrijmoed, J.C., Scambelluri, M. (2017) Fluid escape from subduction zones controlled by channel-forming reactive porosity. *Nat Geosci.* 10: 150-156.
- Quintard, M. (1993) Diffusion in isotropic and anisotropic porous systems: three-dimensional calculations. *Transp Porous Med.* 11(2): 187–199.
- Räss, L., Makhnenko, Y.R., Podladchikov, Y., Laloui, L. (2017) Quantification of viscous creep influence on storage capacity of caprock. *Energy Procedia.* 114: 3237–3246.
- Rass, L., Simon, N.S.C., Podladchikov, Y.Y. (2018) Spontaneous formation of fluid escape pipes from subsurface reservoirs. *Nature Sc Rep.* 8(1): 11116.
- Raven, K.G., Gale, J.E. (1985) Water flow in a natural rock fracture as a function of stress and sample size. *Int J Rock Mech Min Sci Geomech Abstr.* 22: 251-261.
- Revil, A., Cathles, L.M. (1999) Permeability of shaly sands, *Water Resour Res.* 35: 651-662.
- Rice, J.R., Cleary, M.P. (1976) Some basic stress diffusion solutions for fluid-saturated elastic porous media with compressible constituents. *Rev Geophys.* 14: 227-241.

- Romero, E., Senger, R., Marschall, P. (2012) Air Injection Laboratory Experiments on Opalinus Clay. Experimental techniques, Results and Analyses. In 3rd EAGE Shale Workshop-Shale Physics and Shale Chemistry. European Association of Geoscientists & Engineers.
- Rose, W.D. (1948) Permeability and gas-slippage phenomena. *API Drill and Prod Prac.* 209-217.
- Ross, D.J.K., Bustin, R.M. (2009) The importance of shale composition and pore structure upon gas storage potential of shale gas reservoirs. *Mar Petrol Geol.* 26: 916-927.
- Rutqvist, J., Vasco, D.W., Myer, L. (2010) Coupled reservoir-geomechanical analysis of CO₂ injection and ground deformations at In Salah, Algeria. *Int J Greenhouse Gas Control.* 4: 225-230.
- Rutqvist, J. (2012) The geomechanics of CO₂ storage in deep sedimentary formations. *Geotech Geol Eng.* 30(3): 525-551.
- Sakhaee-Pour, A., Bryant, S.L. (2012) Gas permeability of shale. *SPE Reservoir. Eval Eng.* 15: 401–409.
- Salimzadeh, S., Paluszny, A., Zimmerman, R.W. (2017) Three-dimensional poroelastic effects during hydraulic fracturing in permeable rocks. *Int J Solids Struct.* 108: 153–163.
- Schulz, R., Ray, N., Zech, S., Rupp, A., Knabner, P. (2019) Beyond Kozeny-Carman: Predicting the permeability in porous media. *Trans Porous Med.* 130: 487-512.
- Skempton, A.W. (1954) The pore pressure coefficients A and B. *Geotechnique.* 4: 143-147.
- Song, J., Zhang, D. (2012) Comprehensive review of caprock-sealing mechanisms for geologic carbon sequestration. *Environ Sci Technol.* 47(1): 9-22.
- South, D.L., Daemen, J.J.: (1986) Permeameter studies of water flow through cement and clay borehole seals in granite, basalt and tuff. No. NUREG/CR—4748. Arizona Univ, Tucson, AZ, United States.

- Stauffer, D. (1985) Introduction to Percolation Theory. Taylor and Francis, London.
- Suri, P., Azeemuddin, M., Zaman, M., Kukreti, A.R., Roegiers, J.-C. (1997) Stress-dependent permeability measurement using the oscillating pulse technique. *J Petrol Sci Eng.* 17: 247-264.
- Tarokh, A., Detournay, E., Labuz, J. (2018) Direct measurement of the unjacketed pore modulus of porous solids. *Phil Trans R Soc A.* 474: 1–21.
- Tarokh, A., Makhnenko, R.Y. (2019) Remarks on the solid and bulk responses of fluid-filled porous rock. *Geophysics.* 84(4): WA83–WA95.
- Terzaghi, K. (1923) Die berechnung der durchlassigkeitsziffer des tones aus dem verlauf der hydrodynamischen spannungsercheinungen. *Sitzungsber. Akad Wissen. Wien Math Naturwiss Kl Abt Iia.* 132: 105–124.
- Tian, M., Ague, J.J. (2014) The impact of porosity waves on crustal reaction progress and CO₂ mass transfer. *Earth Planet Sc Lett.* 390: 80-92.
- Trimmer, D.A. (1981) Design criteria for laboratory measurements of low permeable rocks. *Geophys Res Lett.* 8: 973-975.
- Tsang, C.-F., Bernier, F., Davies, C. (2004) Geohydromechanical processes in the Excavation Damaged Zone in crystalline rock, rock salt, and indurated and plastic clays in the context of radioactive waste disposal. *Int J Rock Mech Mining Sc.* 42 (1): 109–125.
- Vilarrasa, V., Bolster, D., Olivella, S., Carrera, J. (2010) Coupled hydromechanical modeling of CO₂ sequestration in deep saline aquifers. *Int J Greenh Gas Control.* 4(6): 910-919.
- Walder, J., Nur, A. (1984) Porosity reduction and crustal pore pressure development. *J Geophys Res.* 89: 539-548.
- Walsh, J.B. (1965) The effect of cracks on compressibility of rock. *J Geophys Res.* 70: 381-389.

- Wang, H.F. (2000) Theory of linear poroelasticity with applications to geomechanics and hydrogeology. Princeton, NJ: Princeton University Press.
- Wenzel, R. N. (1936) Resistance of solid surfaces to wetting by water. *Industrial and Engineering Chemistry* 28: 988.
- Witherspoon, P.A. (1986) Flow of groundwater in fractured rocks. *Bulletin of the IAEG* 34: 103-115.
- Wyllie, M.R.J., Gardner, G.H.F. (1958a) The generalized Kozeny-Carman equation, Part 1 – Review of existing theories. *World Oil*. 146: 121-126.
- Wyllie, M.R.J., Gardner, G.H.F. (1958b) The generalized Kozeny-Carman equation, Part 2 – A novel approach to problems of fluid flow. *World Oil*. 146: 210-228.
- Yang, Y., Aplin, A.C. (2007) Permeability and petrophysical properties of 30 natural mudstones. *J Geophys Res*. 112.
- Zimmerman, R.W. (2017) Pore volume and porosity changes under uniaxial strain conditions. *Trans Porous Med*. 119: 481-498.
- Zhang, R., Ning, Z., Yang, F., Wang, X., Zhao, H., Wang, Q. (2015) Impacts of nanopore structure and elastic properties on stress-dependent permeability of gas shales. *J Nat Gas Sci Eng*. 26: 1663-1672.

CHAPTER 9: IMPLICATIONS AND FUTURE WORK

9.1 Implications

A laboratory-scale experimental framework for the effect of CO₂ injection on the poromechanical and multiphase flow responses of subsurface formation is presented in this thesis. A hydro-mechanical-chemical coupled constitutive model is adopted, and the involved parameters are defined and accurately assessed for the reservoir formation. In this section, a practical implication of this study to geologic carbon storage is discussed with the existing limitations that may be improved in the future work.

The implication of this study can be described in four major aspects. First, characterizing the effect of CO₂ injection on the poroelastic response of reservoir rock can provide an understanding of its short-term behavior. In an industrial CO₂ storage site at In Salah, Algeria, it was observed that surface uplift occurred during the injection process, which may jeopardize the integrity of the system and cause an undesirable damage for subsurface infrastructure (Rinaldi and Rutqvist, 2013). Also, as the CO₂ injection instantly increases the pore pressure, changing the effective mean stress closer to the failure criteria, properly understanding the short-term response for CO₂ storage becomes crucial. Moreover, for the limestone reservoirs, such as the one in Weyburn project in Canada, alteration of the pore structures due to dissolution was reported, implying the chemical effect of CO₂ injection may affect this poromechanical response (Verdon et al., 2013).

Secondly, as the CO₂ injection projects aim for thousands of years of permanent CO₂ storage, the time scale of the applicability of the constitutive relationships needs to be extended to consider the time-dependent response of reservoir rock. In Weyburn project, a long-term pressure buildup

of 5-6 MPa was monitored from the modeled pore pressures after stopping the CO₂ injection (Verdon et al., 2013), implying that the time-dependent behavior must be considered for safe permanent CO₂ storage. As this study reveals that the chemical effect can promote the time-dependent deformation, it is believed that the findings may provide more accurate understanding of the long-term response of reservoir rock.

Thirdly, this study suggests a chemo-poro-visco-elastic coupled model to describe the reservoir rock response during CO₂ injection. While most existing studies merely report the effect of CO₂ treatment on separate rock properties such as stiffness, creep, and permeability (Rohmer et al., 2016), the coupled model solely includes the parameters that can be directly measured in laboratory experiments.

Lastly, characterizing the effect of CO₂ treatment on the multiphase flow provides an understanding of the CO₂ injectivity and storage capacity, where the relative permeability can be measured at different degrees of saturation. Additionally, the maximum degree of saturation of water and CO₂ can be evaluated, which is directly related to the storage capacity of the CO₂ storage sites. A schematic illustration of the implication of this study is presented in Figure 9.1.

Although the constitutive equations considering the time-dependent behavior and chemical effect are introduced, they can not be directly utilized for the field-scale geologic carbon storage due to the discrepancy in the scale. Moreover, as faults or cracks exist in the large-scale reservoir, the poromechanical properties and the constitutive equations adopted at the lab scale become inapplicable for the fault region. Therefore, for the short-term response, the poromechanical and hydraulic properties of the fault zone need to be separately determined, that generally has a larger deformation and permeability, compared to that of the intact material (Caine et al., 1996; Cappa and Rutqvist, 2011). The scale effect also needs to be considered for the long-term

response. While the bulk viscosity values of reservoir rock measured in this study are reported in the order of 10^{15} - 10^{16} Pa·s, Karato (2010) stated that the reservoir-scale viscosity values for the solid Earth materials are generally in the range of 10^{19} - 10^{22} Pa·s, much higher than the laboratory-scale measurements. The main reason for this discrepancy is elaborated in Chapter 5, where the field-scale rock formations can be much more permeable and compressible due to the presence of fractures, which eventually reduces the compaction effect on the time-dependent deformation. This implies that there are limitations to this study, as artificial pore pressure buildup measurements are taken for the time-scale of only a few hours right after the rock specimens were taken out of the equilibrium. Despite these limitations, it can be argued that the effect of CO₂ treatment on the time-dependent response is investigated in a laboratory-scale experiment, that can further be extrapolated for the reservoir application in future work.

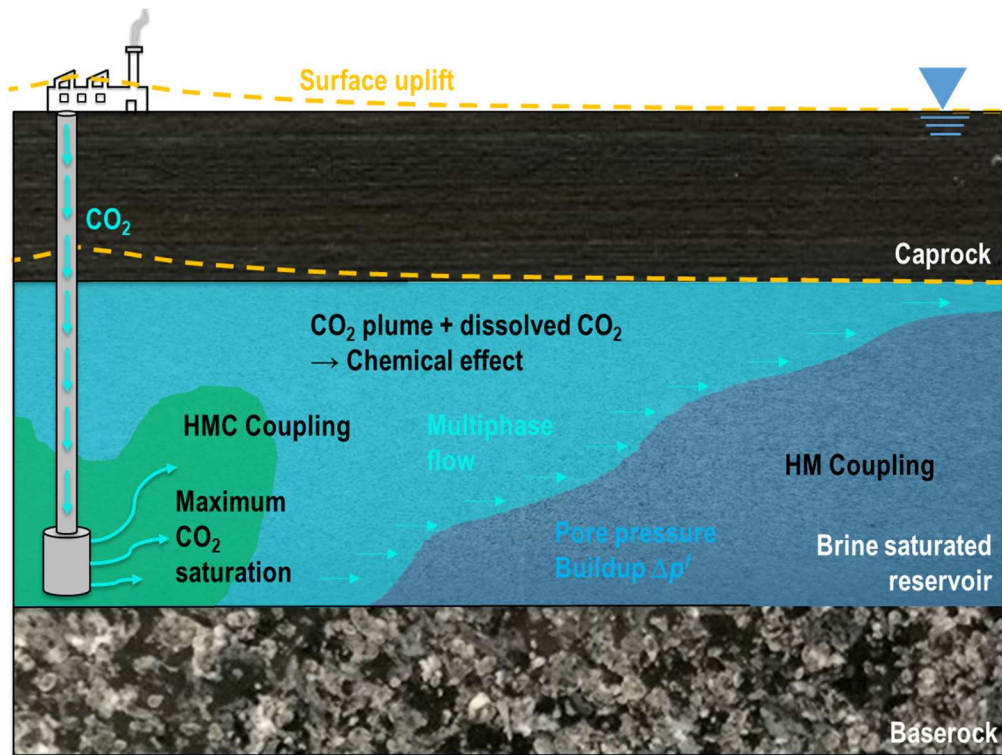


Figure 9.1. Schematic illustration of the implication of this study to geologic carbon storage.

Another important limitation that can be suggested for future work is the time-dependent response under deviatoric loading. For this study, the viscous behavior of reservoir rock is monitored under hydrostatic loading, as it may not be the case for many subsurface rocks. As it has been reported that reservoir rock for GCS at 1-3 km depths is subjected to significant deviatoric in-situ stresses, it becomes important to experimentally characterize the time-dependent behavior under shearing (van der Meer, 1992). Although some preliminary experiments revealed that the viscous response might differ under deviatoric loading from the hydrostatic loading, it still requires further work, as there exist discrepancies among the existing studies (Rohmer et al., 2016).

An important application of the experimental work to geologic carbon storage is to evaluate the stability of the system. As it is important to avoid any inelastic response for safe CO₂ storage, the stress state can be assessed with respect to the yield conditions to assure it is within the elastic regime. For example, the stress state of the reservoir condition can be evaluated by adopting the Mohr-Coulomb failure criteria for Apulian limestone. As the strength and poroelastic properties are accurately measured for the pristine and CO₂ treated specimens in Chapter 3, the P' - q diagram is presented in Figure 9.2. The analysis shows that for the limestone, it is important to consider the chemical effect on the poromechanical properties, since the stress state moves significantly closer to the failure criteria by altering the failure envelope. Moreover, from the pore pressure buildup, it can be seen that the time-dependent response may also jeopardize the stability of the system, indicating the importance of considering it for geologic carbon storage projects. It is to be noted that by measuring the strength properties of any joints with potential failure, the stress state can also be compared with its failure criteria to guarantee stability.

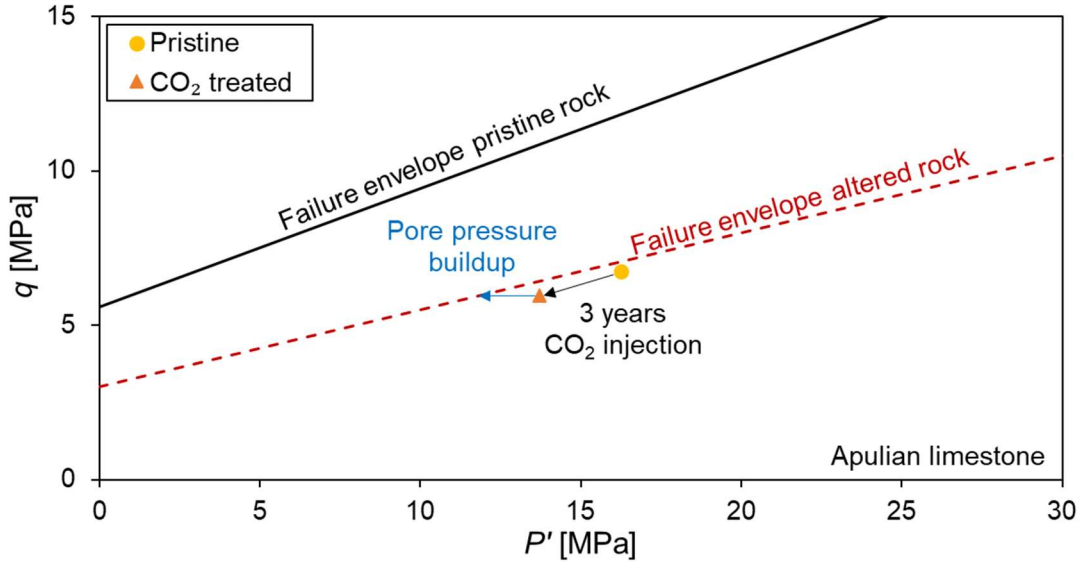


Figure 9.2. P' - q diagram for pristine and CO_2 treated Apulian limestone.

9.2 Future work

Based on the experimental work presented in this thesis, future work is proposed.

First, further investigation may be continued to complete the full coupling of the hydro-mechanical-chemical model for reservoir formation. Although chapter 6 adopts a chemo-poro-visco-elastic model and determines the chemical parameters by measuring the poromechanical properties, the analysis contains assumptions on the chemical perspective that require verification and calibration. As the reservoir formations at field scale GCS sites are generally multimineralic, the chemical effect of CO_2 treatment on the other composing minerals (K-feldspar, albite, anorthite, and others) needs to be considered (Rochelle et al., 2004). This future work could be conducted by installing ion electrodes and pH probes and measuring the chemical aspects of the pore fluid. However, difficulties may exist in measuring the chemical responses at high-pressure conditions, and conducting calibration for all the existing chemical reactions.

Additionally, the study on the multiphase flow behavior in reservoir rock may be extended. A novel method is proposed in this thesis to evaluate the degree of saturation of CO_2 and water by

accurately measuring the poroelastic properties. Although the independent mercury intrusion porosimetry measurement provide some verification, further validation may be achieved by using X-ray CT scanning, as it can visualize the water and CO₂ distribution in the pores. Also, the in-situ contact angle and interfacial tension measurements can be conducted to provide an enhanced understanding of the multiphase flow behavior.

Studies on the sealing layer material (tight rock) have been conducted, where the poromechanical and hydraulic characteristics have been assessed. As the fluid flow is directly related to the in-situ stress state, a coupled porosity-permeability relationship is established. For GCS, understanding these responses is of great interest since the potential leakages can be evaluated for the tight sealing layers. However, to properly assess the sealing efficiency, the relative permeability and breakthrough pressure of CO₂ need to be accurately evaluated (Kaldi et al., 2011; Makhnenko et al., 2017). Future work can be proposed on characterizing the multiphase flow response and breakthrough pressure of the tight sealing layers. In this section, some preliminary measurements are presented.

The relative permeability curves for the sealing layers are presented in Figure 9.3. The novel methods introduced in Chapters 3 and 7 are implemented for tight rock. The two-phase flow tests can only be conducted at a 1:1 ratio for the selected tight rocks because the minimum flow rate the syringe pump can apply is 0.001mL/min and exceeding this limit leads to pressure buildup at specimen interface. For Charcoal granite, the fitting exponent parameter N_w is calculated to be 1.9, while the maximum degree of saturation for CO₂ is determined as 0.59. In contrast, the relative permeability curve for Opalinus Clay provides $N_w = 5.5$ with the maximum degree of CO₂ saturation as 0.60, which is in agreement with previous studies on shales (Bennion and Bachu, 2008). The discrepancy between the exponent parameters of the two materials can be

explained by preferable pathways that may exist in crystalline rock. $N_w = 1.9$ for Charcoal granite can be considered relatively low for a tight rock, where the pore space exists mainly in terms of microcracks. It is possible that water and CO_2 are flowing through the granite's pore network without much interaction between them. Further investigations on relative permeability can be conducted on measuring more discrete points for the $k_r - S$ curve, and also monitoring the evolution of the relative permeability curve with time and hysteresis.

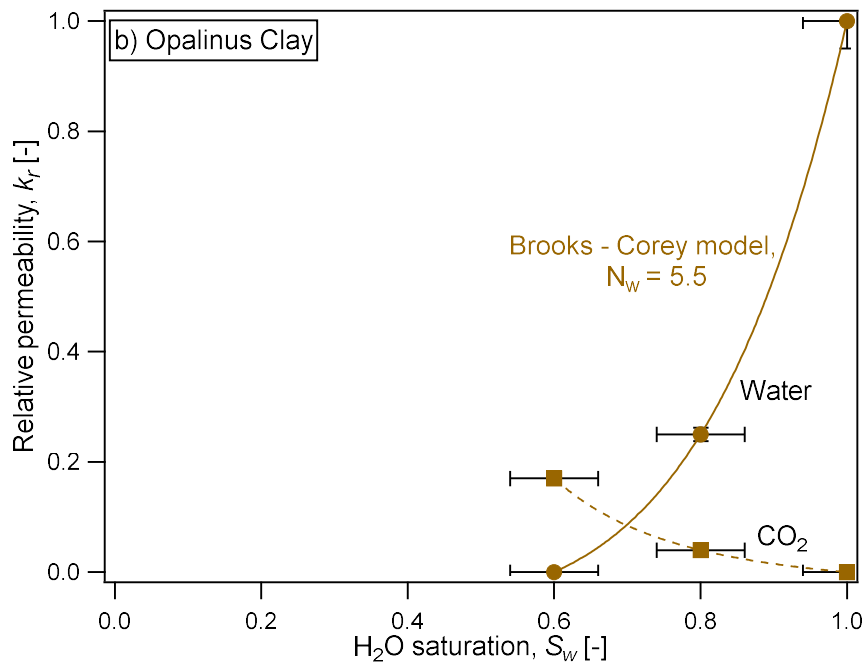
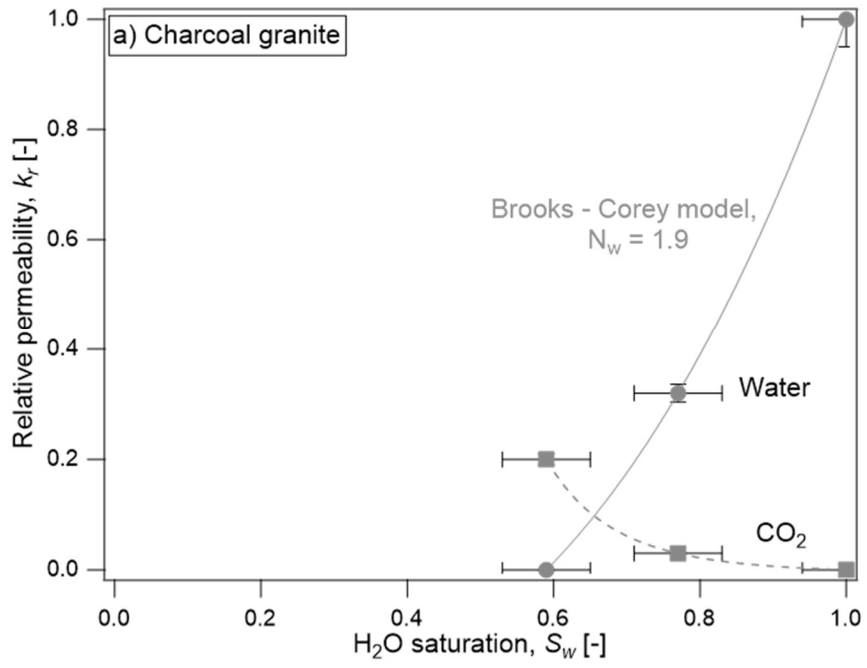


Figure 9.3. Relative permeability curves for a) Charcoal granite and b) Opalinus Clay.

Limited measurements of the breakthrough pressures are provided for different effective stress conditions and compared for the tested materials in this study (Figure 9.4). Preliminary results show that the breakthrough pressures for Opalinus Clay are measured as ~ 2 MPa at different effective stresses. This implies that the nature of the breakthrough itself is not affected by the pore deformation, but once it exceeds the breakthrough pressure, the CO₂ permeability can be promoted by increasing the injection pressure.

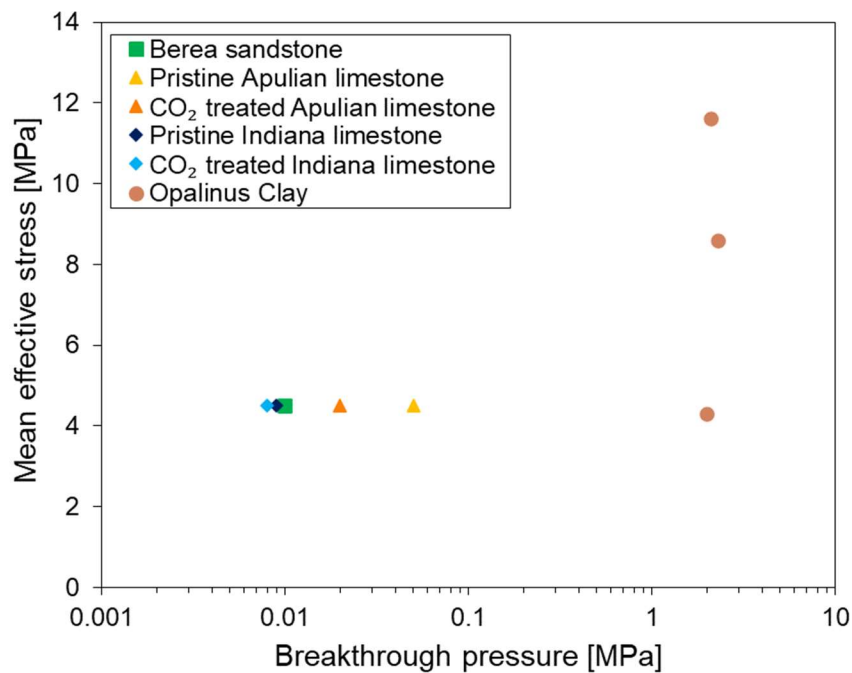


Figure 9.4. CO₂ breakthrough pressures for reservoir and caprock materials at different effective mean stresses.

The effect of CO₂ treatment on the breakthrough pressure of reservoir formation is estimated from the capillary pressure saturation curves provided in chapter 7 (Figure 9.2). The chemical effect of CO₂ injection decreases the breakthrough pressures for limestones, while it does not change for the sandstone.

Future work may also be extended to the practical application for GCS projects. The scale effect, starting from the microscopic to the macroscopic, and finally to the macro to the field scale, needs to be understood. Another important aspect that may be studied in the future is the effect of temperature, which is assumed to be constant for this study. As CO₂ changes its phase into the supercritical at high-temperature/pressure conditions ($p^f > 7.3$ MPa and $T > 31$ °C), the poromechanical and hydraulic experiments can be conducted using supercritical CO₂ as the pore fluid. Moreover, on top of the HMC model, the constitutive equations may be extended to include thermo-hydro-mechanical-chemical (THMC) coupling, where additional sets of material parameters should be introduced.

References

- Bennion, D.B., Bachu, S. (2008) Drainage and imbibition relative permeability relationships for supercritical CO₂/brine and H₂S/brine systems in intergranular sandstone, carbonate, shale, and anhydrite rocks. SPE Reserv Eng. 11(03): 487-96.
- Caine, J.S., Evans, J.P., Forster, C.B. (1996) Fault zone architecture and permeability structure. Geology. 24(11): 1025-8.
- Cappa, F., Rutqvist, J. (2011) Modeling of coupled deformation and permeability evolution during fault reactivation induced by deep underground injection of CO₂. Int J Greenh Gas Control. 5(2): 336-46.
- Goertz-Allmann, B.P., Gibbons, S.J., Oye, V., Bauer, R., Will, R. (2017) Characterization of induced seismicity patterns derived from internal structure in event clusters. J Geophys Res: Solid Earth. 122(5): 3875-94.

- Kaldi, J., Daniel, R., Tenthorey, E., Michael, K., Schacht, U., Nicol, A., Underschultz, J., Backe, G. (2011) Caprock systems for CO₂ geological storage. IAEGHG Rep. 1: 149.
- Karato, S. (2010) Rheology of the Earth's mantle: A historical review. *Gondwana Res* 18(1): 17–45.
- Makhnenko, R.Y., Vilarrasa, V., Mylnikov, D., Laloui, L. (2017) Hydromechanical aspects of CO₂ breakthrough into clay-rich caprock. *Energy Procedia*. 114: 3219-28.
- Rinaldi, A.P., Rutqvist, J. (2013) Modeling of deep fracture zone opening and transient ground surface uplift at KB-502 CO₂ injection well, In Salah, Algeria. *Int J Greenh Gas Control*. 12: 155-67.
- Rochelle, C.A., Czernichowski-Lauriol, I., Milodowski, A.E. (2004) The impact of chemical reactions on CO₂ storage in geological formations: a brief review. *Geol Soc., London, Special Publications*. 233(1): 87-106.
- Rohmer, J., Pluymakers, A., Renard, F. (2016) Mechano-chemical interactions in sedimentary rocks in the context of CO₂ storage: Weak acid, weak effects?. *Earth-Science Rev*. 157: 86-110.
- van der Meer, L.G.H. (1992) Investigations regarding the storage of carbon dioxide in aquifers in the Netherlands. *Energ Convers Manage*. 33(5-8): 611-618.
- Verdon, J.P., Kendall, J.M., White, D.J., Angus, D.A. (2011) Linking microseismic event observations with geomechanical models to minimise the risks of storing CO₂ in geological formations. *Earth Planet Sci Lett*. 305(1-2): 143-152.

CHAPTER 10: CONCLUSIONS

This study aims to establish a comprehensive experimental framework to characterize the effect of CO₂ treatment on the poromechanical and hydraulic characteristics of subsurface rock. Representative materials for the formations participating in geologic carbon storage are selected, and a series of experiments are conducted to accurately evaluate their hydromechanical responses. Berea sandstone is selected as the representative material for silica-rich rock, while Apulian and Indiana limestones are chosen for calcite-rich rock. For the sealing layers, two caprock representative materials, Opalinus Clay (shale) and Eau Claire shale are tested, and Charcoal granite represents the basement rock. The experimental methods for the core flooding device, hydrostatic compression system, triaxial compression system, and mercury intrusion porosimetry are presented. A poroviscoelastic constitutive model is adopted, where the involved parameters are accurately determined for the short- and long-term responses. For the multiphase flow, the relative permeability curves are determined by introducing a novel method, where the degree of saturation is estimated from the changes in poroelastic properties upon CO₂ injection. The chemical effect of CO₂ treatment on the multiphysical processes of reservoir rock is studied by monitoring the change in the poromechanical and hydraulic characteristics, where the pristine and CO₂ treated specimens are compared and a hydro-mechanical-chemical model is suggested. Furthermore, the porosity-permeability relationship is established for tight rock by coupling the poromechanical and flow behavior, as it is important to assure their permeability remains low to prevent the leakage through the sealing layers. The findings of this thesis are separately reported in each chapter and the summary of the essential discoveries are as follows.

1. The effect of CO₂ treatment on the compressibility is investigated for the reservoir rocks and their composing minerals. By measuring the bulk moduli of the rock frame and the composing minerals, it is shown that the chemical effect for the sandstone is minor, while calcite dissolution and precipitation affect the limestones' behavior by creating new connected and non-connected pores.
2. The time-dependent response and the effect of CO₂ treatment are explored. A decrease in the jacketed and unjacketed bulk moduli of limestones is reported as 20%. For Berea sandstone, the unjacketed bulk modulus remains unchanged, while the jacketed bulk modulus decreased by around 15%. The CO₂ treatment decreases the bulk viscosity by 50-60% for all materials, promoting more rapid viscous deformation. It appears that the permeability of all tested rock increases due to CO₂ treatment by 10-15%, while the power-law porosity-permeability relationship remains unchanged. The effect of CO₂ treatment is different for sandstone and limestones, where the dissolution and rearrangement of calcite particles is believed to be the main reason for changes in limestone properties, while apparent extension of microcracks caused by stress corrosion is assumed to be the governing mechanism in the sandstone.
3. A hydro-mechanical-chemical model is suggested, as the poroviscoelastic properties are monitored during the treatment process. From the variation of the rock's porosity, the chemical effect of CO₂ treatment is included in the constitutive model. The data on two monomineralic limestones (Apulian and Indiana) is used to validate the model. The predictions for the hydro-mechanical-chemical vs the hydro-mechanical models differ concerning compaction/dilation. If the chemical effect is not considered – the porosity is expected to decrease with time, while its increased is observed during the CO₂ treatment, highlighting the importance of considering the chemical aspect in the constitutive model.

4. The impact of CO₂ treatment on the multiphase flow in reservoir rock is studied, with measurements of the microscale properties such as capillary pressure, wettability, and surface roughness. The capillary pressure curves for limestones alter due to the chemical effect of CO₂ injection, indicating that the relative permeability increases with maximum CO₂ saturation. This implies that the chemical effect can increase the CO₂ injectivity in calcite-rich rock, emphasizing that it is important to adopt accurate multiphase flow parameters for reservoir models describing the injection processes.
5. An experimental method is proposed to evaluate the porosity-permeability relationship for tight rock representing the sealing layers for CO₂ storage by coupling its mechanical and flow responses. The porosity-permeability relationship is established by integrating the experimental results with a porosity sensitivity exponent, based on accurate measurements of the poroelastic and hydraulic responses of the materials. The analysis presents that the relationship for tight rock has an exponent value around 15-17, while it is significantly larger than that for the porous rock. This indicates that a small change in the porosity may remarkably alter the permeability, which is important for the sealing layers.

Lastly, the implications and future work based on the findings in this thesis are presented. The general applications of the proposed approaches to reservoir modeling are discussed, as well as the limitations regarding the scale effect and deviatoric loading. Future work is proposed for the measurements of the chemical aspects for the hydro-mechanical-chemical coupling model, and validation of the multiphase flow study with different methods. Then, some preliminary results on characterizing the two-phase flow behavior in tight rock are introduced with breakthrough pressure measurements.